HELLENIC REPUBLIC
National and Kapodistrian
University of Athens
EST. 1837

# SPIRAL STRUCTURE AND CHAOS IN N- BODY MODELS OF GALACTIC DISCS

**Zouloumi Konstantina**

A thesis submitted for the degree of
Doctor of Astrophysics

Physics Department
University of Athens
Section of Astrophysics, Astronomy and Mechanics

Greece, 2024

# Contents

# Πρόλογος

Η κατανόηση της φύσης των σπειροειδών βραχιόνων στους γαλαξίες είναι ένα δύσκολο και ανοιχτό αστρονομικό πρόβλημα. Υπάρχουν πολλά ανοιχτά προβλήματα ως προς τη μελέτη της σπειροειδούς δομής, που αφορούν την προέλευση, την εξέλιξη και μακροβιότητα των σπειροειδών βραχιόνων. Η παρούσα διατριβή πραγματεύεται διάφορες δυναμικές προσεγγίσεις που επιτρέπουν την ερμηνεία των παρατηρούμενων γαλαξιακών μορφολογιών. Τέτοιες προσεγγίσεις αναδεικνύουν και το ρόλο του χάους και των μη γραμμικών φαινομένων, και συγκεκριμένα πως αυτά συμβάλλουν στη σταθερότητα και συνοχή των σπειροειδών δομών. Τις τελευταίες δεκαετίες, τα αποτελέσματα πολλών ερευνών στη δυναμική των γαλαξιών έχουν δείξει ότι οι γαλαξίες υφίστανται μια σημαντική μακροχρόνια εξέλιξη. Τα φαινόμενα συγχώνευσης γαλαξιών μπορούν επίσης να επηρεάσουν άμεσα τη δυναμική ενός γαλαξιακού συστήματος. Επιπλέον, οι παρατηρήσεις, καθώς και οι προσομοιώσεις N-σωμάτων ραβδωτών σπειροειδών γαλαξιών δίνουν ισχυρές ενδείξεις για την παρουσία πολλαπλών ταχυτήτων περιστροφής των εκάστοτε δομών σε γαλαξιακούς δίσκους. Αυτό έρχεται σε αντίθεση με την υπόθεση μιας μοναδικής ταχύτητας περιστροφής, που υιοθετείται σε πολλά βασικά θεωρητικά μοντέλα σπειροειδούς δομής. Η θεωρία των κυμάτων πυκνότητας, καθώς και η θεωρία των αναλλοίωτων πολλαπλοτήτων για τη σπειροειδή δομή είναι παραδείγματα τέτοιων μοντέλων. Υπό το φως αυτών των παρατηρήσεων, αναδεικνύεται ότι πρέπει να αναπτυχθούν περαιτέρω δυναμικά μοντέλα σπειροειδούς δομής, ώστε να προσαρμοστούν στα πρόσφατα αποτελέσματα που προέρχονται από παρατηρήσεις και προσομοιώσεις N-σωμάτων.

Στην παρούσα διατριβή κατασκευάζουμε δυναμικά μοντέλα της σπειροειδούς δομής σε δύο διαφορετικές περιπτώσεις: (α) στην περίπτωση μιας προσομοίωσης N-σωμάτων ενός ραβδωτού σπειροειδούς γαλαξία και (β) στην περίπτωση ενός θεωρητικού δυναμικού γαλαξιακού μοντέλου παρόμοιο με τον Γαλαξία μας (Μοντέλο τύπου Milky Way). Η φύση των τροχιών των αστέρων που στηρίζουν τους σπειροειδείς βραχίονες διαφέρει σε αυτές τις δύο περιπτώσεις, αναδεικνύοντας έτσι δύο διαφορετικούς μηχανισμούς υποστήριξης της σπειροειδούς δομής. Στην πρώτη περίπτωση, των ραβδωτών σπειροειδών γαλαξιών, οι σπείρες δημιουργούνται από χαοτικές τροχιές και προσεγγίζονται μέσα από τη θεωρία των αναλλοίωτων πολλαπλοτήτων. Αντίθετα στη δεύτερη περίπτωση, των κανονικών σπειροειδών γαλαξιών, οι σπειροειδείς βραχίονες κατασκευάζονται από οργανωμένες τροχιές («μεταπίπτουσες ελλείψεις»).

Στην περίπτωση της προσομοίωσης N-σωμάτων έχουμε ένα αυτοσυνεπές μοντέλο N-σωμάτων ενός ραβδωτού σπειροειδούς γαλαξία. Από τις θέσεις και τις ταχύτητες των σωμάτων της προσομοίωσης μπορούμε να λάβουμε σημαντικές πληροφορίες που χρησιμοποιούνται στη περαιτέρω μοντελοποίηση, όπως τα σώματα, την επιφανειακή πυκνότητα, τη μέση ταχύτητα και το βαρυτικό δυναμικό σε κάθε σημείο του επιπέδου του γαλαξιακού δίσκου. Στη συνέχεια προχωράμε στον υπολογισμό των αναλλοίωτων πολλαπλοτήτων που υποστηρίζουν τις σπείρες με μία ταχύτητα περιστροφής ή με πολλαπλές ταχύτητες περιστροφής στο γαλαξιακό δίσκο. Παρατη-

ρούμε επίσης την εξέλιξη των αναλλοίωτων πολλαπλοτήτων μαζί με τις μακροχρόνια εξελισσόμενες δομές στο δίσκο. Στην περίπτωση του θεωρητικού μοντέλου για τον Γαλαξία, υπολογίζουμε, αντ' αυτού, μοντέλα σπειρών που βασίζονται στην υπέρθεση περιοδικών τροχιών της οικογένειας των «μεταπιπτουσών ελλείψεων». Σε αυτή την περίπτωση, διερευνούμε πώς συνεργάζονται οι τρεις κύριες παράμετροι του μοντέλου, και πιο συγκεκριμένα η ταχύτητα περιστροφής των σπειροειδών βραχιόνων, το πλάτος της σπειροειδούς διαταραχής και η γωνία κλίσης των σπειρών, ώστε να αναπαράγουν ρεαλιστικά κύματα σπειροειδούς πυκνότητας.

# Preface

Understanding the nature of spiral arms in galaxies is a difficult open astronomical problem. There are many open problems in the study of the spiral structure, concerning the origin, evolution, and, in particular, the longevity of the spiral arms. The present thesis discusses several dynamical approaches allowing to interpret the observed galactic morphologies. Such approaches elucidate, in particular, the role of chaos and non-linear phenomena in the stability and coherence of the spiral structures. In the last decades the results of several researches in galactic dynamics have shown that the galaxies undergo substantial secular evolution. Merging events can also affect directly the dynamics of the system. Moreover, the observations, as well as N-body simulations of barred spiral galaxies give strong indications for the presence of multiple pattern speeds in galactic discs. This is in contradiction to the single pattern speed assumption inherent in many basic theoretical models of spiral structure. Density wave theory, as well as the manifold theory of the spiral structure are examples of such models. In the light of these remarks, it becomes evident that dynamical models of spiral structure need to be developed and adjust to the recent results coming from observations and N-body simulations.

In the present thesis we construct dynamical models of the spiral structure in two different cases: (a) in the case of an N-body simulation of a barred spiral galaxy, and (b) in the case of a Milky Way-like theoretical potential model. The nature of the stellar orbits that support the spiral arms differs in these two cases, thus giving rise to two different mechanisms of support of the spiral structure. In the first case, of barred spiral galaxies, the spirals are generated by chaotic orbits ('manifold spirals'), while in the second case, of normal galaxies, the spiral arms are constructed by ordered orbits ('precessing ellipses').

In the case of the N-body simulation we have a self-consistent N-body model of a barred spiral galaxy, where stemming from the positions and the velocities of the bodies we can obtain important information used in the modelling, namely the bodies, the surface density, mean velocitiy and gravitational potential at each point of the galactic disc plane. We then proceed with the computation of manifold spirals with a single pattern speed or with multiple pattern speeds. We also observe the evolution of the manifold spirals along with the secularly evolving structures in the disc. In the case of the Milky Way-like theoretical model, we compute, instead, models of spirals based on the superposition of periodic orbits of the family of "precessing ellipses". In this case, we investigate how the three main parameters of the model, mamely, the pattern speed of the spiral arms, the amplitude of the spiral pertubation and the pitch angle, collaborate so as to reproduce realistic spiral density waves.

# Acknowledgements

The hospitality of the Research Center for Astronomy and Applied Mathematics (RCAAM) of the Academy of Athens, where the most of the present research was hosted, is gratefully acknowledged. The researchers of RCAAM (G. Contopoulos, P. Patsis, C. Efthymiopoulos, M. Harsoula, T. Tzemos) have provided me with their essential support and assisted in every stage of my PhD thesis. I would like to thank in particular my supervisors C. Efthymiopoulos and M. Harsoula, for their valuable assistance and advice with this PhD. I also thank Prof. P.Ioannou for his support as member of my Phd supervising comittee. They shared with me precious knowledge, made me discover the beauty of our science and greatly helped me to evolve as a young researcher through their own example. The funding support of the Academy of Athens is greatfully acknowledged. Special mentions go to the Academician G. Contopoulos who was the scientific coordinator of the funding programs of the Academy of Athens and contributed significantly to my understanding and deepening on topics of dynamical systems through numerous discussions. Finally, I would like to express my gratitude to my family and my friends. Without their tremendous understanding and encouragement in the past few years, it would have been impossible for me to complete my study.

# Chapter 1

# Introduction

## 1.1 The morphology of the spiral galaxies and our Galaxy

Spiral galaxies have been observed for more than 150 years. Until the 1920s they were referred to as 'spiral nebulae'. The first 'spiral nebula' to be discovered was the galaxy M51 by Lord Rosse in April of 1845 (Rosse E. (1850)), who also gave a sketch of M51 (Fig. 1.1). The morphology of the spiral structure is an indicator of the underlying dynamics and of the evolution of the galaxy.

The American astronomer Edwin Hubble classified galaxies as 'elliptical', 'spiral' and 'irregular'. This classification is essentially based exclusively on a galaxy's observed morphology. According to the 'Galaxy Zoo Project' (Lintott et al. (2008), Willett et al. (2013)) which was developed later, the two thirds of all galaxies are spiral, while approximately one third are ellipticals, and a few per cent merging galaxies (Lintott et al. (2011)).

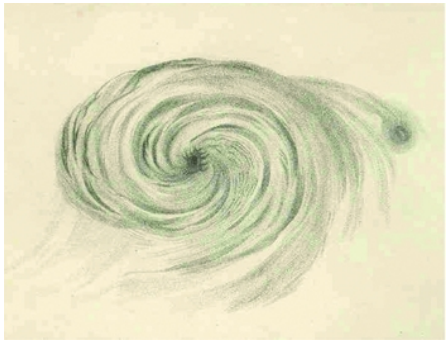

**Figure 1.1**: *The sketch that Lord Rosse gave in 1845 when he identified the spiral structure of M51.*

Hubble introduced a classification scheme for galaxies by criterion of the observed structures in their center (existence of bar or buldge), as well as of the degree of winding of the spiral arms (determined by the pitch angle) (Hubble (1926b), Reynolds (1927), De Vaucouleurs (1959), see Dobbs & Baba (2014) for a review). Spiral galaxies are generally classified as 'S' if they have no bar in their center or 'SB' if a bar is present (barred spiral galaxies). The type SAB refers to weakly barred galaxies. In order to distinguish galaxies with open spirals from the ones whose spirals are tightly wound, he added the letter 'a'-'d', with the 'd' classification representing the most open arms (greater value of the pitch angle), and the 'a' classification the most tightly wound (smaller value of the pitch angle). Thus, normal galaxies are scaled from 'Sa' to 'Sd', and barred galaxies from 'SBa' to 'SBd'. The Hubble sequence also represents a decrease in the size and luminosity of the buldge from Sa (or SBa)

galaxies to Sd (or SBd), and an increase in gas content from Sa to Sd.

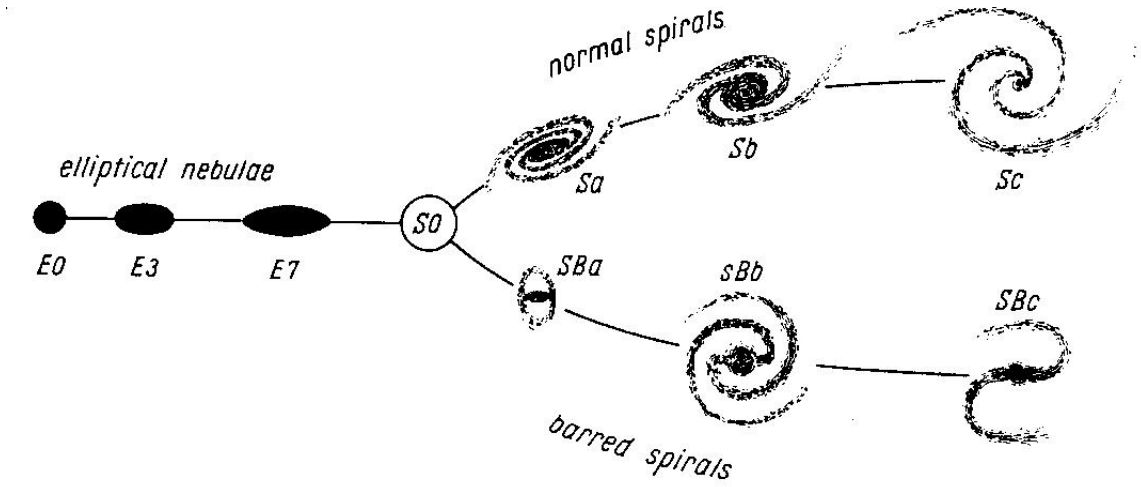


**Figure 1.2**: *Morphological classification of galaxies by Hubble (Hubble (1926b))*

A second classification scheme was proposed by Elmegreen & Elmegreen (Elmegreen & Elmegreen (1982), Elmegreen & Elmegreen (1987)) (see Table 1.1). In this classisfication 12 types of galaxies ('arm classes') are introduced by criterion of the number, length and orderliness of the spiral arms. The first four types of galaxies in the Elmegreen & Elmegreen classification correspond to 'flocculent galaxies' with spiral arms chaotic, unsymmetric and fragmented into short pieces. The arm classes 5-12 correspond to 'grand design' galaxies, with two long, continuous and symmetric spiral arms. This classification also includes 'multi-armed galaxies' that also have two inner arms, as well as multiple outer arms or ringlike outer structure. All of these types may or may not exhibit bars. Around 60 %, of galaxies exhibit some grand design structure, either in the inner or entire part of the disc (Elmegreen & Elmegreen (1982), Dobbs & Baba (2014)).

DESCRIPTION OF ARM CLASSES FOR SPIRAL GALAXIES

| Arm Class | Description |
|---|---|
| 1 | Chaotic, fragmented, unsymmetric arms |
| 2 | Fragmented spiral arm pieces with no regular pattern |
| 3 | Fragmented arms uniformly distributed around the galactic center |
| 4 | Only one prominent arm; otherwise fragmented arms |
| 5 | Two symmetric, short arms in the inner regions; irregular outer arms |
| 6 | Two symmetric inner arms; feathery ringlike outer structure |
| 7 | Two symmetric, long outer arms; feathery or irregular inner arms |
| 8 | Tightly wrapped ringlike arms |
| 9 | Two symmetric inner arms, multiple long and continuous outer arms |
| 10 | No longer used; previously denoted barred galaxies |
| 11 | No longer used; previously denoted galaxies with close companions |
| 12 | Two long symmetric arms dominating the optical disk |

Table 1.1: Morphological classification of galaxies by Elmegreen & Elmegreen (Elmegreen & Elmegreen (1987))

Note also that the morphology of spiral structure often appears different when a galaxy is observed in near-infrared rather than optical wavelengths (Bertin, & Lin (1996)). In the near-infrared we observe the structures that are supported by the older stars. This change of the morphology reflects the different dynamical effects on the disc induced by the motions of the old and younger stars respectively.

Since our solar system is immersed in the galactic disc of the Milky Way, there are many difficulties in observing and open problems in understanding the morphological features of the spiral arms in our own galaxy. The spiral structure of the Milky Way was first explored by observations of the 21 cm line from interstellar atomic hydrogen. Afterwards, the methods for the detection of the spiral structure evolved and the most commonly used are observations of Ionized hydrogen and OB stars for the mapping Galactic structure (e.g. Georgelin & Georgelin (1976)). However, there is still no consensus on whether the Milky Way is a two- armed (e.g. Weaver (1970), Elmegreen (1985)) or a four-armed galaxy (Georgelin & Georgelin (1976)) or whether or not it exhibits a ring-like structure in the inner parts of the galactic disc (Cohen & Thaddeus (1977)).

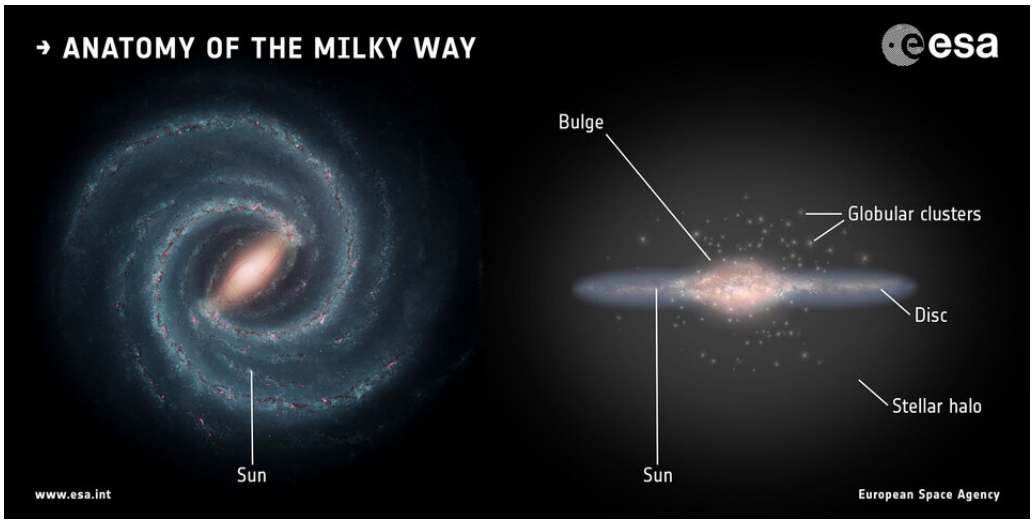


**Figure 1.3**: *A sketch of the Milky Way, seen face-on (left) and edge-on, /(right), Credit: Left: NASA/JPL-Caltech; right: ESA; layout: ESA/ATG medialab*

The Milky Way is generally considered to be a barred spiral galaxy (Burton (1988), Dame et al. (2002), Benjamin et al. (2005), Hou & Han (2014)). However, there are many open questions about the morphology and the behaviour of the central galactic structures. The first indications for the existence of a bar in the galactic center were given by de Vaucouleurs in 1964 (De Vaucouleurs (1964)) through the observation of the gas velocity field in the inner Galaxy. Recent researches assume the co-existence of a boxy buldge (Gerhard (2002), Gerhard (2011)) along with a bar structure extending to $\sim 4$ kpc (Gerhard (2010)).

## 1.2 The Density wave theory of spiral structure

### 1.2.1 Historical background

A radical evolution of perspective, generally adopted by the astronomical community, as regards the spiral structure in galaxies took place in the 1960s, following the pioneering work of Bertil Lindblad in the previous decades. B. Lindblad struggled persistently with the problem of the spiral structure until his death in 1965, and

published a long series of papers. At the time, the dominant concept for the explanation of the origin of spiral structure was that the galactic spiral arms are supported primarly from the dynamics of magnetic fields or gas (see Baade (1963), Toomre (1977)). However, Lindblad pursued the idea that the spiral stucture is generated by the colllective effect of the stellar orbits under the presence of non-axisymmetric gravitational forces in the galactic disc.

Consider the circular stellar orbits in the galactic disc. Their angular velocity $\Omega(r)$ is:

$$\Omega(r) = \sqrt{\frac{1}{r}\frac{\partial V_0(r)}{\partial r}} \tag{1.1}$$

where $V_0(r)$ is the total axisymmetric gravitational potential in the disc plane.

In a disc model in which the mass density falls with distance the angular velocity $\Omega(r)$ decreases with respect to the distance $r$ from the galactic center. As a result, a differential rotation phenomenon appears, and the stars closer are expected to rotate faster than the stars further away from the galactic center. In the scenario of so-called "material spiral arms", the spiral arms are constantly inhabited by the same stars which evolve around the center in nearly circural orbits. However, in such a scenario the differential rotation on the disc would lead the whole structure to start immediately winding. After a few rotations, the spiral arms would then become tightly wound, to an extent inconsistent with the observed morphology of spirals. This is the so-called "tight-winding problem" (Lindblad (1958), Kalnajs (1971)), which led to the conclusion that the non-axisymmetric structures on the galactic disc (the bar and the spiral arms) can not be material structures, but should, instead, be modelled as density waves, i.e. local enhancements of the disc density, which are constructed by stars that constantly travel in and out of the wave.

### 1.2.2 Density wave theory

Lindblad was the first to introduce the theory that spiral arms are density waves (1941, 1942, 1948, 1955, 1962). Later Lin and Shu (1962, 1964) and Toomre (1964) developed the idea of spiral waves, considered as perturbations in an axisymmetric disc that is regarded in the framework of either the Boltzmann equation for collisionless matter or the hydrodynamical equations for gas.

The reader is referred to Contopoulos (2002) and Binney & Tremaine (2008) for detailed reviews on density wave theory. We summarise below the main points, focusing on concepts of use in the present thesis.

In the collisionless approximation of stellar dynamics, the distribution function $f(\mathbf{r}, \mathbf{v}, t)$ provides complete information of the spatial distribution of the stars (density), as well as the velocity distribution of the stars at any point in the galactic disc. The distribution function $f(\mathbf{r}, \mathbf{v}, t)$ is defined so that the quantity $f(\mathbf{r}, \mathbf{v}, t)d^3\mathbf{r}d^3\mathbf{v}$ yields the probability of finding a random star at time t with phase-space coordinates within the six-dimensional phase-space volume $d^3\mathbf{r}d^3\mathbf{v}$ around the position $\mathbf{r}$ and velocity $\mathbf{v}$. The conservation of probability in phase space (Liouville's theorem) is described by the collisionless Boltzmann equation, (also called Vlasov equation):

$$\frac{\partial f}{\partial t} + \mathbf{v}\frac{\partial f}{\partial \mathbf{r}} - \frac{\partial H}{\partial \mathbf{r}}\frac{\partial f}{\partial \mathbf{v}} = 0 \quad . \tag{1.2}$$

Using the Poisson brackets $[\cdot, \cdot]$ the Eq. (1.2) can be written in the following form:

$$\frac{\partial f}{\partial t} + [f, H] = 0 \quad . \tag{1.3}$$

We generally consider that the Hamiltonian of the system is of the form $H = \frac{1}{2}v^2 + V(r,t)$. We call a system "self-consistent" if the density distribution is related to the potential through Poisson's equation

$$\nabla^2 V = 4\pi G\rho = 4\pi G \int dr^3 f(\mathbf{r},\mathbf{v},t) \quad . \tag{1.4}$$

In this case the gravitational potential is $V(r,t) = \int d\mathbf{r}' \frac{G\int f d^3\mathbf{v}'}{|\mathbf{r}-\mathbf{r}'|}$ and the collisionless Boltzmann equation 1.2 takes a nonlinear integro-differential form:

$$\frac{\partial f}{\partial t} + \mathbf{v}\frac{\partial f}{\partial \mathbf{r}} - \frac{\partial}{\partial \mathbf{r}}\left(\int d\mathbf{r}' \frac{G\int f d^3\mathbf{v}'}{|\mathbf{r}-\mathbf{r}'|}\right)\frac{\partial f}{\partial \mathbf{v}} = 0 \quad . \tag{1.5}$$

According to Lindbland's assumption of "quasi-stationary spiral structure" (Lindblad (1962), Lindblad (1963)), the whole spiral structure can be seen as a quasi-steady rotating spiral "pattern". The spiral patterns are "longlived", i.e. they are sustained over many orbital periods.

These concepts led to the Lin–Shu theory of stationary density waves. The linear theory approximates the spiral waves as small perturbations from a stationary, axisymmetric state, assuming that the potential V, density $\rho$ (or the surface density $\Sigma = \int \rho dz$, where z is the direction normal to the disc) and the distribution function $f$ have small deviations from the corresponding axisymmetric terms $(V_0, \rho_0, f_0)$ (Binney & Tremaine (2008), see Efthymiopoulos (2010) for a tutorial presentation). We choose $f_0(\mathbf{r},\mathbf{v})$ as the distribution function corresponding to a solution of Boltzman's equation for a steady-state model of an axisymmetric galaxy. We then define the distribution function of the system with the spiral density pertubation as

$$f(\mathbf{r},\mathbf{v},t) = f_0(\mathbf{r},\mathbf{v}) + \varepsilon f_1(\mathbf{r},\mathbf{v},t) \quad . \tag{1.6}$$

The gravitational potential is modified to

$$V(r,t) = V_0(r) + V_1(r,t) \tag{1.7}$$

where, in view of the linearity of Poisson's equation (1.4), we have:

$$V_0(r) = -\int d\mathbf{r}' \frac{G\int f_0 d^3\mathbf{v}'}{|\mathbf{r}-\mathbf{r}'|}, \quad V_1(r,t) = -\int d\mathbf{r}' \frac{G\int f_1 d^3\mathbf{v}'}{|\mathbf{r}-\mathbf{r}'|} \quad . \tag{1.8}$$

The Hamiltonian becomes

$$H = H_0 + \varepsilon V_1(r,t) \tag{1.9}$$

where $H_0 = \frac{1}{2}v^2 + V_0(r)$. The linearised form of Eq. (1.3) substituting $f$ and $H$ from Eqs. (1.6) and (1.9) is:

$$\frac{\partial f_1}{\partial t} + [f_0, H_0] + \varepsilon\,[f_1, H_0] + \varepsilon\,[f_0, V_1(r,t)] + \mathcal{O}(\varepsilon^2) = 0 \quad . \tag{1.10}$$

From Boltzmann's equation for the time-independent $f_0$ we have that $[f_0, H_0] = -\frac{\partial f_0}{\partial t} = 0$ and the term $[f_0, H_0]$ gets eliminated from Eq. (1.5). Hence:

$$\frac{\partial f_1}{\partial t} + \mathbf{v}\frac{\partial f_1}{\partial \mathbf{r}} - \frac{\partial}{\partial \mathbf{r}}\left(\int d\mathbf{r}' \frac{G\int f_0 d^3\mathbf{v}'}{|\mathbf{r}-\mathbf{r}'|}\right)\frac{\partial f_1}{\partial \mathbf{v}} - \frac{\partial}{\partial \mathbf{r}}\left(\int d\mathbf{r}' \frac{G\int f_1 d^3\mathbf{v}'}{|\mathbf{r}-\mathbf{r}'|}\right)\frac{\partial f_0}{\partial \mathbf{v}} = 0. \tag{1.11}$$

Lin & Shu (1964) did not solve directly Eq. (1.11). Instead, they initially approximated the distribution function $f$ through its velocity moments, i.e. by multiplying both sides of Boltzmann equation with progressively higher power combinations of

the velocities, and integrating the result in the velocity space. This methodology was first applied to stellar dynamics by Jeans (1919) and the respective equations are called "Jeans equations". Analogous hydrodynamical equations can be obtained from a fluid (or gas) distriburion of matter (Lin & Shu (1964, 1966)).

On the other hand, straightforward solutions of Eq. (1.11), which also give a formula for $f$, were given by Kalnajs (1971) (see the Appendix K of Binney & Tremaine (2008)).

### 1.2.3 The orbital version of the density wave theory

The orbital version of density wave theory builds spiral density waves by the superposition of stable elliptical periodic orbits that "collaborate" in a way so as to support and sustain the spiral density wave. These periodic orbits exhibit gradual change in orientation as a function of the distance from the galactic center and their orientations combine coherently so as to produce a local enhancement of density in the disc. The first to stress the contribution of these orbits to the construction and sustainement of the spiral density wave was Lindblad (1956, 1957, 1958, 1960, 1961), who called them "dispersion orbits". Later Kalnajs gave to the periodic orbits the name "precessing ellipses" (Kalnajs (1973)). As a result, the spiral density wave is supported by stars, which travel in elliptical orbits with coherent phases and they construct a 'precessing ellipsis flow' (Kalnajs (1973)).

Contopoulos calculated analytically these orbits (Contopoulos (1970), Contopoulos (1975)). In particular, he developed the theory of "resonant periodic orbits" near the inner Linblad resonance. He specified the number and stability of the corresponding periodic orbits, and identified the family of stable periodic orbits which support the spiral density wave, called the "x1" family. The resonant theory of Contopoulos, based on epicyclic action-angle variables, also allows to predict the structure of the phase space around the periodic orbits, yielding the corresponding invariant curves as the level curves of a resonant "third integral" (see Contopoulos (2002) for a review). The predictions of this theory were confirmed by Vandervoort (1973, 1975), see also Vandervoort & Monet (1975) and Monet & Vandervoort (1978)), Mertzanides (1976) and Berry & Smet (1979). These studies provided figures of the corresponding phase portraits around the elliptical closed orbits computed analytically (by the "third integral") or numerically in simple models of galactic potentials with a spiral perturbation.

The overall limit of applicability of the "precessing ellipses" was considered by Contopoulos (Contopoulos (1985)). The change of the orientation of the elliptical orbits with the energy is explained by resonant perturbation theory (Contopoulos (1975), Monet & Vandervoort (1978), see a tutorial presentation by Efthymiopoulos (2010)). Numerical examples of spirals supported by "precessing ellipses" have been computed in self-consistent models of spiral galaxies (Contopoulos & Grøsbol (1986), Patsis et al. (1991), Patsis & Grosbøl (1996), Pichardo et al. (2003), Efthymiopoulos (2010)).

N-body experiments since the 1960s have been unable to reproduce long-lived spiral density waves and the scenario of quasi-stationary spiral density waves has been strongly criticized (see Toomre (1977), Athanassoula (1984), Binney & Tremaine (2008), Sellwood & Carlberg (1984), Sellwood (2010) and Dobbs & Baba (2014) for reviews). The existence of mechanisms regulating the growth rate of spiral density waves, and hence ensuring their longevity for several pattern periods, remains largely an open question (Donner & Thomasson (1994), see Bertin, & Lin (1996) and Contopoulos (2002) for reviews).

## 1.3 Fourier decomposition of the Surface Density Field and of the potential

The surface mass density $\Sigma(r,\varphi)$ (in cylindrical coordinates) of a galactic disc is obtained through a surface brightness map (amount of light per unit area) which is constructed through photometric data from observations of the galaxy, assuming a constant mass-to-light ratio. The application of Fourier transform to the surface mass density, or to the corresponding gravitational potential, enables us to distinguish the individual structures in the galactic disc (modes of the Fourier Transform) that present a certain symmetry with respect to the galactic center and contribute collectively to the observed galactic morphology and dynamics. The Fourier Transform of the mass surface desity $\Sigma(r,\varphi)$ is given by:

$$\Sigma(r,\varphi) = \Sigma_0(r) + \sum_{m}^{m_{max}} A_m(r)\cos(m\varphi) + \sum_{m} B_m(r)\sin(m\varphi) \tag{1.12}$$

where $m_{max}$ is taken high enough to reach sufficient convergence of the Fourier series, typically we choose $m_{max} \simeq 10$). $\Sigma_0(r)$ corresponds to the axisymmetric part of the surface density:

$$\Sigma_0(r) = \frac{1}{2\pi}\int_0^{2\pi} \Sigma(r,\varphi)d\varphi \tag{1.13}$$

and $A_m(r)$, $B_m(r)$ are the amplitudes of the surface density of the m-th mode computed at a certain radius $r$ from the galactic center:

$$A_m(r) = \frac{1}{\pi}\int_0^{2\pi} \cos(m\varphi)\Sigma(r,\varphi)d\varphi \quad . \tag{1.14}$$

$$B_m(r) = \frac{1}{\pi}\int_0^{2\pi} \sin(m\varphi)\Sigma(r,\varphi)d\varphi \tag{1.15}$$

The $m = 0$ component corresponds to the axisymmetric galactic structures, namely the buldge, and disc. In most 'grand design' spiral galaxies, the m = 2 component dominates over all other. The m = 2 component describes the bisymmetric features of the disc, namely the bar and the spiral arms. The m = 4 component also appears in the bar or the spiral arms. The odd components m = 1, 3,... describe patterns (modes) with a non-even symmetry. Of particular interest is the m = 1 component. This is the main component of lope-sided structures which could result, for example, in cases where the disc galaxy interacts with a satellite galaxy. Early studies tended to disregard odd components as of smaller importance, but modern observations indicate that in many galaxies they might play a key role in dynamics (Efthymiopoulos (2010)).

We cannot recover directly the gravitional potential $V(r,\varphi,z)$ (in cylindrical coordinates) from the sole knowledge of the surface mass density $\Sigma(r,\varphi)$. Poisson equation relates the gravitational potential to the total mass density $\rho(r,\varphi,z)$:

$$\nabla^2 V(r,\varphi,z) = 4\pi\rho(r,\varphi,z) \quad . \tag{1.16}$$

Besides $\Sigma(r,\varphi)$, to obtain the spatial mass distribution $\rho(r,\varphi,z)$, requires a model of the distribution of mass in the vertical z-axis. Moreover, the luminous galactic matter (i.e. disc, bar, buldge, spiral arms) is embedded in a massive dark halo, which contributes significantly to the total gravitational potential. Merging events and external pertubation factors also affect the galactic gravitational potential.

A frequently used process to model the gravitational potential of a galaxy consists in splitting the mass distribution into distinct components (e.g. bulge, disc, bar, spiral arms, dark halo), then utilise photometric and kinematic data to create a fitting model for each component, using either empirical laws or an inverse processing of the observations.

The Fourier decomposition of the gravitational potential of the galaxy in the disc plane ($x$, $y$,$z = 0$) and radius $r$ takes the following form:

$$V(r,\varphi) = V_0(r) + \sum_{m}^{m_{max}} \Phi_m(r)\cos(m\varphi) + \sum_{m}^{m_{max}} \Psi_m(r)\sin(m\varphi) \tag{1.17}$$

where the axisymmetric potential $V_0(r)$ is:

$$V_0(r) = \frac{1}{2\pi}\int_0^{2\pi} V(r,\varphi)d\varphi \tag{1.18}$$

and the coefficients of the m-th mode at a certain radius r are:

$$\Phi_m(r) = \frac{1}{\pi}\int_0^{2\pi} V(r,\varphi)\cos(m\varphi)d\varphi \tag{1.19}$$

$$\Psi_m(r) = \frac{1}{\pi}\int_0^{2\pi} V(r,\varphi)\sin(m\varphi)d\varphi \quad . \tag{1.20}$$

## 1.4 Stellar orbits in an axisymmetric potential

Let us consider the stellar orbits under the influence of an axisymmetric potential $V_0(r)$. In this case, the angular momentum $P_\varphi$ is a constant quantity and, therefore, we are led to the one degree of freedom Hamiltonian in the inertial frame of reference:

$$\mathcal{H}_0 = \frac{{P_r}^2}{2} + \frac{{P_\varphi}^2}{2r^2} + V_0(r) = \frac{{P_r}^2}{2} + V_{eff}(r;{P_\varphi}^2) \tag{1.21}$$

where

$$V_{eff}(r;{P_\varphi}^2) = \frac{{P_\varphi}^2}{2r^2} + V_0(r) \tag{1.22}$$

is the effective potential. In the above equation, $(r,\varphi)$ are cylindrical co-ordinates, and $(P_r, P_\varphi)$ are canonical momenta which correspond to the radial and angular momenta (per unit mass) in the rest frame.

Hamilton's equations are:

$$\dot{r} = \frac{\partial H_0}{\partial P_r} = P_r$$

$$\dot{\varphi} = \frac{\partial H_0}{\partial P_\varphi} = \frac{P_\varphi}{r^2}$$

$$\dot{P_r} = -\frac{\partial H_0}{\partial r} = -\frac{\partial V_{eff}(r;{P_\varphi}^2)}{\partial r} \tag{1.23}$$

$$\dot{P_\varphi} = -\frac{\partial H_0}{\partial \varphi} = 0 \quad . \tag{1.24}$$

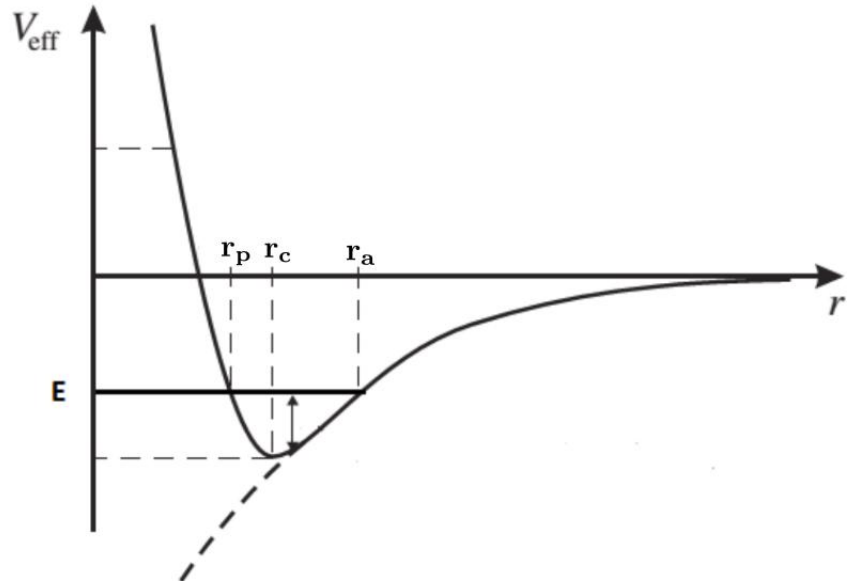


**Figure 1.4**: *The effective potential as a function of radius. The sections of the energy level line with the graph of the effective potential yields the pericenter and apocenter radii $r_p$, $r_a$. The minimum of the effective potential occurs at the radius $r = r_c$ (circular orbit).*

The numerical value of $\mathcal{H}_0$ in Eq. (1.21) for a given set of coordinates (r, $P_r$, $\varphi$, $P_\varphi$) gives orbits of constant value of energy $E$. For a given and constant energy E, the equation $E = V_{eff}(r; {P_\varphi}^2)$, namely the section points of $E$ with the curve of the effective potential give two solutions of r for the apsides of the orbit ($P_r = 0$), namely one for which $\dot{P}_r = -\frac{\partial V_{eff}(r;{P_\varphi}^2)}{\partial r} > 0$ (pericenter of the orbit at distance $r_p$), and another for which $\dot{P}_r = -\frac{\partial V_{eff}(r;{P_\varphi}^2)}{\partial r} < 0$ (apocentre of the orbit at distance $r_{ap}$).

The minimum of the effective potential occurs at a distance which corresponds to the radius of the circular orbit ($r_c$). The condition of the minimum of the effective potential $\left(\frac{\partial V_{eff}(r;{P_\varphi}^2)}{\partial r} = 0\right)$ leads to:

$$ {P_\varphi}^2 = {r_c}^3 \frac{dV_0(r_c)}{dr_c} \quad . \tag{1.25} $$

The angular velocity $\Omega(r_c)$ of the circular orbit is given by :

$$ \Omega(r_c) = \dot{\varphi} = \frac{P_\varphi}{{r_c}^2} = \sqrt{\frac{1}{r_c}\frac{dV_0(r_c)}{dr_c}} \tag{1.26} $$

and the corresponding azimuthal period is:

$$ T = \frac{2\pi}{\Omega(r_c)} \quad . \tag{1.27} $$

The energy of the circular orbit is

$$ E_c = \frac{{P_\varphi}^2}{2{r_c}^2} + V_O(r_c) = \frac{1}{2} r_c \frac{dV_0(r_c)}{dr_c} + V_0(r_c) \quad . \tag{1.28} $$

For orbits of given angular momentum $P_\varphi$, and energy $E_c < E < 0$, the star also performs an oscillation with a frequency $\kappa$ between an inner and outer radius. Then the orbit of the star is called "epicyclic orbit" and the frequency $\kappa$ is called "epicyclic

frequency". For epicyclic orbits approximating circular orbits, i.e. close to the minimum of the effective potential at the radius of the circular orbit $r = r_c$, the epicyclic frequency $\kappa$ approaches the frequency of a linear harmonic oscillation and $\kappa(r_c)$ at $r = r_c$ is given by

$$\kappa(r_c) = \sqrt{\frac{d^2 V_e f f(r_c)}{dr_c{}^2}} = \frac{3P_\varphi{}^2}{r_c{}^4} + \frac{d^2V_0(r_c)}{dr_c^2} = \sqrt{\frac{d^2V_0(r_c)}{dr_c^2} + \frac{3}{r_c}\frac{dV_0(r_c)}{dr_c}} \quad . \tag{1.29}$$

The radial oscillating motion around the galactic disc is performed with period and it is related to the epicyclic frequency $\kappa$:

$$T_r(E, P_\varphi{}^2) = 2\int_{r_p(E,P_\varphi{}^2)}^{r_a(E,P_\varphi{}^2)} \left[2(E - V_0(r)) - \frac{P_\varphi{}^2}{r^2}\right]^{-1/2} dr = \frac{2\pi}{\kappa((r_c)} \quad . \tag{1.30}$$

The ratio of $\Omega(r_c)$ and $\kappa(r_c)$ as a function of the radius $r_c$ is an important quantity which affects the structure of the periodic orbits in the galactic disc. Far from the galactic center the potential approximates the Keplerian case:

$$V_0(r) \simeq -\frac{GM}{r} \quad as \quad r \to \infty \tag{1.31}$$

and for the frequencies $\kappa$, $\Omega$ we find (from Eqs. (1.26), (1.31)):

$$\lim_{r_c\to\infty} \kappa(r_c) = \lim_{r_c\to\infty} \Omega(r_c) = \sqrt{\frac{GM}{r^3}} \quad . \tag{1.32}$$

At distances close to the galactic center, assuming that the center is smooth, the potential takes the form of a quandratic function near its minimum:

$$V_0 \simeq c_0 + c_1 r^2 \quad as \quad r \to 0 \tag{1.33}$$

Then:

$$\lim_{r_c\to\infty} (\kappa(r_c) - 2\Omega(r_c)) = 0 \quad . \tag{1.34}$$

Thus, in general, the value of the epicyclic frequency is between the two extreme values:

$$\Omega \lesssim \kappa \lesssim 2\Omega \quad . \tag{1.35}$$

A remark, due originally to Lindbland, is that for a wide class of galactic disc potentials one has $\kappa(r_c) - 2\Omega(r_c) \simeq constant$ across a wide range of radii $r_c$. This remark forms the basis of density wave theory, as discussed in more detail below.

## 1.5 Disc resonances

We now consider the epicyclic motions of stars in a galactic disc. The stellar motions can be described as the combination of a radial oscillation with frequency $\kappa$ and a circular motion at a certain radius with the azimuthal frequency $\Omega$.

In density wave theory, these stellar periodic orbits contribute collectively to the sustainment of the density wave as a whole. The orbital collaboration of the stars lead to a local density enhancement that takes the form of a "pattern" that rotates at an angular velocity $\Omega_P$, called the "pattern speed".

A resonance occurs when the ratio of the frequency $\kappa$ of the radial oscillation to that of the circular motion around the center of the galaxy with frequency $\Omega - \Omega_P$, in

a frame of reference rotating together with the spiral pattern with frequency $\Omega_P$, is a rational number. The Corotation Resonance (CR) is defined by the relation:

$$\Omega(r) = \Omega_P \quad . \tag{1.36}$$

We consider resonances defined by relation of the form

$$m(\Omega–\Omega_P) = \pm\kappa \quad . \tag{1.37}$$

In most galaxies the dominant mode is the m=2, which corresponds to bisymmetric structures of the galaxy (bar or two-armed spiral arms). For m=2 the resonant condition (1.37) defines the Inner and Outer Lindbland resonance at the radii $r_{ILR}$ , $r_{OLR}$ where

$$\Omega(r_{ILR}) - \Omega_P = \frac{\kappa(r_{ILR})}{2}, \quad \Omega(r_{OLR}) - \Omega_P = -\frac{\kappa(r_{OLR})}{2} \quad . \tag{1.38}$$

More resonances appear to accumulate close to the region of corotation of the form:

$$\frac{k}{q} = \frac{\kappa}{(\Omega - \Omega_P)} \tag{1.39}$$

If the radius r approaches the corrotation radius (where $\Omega = \Omega_P$) the ratio (1.39) tends to infinity. As a result an infinity of resonances lie in the region of corotation ((Contopoulos (1981))). Besides the Lindbland resonances and corrotation, some important resonances in an extended area around the corotation are $k/1 = 4/1, 3/1$ (inside corotation), and $k/1 = -2/1, -1/1$ (outside corotation).

$\Omega$ and $\kappa$ are functions of the radius r, while the pattern speed $\Omega_P$ is a constant quantity. As a result the location of the resonances in the galactic disc depend on the value of the pattern speed $\Omega_P$.

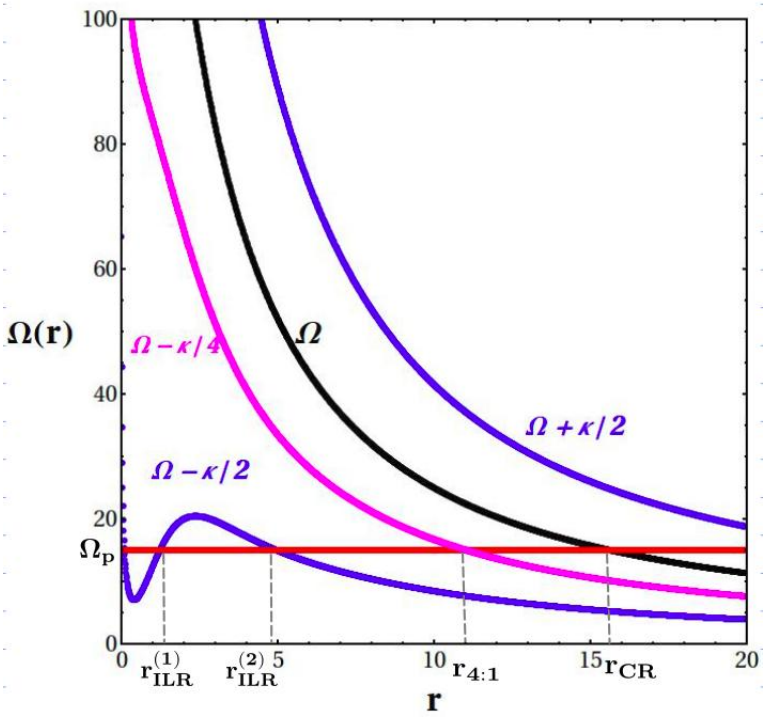


**Figure 1.5**: *The form of the function $\Omega(r)$, and of the resonant combinations of $\Omega(r)$ and $\kappa(r)$, $\Omega - \kappa/2$, $\Omega + \kappa/2$, and $\Omega - \kappa/4$ for a dynamical galctic model that is described in Harsoula et al. (2021). The selected pattern speed $\Omega_P$ (red line) determines the radii of the ILR, the 4:1 resonance and the corotation.*

Figure 1.5 shows the function $\Omega(r)$, as well as the combinations $\Omega - \kappa/2$, $\Omega + \kappa/2$ and $\Omega - \kappa/4$. The inner section of the curve $\Omega(r)$ with the pattern speed $\Omega_P$ defines the radius of the corotation $r_{CR}$, while the inner section of the curve $\Omega - \kappa/2$ with the pattern speed $\Omega_P$ defines the radius of the Inner Lindblad Resonance (ILR) $r_{ILR}$. Depending on the model we may have no ILR or one or two ILR. Finally the inner section of the curve $\Omega - \kappa/4$ with the pattern speed $\Omega_P$ defines the radius of the 4:1 resonance $r_{4:1}$.

In Fig. 1.5 we observe that $\Omega(r)$ and $\kappa(r)$ are decreasing functions of $r$, while the value of $\Omega_P$ is a constant number. Hence, for a fixed potential, the location of resonances depends on the value of $\Omega_P$. The value of $\Omega_P$ plays an important role in the evolution and structure of galactic systems. However, determining the value of $\Omega_P$ in observed galaxies is not a trivial task. Most methods for recovering the value of $\Omega_P$ (Tremaine & Weinberg (1984), Tremaine & Weinberg (1984b)) depend not only on observational data, but also on additional dynamical assumptions. Furhermore, different values of $\Omega_P$ lead, in general, to different structures and morphological characteristics of the various patterns embedded in the galactic disc.

## 1.6 Extent of the spiral density waves

Spiral density waves cannot extend throughout the entire galactic disc because there exist natural inner and outer barriers that limit the extension of these waves. A density wave can only exist if the stars respond to its gravity in a way that they can maintain the structure. A star at radius $r$ traverses an $m$- armed spiral structure with frequency $m|\ \Omega_p - \Omega(r)\ |$. The stellar motions can generally enhance the spiral density wave if their angular frequency $m|\ \Omega_p - \Omega(r)\ |$ is slower than the epicyclic frequency $\kappa(r)$ at this radius (Dobbs & Baba (2014)). Therefore, from Eq. (1.37) a $m = 2$ spiral wave can propagate in the region between the inner and outer Lindblad resonances.

It follows that the inner natural barrier for m=2 spiral arms coincides approximately with the radius of ILR. In fact, the density waves are reflected in this central region before reaching the ILR, and then they are amplified by swing amplification (Goldreich & Tremaine (1978)). Swing amplification offers a mechanism of fast growth of density waves between the ILR and OLR and it works when short leading waves are reflected to short trailing waves at the CR radius, or when a density enhancement formed by self-gravity is stretched out by differential rotation (see Dobbs & Baba (2014) for a review)). Also, the density waves can be absorbed at the ILR due to Landau damping (Lynden-Bell & Kalnajs (1972)). But this absorption of the stellar density waves at the ILR can be avoided if the Toomre's $Q$ parameter (Toomre (1964)) has a high value inside the ILR, forming a so-called $Q$-barrier. Such a barrier reflects a density wave approaching the ILR back to outwards propagation, away from the ILR. The Toomre's $Q$ parameter for a stellar disc is given by the relation:

$$Q = \frac{\kappa \sigma_{\mathrm{R}}}{3.36 G \Sigma_0} \tag{1.40}$$

where $\kappa(r)$ is the epicyclic frequency, $\sigma_{\mathrm{R}}(r)$ is the velocity dispersion and $\Sigma_0$ is the disc surface density at a certain radius r. A high value of the $Q$ parameter implies high value of the velocity dispersion. Inside the ILR this can be caused, for example, by the existence of the central spheroidal (bulge). In such cases, quasi-stationary two-armed spirals can be generated by 'standing-wave' patterns which exist between a reflecting radius from the inner part of the galaxy (i.e. $r_{ILR}$) up to the corotation radius (Bertin et al. (1989)).

However, Contopoulos and Grosbøl, (Contopoulos & Grøsbol (1986), Contopoulos & Grøsbol (1988)) have shown that in the case of normal spirals (without the presence of a galactic bar) where the amplitude of the spiral arms is strong enough, non linear-phenomena arise at the 4:1 resonance, and the spiral density wave necessarily terminates there. In particular, the elliptical periodic orbits become rectangular there and can no longer support the spiral density wave. This result was further confirmed in Patsis et al. (1991), Patsis et al. (1994), Patsis et al. (1997), Lépine et al. (2011) and Junqueira et al. (2013). However, if the spiral pertubation is weaker non-linear phenomena also weaken and the spiral can extend beyond the 4:1 resonance (see for example Grøsbol & Patsis (1998)).

As an overall conclusion, the spiral density waves supported by precessing ellipses should extend in a region starting from a little outside the ILR and up to the 4:1 resonance. The radii of these resonances are defined by the specific pattern speed. According to Fig. 1.5 this region, $r_{ILR} < r < r_{4:1}$, varies for different values of the pattern speed $\Omega_P$.

## 1.7 The role of chaos in galactic discs

In the case of normal spiral galaxies (without a bar at the center) the non- axisymmetric pertubation is rather small (<10 %). We have discussed in this case models of spirals supported by organised orbits ("precessing ellipses") which extend up to the 4/1 resonance. In this case, chaos is a local phenomenon that takes place in the close neighborhood of unstable periodic orbits at the region of the resonances of the disc. Non-linear phenomena are manifested mostly in the form of the periodic orbits, which deviate from the elliptical shape as the amplitude of the non-axisymmetric pertubation in the disc increases. This phenomenon is responsible for the termination of the spiral arms at the 4/1 resonance.

In barred spiral galaxies it is generally accepted that the bar lies inside the region of corotation (Contopoulos (1980)). In many cases the bar induces a strong non-axisymmetric pertubation in the galactic disc. A large number of resonances are accumulated in a small spatial zone around the region of corotation and this phenomenon causes a zone of chaotic motion due to the overlapping of the resonances (Contopoulos (1966), Rosenbluth et al. (1966), Walker & Ford (1969), Voglis et al. (2006b)). The chaotic orbits near corrotation can, however, support both the bar and the spiral arms, as first indicated in Kaufmann & Contopoulos (1996). Moreover, in the case of barred spiral galaxies the spiral arms extend far beyond the corotation. These results highlight the need for a new theory for the spiral structure in barred spiral galaxies. Such a theory is the manifold theory (Romero-Gomez et al. (2006), ,Voglis et al. (2006), Romero-Gomez et al. (2007), Tsoutsis et al. (2008), Tsoutsis et al. (2009), Athanassoula et al. (2009a), Athanassoula et al. (2009b), Athanassoula (2012), Efthymiopoulos (2010), Harsoula et al. (2016), Efthymiopoulos et al. (2019), Zouloumi et al. (2024)), analysed in the following sections.

## 1.8 Hamiltonian model and equations of motion in non-axisymmetric potentials

We consider a barred spiral galaxy where the bar rotates with pattern speed $\Omega_P$ (the angular velocity of the bar) and we choose a galactocentric frame of reference which corotates with the bar. In the corrotating frame of reference the Hamiltonian of the system incorporates the term $V_0(r)$ of the axisymmetric potential (e.g. the buldge, the

disc or the dark halo) and an extra term with azimuthal dependence $V(r,\varphi)$ which corresponds to the potential of a non-axisymmetric perturbation in the disc (e.g. the bar or the spiral arms). The Hamiltonian in the rotating system is:

$$H = \frac{1}{2}\left({p_r}^2 + \frac{{p_\varphi}^2}{r^2}\right) - \Omega_P p_\varphi + V_0(r) + V(r,\varphi) = E_J \tag{1.41}$$

where $H = H(r,\varphi,p_r,p_\varphi)$ and $(r,\varphi)$ are cylindrical co-ordinates, which give the cartesian coordinates through the relations $x = r\cos\phi$, $y = r\sin\phi$. $(P_r, P_\phi)$ are canonical momenta which correspond to the radial and angular momentum (per unit mass). The angular momentum $P_\varphi$ is the angular momentum per unit mass in the inertial frame of reference, although $\varphi$ corresponds to the azimuth in the rotating frame of reference. $(P_r, P_\phi)$ connected to the cartesian velocities $V_x, V_y$ in the corotating frame via $p_r = (xV_x + yV_y)/r$, $P_\varphi = \Omega_P r^2 + (xV_y - yV_x)/r$. The numerical value of the Hamiltonian $H$ remains constant in time along any particular orbit (Jacobi energy $H = E_J$).

The orbits are given by Hamilton's equations for Hamiltonian 1.41:

$$\begin{aligned}
\dot{r} &= \frac{\partial H}{\partial P_r} = P_r \\
\dot{\varphi} &= \frac{\partial H}{\partial P_\varphi} = \frac{P_\varphi}{r^2} - \Omega_P \\
\dot{P}_r &= -\frac{\partial H}{\partial r} = \frac{{P_\varphi}^2}{r^3} - \frac{\partial V_0(r)}{\partial r} - \frac{\partial V(r,\varphi)}{\partial r} \\
\dot{P}_\varphi &= -\frac{\partial H}{\partial \varphi} = -\frac{\partial V(r,\varphi)}{\partial \varphi} \quad .
\end{aligned} \tag{1.42}$$

## 1.9 Lagrangian Equilibrium points in the disc

We consider a frame of reference which corotates with the bar, which is then always seen in the same, e.g., vertical direction (see Fig. 1.7). In the corrotating frame of reference we locate the Lagrangian equilibrium points similarly to the respective equilibrium points in the restricted three-body problem. These points correspond to physical points where the forces (gravitational and apparent) get a zero value.

We can easily compute the Lagrangian points in the case of a simplified bar-like potential model. In this model the Fourier coefficients in Eq. (1.17) are $\Phi_m(R) = 0$, $\Psi_m(R) = 0$, for all $m$ except $m = 2$, while $\Phi_2(R)/\Psi_2(R) = const.$ In such a model the bar-like perturbation leads to a bar with major axis in a fixed azimuthal direction in the rotating frame given by $\varphi_{bar} = 0.5\tan^{-1}(\Psi_2/\Phi_2)$ ($\pm\pi/2$, depending on the signs of the terms $\Phi_2, \Psi_2$). The equations of motion (1.42) combined with the equilibrium condition in the above simplified model:

$$\frac{\partial H}{\partial r} = \frac{\partial H}{\partial \vartheta} = \frac{\partial H}{\partial P_r} = \frac{\partial H}{\partial P_\vartheta} = 0 \tag{1.43}$$

yield four Lagrangian equilibrium points (e.g. Binney & Tremaine (2008)):

1) the unstable points $L_1$ and $L_2$, alligned with the bar, have co-ordinates $r_{L1} = r_{L2} = r_l$, for some radius $r_l > 0$ from the galactic center, $P_{r,L1} = P_{r,L2} = 0$, $\varphi_{L1} = \varphi_{bar}$, $\varphi_{L2} = \varphi_{bar} + \pi$, and $P_{\varphi,L1} = P_{\varphi,L2} = \Omega_P r_l^2$.

2) The stable points $L_4$ and $L_5$ have co-ordinates $r_{L4} = r_{L5} = r_l'$, with $r_l' < r_l$, and $P_{RR,L4} = P_{R,L5} = 0$, $\phi_{L4} = \phi_{bar} + \pi/2$, $\varphi_{L5} = \varphi_{bar} + 3\pi/2$, and $P_{\phi,L4} = P_{\phi,L5} = \Omega_P r_l'^2$.

The radii $r_l$ and $r_l'$ differ (by quantities of the order of the bar's $m = 2$ relative amplitude) from the radius $r_{CR}$ (the corrotation radius) defined by the root for $r$

using the equation (1.26) for the angular velocity $\Omega(r)$ of the circular orbit in the rest frame and the condition (1.36) for the corotation resonance:

$$\Omega_P = \Omega(r_{CR}) = \left( \frac{1}{r} \frac{dV_0(r)}{dr} \right)^{1/2}_{r=r_{CR}} \quad . \tag{1.44}$$

The radius $r_{CR}$ is the co-rotation radius, and $\Omega(r)$ is the angular velocity of the circular orbit in the rest frame under the influence of the axisymmetric potential $V_0$. One finds $r_l > r_{CR}$, $r'_l < r_{CR}$, while the ring $r'_l < r < r_l$ is the corotation zone (or region).

We detect the Lagrangian points through equipotential curves which are called 'zero velocity curves', which satisfy the condition:

$$Veff(r; {P_\varphi}^2) = V_0(r) + V(r, \varphi) - \frac{1}{2}\Omega_P^2 r^2 = E_J \quad . \tag{1.45}$$

The term $\frac{1}{2}\Omega_P^2 r^2$ is called the centrifugal term, and it is derived from the terms $\frac{{p_\varphi}^2}{2r^2} - \Omega_P p_\varphi$ of the Hamiltonian (1.41), by replacing $p_\varphi = r^2(\dot{\varphi} + \Omega_P) = r^2\Omega_P$ for $\dot{\varphi} = 0$. All regions in which $V_{eff}(r; {P_\varphi}^2) > E_J$ are forbidden for stellar motions.

Figure 1.6 shows the zero velocity curves of a simulated barred spiral galaxy. All the Lagrangian points satisfy the condition $\nabla V_{eff} = 0$. The points $L_1$, $L_2$ along the bar are saddle points and represent the unstable Lagrangian points. Stars with values of $E_J$ larger than $V_{eff_{L_{1,2}}}$ or stars that are initially outside the contour through $L_1$ and $L_2$ can in principle escape to infinity. The points $L_4$, $L_5$ in a direction perpendicular to the bar represent the stable Lagrangian points. $L_3$ is a stable Lagrangian equilibrium point in the center of the galaxy (see paragraph 3.3.2 of Binney & Tremaine (2008)). The Lagrangian points appear stationary in the corotating frame of reference, where the gravitational and centrifugal forces precisely balance, but they can be regarded also as circular orbits in the inertial frame of reference.

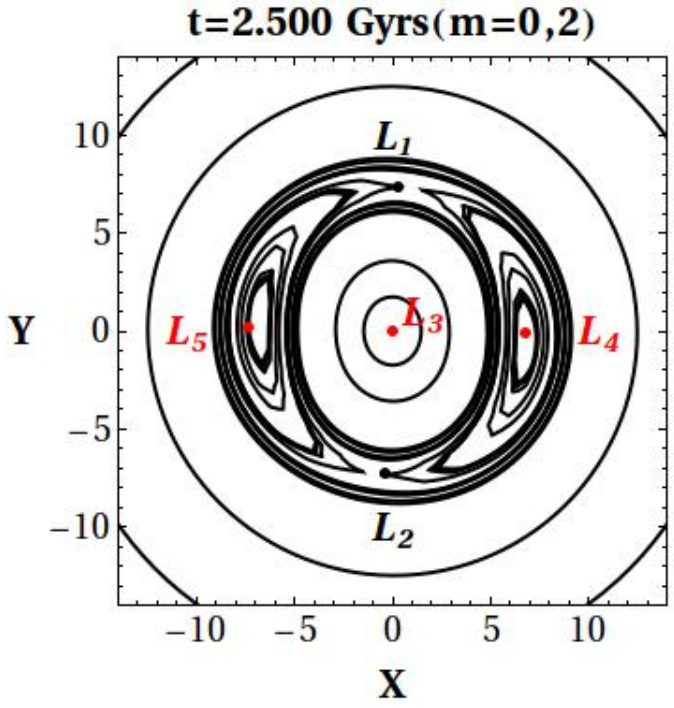


**Figure 1.6**: *Zero velocity curves constructed from the potential of a N-body simulated barred spiral galaxy (from Kyziropoulos et al. (2016)) at time $t = 2.5$ Gyr of the simulation*

For weak non-axisymmetric disturbances the Lagrangian points $L_1$, $L_2$ and $L_4$, $L_5$ are close to the corotation circle as shown in Fig. 1.7. But they move away from the corotation circle if the non-axisymmetric pertubation is strong. When one considers the full non-axisymmetric potential (Eq. (1.17)), the unstable Lagrangian points $L_1$, $L_2$ need no longer be at symmetric positions with respect to the center of the disc, nor aligned with the bar. In fact, time variations in the non-axisymmetric Fourier modes of the gravitational potential can alter significantly the form of 'zero velocity curves' within the co-rotation zone, influencing the radial and azimuthal position of the Lagrangian points (see below, and also Tsoutsis et al. (2009), Wu et al. (2016)), and even their number (e.g. Kalapotharakos et al. (2010)).

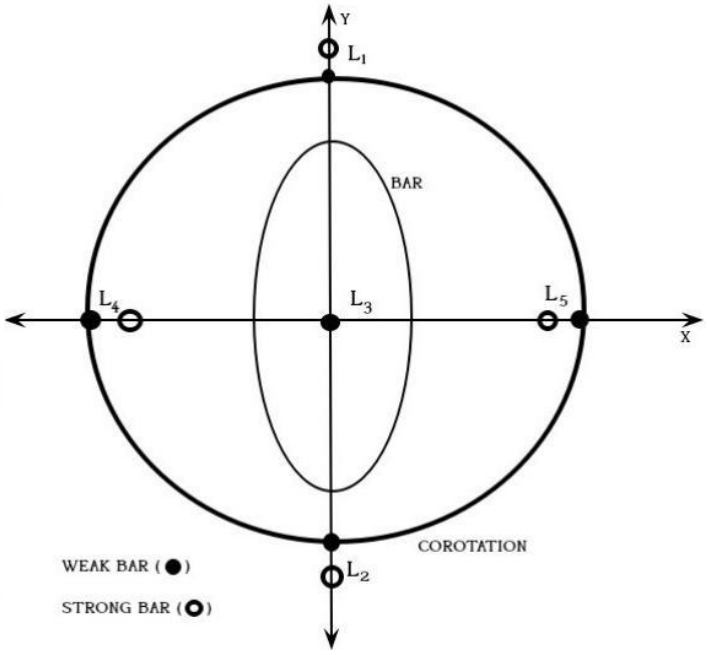


**Figure 1.7**: *The Lagrangian points $L_1$, $L_2$,$L_3$, $L_4$, $L_5$ in an the case of weak bar and in the case of a strong bar*

## 1.10 The Main Families of Periodic Orbits

In simple dynamical systems we distinguish three main types of orbits: (a) Periodic Orbits (Ordered orbits) (b) Quasi-periodic orbits (Ordered orbits) and (c) Chaotic Orbits. (see Contopoulos (2002) for a review) In the orbital study of the galactic systems the study of the periodic orbits are of great significance. The stable orbits trap around them sets of quasi-periodic orbits which also support the galactic structures. On the other hand, the unstable orbits separate the various types of ordered orbits and demarcate the chaotic domains in a galaxy.

The main families of periodic orbits encountered in this particular problem (see Efthymiopoulos (2010) for a review) are the following: a) The $x_1$ family of Contopoulos & Papayannopoulos (1980) are the main stable orbits beyond the inner Lindblad resonance (ILR), which in the case of normal galaxies construct the precessing ellipses" and they support the density wave. Near the ILR resonance this family of periodic orbits are elliptical orbits. However, at longer distances, closer to higher order resonances, the trajectory tends to acquire a polygonal shape, which corresponds to the type of epicyclic oscillations of the corresponding resonance (e.g. in the 4/1 resonance where four epicyclic oscillations are performed in a azimuthal

period the orbit tends to take a rectangular shape). The family of periodic trajectories $x_1$ also continues beyond the corotation, where it is performed in retrograde direction.

b) The families of periodic orbits $x_2$, $x_3$, $x_4$. The $x_2$, $x_3$ families lie between the two ILR resonances (if they exist) and extend perpendicular to the bar. Family $x_2$ is stable, while family $x_3$ is unstable. The $x_4$ family is retrograde and plays an important role only near the center. Contopoulos & Grøsbol (1989)

c) Periodic orbits of $2/1$ resonances. $3/1$, $4/1$ etc, resulting from the application of the Poincaré-Birkhoff theorem (Birkhoff (1917), Poincaré (1912)).

d) Short and long period periodic orbits around the equilibrium points $L_4$, $L_5$. The short-period orbits form small loops around the equilibrium points, while the long-period orbits are more elongated and take a "banana" shape around $L_4$, $L_5$.

e) Short-period periodic orbits around the equilibrium points $L_1$, $L_2$, which will be mentioned in the following subsection. These short period periodic orbits are also called $PL_1$, $PL_2$ and their unstable invariant manifolds support the structure of the spiral arms or the outer shell of the bar. (see details in Section 1.11).

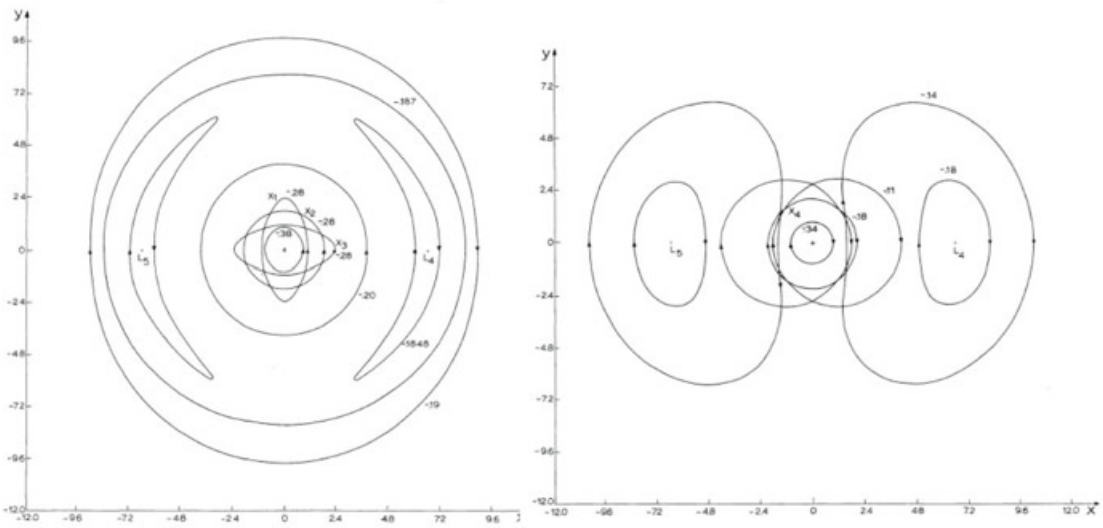

**Figure 1.8**: *(a) The main families of periodic orbits in a barred galaxy. We distinguish $x_1$, but also the $x_2$, $x_3$ families of periodic orbits as well as the long-period ("banana-shaped") orbits around $L_4$ and $L_5$. (b) Short-period periodic orbits around $L_4$, $L_5$ as well as $x_4$ orbits are depicted. (source: Contopoulos & Grøsbol (1989))*

Additionally to the periodic orbits, other types of orbits are also located in galactic dynamical models and they are the following:

i) Around the stable periodic orbits there are "quasi-periodic orbits" that form tube-like structures ("tubes"), which respond to motions on the invariant tori of the phase space. These orbits also construct the main body of the organized orbits in the system.

ii) Chaotic trajectories are very important, especially for values of the Jacobi constant $E_{J,L4} < E_J < E_{J,L1}$. The structure of the zero-velocity curves presents that in this energy region an orbit may be moving partly inside and partly outside the corotation region (Kaufmann & Contopoulos (1996)). Thus the chaotic orbits can partially support the outer shell of the bar and partially the spiral arms. These orbits are called the "hot population" (Sparke & Sellwood (1987), Kaufmann & Contopoulos (1996)) because of the large dispersion of velocities of the stars moving along them.

The fact that the bars essentially terminate near the corotation is mainly due to the large degree of chaos which is located at this region. In that region a large number of

periodic orbits become unstable. An additional factor is the change of the orientation of the main periodic orbits outside the corotation.

## 1.11 The manifold theory for the spiral structure of barred spiral galaxies

### 1.11.1 Definitions and the two versions of the manifold theory

In barred spiral galaxies the bar is a strong pertubation that leads to chaotic motion in the region of corotation (Kaufmann & Contopoulos (1996), Patsis (2006)). The work Patsis (2006) introduces the idea of 'chaotic spirals' and presents stellar response models fitting a real barred spiral galaxy in which the spiral arms are supported almost entirely by chaotic orbits. Someone would expect that the orbital escapes would increase rapidly due to the chaotic motion and the system could not sustain for times comparable to Hubble times. However, this speculation has not been assumed by observations and N-body simulations. These problems arose the need for a new theory for the barred spiral galaxies which would provide a mechanism that gives coherent and long-lived spiral structure in barred spiral galaxies.

A central question in the study of barred spiral galaxies was whether the bar drives spiral dynamics (e.g. Goldreich & Tremaine (1978), Athanassoula (1980), Schwarz (1984)), or the spiral structure is a recurrent collective instability characterized by its own independent dynamics which interacts with the bar (e.g. Sellwood (2000)). Sellwood & Sparke proved that if the spiral would be bar-driven they would rotate with the same angular velocity (which is not generally observed in real galaxies or in N-body simulations, see 1.12.2 for more details) and they would be encountered to lie outside the corotation (Sellwood & Sparke (1988)).

The manifold theory introduced a mechanism for the long-lived spiral structure in barred spiral galaxies, applicable whenever the bar is a strong pertubation in the galactic disc and the orbits in the region of corotation are chaotic. The manifold theory for the spiral structure in barred spiral galaxies was first introduced in two versions in 2006 by Romero-Gomez et al. (2006) and Voglis et al. (2006). Since then it has been tested in N- body simulations and analytical potential models of barred spiral galaxies (Romero-Gomez et al. (2007), Tsoutsis et al. (2008), Tsoutsis et al. (2009), Athanassoula et al. (2009a), Athanassoula et al. (2009b), Athanassoula et al. (2010), Athanassoula (2012), Efthymiopoulos (2010), Harsoula et al. (2016), Efthymiopoulos et al. (2019)).

For values of the Jacobi constant greater than the values of the unstable equilibrium points $L_{1,2}$ , there exists a family of short-period periodic orbits (approximately equal to the epicyclic period) branching around the points $L_1$ , $L_2$ . These trajectories form loops around $L_{1,2}$ of increasing size as the value of the Jacobi constant increases. Hereafter, we will refer to these short-period periodic orbits (or 'Liapunov orbits' in Romero-Gomez et al. (2006)) themselves as $PL_1$ or $PL_2$ as called in Voglis et al. (2006). These orbits are prograde with respect to the galaxy's rotation inside the cototation region and retrograde outside the corotation (Fig. 1.9). A similar family of periodic short-period orbits with epicenters $PL_{4,5}$ can also exist for the stable points $L_{4,5}$ for values of constant Jacobi that exceeds the corresponding values in $L_{4,5}$.

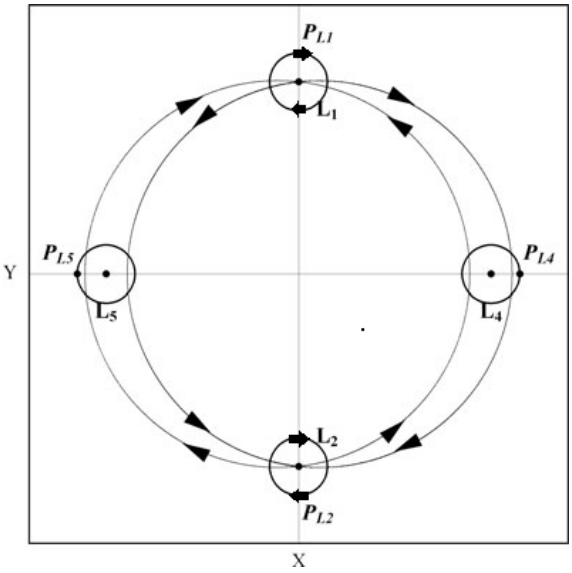


**Figure 1.9**: *Short-period orbits $PL_{1,2}$ around the Lagrangian equilibrium points $L_{1,2}$ (unstable) and $L_{4,5}$ (stable). Arrows indicate the direction of rotation in and out of the corotation. (source:Voglis et al. (2006))*

The unstable manifolds $\mathcal{W}^U_{PL_{1,2}}$ of the unstable short-period periodic orbits $PL_1$ and $PL_2$ are defined as the set of initial conditions with coordinates $(r_0, \vartheta_0, P_{r_0}, P_{\vartheta_0})$ in the phase space that tend asymptomatically to the respective periodic orbits $PL_{1,2}$, integrated in the backward sense of time, namely $t \to -\infty$. Denote by $O(t; R_0, \phi_0, p_{R,0}, p_{\phi,0})$ one orbit $(R(t), \phi(t), p_R(t), p_\phi(t))$, with initial conditions $(R_0, \phi_0, p_{R,0}, p_{\phi,0})$ at time t and $O_{PL_1}$ the locus of all the phase space points of the periodic orbit $PL_1$. Thus, the unstable manifold $\mathcal{W}^U_{PL1}$ is the ensemble of all different initial conditions for which the distance between $O(t; R_0, \phi_0, p_{R,0}, p_{\phi,0})$ and $O_{PL_1}$ tends to zero as $t \to -\infty$:

$$\mathcal{W}^U_{PL_1} = \left\{ \text{All } (R_0, \phi_0, p_{R,0}, p_{\phi,0}) : dist[O(t; R_0, \phi_0, p_{R,0}, p_{\phi,0}), O_{PL_1}] \to 0 \text{ as } t \to -\infty \right\} . \tag{1.46}$$

Thus, an integration of these trajectories in the forward sense of time from $PL_{1,2}$ leads a rich outflow in space away form $L_{1,2}$. This outflow of trajectories yield spiral patterns in the configuration space and can support the outer shell of the bar and the spiral arms of the galaxy.

Similarly, the stable manifold $\mathcal{W}^S_{PL_{1,2}}$ is the set of points in phase space with images approaching asymptotically the orbit $PL_1$ in the forward direction of time ($t \to +\infty$). Both sets, $\mathcal{W}^{\mathcal{U}}$ and $\mathcal{W}^{\mathcal{S}}$ are two-dimensional manifolds embedded in the three-dimensional Jacobi constant hypersurface of the four-dimensional phase space. Similar definitions hold for the unstable manifold of the Lagrangian points $L_{1,2}$, namely the sets $\mathcal{W}^U_{L1}$ (or $\mathcal{W}^U_{L2}$):

$$\mathcal{W}^U_{L1} = \left\{ \text{All } (R_0, \phi_0, p_{R,0}, p_{\phi,0}) : dist[O(t; R_0, \phi_0, p_{R,0}, p_{\phi,0}), O_{L1}] \to 0 \text{ as } t \to -\infty \right\} . \tag{1.47}$$

The geometric shapes and properties of the manifolds $\mathcal{W}^U_{PL1,2}$ are similar to those of the manifolds $\mathcal{W}^U_{L1,2}$. However, a main difference is that the the unstable points $L_{1,2}$ and their manifolds represent only one value of the Jacobi constant, while the periodic orbits $PL_{1,2}$ and their manifolds form families which span a whole set of values of the Jacobi constant $E_{J,PL_{1,2}} > E_{J,L_{1,2}}$. Furthermore, all the families of orbits with energies $E_J > E_{L_{1,2}}$ give manifolds that are trailing parallel paths to $W^U_{PL_{1,2}}$ and

contribute to the outflow away from $L_1$ and $L_2$ (Patsis (2006), Tsoutsis et al. (2008)) due to the phenonomen of phenomenon of 'stickiness in chaos' (G.Contopoulos and M. Harsoula 2008). The manifolds represent the motion of the material at all energies beyond the Jacobi energy at corotation. The manifolds play the role of the attractor of chaotic orbits and provide a dynamical skeleton to the structure of the galaxy.

Two versions of the manifold theory have been developed so far in the literature:

i) The 'flux-tube' version of the manifold theory (Romero-Gomez et al. (2006), Romero-Gomez et al. (2007), Athanassoula et al. (2009a), Athanassoula et al. (2009b), Athanassoula (2012)) considers continuous-in-time orbits describing the flow of matter away from the bar's unstable Lagrangian points $L_1$ and $L_2$, as viewed in a frame of reference rotating with angular speed equal to the bar's pattern speed $\Omega_P$. The unstable 'flux-tube' manifolds $\mathcal{W}^U_{L1}$, $\mathcal{W}^U_{L2}$ from Eq. (1.47) are invariant sets formed by all orbits tending asymptotically towards $L_1$ or $L_2$ in the backward sense of time. This means that, in the forward sense of time, these orbits form outflows ('flux-tubes') directed away from $L_1$ or $L_2$. Besides $L_1$ and $L_2$, similar flux-tube manifolds can be constructed for the whole family of epicyclic periodic orbits (called 'Lyapunov orbits') around $L_1$ or $L_2$. This outflow of trajectories yields with initial conditions selected to lie in the set (1.14) or (1.46).

An elementary linearization of the equations of motion around $L_1$ or $L_2$ shows that these outflows, have the form of trailing spiral arms in the configuration space. In particular, the flux-tube manifolds are consisted of two branches: one that is directed outside co-rotation and takes the form of a trailing spiral arm and a second that is directed inside corotation, creating a ring-like structure around the bar. Thus, the flux-tube manifolds can give rise to several morphological structures, from outer or inner ring-like to open spirals, depending on the model's parameters (e.g. pattern spead, $m = 2$ amplitude and asymmetry (Athanassoula et al. (2009a)).

ii) In the version of the manifold theory called 'apocentric manifolds' (Voglis et al. (2006), Tsoutsis et al. (2008), Tsoutsis et al. (2009), Efthymiopoulos (2010), Harsoula et al. (2016)) one computes first the flux-tube manifolds $\mathcal{W}^U_{L_{1,2}}$, and then isolates only those points which correspond to apsidal positions, i.e., local apocentric or pericentric points of each orbit in the flux-tube. The locus formed by the union of the apocentric points yields again trailing spiral arms. The apocentric manifolds $\mathcal{W}^{UA}_{L_{1,2}}$ are defined through the flux-tube manifolds $\mathcal{W}^U_{L_{1,2}}$ as follows:

$$\mathcal{W}^{UA}_{L_{1,2}} = \left\{ \text{All points of } \mathcal{W}^U_{L_{1,2}} : p_r = 0, \dot{p}_r < 0 \right\} \ , \tag{1.48}$$

where $\dot{p}_r$ is given by the Eqs.(1.42). A similar definition holds for the apocentric manifolds $\mathcal{W}^{UA}_{PL_{1,2}}$ of the families $PL_{1,2}$. The form of pocentric manifolds is presented in Fig. 1.10

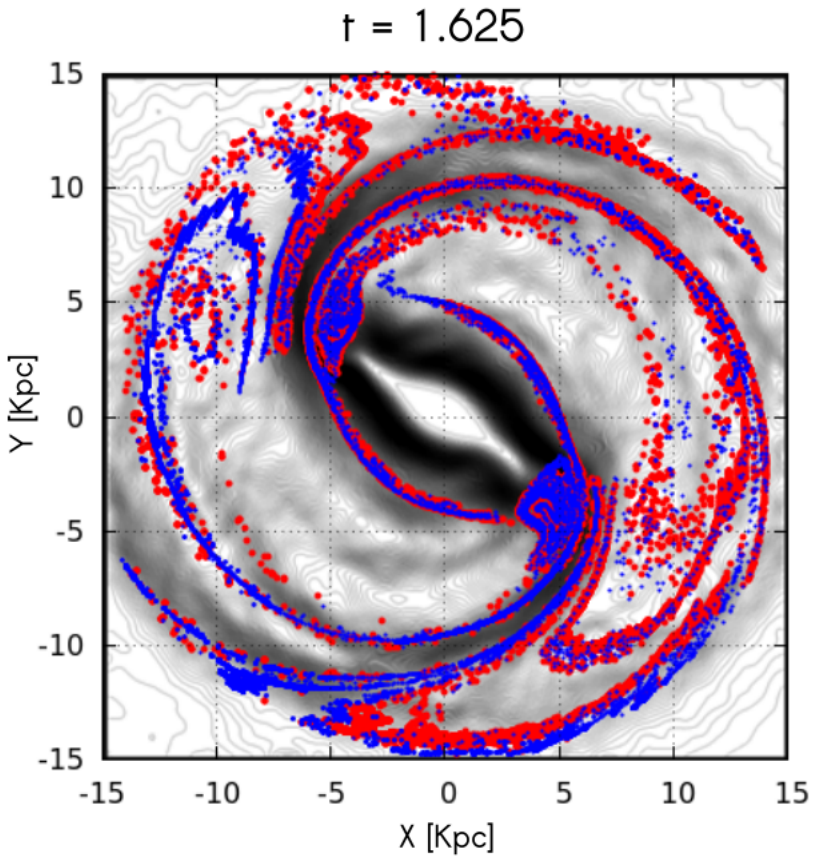


**Figure 1.10**: *The apocentric unstable invariant manifolds $\mathcal{W}^{UA}_{PL_{1,2}}$ from the unstable periodic orbits $PL_1$ and $PL_2$ in the physical space positioned over a snapshot of the N-body simulation Kyziropoulos et al. (2016) at time $t = 1.625$ Gyr of the simulation. The calculation of these invariant manifolds is described in Efthymiopoulos et al. (2019)*

The set $\mathcal{W}^{U}_{L_{1,2}}$ reproduces through continous in time orbits the manifolds as geometric objects which show the direction of the flux of matter beyond the corotation. However, the flux tube version of the manifold theory struggles to approach the real distribution of matter along the manifolds, which depends on the distribution function of the N-body system. Despite the fact that a precise knowledge of the distribution function is hardly tractable, the set $\mathcal{W}^{UA}_{L_{1,2}}$ can be representative of the mass density distribution. This is because the method of apocentric manifolds (Voglis et al. (2006)) exploits the fact that local density maxima along the manifolds are expected at points close to apsidal (i.e. pericentric or apocentric) positions of the orbits. This assumption is verified in N-body experiments (see Tsoutsis et al. (2008)), the successive apocenters reached by the orbits of the N-body particles are all on the same locus determined by the coalescence of invariant manifolds.

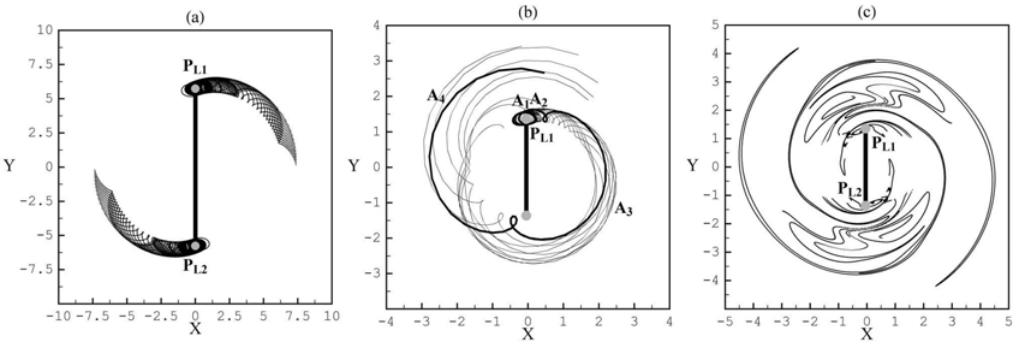


**Figure 1.11**: *(a) The unstable invariant tube manifolds $\mathcal{W}^{U}_{PL_{1,2}}$ into the physical space from the short period unstable periodic orbits periodic orbits $P_{L_1}$ and $P_{L_2}$. The bar is aligned on the y axis and rotates counterclockwise. (b) Same as (a) but in a strongly nonlinear model. (c) The apocentric unstable invariant manifolds $\mathcal{W}^{UA}_{PL_{1,2}}$ of the model (b) from $PL_1$ and $PL_2$ in the configuration space (source:Efthymiopoulos (2010))*

In Efthymiopoulos (2010) (See Fig. 1.11) and Efthymiopoulos et al. (2019) a detailed comparison of the two versions of the manifold-theory is exhibited. In the flux tube manifolds case the spiral arms are quite open and extend away from the corotation and the stars on them do not likely return into the galaxy (See Fig. 1.11(b)). In this case, one must devise a mechanism of matter renewal in order to assure that these spiral structures are long-lived. The flux tube manifolds can lead to escapes without recurrences (as presented in Fig. 1.11(a)), while in the case of the apocentric manifolds a large number of recurrences is observed inside and outside the corotation region (see Fig. 1.11(c) and Fig. 1.10). The orbits which exhibit recurrences belong to the family known as the 'hot population' (Sparke & Sellwood (1987), Kaufmann & Contopoulos (1996)).

Near $L_1$ or $L_2$ the shapes of the flux-tube and apocentric manifolds coincide. However, far from the Lagrangian points, the shapes of the apocentric manifolds allow to visualize the intricate chaotic dynamics known in dynamical systems' terminology as the 'homoclinic tangle' (see Wiggins (1990)). Thus, the flux-tube and the apocentric manifolds are the same phase-space objects, but visualized differently in physical space.

In Harsoula et al. (2016) the various manifold theories are generalised and an analytical theory for the chaotic spirals is presented. In particular, the Moser theory (Moser (1956), Moser (1958)) of invariant manifolds around unstable periodic orbits is applied. Moser proved the convergence of the normal form series describing the Hamiltonian dynamics near an unstable equilibrium point or an unstable periodic orbit. In Harsoula et al. (2016) is proved that the domains of the chaotic orbits around the invariant manifolds in barred spiral galaxies correspond to the domains of convergence of the Moser normal form around the unstable manifolds.

### 1.11.2 Computation of the apocentric invariant manifolds

In the sequel we focus on computations based on the representation of manifold spirals via the apocentric manifolds. The algorithm of calculation of the apocentric invariant manifolds $\mathcal{W}^{U}_{PL_{1,2}}$ is described in detailed in Voglis et al. (2006) and in the review Efthymiopoulos (2010). For the computation of the apocentric manifolds $\mathcal{W}^{UA}_{L1,2}$ and $\mathcal{W}^{UA}_{PL1,2}$ we work on an 'apocentric surface of section' for all trajectories of given Jacobi energy $E_J$.

1) We first build an apocentric Surface of section **S**. Every orbit corresponds to a point of $(\vartheta, P_\vartheta)$ on **S** and satisfies the condition of $P_r = 0$, $\dot{P}_r > 0$, which describes the apsidal position of the orbits. Every point $(\vartheta, P_\vartheta)$ on **S** defines an initial condition

with coordinates $(r, \vartheta, P_r = 0, P_\vartheta)$, where $r$ is the local radius at which a particle with trajectory corresponding to the Jacobi energy $E_J$ reaches a local apocentric passage with values of its angular variables equal to $(\phi, P_\varphi)$. Setting $P_r = 0$, $\dot{P}_r < 0$ in the Hamiltonian 1.41, the equation:

$$H(r, \varphi, P_r = 0, P_\varphi) = E_J \tag{1.49}$$

allows to compute the local radius $r$. In particular, this equation has two roots, for the pericentre and the apocentre of the orbits respectively. We choose the one that has the greater value of r, which corresponds to the apocentre of the orbits.

2) The Eq. (1.49) fixes the value of $r$ as function of $(\varphi, P_\varphi)$. Thus, for a randomly chosen trajectory undergoing epicyclic oscillations, the transition from one to the next apocentric passage can be viewed as a Poincaré mapping

$$(\varphi, P_\varphi) \rightarrow (\varphi' = F(\varphi, P_\varphi), \quad P'_\varphi = G(\varphi, P_\varphi)) \tag{1.50}$$

where the functions $F(\varphi, P_\varphi)$ and $G(\varphi, P_\varphi)$ are approximated numerically through the integration of the orbits. By integration, using the Hamilton equations 1.42, we can locate the images $(\varphi', P'_\varphi)$ under Poincaré mapping of the initial conditions $(\varphi, P_\varphi)$ on **S**.

3) The location of the unstable periodic orbits $PL_1$ and $PL_2$ from Eq. (1.50) is performed through the location of their apocentric intersections with the surface **S**. In particular, the orbits $PL_{1,2}$ correspond to fixed points $(\varphi_0 \ , \ P_{\varphi_0})$ of the mapping (1.50), i.e., where the following condition is satisfied:

$$\varphi' = F(\varphi_0, P_{\varphi_0}) = \varphi_0, \quad P'_\varphi = G(\varphi_0, P_{\varphi_0}) = P_{\varphi_0} \quad . \tag{1.51}$$

Eqs. [(1.51) can be viewed as a $2\times2$ algebraic system which can be solved numerically, using a root-finding technique (e.g. Newton-Raphson method), in order to compute the initial conditions $(\varphi_0, P_{\varphi_0})$ of the corresponding $PL_1$ or $PL_2$ orbit.

4) We construct the monodromy matrix of the fixed point $PL_1$ or $PL_2$ and compute its components through numerical differentiation:

$$M = \left[ \begin{array}{cc} \frac{\partial F}{\partial \varphi} & \frac{\partial F}{\partial P_\varphi} \\ \frac{\partial G}{\partial \varphi} & \frac{\partial G}{\partial P_\varphi} \end{array} \right]_{\varphi=\varphi_0, P_\varphi = P_{\varphi_0}} \quad . \tag{1.52}$$

We calculate its eigenvalues and eigenvectors of the matrix $M$. The monodromy matrix gives two opposite stable eigendirections and two unstable eigendirections respectively. We expect two real snd reciprocal eigenvalues $\lambda_{1,2}$ of the $M$, satisfying $\lambda_1 \lambda_2 = 1$.

In the work of Voglis et al. (2006b) a well-known theorem of dynamics is used for the calculation of the unstable invariant manifolds, the so called 'Grobman – Hartman theorem' (Grobman (1959), Hartman (1960), which proves the following:

(i) In autonomous Hamiltonian systems the manifolds on the Poincaré surface of section are invariant, i.e. they coincide with their images under the Poincaré map.

(ii) They approach the fixed points $PL_{1,2}$ in the directions tangent to the eigenvectors of the linearized map around $PL_{1,2}$ .

In particular, the unstable manifold $\mathcal{W}^{UA}_{L1,2}$ is tangent to the eigenvectors associated with the absolutely larger real eigenvalue (say $\lambda_1$) of the monodromy matrix $M$ at fixed point $(\varphi_0, P_{\varphi_0})$, while the stable manifold $\mathcal{W}^{SA}_{L1,2}$ is tangent to the eigenvectors associated with the absolutely smaller eigenvalue, $\lambda_2$, of the same matrix. By the symplecticity property of Poincaré maps we have $\lambda_1 \lambda_2 = 1$, thus the two eigenvalues are reciprocal and it holds that $|\lambda_1| > 1$ and $|\lambda_2| < 1$.

5) In order compute and visualize the apocentric invariant manifolds $\mathcal{W}^{UA}_{PL1,2}$ we take many initial conditions equi-spaced on a linear segment of small total length $dS$ on the apocentric surface of section $(\varphi, P_\varphi)$ along the unstable eigendirection which is determined by the equation:

$$\tan\Theta = \frac{\lambda_{1,2} - \frac{\partial F}{\partial \varphi}}{\frac{\partial F}{\partial P_\varphi}} \quad . \tag{1.53}$$

The set of initial conditions is uniformly distributed with respect to the angle $\varphi$ in a small interval $d\varphi$, starting from the angle $\varphi_0$ of the periodic orbit. The corresponding coordinate at the momentum axis $dP_\varphi$, is located through the condition that the vector $(d\varphi,\, dP_\varphi)$ coincides with the unstable eigenvector ofthe monodromy matrix of the unstable periodic orbit $PL_1$. Thus,

$$dP_\varphi = \tan\Theta d\varphi \quad . \tag{1.54}$$

Integrating all these trajectories from the initial conditions on $dS$ forward in time yields the 'flux-tube' manifolds $\mathcal{W}^{U}_{PL1,2}$, while taking only consecutive iterates of the mapping (1.50) on the apocentric surface of section **S** yields the apocentric manifolds $\mathcal{W}^{UA}_{PL1,2}$. Note that the iterates of the mapping (1.50) are pairs of values $(\varphi, P_\varphi)$. Plotting the manifold's iterated points $(\varphi, P_\varphi)$ allows the visualization of the manifolds $\mathcal{W}^{UA}_{PL1,2}$ in the phase space (phase portrait).

However, the constant energy condition $H(r, \varphi, P_r = 0, P_\varphi) = E_J$ (Eq. (1.49)) allows to compute an extra coordinate, the apocentric radius $r$ for any pair $(\varphi, P_\varphi)$. Thus, any point on the apocentric surface of section corresponds to a triplet of values $(r, \varphi, P_\varphi)$. The visualization of the apocentric manifold in physical space is obtained by plotting the manifold's computed iterated points $x = r\cos\varphi$, $y = r\sin\varphi$.

### 1.11.3 The apocentric invariant manifolds in the phase space and the configuration space

The properties of the apocentric manifolds in the phase space and the configuration space have been exhibited in Voglis et al. (2006), Tsoutsis et al. (2008), Tsoutsis et al. (2009), Efthymiopoulos (2010), Harsoula et al. (2016), Efthymiopoulos et al. (2019).

In order to interpret the contribution of the invariant manifolds in the dynamics of the orbits, we can constuct the phase portrait of a barred spiral galaxy. For the construction of the phase portrait, one takes a series of initial conditions at a fixed angle $\varphi$ on **S** and changes the azimuthal component of momentum $P_\varphi$ on the unstable equilibrium points $L_{1,2}$ and on the stable equilibrium points $L_{3,4}$ respectively. The points on the phase portrait correspond to succesive image of the Poincaré mapping on **S**.

In Fig. 1.12 we notice that these points construct orbits of different nature in the phase space. Thus, in the phase portrait of Fig. 1.12, we observe that there are closed elliptical orbits in the phase space around the stable equilibrium points $L_{3,4}$ and open orbits respectively from the unstable points $L_{3,4}$.

In Fig. 1.12 the phase space is consisted by two distinct domains. In the domain inside the corotation, for values of $P_\varphi < P_{\varphi,L1,2}$, there coexist islands of stability and organized orbits with chaotic regions that enclose them. Such extended chaotic domains are responsible for the termination of the bar (Tsoutsis et al. (2009)). The white circular domains devoid of points, embedded in the chaotic sea in this domain, correspond to prohibited domains of motion, e.g. for $E_J < E_{J_{L_4}}$. The upper domain

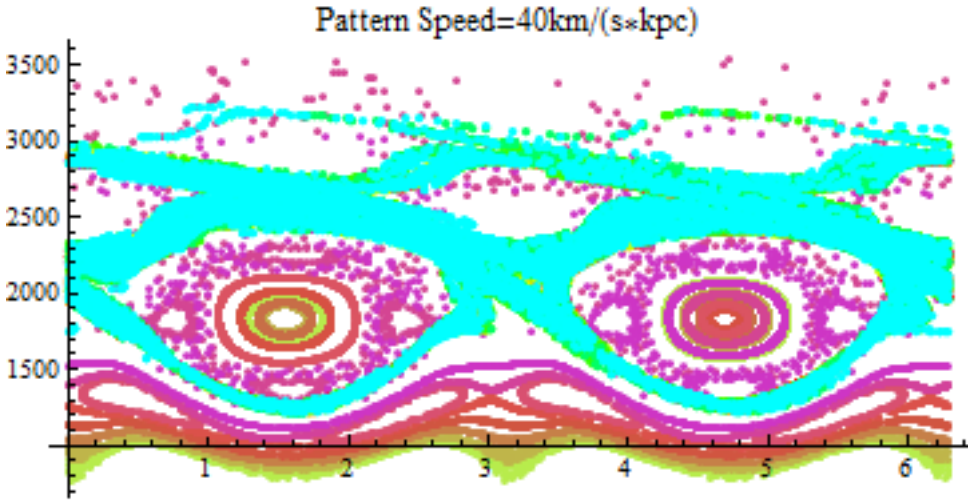


**Figure 1.12**: *The phase portrait constructed by consecutive images* $(\varphi, p_\varphi)$ *of the Poincatré mapping on* $\boldsymbol{S}$ *calculated for an analytical potential model described in Pettitt et al. (2014) and for a pattern speed* $\Omega_P = 40$ $kms^{-1}kpc^{-1}$

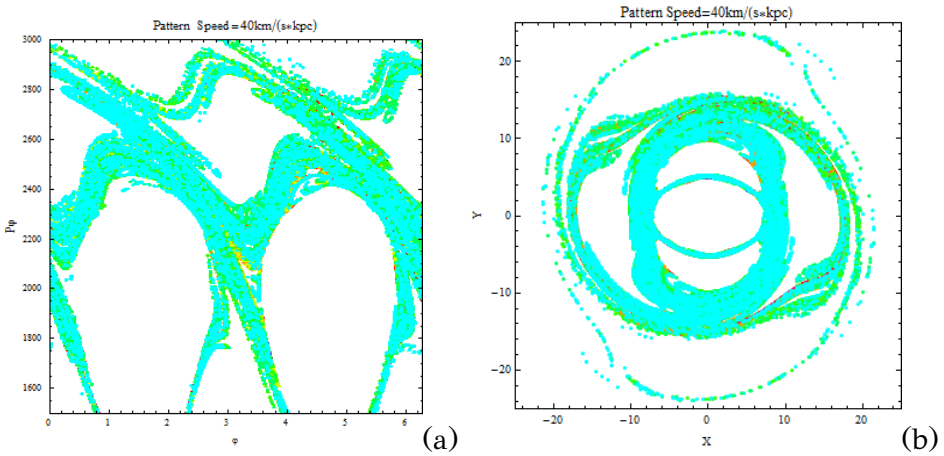


**Figure 1.13**: *The form of the invariant manifolds for an analytical potential model of the two-arm Milky Way described in Pettitt et al. (2014) with a pattern speed* $\Omega_P = 40$ $kms^{-1}kpc^{-1}$ *(a) in phase space and (b) in the configutation space*

(beyond corotation) for values of $P_\varphi > P_{\varphi,L1,2}$, is characterized almost entirely by chaos and orbital escapes. The manifolds are visualised in the phase space (Fig. 1.12 and Fig. 1.13(a)) and the configuration space (Fig. 1.13(b)) and they show the following properties:

1) The invariant manifolds contribute to the sustainment of the structure and the trajectories with initial conditions close to the invariant manifolds do not escape, remain trapped to 'sticky' orbits near the manifolds for times comparable to the age oφ the galaxy. Near the bundles of preferred directions, the invariant manifolds act as attractors of the orbits along those directions, enhancing iterative chaos and preventing escapes. These phenomena are similar to the 'stickiness' phenomena caused by invariant manifolds in Hamiltonian dynamical systems (Efthymiopoulos et al. (1997), Efthymiopoulos et al. (1999), Contopoulos & Harsoula (2008), Contopoulos & Harsoula (2010))

2) Except for the manifolds from $PL_{1,2}$, all the families of periodic orbits with Jacobian energies $E_J > E_{J,L_{1,2}}$ give manifolds. One of the main topological properties of the manifolds is that the unstable (stable) manifolds of one family cannot intersect

the unstable (stable) manifolds of any other family. As a result, the unstable manifolds of all families of periodic orbits with $E_J > E_{J,L_{1,2}}$ are forced to follow nearly parallel paths in either the phase space or the configuration space. The superposition of the invariant manifolds of all the different families generates a pattern which is called the 'coalescence' of the invariant manifolds. The coalescence of the invariant manifolds yields a trailing spiral pattern in the configuration space. In particular, it provides a dynamical skeleton for the outer shell of the bar and the spiral arms in the configuration space which is the locus of points corresponding to the successive apocentric passages of the chaotic orbits.

3) The form of the invariant manifolds originating from e.g. $PL_1$ as they approach the neighborhood of $PL_2$ is intricate and pronounces the 'homoclinic chaos' phenomenon, predicted by the theory of Hamiltonian systems. In particular, the stable and unstable manifolds have cross-sections, which are called 'homoclinic points'. The part of the invariant manifold located between two consecutive homoclinic points is called a 'lobe'. Successive images of the Poincaré mapping yield lobes increasingly elongated along the two eigendirections, creating a complex structure. This complexity is the source of chaos in Hamiltonian systems, as pointed out by Poincaré (Poincaré (1957))

4) In the disc plane, the homoclinic lobes appear as oscillations of the patterns formed by the manifolds, which give rise to the systematic appearance of several features called 'gaps', 'bridges' and 'bifurcations'. It is usually observed in the apocentric manifolds case that weak extensions of the spiral arm emanating from one end of the bar form 'bridges', which join the spiral arm emanating from the opposite end or the bar, aproaching it from its exterior side.

5) Another property of the manifolds is that they are recurrent (Contopoulos & Polymilis (1995)), i.e. the manifold lobes return many times near the points $PL_{1,2}$ even if they temporarily go to large excursions away from $PL_{1,2}$. This property introduces a dynamical mechanism of replenishment of the material in the galactic system. It is also remarkable that the recurrence of the manifolds can create new stickiness phenomena ('recurrent stickiness'), leading to further accumulation of points in the narrow stickiness zone along the manifolds (Contopoulos & Harsoula (2010)).

## 1.12 Multiple pattern speeds and manifold spirals

### 1.12.1 Multiple pattern speeds in the Milky Way and in other galaxies

Recent observations in our Galaxy and in other galaxies and N- body simulations of barred spiral galaxies prove that the spiral arms rotate at a different pattern speed than the bar. Moreover, the values of the pattern speeds gradually change with time as the disc goes through secular evolution. These facts should be taken into account in a dynamical study of the spiral structure of the galaxies.

The multiple pattern speed scenario holds for our Galaxy (as reviewed e.g. in Bland-Hawthorn & Gerhard (2016); see also Antoja et al. (2014), Junqueira et al. (2015) and references therein, Gerhard (2010), Dias & Lépine (2005)).

In the Milky Way the bar rotates rapidly at a pattern speed that is estimated at $45 - 60\ km/s/kpc$ (Bland-Hawthorn & Gerhard (2016), Gerhard (2011), Dias & Lépine (2005)). The corotation is estimated at $3.5 - 4.5$ kpc (Englmaier & Gerhard (1999), Fux (1999)). The velocities in the solar neighbourhood are influenced more by the bar, and somewhat by the spiral arms. Some of the used methods for the estimation of the pattern speed of the bar in our Galaxy are the following (see Bland-Hawthorn & Gerhard (2016) review):

1) The application of the Tremaine-Weinberg method (Tremaine & Weinberg (1984)) to a complete sample of OH/IR stars in the inner Galaxy (Debattista et al. (2002)). This method was first discussed in the context of external galaxies but it can be applied also in our Galaxy.

2) Using hydrodynamic simulations comparing the gas flow with observed Galactic CO and HI lv-diagrams (longitude–velocity diagrams). These simulations (Englmaier & Gerhard (1999), Fux (1999)) cannot reproduce all the observed features equally well, as they depend explicitely on the galactic gas features and they lack the information of the effect of the gravitational potential (Bland-Hawthorn & Gerhard (2016).

3) Another method is based on the interpretation of star streams observed in the distribution of stellar velocities in the solar neighborhood. Hydrodynamic modeling of the inner Galaxy suggests that the radius of the outer Lindblad resonance (OLR) of the Galactic bar lies in the solar neighbourhood. The study of the stellar kinematics in the solar neighbourhood can lead to the location of the resonances and to an approximately estimation the pattern speed of the bar. (Kalnajs (1991), Dehnen (2000), Antoja et al. (2014)).

The galactic spiral arms rotate with a distinctively slower pattern speed in the Milky Way. The angular velocity of the spiral arms has been estimated to be $17 - 28$ $km/s/kpc$ (Dias & Lépine (2005), Gerhard (2010)). The method of 'open cluster birthplace analysis' and the velocity field of nearby younger stars indicate that the spiral arms corotation is outside from the bar's corotation. For the determination of the pattern speed of the spiral arms of the Milky Way, some of the most commonly used methods are the following:

1) The method 'open clusters birthplace analysis' (Dias & Lépine (2005), Gerhard (2010)) is the most common. In the 'open clusters birthplace analysis' the pattern speed of the spiral arms of the Galaxy is determined by direct observation of the birthplaces of open clusters of stars in the Galactic disc as a function of their age. Given the current locations, distances, proper motions and ages of these stars, they integrate their orbits backwards in time according to their known ages, using a model for the local circular speed in the disc. In Dias & Lépine (2005) they confirmed that open clusters are born in spiral arms. As a result, the distribution of birthplaces for some age bins is expected to be spiral-like, and by comparing the spiral patterns obtained from different age bins, the angle of rotation of the pattern can be estimated and therefore, the pattern speed of the spiral arms.

2) Another method to derive the spiral pattern speed of the Milky Way is based on the interaction between the spiral arms and the stellar objects (Junqueira et al. (2015)). In this method, a sample of OCs and red giant stars used and they make an assumption that the initial energy and the angular momentum of the objects can be approximated as the circular orbit at the mean radius.

3) Some older determinations for the angular velocity of the spiral pattern yield from OB and Cepheid stars (see Fernández et al. (2001)).

Similar works in other galaxies also give evidence for different pattern speeds for the bar and the spiral arms (e.g. Vera-Villamizar et al. (2001), Boonyasait et al. (2005), Patsis et al. (2009), Meidt et al. (2009), Speights & Westpfahl (2012), Speights & Rooke (2016)). In Speights & Rooke (2016) the galaxy NGC 1365 the detection of two different pattern speeds for the bar and the spiral arms respectively, is implemented through the radial profile of the pattern speed, which is obtained by fitting mathematical models based on the Tremaine–Weinberg method (Tremaine & Weinberg (1984)). In Patsis et al. (2009) the dynamics of the barred-spiral galaxy NGC 3359 is studied, where the galactic gravitational potential is estimated through

observations and orbital theory and response models are applied for the study of the stellar motions. This study proves that the bar and the spiral arms rotate at a different pattern speed.

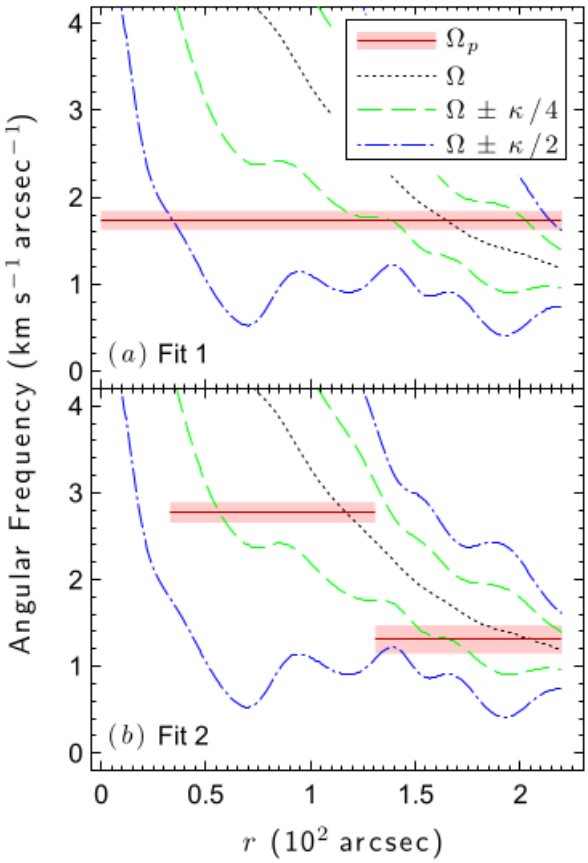


**Figure 1.14**: *The radial profile of the angular velocity for the galaxy NGC 1365 which reveals two different pattern speeds in Speights & Rooke (2016)*

.

As regards simulations, the leading paradigm over the years refers to simulations showing the co-existence of multiple pattern speeds (Sellwood & Sparke (1988), Little & Carlberg (1991), Rautiainen & Salo (1999), Quillen (2003), Minchev & Quillen (2006), Dubinski et al. (2009), Quillen et al. (2011), Minchev et al. (2012), Baba et al. (2013), Roca-Fabrega et al. (2013), Font et al. (2014), Baba (2015)). The first indication for different pattern speeds in the galactic disc in an N- body of a barred spiral galaxy was given by Sellwood and Sparke in 1988. The contour plots of the power spectrum of m=2 modes of the Fourier transform yield two maxima which correspond to two different pattern speeds (see Fig. 1.15). Someone would expect the bar to be observed disconnected from the spiral arms, due to the difference of their angular velocities. However, Sellwood and Sparke proved through the contours of the surface density in the physical space, that most of the time of the simulation the spiral arms emanate from the ends of the bar (see Fig. 1.16).

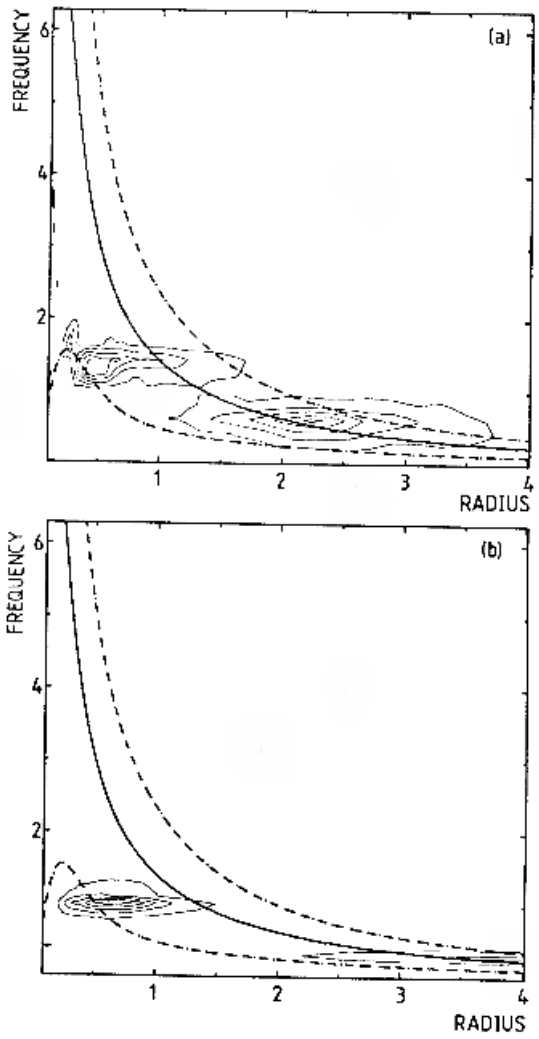


**Figure 1.15**: *The Contours of power spectrum of m=2 galactic modes as a function of frequency and radius in Sellwood & Sparke (1988)*

### 1.12.2 The manifold theory with multiple pattern speeds

The basic form of the manifold theory assumes a single pattern speed in the galactic disc, which is considered to be the angular velocity of both the bar and the spiral arms connected to it. This is in conflict with observations and N-body simulations, as described in 1.12.1. The manifold theory has been extended in a recent work by Efthymiopoulos et al. (2020) to cover the case of the spiral arms having a pattern speed different than the one of the bar. In particular, it has been shown that the spiral arms can be modelled by the manifolds of the so-called $GL_1$ and $GL_2$ families of periodic orbits, which play, in the multiple pattern speed case, a role analogous to the one of $L_1$ and $L_2$ equilibrium points of the single pattern speed case.

Since the unstable equilibria $L_1$ and $L_2$ are possible to define only when the potential is static in a frame co-rotating with the bar, manifold spirals emanating from $L_1$ and $L_2$ are necessarily also static in the same frame, hence, they should co-rotate with the bar. As shown in Efthymiopoulos et al. (2020) the orbits $GL_1$ and $GL_2$ lead to invariant manifolds which can be regarded as the generalization of the manifolds of the $L_1$, $L_2$ points in the single pattern speed case. As an example they compute the generalized orbits $GL_1$, $GL_2$ and their manifolds in a Milky-way like model with bar and spiral pattern speeds assumed different. They find that the man-

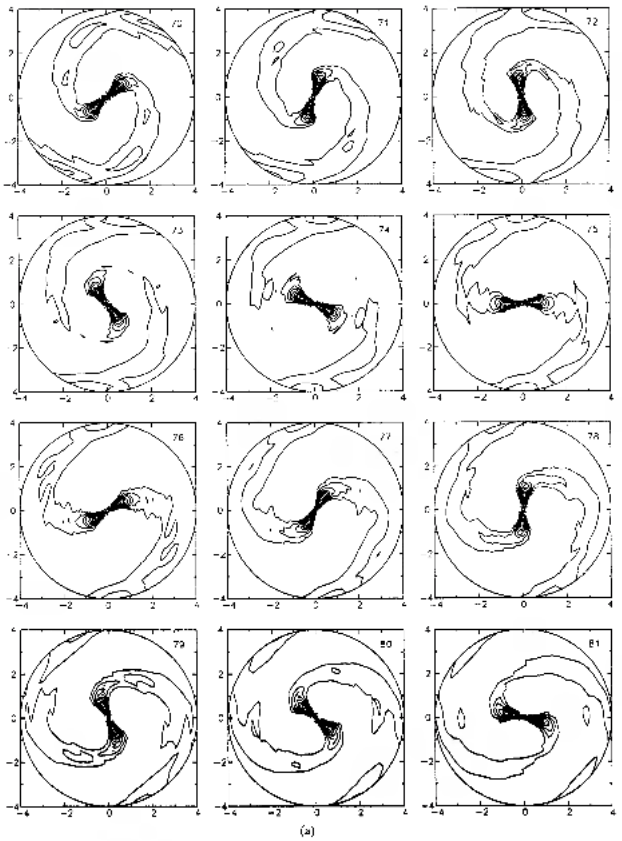

**Figure 1.16**: *The Contours of the fractional perturbation in the surface density at different times of the N-body simulation in Sellwood & Sparke (1988)*

ifolds are time-varying because of the time dependency in our system. The resulting morphology consisting of segments of spirals or 'pseudorings'. These structures are repeated after a period equal to half the relative period of the imposed spirals with respect to the bar. Along one period, the manifold-induced time-varying structures are found to continuously support at least some parts of the imposed spirals, except at short intervals around those times at which the relative phase of the imposed spirals with respect to the bar becomes equal to $\pm\pi/2$. A connection of these effects to the phenomenon of recurrent spirals is discussed below in Chapter 3.

## 1.13 The secular evolution in galactic discs

Even isolated barred galaxies undergo substantial secular evolution (see Athanassoula (2013), Binney (2013), Kormendy (2013) in the tutorial volume Falcon-Barroso and Knapen (2013)) and this also a substantial effect on the dynamics of these galaxies. Sellwood at Sellwood (1980) was the first to prove the exchange of angular momentum between the disc and the dark halo, which causes the bar slow-down. Later, Weinberg at Weinberg (1985) made an estimation for the bar deceleration rate. It is well known that the tendency to transfer angular momentum outwards (e.g. towards the halo or across the disc, Tremaine & Weinberg (1984), Debattista & Sellwood (1988), Debattista & Sellwood (2000), Athanassoula (2002), Athanassoula & Misiriotis (2002), Athanassoula (2003), OŃeill & Dubinski (2003), Holley-Bockelmann et al. (2005), Berentzen et al. (2006), Martinez-Valpuesta et al. (2006)) leads the bars to slow down in time and grow in size at a rate which produces non-negligible change in dynamics at timescales comparable even to a few bar periods. The bars

experience a drag due to the dynamical friction with the dark halo and this leads to the bar slow down and the gradual overlapping of the corotation and of the other resonances in further distances from the galactic center. As a result, the pattern speed of the bar is evolving along with the disc, due to the exchange of angular momentum among the different parts of the disc (Athanassoula (2003)).

This process becomes complex, and even partially reversed due to the growth of 'pseudo-bulges' or 'peanuts' (Kormendy & Kennicutt (2004)), caused by dynamical instabilities such as chaos or the 'buckling instability' Combes & Sanders (1981), Combes et al. (1990), Pfenniger & Friedli (1991), Raha et al. (1991), Bureau & Athanassoula (1999), Martinez-Valpuesta & Shlosman (2004), Bureau & Athanassoula (2005), Debattista et al. (2006)). The reduction in size of the bar by transfer of angular momentum under constant pattern speed is discussed in Weinberg & Katz (2007). Spiral activity acts as an additional factor of outwards transfer of angular momentum (Lynden-Bell & Kalnajs (1972)), while a radial re-distribution of matter can take place even under a nearly-preserved distribution of angular momentum (Hohl (1971), Sellwood & Binney (2002), Avila-Reese et al. (2005)). Radial migration is enhanced by the amplification of chaos due to the overlapping of resonances among the various patterns (Quillen (2003), Minchev & Quillen (2006), Quillen et al. (2011)).

The secular evolution of barred spiral galaxies should be taken into account in every study that attempts to investigates the dynamics of these systems. The morphology of the bar and the pattern speed change gradually with time and also other non-axisymmetric structures may be affected by the secular evolution. The manifold theory explains the intricate dynamics of barred spiral galaxies and there is an open problem if the manifold spirals also follow the secular ecolution of the disc. The morphology of the invariant manifolds found by momentarily 'freezing' the potential and pattern speed value are exected to undergo important changes in time so as to support the evolving structures of the disc. An implementation of this problem was made in an N-body simulation by Lia Athanassoula and it was shown that, despite these changes, the stars out-flowing from the neighborhood of the Lagrangian points $L_1$ and $L_2$ develop orbits which, in general keep track of the change of the form of the invariant manifolds (Athanassoula (2012), see also Baba (2015), Lokas (2016)). As a rule, the material which populates the manifolds comes from orbital outflows originating from the interior of co-rotation, at the end of the bar (Contopoulos (1980)). As these outflows are adapted to the slowly-changing form of the manifolds, they are able to yield time-varying spiral or ring-like patterns. However, since the potential of the N-body simulations is constantly evolving with time, the manifold theory should develop and get adjusted to the secular evolution of the disc.

## 1.14 The object and structure of the thesis

In the present thesis we study the spiral structure of the galaxies, a still open astronomical problem. Some open subjects regarging the spiral arms of the galaxies are their morphology, nature, i.e., the mechanism that generates them, as well as their longevity and evolution. The spiral structure is supported by mechanisms arising from the intricate dynamics of the galactic systems. In the present thesis, we examine two models of spiral galaxies, where the spiral structure is generated by two different mehanisms. We apply the theories of the spiral structure and test whether they reproduce the spirals in any of the two cases. In particular, we conduct a dynamical study in following cases of galactic models:

**(a)** In a **Milky Way-like theoretical potential model**. We examine how the

spiral density waves are reproduced by organised orbits, which are called "precessing ellipses" in any normal galaxy and in a Milky Way-like model.

**(b)** In a **self-consistent N-body model of barred spiral galaxy**, where the spirals are chaotic. One main question is how coherent spiral structures can emerge from chaotic orbits. The manifold theory attempts to answer this problem. We reproduce the manifold spirals for the N-body simulation and we examine whether the manifold spirals are consistent with the assumption of multiple pattern speed.

Subsequently, we are going to present in detail the structure and the objectives of every Chapter which constructs the thesis:

In **Chapter 2** we study spirals generated by the "precessing ellipses" mechanism, which evolves the $x_1$ closed orbits. These orbits are elongated ellipses that gradually change orientation and enhance the spiral. We first present an algorithm, based on the resonant pertubation theory, which gives analytical solutions of the periodic orbits of the system, as well as the $x_1$ closed orbits. In particular, we proceed consecutive transformations in the Hamiltonian in order to end up to a resonant normal form which reveals the two fundamental frequencies and their relation. This work was first introduced in Contopoulos (1970), Contopoulos (1975) (see also the review Efthymiopoulos (2010)). This algorithm can be applied in every toy model of a normal spiral galaxy and help us make an effective study of its geometric and dynamical parametrese.

We apply this algorithm in a Milky Way-like potential model (Pettitt et al. (2014)). We compare the analytical $x_1$ orbits with the ones produced by numerical methods. The construction of the phase space is going to reveal in which areas of the galactic disc, determined by the resonances, the precessing ellipses support the spiral density wave. In this case, we are going to study the range of free parametres (the pattern speed of the spiral arms, the amplitude of the spiral pertubation and the pitch angle) and how they collaborate in order to generate realistic density waves. In the extreme condition of these parameters, the "precessing ellipses" become largely distorted, chaos is introduced in the system, and the orbits can no longer support the spiral arms.

In **Chapter 3** we examine the application of the manifold theory in a self- consistent N-body simulation of a barred spiral galaxy (Kyziropoulos et al. (2016)). Whenever a bar is formed in a simulation, one finds manifold-driven spirals, as well as traces of secular evolution. The manifold theory of the spiral structure relies on a few simplifications, the most important of which is that the potential is time-independent in the frame of reference corotating with the bar. On the other hand, in simulations and in real galaxies the potential evolves with time, due to redistribution of angular momentum via the resonances. In this chapter, we are going to study the time evolution of the manifold spirals along with the secular ecolution of the disc and the vividly evolving morphologies of the N-body we observe. Through this time evolution we investigate in which extend the N-body spiral arms, as well as other non-axisymmetric features, are supported by the manifolds.

We are going to present the reproduction of the apocentric manifolds $\mathcal{W}^{UA}_{PL1,2}$ both in the phase space and the configuration space and detect some recognisable manifolds' morphological features ('bridges' and 'gaps'). We compare the evolving disc morphologies with the manifolds at various times and identify the role of the invariant manifolds as a skeleton of chaotic orbits in phase space, or, the dynamical avenues to be followed by particles whenever an incident of spiral or other non-axisymmetric activity is triggered in the disc. We will also correlate the agreement of the manifolds with the incidents of the spiral activities in the disc.

In **Chapter 4** we compute the manifold spirals under the multiple pattern speeds

assumption. The manifold theory in its basic form made the assumption that the whole disc corotates with the bar in a single pattern speed. This assumption is in conflict with observations of real galaxies and N-body simulations (see subsection 1.12.1). In Chapter 3 the manifolds are computed with the simplified assumption of a unique pattern speed in the galactic disc. However, we discover the limitations of that assumption as, by a rough estimate of the angular speed of the maxima of m=2 mode, we observe the presence of a second pattern speed beyond the bar.

In this chapter, we revisit the N-body simulation of Chapter 3 and we propose an accurate method to identify the different pattern speeds in the simulation's disc and estimate their values, based on the algorithm of Numerical Analysis of the Fundamental Frequencies (NAFF, Laskar (1990), Laskar et al. (1992), Laskar (1993), Laskar (2003), Fu & Laskar (2019)). This is particularly convenient in cases where the pattern speeds slowly change in time due to secular evolution in the disc, and/or, the different modes spatially overlap in the disc. Once we get the frequences, we compute the approximate gravitational potential, and produce the manifold spirals, applying the theory of Efthymiopoulos et al. (2020). In the case of multiple pattern speeds the potential becomes time-dependent, thus the Lagrangian equilibrium point $L_{1,2}$ generalise to periodic equilibrium orbits $GL_{1,2}$ and the manifolds are time-evolving. Finally, we examine whether the observed structures formed by the spiral arms in the simulation (change of form, formation of 'bridges', etc.) can be modelled by manifolds, consistent with the fact that the bar and spirals have different pattern speeds.

V) Finally, **Chapter 5** summarises the main conclusions of this research work, which is incorporated in the Chapters 2- 4 and discusses some aspects of future work in all these subjects that we are going to present.

# Chapter 2

# Precessing ellipses as the building blocks of the spiral arms

*Parts of the results of the present chapter were published as:*
*Harsoula M., Zouloumi K., Efthymiopoulos C., and Contopoulos G., 2021, A& A, 655, A55.*

The main families of periodic orbits, located in the case of normal spiral galaxies, were first calculated analytically by Contopoulos (Contopoulos (1970), Contopoulos (1975)). These orbits are called 'x1', 'x2' which are stable periodic orbits, and 'x3' which is unstable. The stable periodic orbits 'x1' are elongated 'precessing ellipses' in the physical space which gradually change their orientation and their apocenters support the spiral density wave. In this Chapter we are going to present a procedure for the calculation of the families of periodic orbits. In particular we show that the application of the resonant pertubation theory near the Inner Lindbland resonance in a simple model of a normal galaxy can give us the three families of periodic orbits 'x1', 'x2' and 'x3'. We develop an algorithm that allows the analytical prediction of the periodic orbits in any toy model of a normal spiral galaxy. For this purpose, we test the algorithm in an analytical Milky Way-like potential model and we compute the orbits $x_1$. We compare the analytical orbits to the ones produced by numerical methods. We also study the range in parameter space for which the amplitude of the spiral perturbation, the pattern speed and the pitch angle collaborate so as to lead to the creation of realistic density waves supported by "precessing ellipses" and their surrounding matter in ordered motion.

## 2.1 The resonant pertubation theory for the location of the periodic orbits in a normal spiral galaxy

### 2.1.1 Hamiltonian Expansion

The Hamiltonian of the orbits for an axisymmetric galactic potential in the inertial system of reference is

$$\mathcal{H}_0(r) = \frac{{P_r}^2}{2} + \frac{{P_\varphi}^2}{2r^2} + V_0(r) \quad . \tag{2.1}$$

The term $V_0(r)$ corresponds to the axisymmetric potential of a normal galaxy. This term can incorporate the potential of a buldge, of a disc and a dark halo.

In Section 1.4 we studied the behaviour of the orbits in the case of an axisymmetric

potential and presented the main frequencies. Two fundamental frequencies of the stellar orbits are located, the epicyclic frequency $\kappa(r)$ and the angular frequency $\Omega(r)$. The stellar motions can be seen as elliptic orbits peforming a revolution with frequency $\Omega(r)$ and travelling from an apocentric to a pericentric distance with an oscillating frequency $\kappa$.

We also presented the circular orbit in the axisymmetric problem which is located at the minimum of the effective potential and for the minimum of the effective potential. As described in Section 1.4 the condition of the minimum of the effective potential leads to the relation:

$$P_\varphi{}^2 = r_c{}^3 \frac{dV_0(r_c)}{dr_c} \quad . \tag{2.2}$$

These frequencies are given as a function of $V_0(r)$ (see the proof in Section 1.4). The angular velocity of the circular orbit is:

$$\Omega(r_c) = \sqrt{\frac{1}{r_c}\frac{dV_0(r_c)}{dr_c}} \tag{2.3}$$

and the epicyclic frequency takes an oscillating form:

$$\kappa(r_c) = \sqrt{\frac{d^2 V_e f f(r_c)}{dr_c{}^2}} = \frac{3P_\varphi{}^2}{r_c{}^4} + \frac{d^2V_0(r_c)}{dr_c^2} \tag{2.4}$$

The spiral potential $V_{sp}(r,\varphi)$ is a non-axisymmetric term which is expected to take the form:

$$V_{sp}(r,\varphi) = -A_{sp}(r)\cos(2\varphi - \phi_2(r)) \tag{2.5}$$

where $A_{sp}(r)$ is the amplitude of the spiral pertubation and the term $\phi_2(r)$ is related to the geometric characteristics of the spiral arms (e.g. the pitch angle or the length of the spiral arms). The Hamiltonian with the import of the spiral potential $V_{sp}(r,\varphi)$ yields:

$$\mathcal{H}(r,\varphi) = \frac{P_r{}^2}{2} + \frac{P_\varphi{}^2}{r^2} + V_0(r) + V_{sp}(r,\varphi) \quad . \tag{2.6}$$

Conseqently, the Hamiltonian is written in the form:

$$\mathcal{H}(r,\varphi) = \mathcal{H}_0(r) + V_{sp}(r,\varphi) = \mathcal{H}_0(r) + \mathcal{H}_1(r,\varphi) \quad . \tag{2.7}$$

By the form of the Hamiltonian in 2.7 we observe that the system is described by two parts of the Hamiltonian: by a term $\mathcal{H}_0(r)$, which is the Hamiltonian of the unperturbed system and a term $\mathcal{H}_1(r,\varphi)$ which is the pertubation of the system. As a result, the spiral potential plays the role of a pertubation in the galactic system.

The orbits in this case are considered to be a continuation from the circular orbit of the axisymmetric problem in the 2/1 resonant domain. The relation of the two fundamental frequencies define the resonances of the orbits which are presented in Section 1.5 (see Eq. (1.39) in Section 1.5). The 2/1 resonance is given by the relation:

$$\frac{2}{1} = \frac{\kappa}{(\Omega - \Omega_P)} \quad . \tag{2.8}$$

In order to locate these orbits we expand the Hamiltonian around the circular orbit with coordinates ($r_c$, $P_c$). $P_c$ is the angular momentum $P_\varphi(r_c)$ of the circular orbit and from Eq. (1.26) of Section 1.4 it is given by the relation:

$$P_c = \Omega_c{}^2 r_c \quad . \tag{2.9}$$

We also symbolise for simplicity $\Omega_c = \Omega(r_c)$ and $\kappa_c = \kappa(r_c)$ We proceed Taylor-expanding up to 4th degree in $r - r_c$ in $\mathcal{H}_0$, where the coordinates are:

$$\begin{aligned} r &= r_c + \varepsilon dr \\ P_\varphi &= P_c + \varepsilon^2 J_\varphi \\ P_r &= P_r \varepsilon \quad . \end{aligned} \tag{2.10}$$

The Hamiltonian takes the form:

$$\begin{aligned} \mathcal{H}_0 = \frac{{P_r}^2}{2} + \frac{{P_c}^2}{2{r_c}^2} \sum_{n=0}^{n=4} (-1)^n \frac{(n+1)dr^n}{{r_c}^n} + \frac{{J_\varphi}^2}{2{r_c}^2} + \frac{J_\varphi P_c}{{r_c}^2} - \frac{2dr J_\varphi P_c}{{r_c}^3} \\ + \frac{3dr^2 J_\varphi P_c}{{r_c}^4} + \sum_{n=0}^{n=4} \frac{V_0^{(n)}(r_c) dr^n}{n!} \quad . \end{aligned} \tag{2.11}$$

In the expanding form of Hamiltonian we locate the 1st and the 2nd derivative of the axisymmetric potential, which can be written as a function of the fundamental frequencies. The 2nd derivative of the axisymmetric potential ${V_0}''(r_c)$ is given as a function of the epicyclic frequency $\kappa_c$:

$$V0''(rc) = {k_c}^2 - \frac{3{P_c}^2}{{r_c}^4} \quad . \tag{2.12}$$

Using the condition of the minimum of the effective potential 2.2 the 1st derivative $V_0'(r_c)$ is given as a function of the angular momentum of the circular orbit $P_c$:

$${V_0}'(r_c) = \frac{{P_c}^2}{{r_c}^3} \quad . \tag{2.13}$$

The Hamiltonian $\mathcal{H}_0$ from Eq. (2.11) using Eqs. (2.12),(2.13) becomes:

$$\begin{aligned} \mathcal{H}_0 = \frac{{P_r}^2}{2} + \frac{{P_c}^2}{2{r_c}^2} + \frac{{J_\varphi}^2}{2{r_c}^2} + \frac{J_\varphi P_c}{{r_c}^2} - \frac{2dr J_\varphi P_c}{{r_c}^3} + \frac{3dr^2 J_\varphi P_c}{{r_c}^4} + V_0(r) + \\ \frac{{P_c}^2}{2{r_c}^2} \sum_{n=3}^{n=4} (-1)^n \frac{(n+1)dr^n}{{r_c}^n} + \sum_{n=3}^{n=4} \frac{V_0^{(n)}(r_c) dr^n}{n!} \quad . \end{aligned} \tag{2.14}$$

We also implement the same Taylor-expanding in the spiral potential $V_{sp}$:

$$\begin{aligned} \mathcal{H}_1(r, \varphi) = - dr A'(r_c) \cos(2\varphi - \phi_2(rc)) - A(r_c)(dr {\phi_2}'(r_c) \sin(\varphi_2 - \phi_2(\mathrm{rc})) + \\ \cos(\varphi_2 - \phi_2(r_c))) \quad . \end{aligned} \tag{2.15}$$

### 2.1.2 The Hamiltonian in action angle variables

Writing the Hamiltonian $\mathcal{H}_0$ in action angle variables helps us define the local motions around the circular orbit $r_c$ and reveals the fundamental frequencies of the orbits.

In order to interpret the purpose of this transformation we first consider the case of a simple harmonic oscillator. In particular if we consider an harmonic oscillator of mass $m$ and energy $E$, which oscillates with frequency $\omega$ and its motion is described by a Hamiltonian:

$$\mathcal{H}_{osc}((q,p)) = \frac{p^2}{2m} + \frac{m\omega^2 q^2}{2} \quad . \tag{2.16}$$

This simple model of periodic motion is a common paradigm in Classical Mechanics for the definition of the action angle variables. In this model it is proved that the old

Hamiltonian $\mathcal{H}_{osc}((q,p))$ is going to be expressed through a canonical set of coordinates $(I,\vartheta)$, where $\vartheta$ is the angle and $I$ its conjugate action, given by the relations:

$$q = \sqrt{\frac{2I}{m\omega}}\sin(\vartheta)$$
$$p = \sqrt{2Im\omega}\cos(\vartheta) \tag{2.17}$$

and the new Hamiltonian ends up to the form:

$$\mathcal{H}'_{osc}(I,\vartheta) = I\omega \quad . \tag{2.18}$$

If a pair $(I,\vartheta)$ is an action angle variable, we expect the Hamiltonian to be periodic in angle $(\vartheta)$ with one of the fundamental frequencies of the system. In Hamiltonian $\mathcal{H}_0$ from Eq. (2.14) the pair $(\varphi,\ P_\varphi)$ is already an action-angle variable pair with frequency $\Omega_c$. We expect an action angle $(\varphi_r$,$J_r)$ variable pair to coexist in the system in order to describe the epicyclic motions with frequency $\kappa_c$. These new coordinates $(\varphi_r$,$J_r)$ are related to the old ones $(dr = r - r_c,\ P_r)$ and take a form analogous to the ones in Eq. (2.17) of a simple harmonic oscillator:

$$dr = r - r_c = \sqrt{\frac{2J_r}{k_c}}\sin(\varphi_r)$$
$$P_r = \sqrt{2J_r k_c}\cos(\varphi_r) \quad . \tag{2.19}$$

The variable $dr$ in Hamiltonian describes the deviation from the circular orbit. We write the old variables $(dr = r - r_c,\ P_r)$ as a function of $(\vartheta_r$,$J_r)$ through the Eq. (2.19) and we substitute $P_c$ from the relation $P_c = \Omega_c {r_c}^2$. The Hamiltonian $\mathcal{H}_0$ from Eq (2.14), in the rotating frame of reference with the pattern speed of the spiral arms $\Omega_{sp}$, takes the form:

$$\begin{aligned}
&\mathcal{H}_0(\varphi, J_\varphi, \varphi_r, J_r) = J_r k_c + J_\varphi(\Omega_c - \Omega_{sp}) + \frac{{J_\varphi}^2}{2{r_c}^2} + \frac{{\Omega_c}^2 rc^2}{2} + \frac{15{J_r}^2{\Omega_c}^2}{4{k_c}^2{r_c}^2} + \frac{3J_r J_\varphi \Omega_c}{k_c {r_c}^2} \\
&\frac{J_r\Omega_c\cos(2\varphi_r)(5J_r\Omega_c - 3J_\varphi kc)}{{k_c}^2{r_c}^2} + \frac{5{J_r}^2{\Omega_c}^2\cos(4\varphi_r)}{4{k_c}^2{r_c}^2} - \\
&\frac{\sqrt{2}\sqrt{J_r}\Omega_c\sin(\varphi_r)(3J_r\Omega_c + 2J_\varphi k_c)}{{k_c}^{3/2}r_c} + \frac{\sqrt{2}{J_r}^{3/2}{\Omega_c}^2\sin(3\varphi_r)}{{k_c}^{3/2}r_c} + V_0(r_c) + \mathcal{O}({V_0}^{(n)}(r_c)) \quad .
\end{aligned} \tag{2.20}$$

We also implement the same transformation in the Hamiltonian term $\mathcal{H}_1(r,\varphi)$ from Eq. (2.15) and it ends up to the form:

$$\begin{aligned}
&\mathcal{H}_1(\varphi, J_\varphi, \varphi_r, J_r) = \frac{\sqrt{J_r}A'(r_c)\sin[(2\varphi - \varphi_r) - \varphi_2(r_c)]}{\sqrt{2}\sqrt{kc}} - \frac{\sqrt{J_r}A'(r_c)\sin[(2\varphi + \varphi_r) - \varphi_2(r_c)]}{\sqrt{2}\sqrt{k_c}} \\
&- \frac{\sqrt{J_r}A(r_c)phir'(r_c)\cos[(2\varphi - \varphi_r) - \varphi_2(r_c)]}{\sqrt{2}\sqrt{k_c}} + \frac{\sqrt{J_r}A(r_c)phir'(r_c)\cos[(2\varphi + \varphi_r) - \varphi_2(r_c)]}{\sqrt{2}\sqrt{k_c}} \\
&- A(r_c)\cos(2\varphi - \varphi_2(r_c)) \quad .
\end{aligned} \tag{2.21}$$

### 2.1.3 First Normalization of the Hamiltonian

We are going to implement consecutive transformations in the Hamiltonian $\mathcal{H}(\varphi, J_\varphi, \varphi_r, J_r)$ (Eq. (2.20)) in order to eliminate unwanted terms. For this purpose we apply through the Lie method a canonical transformation in the Hamiltonian and we implement the following steps:

1) The Hamiltonian has the terms $\mathcal{H}_0(\varphi, J_\varphi, \varphi_r, J_r)$ and $\mathcal{H}_1(\varphi, J_\varphi, \varphi_r, J_r)$ from Eqs(2.21):

$$\mathcal{H}(\varphi, J_\varphi, \varphi_r, J_r) = \mathcal{H}_0(\varphi, J_\varphi, \varphi_r, J_r) + \mathcal{H}_1(\varphi, J_\varphi, \varphi_r, J_r) \quad . \tag{2.22}$$

We expand the Hamiltonian (2.22) considering that:

$$\begin{aligned} J_r &\propto \varepsilon^2 J_r \\ J_\varphi &\propto \varepsilon^2 J_\varphi \quad . \end{aligned} \tag{2.23}$$

The final Hamiltonian is :

$$\mathcal{H}^{(0)}(\varphi, J_\varphi, \varphi_r, J_r) = J_r k_c + J_\varphi(\Omega_c - \Omega_{sp}) + \varepsilon^1 h_1 + \varepsilon^2 h_2 + +\mathcal{O}(\varepsilon^n) \tag{2.24}$$

where $h_1$ are the linear terms of the Hamiltonian:

$$\begin{aligned} h_1 = &-A(rc)\sin(2\varphi)\sin(\varphi_2(r_c)) - A(r_c)\cos(2\varphi)\cos(\varphi_2(r_c)) + \frac{\sqrt{2}{J_r}^{3/2}\sin(3\varphi_r)\Omega_c}{{k_c}^{3/2} r_c} - \\ &\frac{\sqrt{2}\sqrt{J_r}\sin(\varphi_r)\Omega_c\,(3Jr\Omega_c + 2J_\varphi k_c)}{{k_c}^{3/2}{r_c}^2} + \mathcal{O}(\varepsilon {V_0}^{(n)}) \end{aligned} \tag{2.25}$$

and $h_2$ are the terms of 2nd order of the Hamiltonian:

$$\begin{aligned} h_2 = &\frac{P(J_r, J_\varphi, \Omega_c, k_c)}{4{k_c}^4{r_c}^2} - \frac{Jr\Omega_c\cos(2\varphi_r)(5Jr\Omega_c + 3J_\varphi k_c)}{{k_c}^2{r_c}^2} + \frac{5{J_r}^2{\Omega_c}^2\cos(4\varphi_r)}{4{k_c}^2{r_c}^2} + \\ &\frac{\sqrt{2}\sqrt{J_r}\sin\left(\frac{\Delta\varphi_- - \Delta\varphi_+}{2}\right)}{\sqrt{k_c}}[A'(r_c)\cos\left(\frac{1}{2}(\Delta\varphi_- + \Delta\varphi_+ - 2\varphi_2(r_c))\right) + \\ &A(r_c){\varphi_2}'(r_c)\sin\left(\frac{1}{2}(\Delta\varphi_- + \Delta\varphi_+ - 2\varphi_2(r_c))\right)] + \mathcal{O}(\varepsilon^2 {V_0}^{(n)}) \end{aligned} \tag{2.26}$$

where

$$\begin{aligned} \Delta\varphi_+ &= 2\varphi + \varphi_r \\ \Delta\varphi_- &= 2\varphi - \varphi_r \end{aligned} \tag{2.27}$$

and $P(J_r, J_\varphi, \Omega_c, k_c)$ a polynomial of 4th degree in $(J_r, J_\varphi, \Omega_c, k_c)$:

$$P(J_r, J_\varphi, \Omega_c, k_c) = \sum_{|k|+|l|+|m|+|n|=s,\, s\leq 4} a_{k,l,m,n}{J_r}^k, {J_\varphi}^l, {\Omega_c}^m, {k_c}^n \quad . \tag{2.28}$$

and $a_{k,l,m,n}$ are numerical coefficients of the polynomial terms.

2) Our aim is to eliminate the linear terms($\propto \varepsilon^1$) and we apply a canonical transformation through Lie Transformation Method (see more details in Efthymiopoulos (2012)). This method helps us simplify the Hamiltonian through a canonical transformation. We rewrite the Hamiltonian in the form:

$$\mathcal{H}^{(0)}(\varphi, J_\varphi, \varphi_r, J_r) = \mathcal{H}_r(\varphi, J_\varphi, \varphi_r, J_r) + h_{kill}(\varphi, J_\varphi, \varphi_r, J_r) \tag{2.29}$$

where $\mathcal{H}_r(\varphi, J_\varphi, \varphi_r, J_r)$ are the terms of the Hamiltonian that we wish to keep and $h_{kill}$ are the terms that we want to eliminate, thus the linear terms of the Hamiltonian:

$$h_{kill} = h_1 \quad . \tag{2.30}$$

3) An essential step of the method is to calculate the generating fuction $\chi_1$ which sattisfies the homological equation:

$$\left\{\mathcal{H}^{(0)}, \chi_1\right\} + h_{kill} = 0 \quad . \tag{2.31}$$

One practical way to calculate the generating fuction of $\chi_1$ through the homological equation is the following:

In general if the unwanted terms of the Hamiltonian are written in the form:

$$h_{kill} = \sum_{i,j} A(i,j)\cos(a_i\vartheta_j \pm b_i\vartheta_j) + B(i,j)\sin(a_i\vartheta_j \pm b_i\vartheta_j) \tag{2.32}$$

where $\vartheta_{i,j}$ are the appearing angles and $\omega_{i,j}$ its respective frequencies, then the generating fuction $\chi_1$ that is given by the homological equation Eq. (2.31) takes the form:

$$\chi_1 = \sum_{i,j} A(i,j)\frac{\sin(a_i\vartheta_j \pm b_i\vartheta_j)}{(a_i\omega_j \pm b_i\omega_j)} + B(i,j)\left(-\frac{\cos(a_i\vartheta_j \pm b_i\vartheta_j)}{(a_i\omega_j \pm b_i\omega_j)}\right) \quad . \tag{2.33}$$

Consequently, the generating function $\chi_1$ in our case is calculated through the following substitutions in $h_{kill} = h_1$ in Eq. (2.25): $\sin(\varphi_r) \to \frac{\cos(\varphi_r)}{\kappa_c}$, $\sin(3\varphi_r) \to -\frac{\cos(3\varphi_r)}{3\kappa_c}$, $\cos(2\varphi) \to \frac{\sin(2\varphi)}{2(\Omega_c-\Omega_{sp})}$, $\sin(2\varphi) \to -\frac{\cos(2\varphi)}{2(\Omega_c-\Omega_{sp})}$ and it takes the form:

$$\chi_1 = \frac{A(r_c)\cos(2\varphi)\sin(\varphi_2(r_c))}{2(\Omega_c-\Omega_{sp})} - \frac{A(r_c)\sin(2\varphi)\cos(\varphi_2(r_c))}{2(\Omega_c-\Omega_{sp})} - \frac{\sqrt{2}{J_r}^{3/2}\cos(3\varphi_r){\Omega_c}^2}{3{k_c}^{5/2}r_c} + \frac{\sqrt{2}\sqrt{J_r}\cos(\varphi_r)\Omega_c\,(3J_r\Omega_c + 2J_\varphi k_c)}{{k_c}^{5/2}r_c} + \mathcal{O}(\varepsilon {V_0}^{(n)}) \quad . \tag{2.34}$$

4) According to the Lie method of transformation the Hamiltonian is written in the form:

$$\mathcal{H}^{(1)}(\varphi, J_\varphi, \varphi_r, J_r) = \mathcal{H}^{(0)} + \left\{\mathcal{H}^{(0)}, \chi_1\right\} + \frac{1}{2}\left\{\left\{\mathcal{H}^{(0)}, \chi_1\right\}, \chi_1\right\} \tag{2.35}$$

where $\{...\}$ are the Poisson brackets.

Using the Eq. (2.35) the Hamiltonian takes its final form:

$$\mathcal{H}^{(1)}(\varphi, J_\varphi, \varphi_r, J_r) = {h_0}'(\varphi, J_\varphi, \varphi_r, J_r) + \varepsilon^2 {h_2}'(\varphi, J_\varphi, \varphi_r, J_r) + \mathcal{O}(\varepsilon^n) \tag{2.36}$$

where the first order terms have been eliminated.

The Hamiltonian term ${h_0}'(\varphi, J_\varphi, \varphi_r, J_r)$ in Eq. (2.36) are the constant terms:

$${h_0}'(\varphi, J_\varphi, \varphi_r, J_r) = J_r k_c + J_\varphi(\Omega_c - \Omega_{sp}) \tag{2.37}$$

which are related to the fundamental frequencies of the system.

The 2nd order terms in the Hamiltonian (2.36) are:

$$\begin{aligned} {h_2}'(\varphi, J_\varphi, \varphi_r, J_r) &= \frac{P_0(J_r, J_\varphi, \Omega_c, k_c)}{4{k_c}^4{r_c}^2} + \frac{P_1(J_r, J_\varphi, \Omega_c, k_c)\cos(2\varphi_r)}{{k_c}^4{r_c}^2} + \\ &\frac{P_2(J_r, J_\varphi, \Omega_c, k_c)\cos(4\varphi_r)}{4{k_c}^4{r_c}^2} + \frac{\sqrt{J_r}}{\sqrt{2}{k_c}^{3/2}(\Omega_c - \omega_{sp})r_c}[f_{1c}(\varphi_2(r_c))\cos(\Delta\varphi_-) + \\ &f_{1s}(\varphi_2(r_c))\sin(\Delta\varphi_-) + (f_{2c}(\varphi_2(r_c))\cos(\Delta\varphi_+) + f_{2s}(\varphi_2(r_c))\sin(\Delta\varphi_+)] \end{aligned} \tag{2.38}$$

where $P_i(J_r, J_\varphi, \Omega_c, k_c)$ are polynomials of 6th degree in $(J_r, J_\varphi, \Omega_c, k_c)$:

$$P_i(J_r, J_\varphi, \Omega_c, k_c) = \sum_{|k|+|l|+|m|+|n|=s,\, s\le 6} a_{k,l,m,n}{J_r}^k, {J_\varphi}^l, {\Omega_c}^m, {k_c}^n \quad . \tag{2.39}$$

and the $f_{ic}(\varphi_2(r_c))$ and $f_{is}(\varphi_2(r_c))$ (i=1,2) are trigonometric fuctions of $\varphi_2(r_c)$ of the form:

$$f_{i(c,s)} = g_{1_{i(c,s)}}\cos(\varphi_2(r_c)) + g_{2_{i(c,s)}}\sin(\varphi_2(r_c)) \tag{2.40}$$

where the functions $g_{1,2_{i(c,s)}}$ are polynomial coefficients:

$$g_{1,2_{i(c,s)}} = g(A(r_c), A'(r_c), {\varphi_2}'(r_c), \Omega_c, \kappa_c, (\Omega_c - \omega_{sp}), r_c) \quad . \tag{2.41}$$

### 2.1.4 The Hamiltonian in resonant normal form

The variable $\Delta\varphi_- = 2\varphi - \varphi_r$ appearing in Hamiltonian $\mathcal{H}^{(1)}(\varphi, J_\varphi, \varphi_r, J_r)$ (see Eq. (2.38)) is the relation of the two angles and describes the phase difference between its two different corresponding frequencies $\Omega_c$ and $\kappa_c$. Thus, the $\Delta\varphi_-$ reveals the relation between the two fundamental frequencies $\Omega_c$ and $\kappa_c$ and it is a resonant variable in the Hamiltonian. Our purpose is to express the Hamiltonian in resonant variables:

$$\begin{aligned} -\psi &= 2\varphi - \varphi_r \\ J_F &= J_\varphi + 2J_r \end{aligned} \tag{2.42}$$

where the index F in $J_F$ stands for 'fast'.

For this purpose we implement a second Lie transformation in the Hamiltonian $\mathcal{H}^{(1)}(\varphi, J_\varphi, \varphi_r, J_r)$ (Eq. (2.36)) in order to write the Hamiltonian in a normal form where it has only the Hamiltonian ${h_0}'(\varphi, J_\varphi, \varphi_r, J_r)$ (Eq. (2.37)), the constant terms and the terms that are trigonometric functions of $\Delta\varphi_- = -\psi$ in ${h_2}'(\varphi, J_\varphi, \varphi_r, J_r)$ (Eq. (2.38)). The purpose of the canonical trasformation of the Hamiltonian is to make an alteration to the coordinates of the Hamiltonian as follows:

$$(\varphi_r, J_r, \varphi, J_\varphi) \to (\psi, J_r, \varphi, J_F) \tag{2.43}$$

where the pairs $(\psi, J_r)$, $(\varphi, J_F)$ are canonical.

We folllow a similar procedure we described in section 2.1.3:

1) We first collect the unwanted terms in Hamiltonian $\mathcal{H}^{(1)}(\varphi, J_\varphi, \varphi_r, J_r)$. The terms we intend to eliminate are located in the 2nd order part ${h_2}'(\varphi, J_\varphi, \varphi_r, J_r)$ of the Hamiltonian. The unwanted terms in Eq. (2.38) are those we incorporate trigonometric functions other than $\cos(\Delta\varphi_-)$ and $\sin(\Delta\varphi_-)$. Thus, the unwanted part of the Hamiltonian is:

$$\begin{aligned} h_{kill_2} = &\frac{P_1(J_r, J_\varphi, \Omega_c, k_c)\cos(2\varphi_r)}{{k_c}^4 {r_c}^2} + \frac{P_2(J_r, J_\varphi, \Omega_c, k_c)\cos(4\varphi_r)}{4{k_c}^4 {r_c}^2} + \\ &\frac{\sqrt{J_r}}{\sqrt{2}k_c^{3/2}(\Omega_c - \omega_{sp})r_c}[(f_{2c}(\varphi_2(r_c))\cos(\Delta\varphi_+) + f_{2s}(\varphi_2(r_c))\sin(\Delta\varphi_+)] \end{aligned} \tag{2.44}$$

where the polynomials $P_{1,2}(J_r, J_\varphi, \Omega_c, k_c)(\varphi_r)$, $f_{2c,s}(\varphi_2(r_c))$ are described in Eqs. (2.39)-(2.41).

We set The Hamiltonian $\mathcal{H}^{(1)}(\varphi, J_\varphi, \varphi_r, J_r)$ as

$$\mathcal{H}^{(1)}(\varphi, J_\varphi, \varphi_r, J_r) = {\mathcal{H}^{(0)}}'(\varphi, J_\varphi, \varphi_r, J_r) \tag{2.45}$$

and we write it in the form:

$${\mathcal{H}^{(0)}}'(\varphi, J_\varphi, \varphi_r, J_r) = \mathcal{H}_{r_2}(\varphi, J_\varphi, \varphi_r, J_r) + h_{kill_2} \tag{2.46}$$

where $\mathcal{H}_{r_2}(\varphi, J_\varphi, \varphi_r, J_r)$ are the rest terms of the Hamiltonian that we wish to keep in the final normal form of the Hamiltonian.

2) We build the generating function $\chi_2$ which sattisfies the homological equation:

$$\left\{{\mathcal{H}^{(0)}}', \chi_2\right\} + h_{kill_2} = 0 \quad . \tag{2.47}$$

We apply similar rules in order to calculate the generating function from the form of $h_{kill_2}$ as described in step 3) of the Section 2.1.3 by the rule (2.32)-(2.33) and the

generating fuction $\chi_2$ is:

$$\chi_2 = \frac{P_1(J_r, J_\varphi, \Omega_c, k_c)\sin(2\varphi_r)}{2{k_c}^5{r_c}^2} + \frac{P_2(J_r, J_\varphi, \Omega_c, k_c)\sin(4\varphi_r)}{16{k_c}^5{r_c}^2} + \frac{\sqrt{J_r}}{\sqrt{2}k_c^{3/2}(\Omega_c - \omega_{sp})r_c}\left[(f_{2c}(\varphi_2(r_c))\frac{\sin(2\varphi+\varphi_r)}{2(\Omega_c-\Omega_{sp})+\kappa_c} - f_{2s}(\varphi_2(r_c))\frac{\cos(2\varphi+\varphi_r)}{2(\Omega_c-\Omega_{sp})+\kappa_c}\right] \quad . \tag{2.48}$$

3) The Lie trasformation will give us the final form of the Hamiltonian $\mathcal{H}^{(1)'}$ :

$$\mathcal{H}^{(1)'} = \mathcal{H}^{(0)'} + \left\{\mathcal{H}^{(0)'}, \chi_2\right\} + \frac{1}{2}\left\{\left\{\mathcal{H}^{(0)'}, \chi_2\right\}, \chi_2\right\} \quad . \tag{2.49}$$

Using the equation Eq. (2.42) the resonant Hamilonian is:

$$\mathcal{H}^{(1)'} = \mathcal{H}_{res}(\psi, J_r, \varphi, J_F) \tag{2.50}$$

In particular the resonant Hamiltonian is:

$$\mathcal{H}_{res}(\psi, J_r, \varphi, J_F) = (\kappa_c - (\Omega_c - \omega_{sp}))J_r + (\Omega_c - \Omega_{sp})J_F + (2c_0 - 6c_1 - \frac{17}{4}c_2 + 24c_3 - 15c_4){J_r}^2 + (-2c_0 + 3c_1 + 8c_2 - 12c_3)J_F J_r + (\frac{1}{2}c_0 - 2c_2){J_F}^2 + \frac{\sqrt{J_r}}{\sqrt{2k_c}}D_c(A(r_c), \varphi_2(r_c))\cos(\psi) + \frac{\sqrt{J_r}}{\sqrt{2k_c}}D_s(A(r_c), \varphi_2(r_c))\sin(\psi) + \mathcal{O}(V^{(n)}) \tag{2.51}$$

where $c_n$ are terms that appear in the Hamiltonian and are:

$$c_n = \frac{1}{{r_c}^2}\frac{{\Omega_c}^n}{{\kappa_c}^n} \tag{2.52}$$

and $d_{c,s}(\varphi_2(r_c))$ are trigonometric functions of the form:

$$\begin{aligned} D_c(A(r_c), \varphi_2(r_c)) = &-\left(\frac{2\Omega_c A(r_c)}{\kappa_c r_c} + \frac{\Omega_c A(r_c)}{(\Omega_c - \omega_{sp}))r_c} + A(r_c)'\right)\sin(\varphi_2(r_c)) - \\ &A(r_c)\varphi_2(r_c)'\cos(\varphi_2(r_c)) \\ D_s(A(r_c), \varphi_2(r_c)) = &-\left(\frac{2\Omega_c A(r_c)}{\kappa_c r_c} + \frac{\Omega_c A(r_c)}{(\Omega_c - \omega_{sp}))r_c} + A(r_c)'\right)\cos(\varphi_2(r_c)) + \\ &A(r_c)\varphi_2(r_c)'\sin(\varphi_2(r_c)) \quad . \end{aligned} \tag{2.53}$$

### 2.1.5 Location of the periodic orbits

The periodic orbits are expected to be given by the roots of the following equations:

$$\begin{aligned} &\mathcal{H}_{res} = 0 \\ &\dot{\psi} = \frac{\partial \mathcal{H}_{res}}{\partial J_r} = 0 \\ &\dot{J}_r = -\frac{\partial \mathcal{H}_{res}}{\partial \psi} = 0 \quad . \end{aligned} \tag{2.54}$$

The location of the periodic orbits in the $(\psi, J_r)$ space is a difficult task. Therefore, we make a 3rd canonical transformation in the Hamiltonian in new variables $(\xi, p_\xi)$ which are given by the relation:

$$\begin{aligned} &\xi = \sqrt{2J_r}\sin(\psi) \\ &p_\xi = \sqrt{2J_r}\cos(\psi) \quad . \end{aligned} \tag{2.55}$$

Thus, we substitute $\sin(\psi) \to \frac{\xi}{\sqrt{2J_r}}$ and $\cos(\psi) \to \frac{p_\xi}{\sqrt{2J_r}}$ and $J_r \to \frac{\xi^2+{p_\xi}^2}{2}$ in the form of $\mathcal{H}_{res}$ in Eq. (2.51) and the Hamiltonian becomes:

$$\mathcal{H}_{res}(\xi, p_\xi) = (\kappa_c - (\Omega_c - \Omega_{sp}))\frac{\xi^2 + {p_\xi}^2}{2} + (\Omega_c - \Omega_{sp})J_F + (2c_0 - 6c_1 - \frac{17}{4}c_2 + 24c_3 - 15c_4)\frac{(\xi^2 + {p_\xi}^2)^2}{4} + (-2c_0 + 3c_1 + 8c_2 - 12c_3)J_F\frac{\xi^2 + {p_\xi}^2}{2} + (\frac{1}{2}c_0 - 2c_2){J_F}^2 + \frac{1}{2\sqrt{k_c}}D_c(A(r_c), \varphi_2(r_c))p_\xi + \frac{1}{2\sqrt{k_c}}D_s(A(r_c), \varphi_2(r_c))\xi + \mathcal{O}(V^{(n)}) \tag{2.56}$$

where the terms $c_n$, $D_{c,s}(A(r_c), \varphi_2(r_c))$ are given by the Eqs.(2.52)-(2.53). The Hamiltonian $\mathcal{H}_{res}(\xi, p_\xi)$ has terms of $J_F$, but it does not have a corresponding angle for $J_F$. Therefore, $J_F$ plays the role of constant in the Hamilton equations. The root of the following equations can now give us the periodic orbits:

$$\begin{aligned} \dot{\xi} &= \frac{\partial \mathcal{H}_{res}}{\partial p_\xi} = 0 \\ \dot{p_\xi} &= -\frac{\partial \mathcal{H}_{res}}{\partial \xi} = 0 \quad . \end{aligned} \tag{2.57}$$

The above calculations can be applied in any toy potential model of normal spiral galaxy. The Hamiltonian $\mathcal{H}_{res}(\xi, p_\xi)$, $\kappa_c$ (Eq. (2.56)), the Hamilton equations (2.57), $\Omega_c$ are functions of the axisymmetric part of the potential $V_0(r_c)$ given by Eqs. (2.4).(2.3). If the potential of the galaxy is given then $\kappa_c$, $\Omega_c$ are known quantities.

The other parameters that appear in Eqs. (2.56)- (2.57) are related to the spiral potential $V_{sp}(r_c)$ of the model. These parameters are:

1) $\Omega_{sp}$ the pattern speed of the spiral arms

2) $A(r)$ the amplitude of the spiral potential

3) $\varphi_2(r_c)$ which is related to other parameters and geometric features of spirala arms e.g. the pitch angle of the spiral arms

Having the ability to make analytical calculations of the periodic orbits enable us to conduct a more effective parametric investigation in our model. We are going to present this study in the following section.

If we insert the above known quantities for a: $\kappa_c$, $\Omega_c$,$A(r)$,$\varphi_2(r_c)$ in Eqs. (2.56)-(2.57). The Hamiltonian equations (2.57) for every chosen value of $r_c$ are a 3rd degree polynomial equation of the form:

$$\sum_{i+j\leq 3} a_i \xi^i {p_\xi}^j = 0 \quad . \tag{2.58}$$

This polynomial equations give one or three solutions depending on the value $r_c$. The three solutions correspond to three different families of periodic orbits: two families of stable periodic orbits $x_1$ and one family of unstable periodic orbits $x_3$. For different values of $r_c$ we can make the phase portraits in $(\xi, p_\xi)$ space and the families of periodic orbits are revealed in each case. This work is going to be presented in detail in the next sections.

The resonances determine the areas of $r_c$ where every family of periodic orbits appear. In particular for the solutions we identify:

(a) The stable family of periodic orbits $x_1$ is located in the region of $r_c$ inside the first ILR and also between the first and the second ILR, up to the 4:1 resonance. In the regions inside the first ILR and between the second ILR and the 4:1 resonance the Eq. (2.57) give only one solution because there exists only the $x_1$ family. The family

$x_1$ are precesssing ellipses in the cartesian space and support the spiral density wave. In the region outside the 4:1 resonance there still exists the $x_1$ family, but it can no longer support the spiral density wave.

(b) The stable family of periodic orbits $x_2$ and the unstable family $x_3$ are located for values of $r_c$ in the region between the first and the second ILR. There coexist the three families of periodic orbits and Eq. (2.57) give three solutions.

### 2.1.6 The periodic orbits in the cartesian spase

The final step of our method is to present the solution $x_1$ in the physical space and examine whether it gives an elliptical orbit for a certain value of $r_c$. For different values of $r_c$ we expect to see precessing ellipses in the cartesian space $(X, Y)$ which support the spiral density wave. The equations (2.57) correspond to the Hamiltonian $\mathcal{H}_{res}(\xi, p_\xi)$ in Eq. (2.56) and give solutions in $(\xi, p_\xi)$. We should a make a transformation in the coordinates $(\xi, p_\xi)$ of the solution. This transformation is: $(\xi, p_\xi) \rightarrow (r, \varphi) \rightarrow (X, Y)$ where:

$$\begin{aligned} X &= r\cos(\varphi) \\ Y &= r\sin(\varphi) \quad . \end{aligned} \tag{2.59}$$

We can have a relation for radius $r$ from the equation of dr in Eq. (2.19). Thus the variable r is:

$$r = r_c + \sqrt{\frac{2J_r}{k_c}}\sin(\varphi_r) \quad . \tag{2.60}$$

Considering that the angle $\varphi_r$ is: $\varphi_r = \psi + 2\varphi$, the Eq. (2.60) becomes:

$$r = r_c + \sqrt{\frac{2J_r}{k_c}}\sin(\psi)\cos(2\varphi) + \sqrt{\frac{2J_r}{k_c}}\cos(\psi)\sin(2\varphi) \quad . \tag{2.61}$$

The trigonometric terms $\sin(\psi)$, $\cos(\psi)$ can be written by the Eq. (2.55) as a function of $\xi$, $p_\xi$:

$$\sin(\psi) = \frac{\xi}{\sqrt{2J_r}}, \quad \cos(\psi) = \frac{p_\xi}{\sqrt{2J_r}} \quad . \tag{2.62}$$

The Eq. (2.61) using the Eq. (2.62) becomes:

$$r = r_c + \frac{\xi}{\sqrt{k_c}}\cos(2\varphi) + \frac{p_\xi}{\sqrt{k_c}}\sin(2\varphi) \quad . \tag{2.63}$$

Thus the cartesian coordinates $(X, Y)$ of the periodic orbits can be given from $(\xi, p_\xi)$ through the relations:

$$\begin{aligned} X &= \left(r_c + \frac{\xi}{\sqrt{k_c}}\cos(2\varphi) + \frac{p_\xi}{\sqrt{k_c}}\right)\cos(\varphi) \\ Y &= \left(r_c + \frac{\xi}{\sqrt{k_c}}\cos(2\varphi) + \frac{p_\xi}{\sqrt{k_c}}\right)\sin(\varphi) \quad . \end{aligned} \tag{2.64}$$

The above relations enable us to draw in the cartesian space (X,Y) the periodic orbit $x_1$ which is the solution of Eq. (2.56).

## 2.2 Precessing ellipses in a Milky Way-like model

### 2.2.1 An analytical Milky Way-like model

We consider a Milky Way theoretical potential model of a spiral galaxy, whose components are presented also on the works of Pettitt et al. (2014) and Efthymiopoulos (2010). This model is consisted of a combination of an axisymmetric and a spiral potential:

$$V = V_{\rm ax} + V_{\rm sp}. \tag{2.65}$$

The axisymmetric potential $V_{\rm ax}$ is composed by a disc, a bulge and a halo:

$$V_{\rm ax} = V_{\rm d} + V_{\rm b} + V_{\rm h}. \tag{2.66}$$

For the disc potential $V_{\rm d}$ we use a Miyamoto-Nagai model (Miyamoto & Nagai (1975)) given by the relation :

$$V_{\rm d} = \frac{-GM_{\rm d}}{\sqrt{r^2 + (a_{\rm d} + \sqrt{z^2 + b_{\rm d}^2})^2}} \tag{2.67}$$

where $M_{\rm d} = 8.56 \times 10^{10}\ M_{\odot}$ is the total mass of the disc, $a_{\rm d} = 5.3$ kpc and $b_{\rm d} = 0.25$ kpc. In order to have a 2-D disc model we take $z = 0$ and $r = \sqrt{x^2 + y^2}$. For the bulge we use a Plummer potential $V_b$ given by the relation:

$$V_{\rm b} = \frac{-GM_{\rm b}}{\sqrt{r^2 + b^2}} \tag{2.68}$$

where $M_{\rm b} = 5 \times 10^{10}\ M_{\odot}$ is the total mass of the bulge, $r = \sqrt{x^2 + y^2}$ and $b = 1.5$ kpc.

The halo potential is a $\gamma$-model (Dehnen (1993)) with parameters as in Pettitt et al. (2014):

$$V_{\rm h} = \frac{-GM_{\rm h(r)}}{r} - \frac{-GM_{\rm h,0}}{\gamma r_{\rm h}} \left[ -\frac{\gamma}{1 + (r/r_{\rm h})^{\gamma}} + \ln(1 + \frac{r}{r_{\rm h}})^{\gamma} \right]_{r}^{r_{h,max}} \tag{2.69}$$

where $r_{h,max} = 100$ kpc, $\gamma = 1.02$, and $M_{\rm h,0} = 10.7 \times 10^{10} M\odot$, and $M_{\rm h(r)}$ is given by the function:

$$M_{\rm h(r)} = \frac{M_{\rm h,0}(r/r_{\rm h})^{\gamma+1}}{1 + (r/r_{\rm h})^{\gamma}} \quad . \tag{2.70}$$

The spiral potential is given by the value $V_{\rm sp}$ for $z = 0$ of the 3D logarithmic spiral model $V_{\rm sp}(r, \phi, z)$ introduced by Cox & Gómez (2002) (see formula (19) in Efthymiopoulos (2010)). We have on the disc plane:

$$V_{\rm sp} = 4\pi G h_{\rm z} \rho_0\ G(r)\ \exp\left( -\left( \frac{r - r_0}{R_{\rm s}} \right) \right) \frac{C}{KB}\ \cos\left[ 2\left( \varphi - \frac{\ln(r/r_0)}{\tan(\alpha)} \right) \right] \tag{2.71}$$

where

$$K = \frac{2}{r|\ \sin(\alpha)\ |}, \quad B = \frac{1 + Kh_z + 0.3(Kh_z)^2}{1 + 0.3Kh_z} \tag{2.72}$$

and $C = 8/(3\pi)$, $h_{\rm z} = 0.18$ kpc, $r_0 = 8$ kpc, $R_{\rm s} = 7$ kpc, $\alpha = -13^0$ is the pitch angle of the spiral arms. The function $G(r)$ plays the role of a smooth envelope determining the radius beyond which the spiral arms are important. We adopt the form $G(r) = b - c\arctan((R_{\rm s0} - r))$, with $R_{\rm s0} = 6$ kpc, $b = 0.474$, $c = 0.335$. The density of the spiral arms is $\rho_0 = 5 \times 10^7$, $15 \times 10^7$ or $30 \times 10^7\ M \odot /{\rm kpc}^3$ in the three different models under study, respectively. These three values of the density

are chosen so as to yield spiral $F$-strength values consistent with those reported in the literature for a weak intermadiate and strong spiral respectively (see for example Block et al. (2004)).

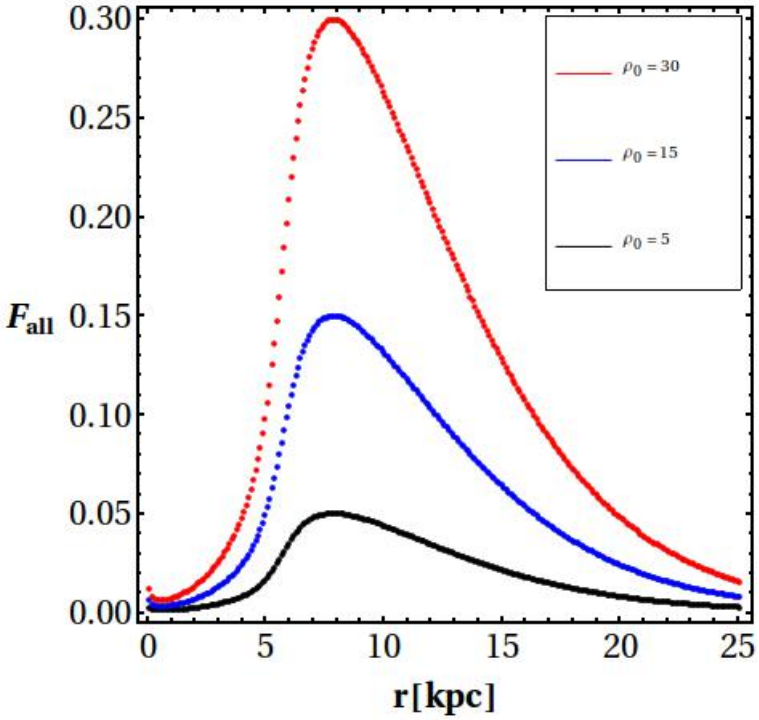


**Figure 2.1**: *The total force perturbation $F_{\rm all}$ for different amplitudes of the spiral potential as a function of the radius.*

The $F-$strength (Buta et al. (2009)) can be defined as either the ratio of the maximum tangential force of the spiral perturbation over the radial force of the axisymmetric background:

$$F_{\rm tan}(r) = \frac{\left\langle F_{\rm sp}^{\rm tan}(r) \right\rangle_{\rm max}}{F_{\rm r}(r)} = \frac{\left\langle \frac{1}{r}\frac{\partial V_{\rm sp}}{\partial \varphi} \right\rangle_{\rm max}}{\frac{\partial V_{\rm ax}}{\partial r}} \tag{2.73}$$

or the ratio of the maximum total force of the spiral perturbation over the radial force of the axisymmetric background, given by the relation:

$$F_{\rm all}(r) = \frac{\left\langle F_{\rm sp}(r) \right\rangle}{F_r(r)} = \frac{\left\langle \sqrt{\left(\frac{1}{r}\frac{\partial V_{\rm sp}}{\partial \varphi}\right)^2 + \left(\frac{\partial V_{\rm sp}}{\partial r}\right)^2} \right\rangle_{\rm max}}{\frac{\partial V_{\rm ax}}{\partial r}} \quad . \tag{2.74}$$

Figure 2.1 shows $F_{\rm all}$ as a function of the radius derived from Eq. (2.74), for three different values of the density $\rho_0$ of Eq. (2.71), namely $\rho_0 = 5, 15, 30 (\times 10^7)\ M\odot/{\rm kpc}^3$. The maximum values of the spiral $F$-strength are 5%, 15% and 30% respectively. In the intermediate model, the $F$-strength varies between 5% and 15% in the region 5 kpc $\leq r \leq$ 15 kpc. Let us note that the observed amplitudes (in $F-$strength) of the spirals in grand design galaxies with respect to the axisymmetric background have typical values between 5% and 10% (Patsis et al. (1991), Grøsbol & Patsis (1998)).

The radial profile of the angular velocity and the rational combinations of the main frequencies of the model are given in Fig. 2.2. They can help us specify the position

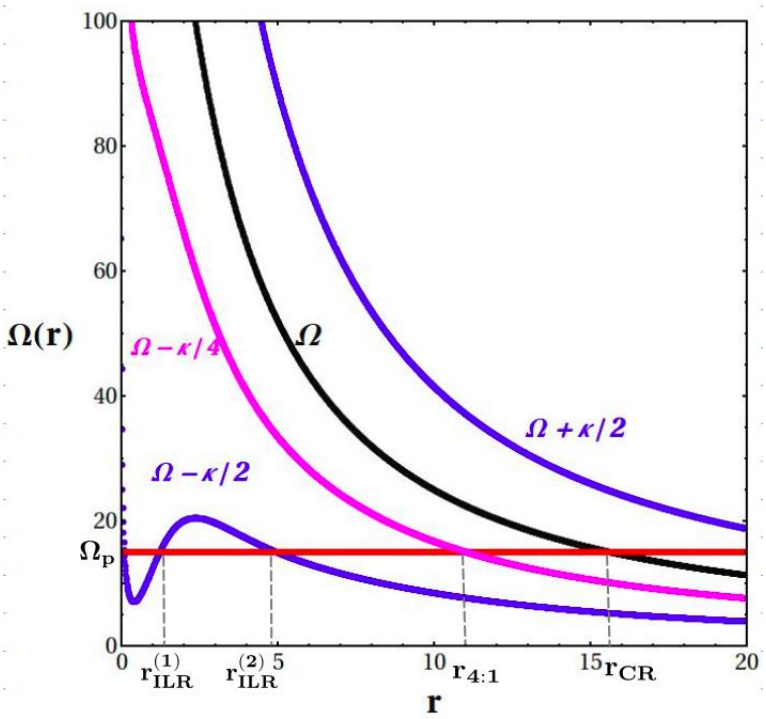


**Figure 2.2**: *The form of the function $\Omega(r)$, and of the resonant combinations of $\Omega(r)$ and $\kappa(r)$, $\Omega-\kappa/2$, $\Omega+\kappa/2$, and $\Omega-\kappa/4$. The selected pattern speed $\Omega_{\rm sp}$ determines the radii of the ILR, the 4:1 resonance and the corotation.*

of the resonances. Figure 2.2 shows the function $\Omega(r)$, as well as the combinations $\Omega-\kappa/2$, $\Omega+\kappa/2$ and $\Omega-\kappa/4$ in our potential model, where $\Omega(r)$ and $\kappa(r)$ frequencies are given by Eqs. (2.3)-(2.4). The section points of these curves with the constant pattern speed $\Omega_{\rm sp}$ defines the resonances in the galactic disc (see section 1.5) for more details). These resonances demarcate a lot of phenomena and different families of periodic orbits located in the galactic disc. The determination of the location of the resonances also reveals the area in which a spiral density wave grows.

In the subsection 1.6 we presented a series of works which demonstrate that the spiral density waves cannot propagate in whole galactic disc, but they can grow between some natural barriers. As it is mentioned, once the 4:1 radius is approached the orbits become rectangular and they cannot support the spiral density wave. The extent of the area where the spiral density waves grow is determined by the value of the pattern speed. In Fig. 2.2 we observe that in the case of greater values of pattern speeds in our model, this region which is demarcated by the ILR and 4:1 resonance becomes smaller.

### 2.2.2 Analytical and numerical precessing ellipses in the Milky Way-like potential model

In this section we attempt to identify the families of the periodic orbits in our model and the regions that they appear, as well as which periodic orbits are responsible for the generation of the spiral density wave. We are going to compare the $x_1$ orbits which are produced through the algorithm of section 2.1 with the ones produced through numerical methods. The parameters we choose in this case for the pattern speed of the spiral arms and amplitude of the spiral density wave are: $\Omega_{sp} = 15$ $km/s/kpc$, $\rho_0 = 510^7\ M\odot/kpc^3$.

We first apply all the steps of the analytical calculation presented in section 2.1

for the Milky Way like- model. The analytical $x_1$ orbits are presented in Fig. 2.7.

We then proceed some numerical calculations. We are going to reproduce the phase space and the numerical orbits $x_1$ in the physical space. A useful tool for this study is the construction of the phase space structure. The phase space for different values of the circular orbit $r_c$ corresponds to different values of the energy. The space space structure reveals all the different families of periodic orbits and the regions where we locate them.

As it was shown in section 2.1 families of the stable periodic orbits having shapes of precessing ellipses correspond to the continuation of the circular orbits of the axisymmetric part of the potential in the region of the 2:1 resonance (see also the section 1.4). The pair of canonical variables $(\xi, P_\xi)$ represents the deviation from the circular orbit. Using equations (2.19) and (2.55) the functions $\xi = \xi(r, p_r, \varphi)$ and $P_\xi = P_\xi(r, p_r, \varphi)$ are:

$$\xi = (r - r_c)\cos(2\varphi) - \frac{p_r}{\kappa(r_c)}\sin(2\varphi) \tag{2.75}$$

$$P_\xi = p_r \cos(2\varphi) + (r - r_c)\kappa(r_c)\sin(2\varphi) \quad . \tag{2.76}$$

Equations (2.75) and (2.76) can now be used in order to construct a Poincaré surface of section $(\xi, P_\xi)$ for a fixed value of $\varphi$ and a fixed Jacobi constant $E_j$. We find a sequence of surfaces of sections in our model defined by the following procedure: For a specific value of the pattern speed $\Omega_{\rm sp}$, we specify a certain value for the radius of the circular orbit $r_c$ and calculate the corresponding angular momentun $p_{\varphi_c} = r_c^2\Omega(r_c)$ and the corresponding Jacobi integral $E_j(r_c) = H_{\rm ax}(r_c) - \Omega_{\rm sp}\ p_{\varphi_c}$. For the value of the total Hamiltonian $H = E_j(r_c)$ we then define various initial values $\xi_0$ and $P_{\xi_0}$ taking as initial value of $\varphi$ the value $\varphi_0 = \pi/2$. Then we calculate the initial values of the coordinates $(r, p_r, p_\varphi)$ using Eqs. (2.75) and (2.76) repsectively, i.e. $r_0 = r_c - \xi_0$ (from Eq. (2.75)), $p_{r_0} = -P_{\xi_0}$ (from Eq. (2.76))) and $p_{\varphi_0} = r_0^2\Omega(r_0)$. Finally, we use Hamilton's equations:

$$\frac{dr}{dt} = \frac{\vartheta H}{\vartheta p_r}, \qquad \frac{d\varphi}{dt} = \frac{\vartheta H}{\vartheta p_\varphi}, \qquad \frac{dp_r}{dt} = -\frac{\vartheta H}{\vartheta r}, \qquad \frac{dp_\varphi}{dt} = -\frac{\vartheta H}{\vartheta \varphi} \tag{2.77}$$

with the Hamiltonian (2.7) in order to integrate orbits with initial conditions $(\varphi_0, r_0, p_{r_0}, p_{\varphi_0})$ and find the consecutive iterates $(\xi, P_\xi)$ on the Poincaré section $\varphi = \pi/2$.

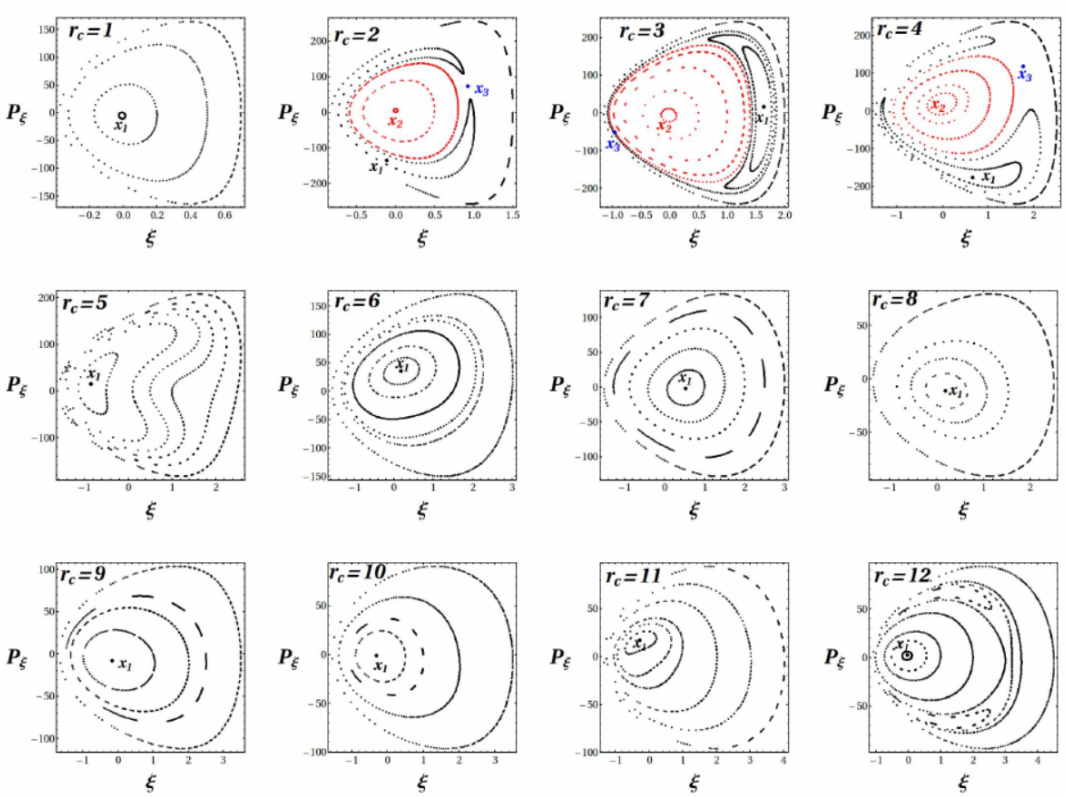


**Figure 2.3**: *The phase space portraits* $(\xi, P_\xi)$ *for the model (2.71) with pattern speed* $\Omega_{\rm sp} = 15$ km.sec$^{-1}$.kpc$^{-1}$ *and density of the spiral potential* $\rho_0 = 5 \times 10^7 M \odot /\text{kpc}^3$ *for twelve different values of the radius* $r_c$ *namely* $r_c$*=1, 2,..., 12 kpc. Precessing ellipses responsible for the spiral density waves are periodic orbits of the* $x_1$ *family that correspond to radii between approximately 5 kpc (second ILR) and 11 kpc (4:1 resonance).*

We construct the phase portraits for different values of $r_c$. This value of the pattern speed $\Omega_{\rm sp} = 15$ km.sec$^{-1}$.kpc$^{-1}$ places the second ILR not far from the inner break of the surface density profile of the axisymmetric part of the potential due to the presence of the bulge (see Fig. 2.1). Figure 2.3 shows the phase portraits (surfaces of section $(\xi, P_\xi)$) for these chosen parameters for twelve different values of the radius $r_c$ namely $r_c$=1, 2, ..., 12 kpc, spanning a region from the center of the galaxy and up to a radius just outside the 4:1 resonance.

The phase portraits of Fig. 2.3 reveal the main families of periodic orbits which Contopoulos (1975) identified as the families of periodic orbits in a spiral galaxy and named $x_1$, $x_2$ (stable periodic orbits) and $x_3$ (unstable periodic orbit). In the case of our model, precessing ellipses responsible for the spiral density waves are the stable periodic orbits of the $x_1$ family. Four different regions can be distinguished according to the number and stability of periodic orbits. These regions are demarcated by the presence of resonances in the galactic disc and they are shown in Fig. 2.2:

(a) in the region inside the first ILR there exists only the $x_1$ family (stable family),

(b) in the region between the first and the second ILR there exist three families of periodic orbits, namely the $x_1$ (stable family), the $x_2$ (stable family) and the the $x_3$ (unstable family),

(c) in the region between the second ILR and the 4:1 resonance where exists only the $x_1$ (stable or unstable family) that supports the spiral density wave via the precessing ellipses mechanism and

(d) in the region outside the 4:1 resonance there still exists the $x_1$ family, but it can no longer support the spiral density wave (see figures below). From Fig. 2.2

we see that for $\Omega_{sp} = 15$ km.sec$-1$.kpc$^{-1}$, the radii that correpsonds to the second ILR and the 4:1 resonance are approximately 5 kpc and 11 kpc respectively. As a consequence, the spiral density wave should extend between these two radii.

The $x_1$ family of periodic orbits is found at the center of the islands of stability marked with black points in Fig. 2.3. The $x_1$ family exists at all the radii from the center of the galaxy up to the 4:1 resonance. The $x_2$ family of periodic orbits is found, instead, at the center of the islands of stability marked with red points in Fig. 2.3, while the unstable periodic orbit $x_3$ is plotted with a blue dot. These orbits exist only in the region between the first and the second ILR and they do not support the spiral density wave (see below).

In Fig. 2.3 we observe that the $x_1$ family remains stable at all radii and no large scale chaos exists at least up to the radius corresponding to the 4:1 resonance. Beyond this resonance, orbits of greater multiplicity, bifurcating from the $x_1$ periodic family, appear in the phase space (see the last panel of Fig. 2.3 which corresponds to $r_c = 12$ kpc and is found just outside the 4:1 resonance).

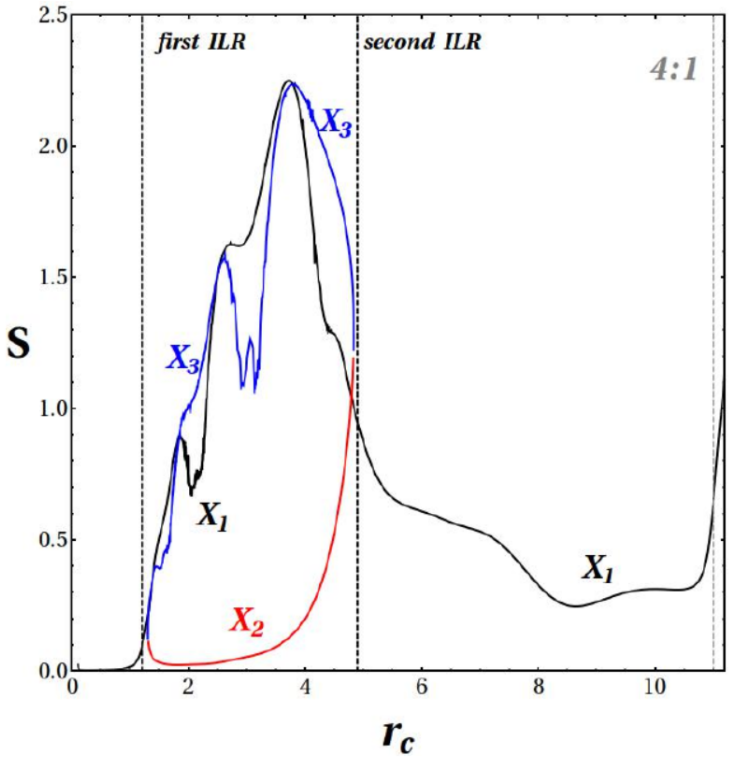


**Figure 2.4**: *The characteristic curves* $S(r_c) = \sqrt{\xi^2 + p_\xi^2/\kappa_c^2}$ *of the periodic families* $x_1$ *(black),* $x_2$ *(red) and* $x_3$ *(blue) for the model (2.71) with* $\Omega_{sp} = 15$ km.sec$^{-1}$.kpc$^{-1}$ *and density of the spiral potential* $\rho_0 = 5 \times 10^7 M\odot/\text{kpc}^3$. *The black dashed vertical lines correspond to the first and second ILR resonance, while the gray dashed vertical line corresponds to the 4:1 resonance.*

Figure 2.4 shows, now, the normalized characteristic curves as a function of the radius $r_c$ for the same parameters as in Fig. 2.3 which are given by the relation:

$$S(r_c) = \sqrt{\xi^2 + P_\xi/\kappa_c^2} \tag{2.78}$$

where $\kappa_c$=$\kappa_c(r_c)$ is the epicyclic frequency given by the relation (1.31)). The periodic family $x_1$ is plotted in black, the periodic family $x_2$ in red and the (unstable) periodic family $x_3$ in blue. The black dashed vertical lines correspond to the first and second ILR, while the gray vertical line corresponds to the 4:1 resonance.

The existence of the $x_2$ and $x_3$ families of orbits is delimited between the black dashed vertical lines. In fact, the $x_2$ and $x_3$ periodic orbits are created together at a tangent bifurcation close to the first ILR and then they join and disappear close to the second ILR. The value of $S(r_c)$, in each case, corresponds to the amplitude of the epicyclic oscillation of the elliptical orbit around the circular one.

A key remark in Fig. 2.78 is that, in the range of the radii where $S(r_c)$ decreases, between the second ILR (at $r_c \approx 5$ kpc) and $r_c \approx 8.5$ kpc, the ellipses become more circular and so they do not intersect with each other. The value of $S(r_c)$ reaches a minimum value around $8.5$ kpc and then it increases, first smoothly and then abruptly. After this latter radius, the orbits become rectangular as they approach closer to the 4:1 resonance. Hence, the $x_1$ orbits start intersecting each other and no longer support the imposed spirals. As a conclusion, the end of the response spiral density wave should be placed somewhere between the radius $r_c$ corresponding to the minimum of the curve $S(r_c)$ and the 4:1 resonance.

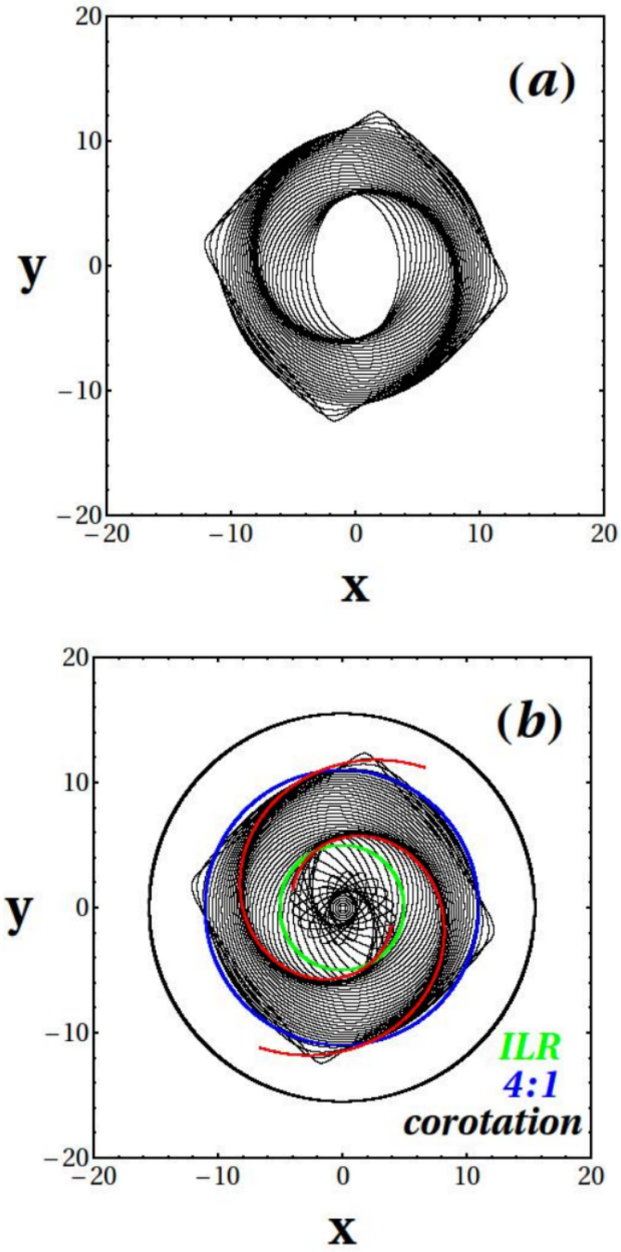


**Figure 2.5**: *(a) The spiral density waves formed by the "precessing ellipses" of the elliptical closed orbits of the $x_1$ family, for the Milky-Way like model and for pattern speed $\Omega_{sp} = 15$ km.sec$^{-1}$.kpc$^{-1}$ and density of the spiral potential $\rho_0 = 5 \times 10^7 M \odot$ /kpc$^3$, between the second ILR and the 4:1 resonance. (b) Same as in (a) but with the ellipses of the $x_1$ family inside the second ILR. Superposed are plotted circles corresponding to the second ILR (green circle), 4:1 resonance (blue circle) and corotation (black circle). The imposed spiral arms (in red) are derived from the minima of the spiral potential (9). The coincidence of the imposed spirals with the spiral density wave created by the "precessing ellipses" is nearly complete.*

We then procced the reproduction of the numerical $x_1$ orbits in the physical space which we located at Fig. 2.3 at the same region of the values $r_c$. As shown in Fig. 2.5, the orbits of the $x_1$ family form precessing ellipses supporting the spiral density wave in the whole region between the second ILR ($\approx 5$ kpc) and a little inside the 4:1 resonance. In Fig. 2.5(a) we see that the $x_1$ family forms a dense and well defined spiral density wave. In Fig. 2.5(b) the $x_1$ family of orbits is plotted both inside and outside the second ILR. Between the first ILR ($\approx 1.5$ kpc) and the second ILR ($\approx 5$ kpc) the orbits form a less dense and well defined spiral density wave, while inside

the first ILR the orbits are more circular. In fact, inside the second ILR, the spiral density wave is greatly weakened, as the amplitude of the spiral perturbation is close to zero (see Fig. 2.1). In Fig. 2.5b, superposed are plotted circles corresponding to the second ILR (green circle), 4:1 resonance (blue circle) and corotation (black circle). The imposed spiral arms (superposed to the figure in red) are derived from the minima of the spiral potential (2.71). The coincidence with the spiral density wave formed by the elliptical orbits is nearly complete.

We then compare the $x_1$ orbits given by the analytical method with the ones given by the numerical method. The orbits $x_1$ in the cartesian space allows us to make a better comparison between the numerical and the analytical orbits. The comparison is shown in Figs. 2.6, 2.7. We observe that both models give elongated orbits that support the precessing ellipses mechanism for the generation of the spiral density wave. The analytical and the numerical spiral density wave in each case presents many similarities.

Figure 2.6 shows the comparison of the numerical and analytical single $x_1$ orbit at $r_c$=7 kpc. In $r_c = 7$ kpc the 3rd degree polynomial equation (2.58), gives one solution, which is $x_1$. In this region of $r_c$ we expect the existence of a single family of periodic orbit which is $x_1$. This is also confirmed by the phase portrait in $r_c = 7$ in Fig. 2.3.

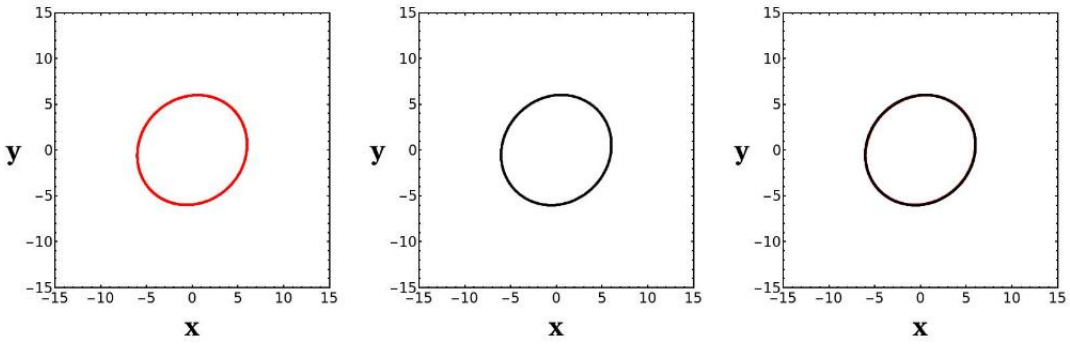


**Figure 2.6**: *The numerical orbit $x_1$ (left panel) compared to the analytical orbit $x_1$ (central panel). In the right panel the numerical orbit is superposed over the analytical. All the orbits have been computed for the Milky-Way like model and for pattern speed $\Omega_{sp} = 15$ km.sec$^{-1}$.kpc$^{-1}$ and density of the spiral potential $\rho_0 = 5 \times 10^7 M \odot$/kpc$^3$.*

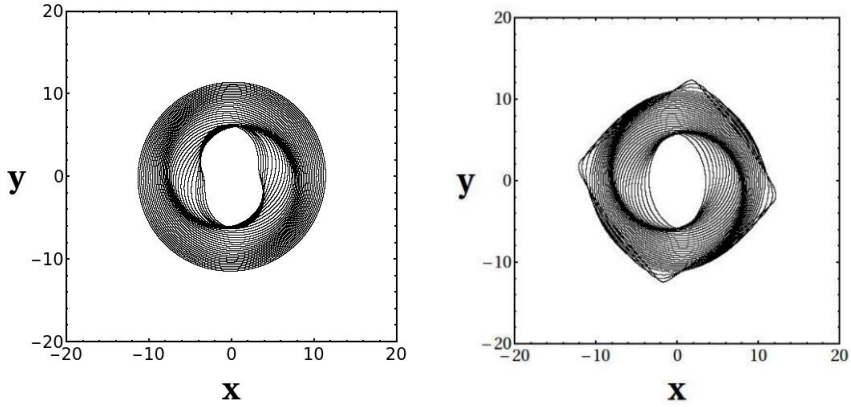


**Figure 2.7**: *The analytical spiral density wave formed by the analytical orbits $x_1$ (left panel) compared to the numerical spiral density wave (right panel). All the orbits have been computed for the Milky-Way like model and for pattern speed $\Omega_{sp} = 15$ km.sec$^{-1}$.kpc$^{-1}$ and density of the spiral potential $\rho_0 = 5 \times 10^7 M \odot$/kpc$^3$, between the second ILR and the 4:1 resonance*

The comparison of the analytical and numerical precessing ellipses in Fig. 2.7 shows the region, demarcated by the resonances, where the spiral density wave propagates, is the same in both cases. However, when the spiral density wave approaches the natural barrier of $4:1$ resonance, where the density wave terminates, the orbits in the analytical model are not rectangular but circular, contrary to those of the numerical case. A parametric study can also test the range of the parameters in which the two orbits are in agreement.

### 2.2.3 Parametric study

In this section we choose various values for the spiral amplitude (parameter $\rho_0$ in Eq. (2.71)), pattern speed $\Omega_{\rm sp}$ and pitch angle $a$. Our study focuses on the form and stability of periodic orbits which support the spiral arms as well as the shape of the phase space around these orbits. The agreement between the "imposed" spirals (minima of the potential (2.71)) and the "response" spirals (formed by the elliptical periodic orbits), as well as the regularity of the phase space structure observed in the previous example holds for a particular choise of parameters $(\rho_0, \Omega_{\rm sp}, a)$. We will now study how the above picture is altered by varying independendly the amplitude $\rho_0$, the pattern speed $\Omega_{\rm sp}$ or the pitch angle $a$ in the imposed spirals. We are going to examine the range of these parameters in which they give realistic spiral density waves.

#### The role of the amplitude of the perturbation

We start by investigating the role of the amplitude of the spiral perturbation ($\rho_0$ in Eq. (2.71)) in the creation of the spiral wave. To this end, we increase the value of $\rho_0$ in Eq. (2.71) and repeat the study of the subsection 2.2.2.

Figure 2.8 shows the same phase space portraits $(\xi, P_\xi)$ as in Fig. 2.3, but for a value of the amplitude of the spiral potential three times larger, namely $\rho_0 = 15 \times 10^7 M\odot/\text{kpc}^3$. Increasing the amplitude, the main observation is that while the $x_1$ family is stable for most values of $r_c$, chaos is introduced in the phase space for radii $r_c > 5$ kpc covering a great part of the phase space around the island of stability corresponding to the $x_1$ periodic orbit. In fact, the $x_1$ family becomes itself unstable within a small interval of $r_c$ values (see Fig. 2.8).

Figure 2.9 shows the normalized characteristic curves $S(r_c) = \sqrt{\xi^2 + P_\xi/\kappa_c^2}$ as a function of the radius $r_c$, same as in Fig. 2.4, but for the amplitude $\rho_0 = 15 \times 10^7 M\odot$ $/\text{kpc}^3$. As in Fig. 2.4, here too the $x_2$ and $x_3$ periodic orbits are created together at a tangent bifurcation close to the first ILR and then they join and disappear close to the second ILR. The value of $S(r_c)$ reaches a minimum value around $8.5$ kpc (same as in Fig. 2.4) and then it increases abruptly. Therefore, the end of the response spiral density wave should be placed, here again, somewhere between the radius $r_c$ corresponding to the minimum $S(r_c)$ and the radius corresponding to the 4:1 resonance.

Figure 2.10 shows the spiral density waves generated by the $x_1$ family in this model, extending for radii between the second ILR ($r_c \approx 5$ kpc) and a little inside the 4:1 resonance. The response spirals appear now more concentrated than the spirals in Fig. 2.5, around the locus of the maximum of the density wave. This is because the forced ellipticity of the $x_1$ orbits increases with the amplitude of the spiral perturbation $\rho_0$ (see Efthymiopoulos 2010 for a review). In Fig. 2.10b the $x_1$ family of orbits is plotted both inside and outside the second ILR. Here again, the orbits between the first ILR ($\approx 1.5$ kpc) and the second ILR ($\approx 5$ kpc) form a less dense and well defined spiral density wave, while inside the first ILR the orbits are more

circular. In Fig. 2.10b, superposed are plotted circles corresponding to ILR (green circle), 4:1 resonance (blue circle) and corotation (black circle). The superposed red spiral arms are derived from the minima of the spiral potential (2.71). We observe again a nearly complete coincidence between imposed and response spirals.

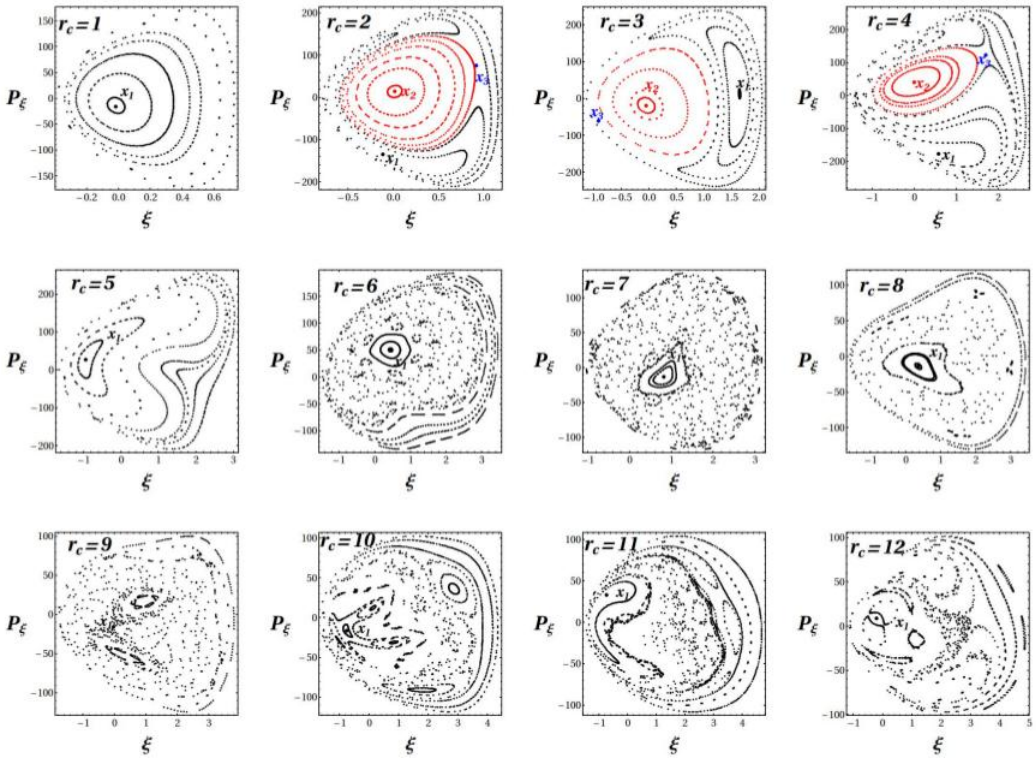


**Figure 2.8**: *Same as Fig. 2.3, but for* $\rho_0 = 15 \times 10^7 M\odot/\mathrm{kpc}^3$.

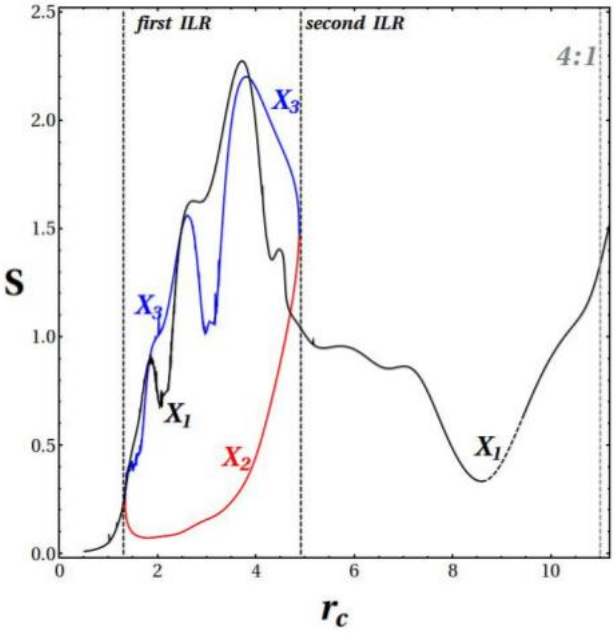


**Figure 2.9**: *Same as in Fig. 2.4, but for the density parameter of the spiral potential* $\rho_0 = 15\times10^7 M\odot/\mathrm{kpc}^3$. *The dashed part of the black curve denotes that the periodic orbit* $x_1$ *is unstable.*

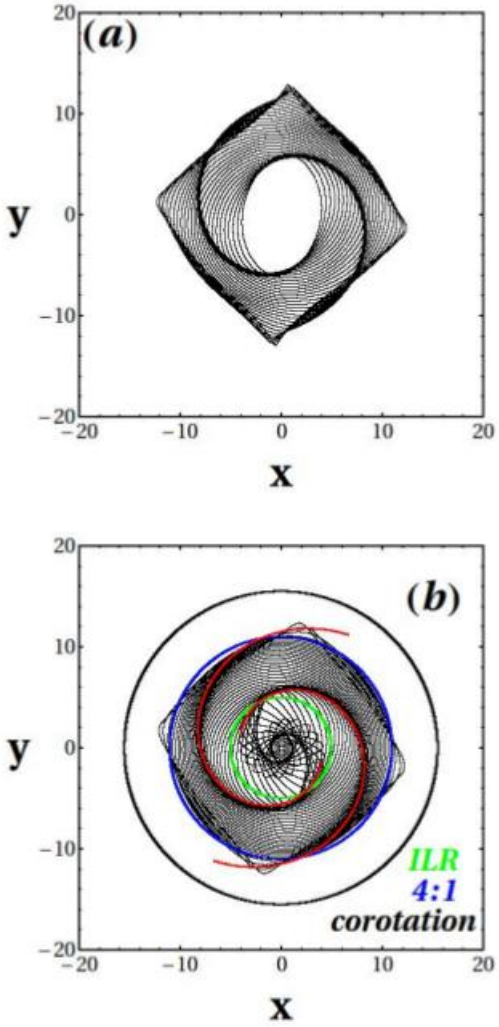


**Figure 2.10**: *Same as in Fig. 2.5, but for* $\rho_0 = 15 \times 10^7 M \odot /\text{kpc}^3$.

Figure 2.11, now, shows the phase portraits $(\xi, P_\xi)$ as in Fig. 2.3, but for even greater (by a factor 6) value of the amplitude of the spiral potential, namely $\rho_0 = 30 \times 10^7 M \odot /\text{kpc}^3$. In comparison with the phase space portraits of Fig. 2.8, we observe that here chaos is introduced at approximately the same values of $r_c$ (namely for $r_c > 5$ kpc) as in the previous example. However, the main qualitative difference between these two cases is that, in the latter case the $x_1$ family becomes unstable by a sequence of period doubling bifurcations starting at $r_c \approx 6.8$ kpc and there are no ordered orbits around it from there on. As a consequence, no ordered matter is collected around it, that could support a realistic spiral density wave.

Figure 2.12 shows the normalized characteristic curves $S(r_c) = \sqrt{\xi^2 + P_\xi/\kappa_c^2}$ of this model. The main difference with respect to the previous cases is that the curve $S(r_c)$ forms a nearly constant plateau from the second ILR to the point $r_c \approx 7$ kpc and then marks an abrupt fall to a minimum at $r_c \approx 8$ kpc. As a consequence, the ellipticity of the $x_1$ orbits remain nearly constant in the region between the second ILR and the radius $r_c \approx 7$ kpc. Also, plotting the elliptical orbits of the unstable $x_1$ periodic orbit for this model (Fig. 2.13a), we see that the ellipses intersect each other in the whole range of radii and they form a less dense and more wide spiral density wave, in comparison with the waves of Fig. 2.10. Some secondary, less intense spiral arms, also appear. This is an unrealistic spiral density wave that cannot be observed in real galaxies, as there exists no ordered matter around the $x_1$ family

that could support this spiral wave. Fig. 2.13b is the same as Figs. 2.5b and 2.10b for $\rho_0 = 30 \times 10^7 M \odot /\mathrm{kpc}^3$.

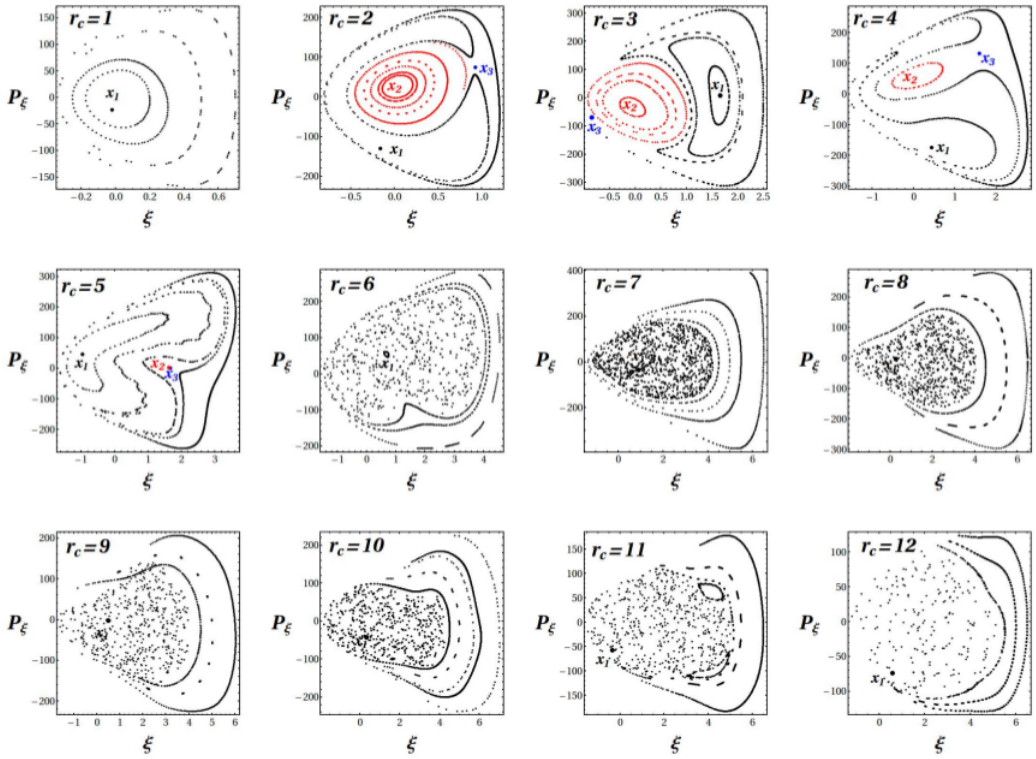


**Figure 2.11**: *Same as Fig. 2.3, but for* $\rho_0 = 30 \times 10^7 M \odot /\mathrm{kpc}^3$.

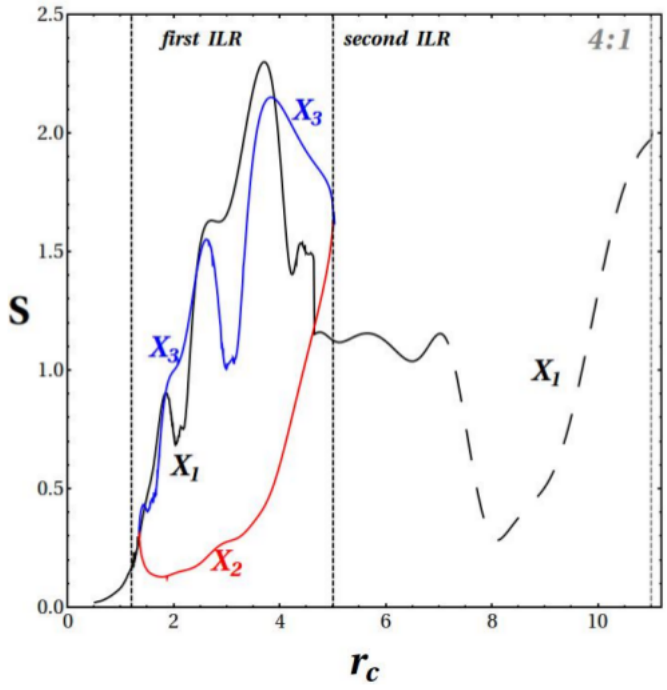


**Figure 2.12**: *Same as in Fig. 2.4 but for* $\rho_0 = 30 \times 10^7 M \odot /\mathrm{kpc}^3$. *The dashed part of the black curve denotes that the periodic orbit* $x_1$ *is unstable.*

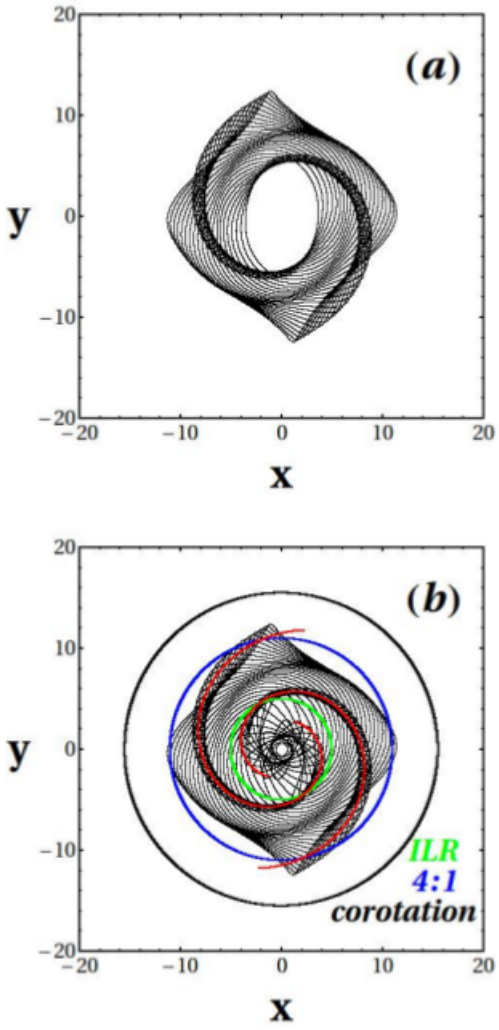


**Figure 2.13**: *Same as in Fig. 2.5, but for* $\rho_0 = 30 \times 10^7 M\odot/\mathrm{kpc}^3$.

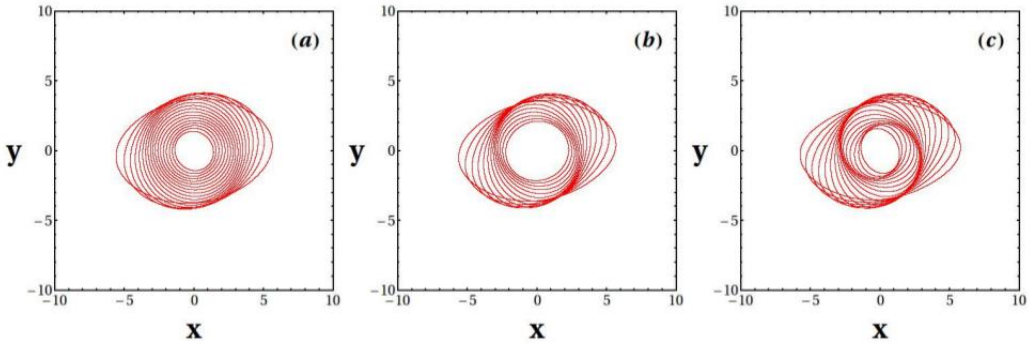


**Figure 2.14**: *The* $x_2$ *family of orbits for the model (9) for (a) pattern speed* $\Omega_{sp}$*=15* $\mathrm{km.sec}^{-1}.\mathrm{kpc}^{-1}$ *and density of the spiral potential* $\rho_0 = 5 \times 10^7 M\odot/\mathrm{kpc}^3$ *in (a)* $\rho_0 = 15 \times 10^7 M\odot/\mathrm{kpc}^3$ *in (b) and* $\rho_0 = 30 \times 10^7 M\odot/\mathrm{kpc}^3$ *in (c) In all three cases these elliptical orbits do not suport the spiral wave derived from the galactic potential and have main axes perpendicular to the main axes of the* $x_1$ *family.*

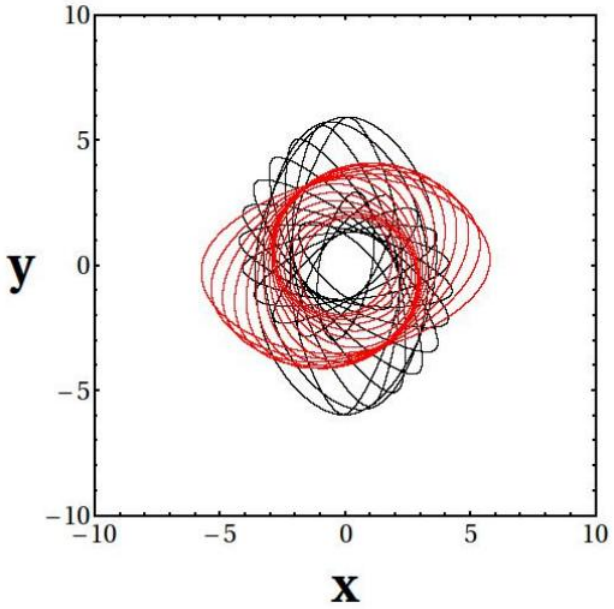


**Figure 2.15**: *Some precessing ellipses of the $x_1$ family (black orbits) together with the precessing ellipses of the $x_2$ family (red orbits) that correspond to the same radii $r_c$, for density of the spiral potential $\rho_0 = 30 \times 10^7 M\odot/\text{kpc}^3$ and for pattern speed $\Omega_{\text{sp}}$=15 km.sec$^{-1}$.kpc$^{-1}$. The $x_2$ ellipses have main axes perpendicular to the main axes of the $x_1$ family and do not support the spiral density wave.*

As an overall conclusion, comparing the $F-$strength in all three models, we find that the precessing ellipses of the $x_1$ family can support the spirals for amplitudes ($F$-strengths) not exceeding the level $15-20\%$. Beyond that value, the $x_1$ family becomes unstable at a rather small distance beyond the second ILR ($\Delta r_c \approx 2$ kpc), while chaos dominates in the phase space, thus preventing the existence of any regular set of orbits to support the spirals. In fact, estimates of the amplitude of the spiral perturbation of the spiral arms in real grand design galaxies give a relatively low upper limit which is $\approx 10-15\%$ in the forces (Grøsbol & Patsis (1998), Grøsbol et al. (2004)). Moreover, long-term evolution of self-gravitating models shows that spiral density waves will not remain viable over many revolutions if the spiral forcing is higher than 5% (Chakrabarti (2003)).

Regarding the role of other families of periodic orbits, Fig. 2.14 shows the precessing ellipses of the $x_2$ family for the model (2.71) for pattern speed $\Omega_{\text{sp}} = 15$ km.sec$^{-1}$.kpc$^{-1}$ and density of the spiral potential $\rho_0 = 5 \times 10^7 M\odot/\text{kpc}^3$ in Fig. 2.14(a), $\rho_0 = 15 \times 10^7 M\odot/\text{kpc}^3$ in Fig. 2.14(b) and $\rho_0 = 30 \times 10^7 M\odot/\text{kpc}^3$ in Fig. 2.14c. In all three cases the response spirals are orthogonal to the response spirals of the $x_1$ family (see Contopoulos (1975)). In Figs. 2.14b,c they form weak spiral arms in the region between the first and the second ILR, where the amplitude of the spiral potential is close to zero (see Fig. 2.1).

In Figure 2.15 some precessing ellipses of the $x_1$ family (black orbits) are plotted together with some precessing ellipses of the $x_2$ family (red orbits) for a density of the spiral potential $\rho_0 = 30 \times 10^7 M\odot/\text{kpc}^3$ and for the pattern speed $\Omega_{\text{sp}} = 15$ km.sec$^{-1}$.kpc$^{-1}$, corresponding to the same radii $r_c$, namely from $r_c = 2$ kpc to $r_c = 5$ kpc. The ellipses of the $x_2$ family have main axes perpendicular to the main axes of the $x_1$ family and they exist in radii where the amplitude of the spiral perturbation is close to zero (see Fig. 2.1). Therefore they do not support the spiral density wave. One can easily verify that the same is true for the unstable $x_3$ family of periodic orbits (not shown in the figures).

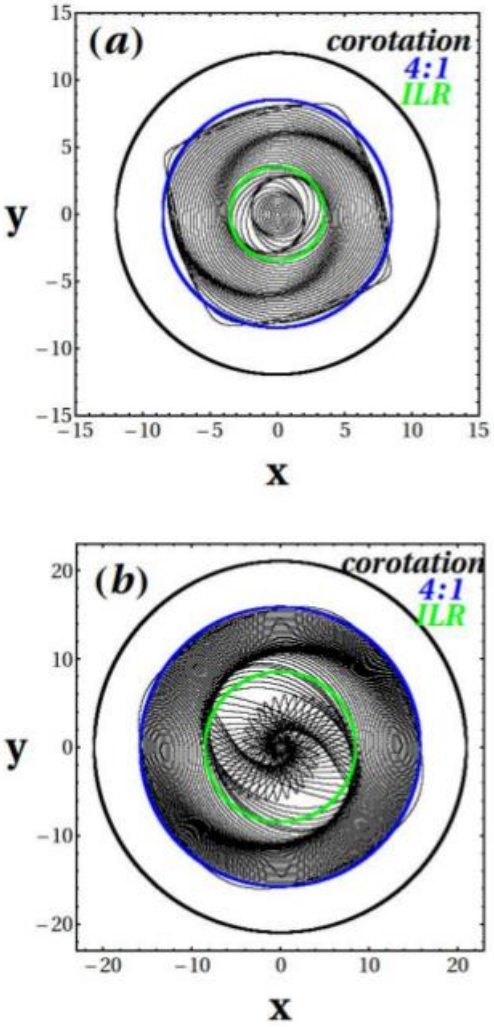


**Figure 2.16**: *The spiral density waves formed by the elliptical orbits of the $x_1$ family, from the model (9) for pattern speed $\Omega_{sp} = 20$ km.sec$^{-1}$.kpc$^{-1}$ in (a) and $\Omega_{sp} = 10$ km.sec$^{-1}$.kpc$^{-1}$ in (b) and density of the spiral potential $\rho_0 = 5 \times 10^7 M\odot$/kpc$^3$. Superposed are plotted circles corresponding to ILR (green circle), 4:1 resonance (blue circle) and corotation (black circle).*

### The role of the pattern speed

In this subsection we examine the dependence of the response spiral density wave on the pattern speed $\Omega_{sp}$. In particular, we fix the amplitude of the spiral perturbation to $\rho_0 = 5 \times 10^7 M\odot$/kpc$^3$ and change the pattern speed of the spiral potential, comparing the cases $\Omega_{sp}$=10, 15 and 20 km.sec$^{-1}$.kpc$^{-1}$. We reproduce the phase space and the orbits and we examine how their stability of the $x_1$ orbits is affected by the alteration of the pattern speed and in which case the spiral density wave can be supported by these orbits.

Figure 2.16 shows the spiral density waves formed by the precessing ellipses of the $x_1$ family (black orbits) for the pattern speed $\Omega_{sp} = 20$ km.sec$^{-1}$.kpc$^{-1}$ (in Fig. 2.16(a) and $\Omega_{sp} = 10$ km.sec$^{-1}$.kpc$^{-1}$ (in Fig. 2.16(b). Superposed are plotted the circles corresponding to the ILR radius (green circle), to the 4:1 resonance (blue circle) and to corotation (black circle). By comparing Figs. 2.16a,b and Fig. 2.5a,b, which have all the same amplitude $\rho_0 = 5 \times 10^7 M\odot$/kpc$^3$, but different values of the pattern speed we derive the following conclusions. When the pattern speed decreases:

(a) all the resonances are shifted outwards (see Fig. 2.2) and therefore the spiral

density waves reach larger radii. However, the ellipses become rounder when they get closer to the 4:1 resonance and therefore the spiral density wave becomes less cospicuous at larger radii.

(b) The region inside the first ILR becomes smaller while the region between the first and the second ILR increases. The elliptical orbits of the $x_1$ family in this latter region become much more elongated and intersect each other.

(c) The width of the spiral arms is growing with radius (see Fig. 2.16b). In Savchenko et al. (2020) it is claimed that in the 86% of a sample of 155 face-on grand design spiral galaxies they observe that the arm width increases with radius (see Mosenkov et al. (2020), for an alternative interpetation of this phenomenon based on the mechanism of swing amplification).

### The role of pitch angle

In the present subsection, we choose the model $\rho_0 = 15 \times 10^7 M \odot /kpc^3$, $\Omega_{\rm sp} = 15$ km.sec$^{-1}$.kpc$^{-1}$, but vary the pitch angle from the low value $a = -5^o$ to the high value $a = -25^o$, instead of the "intermediate" value $a = -13^o$ used in all previous numerical experiments.

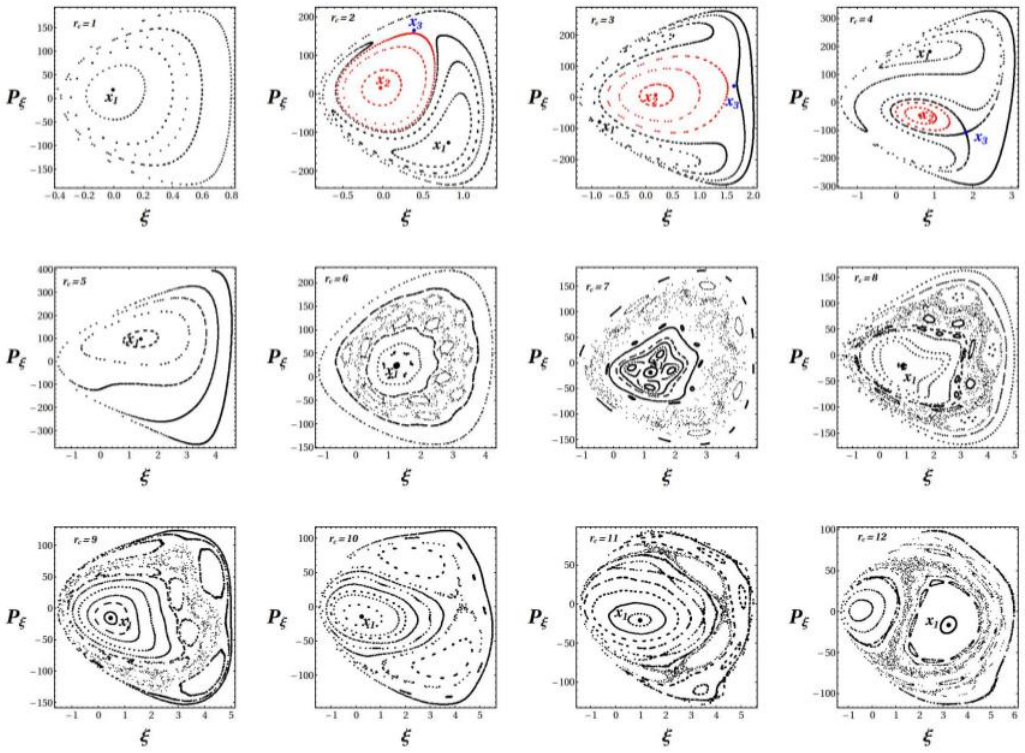

**Figure 2.17**: *Same as in Fig. 2.3 but for pitch angle* $a = -25^o$.

Figure 2.17 shows the phase portraits $(\xi, P_\xi)$ for $a = -25^o$. By comparing Figs 2.3 and 2.17, which differ only in the value of the pitch angle, we conclude that for increasing pitch angle (more open spiral arms), more order is introduced in the phase space and the chaotic areas are shrinked. Therefore, there exists more matter in ordered motion around the $x_1$ stable periodic orbit that can better support the spiral density wave. The corresponding response spirals (Fig. 2.19) are also more open and extend in the whole region between the second ILR and the 4:1 resonance.

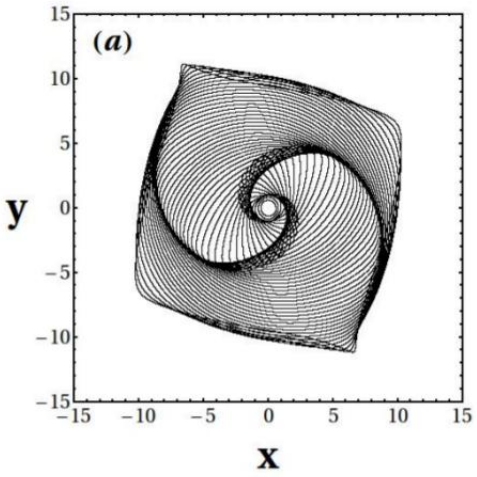


**Figure 2.19**: *The spiral density wave formed by the precessing ellipses of the $x_1$ family for $\rho_0 = 15 \times 10^7 M\odot$ /kpc$^3$, pattern speed $\Omega_{\rm sp} = 15\ sec^{-1}$.kpc$^{-1}$ and pitch angle $a = -25^o$.*

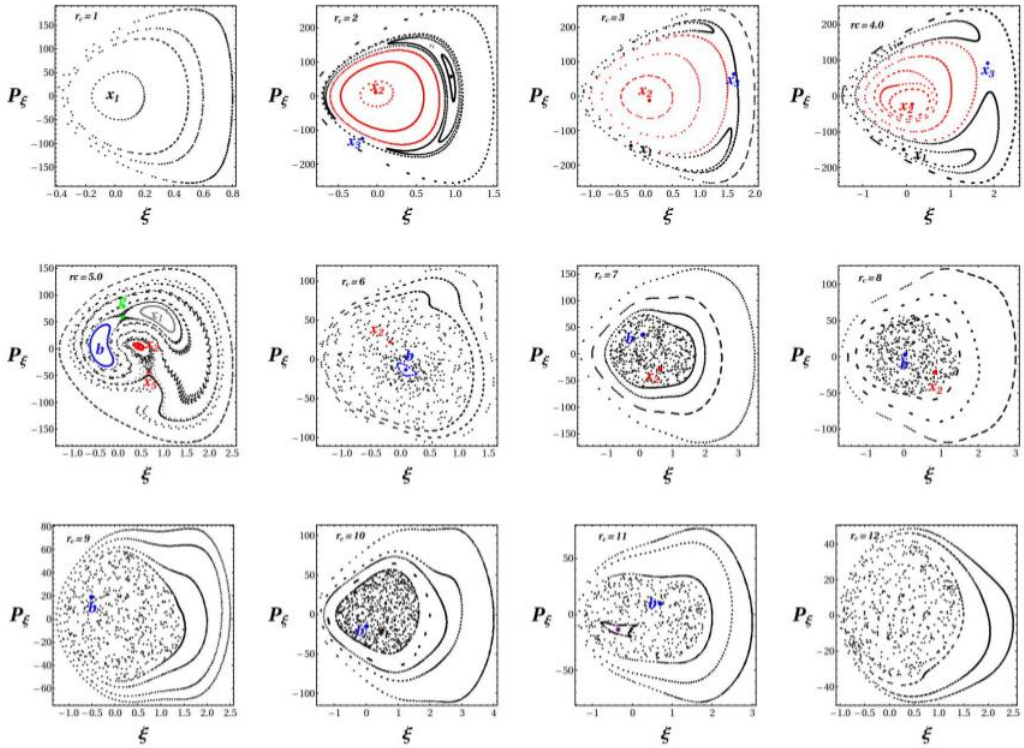

**Figure 2.18**: *Same as in Fig. 2.3 but for pitch angle $a = -5^o$.*

Figure 2.18 shows, instead, the phase portraits $(\xi, P_\xi)$, when $a = -5^o$. The key observation is that the $x_1$ family becomes unstable, now, a little outside the second ILR (at $r_c \approx 6.65$ kpc) and up to the 4:1 resonance, and the region around it is fully chaotic.

By comparing figures 2.3, 2.17 and 2.18 we conclude that for increasing pitch angle (more open spiral arms), more order is introduced in the phase space. In fact, for very small pitch angles chaos dominates in the phase space and we always get that the $x_1$ family of orbits becomes unstable almost immediately after the second ILR. The $x_2$ family is aslo unstable in the region outside the second ILR.

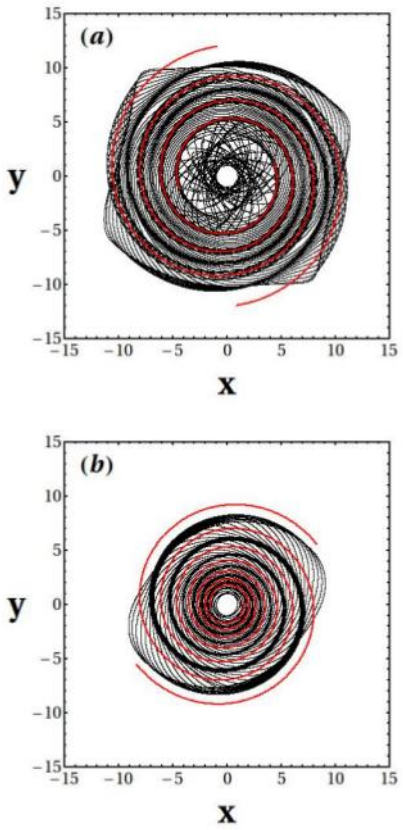


**Figure 2.20**: *The spiral density waves formed by the precessing ellipses of the (a) $x_1$ family and (b) $x_2$ family for $\rho_0 = 15 \times 10^7 M \odot /\mathrm{kpc}^3$, pattern speed $\Omega_{\mathrm{sp}} = 15\ \mathrm{sec}^{-1}.\mathrm{kpc}^{-1}$ and pitch angle $a = -5^o$. Superposed (in red) is the theoretical spiral derived from the minima of the spiral potential (9).*

In conclusion, there is a lower limit of the value of the pitch angle $a$, below which the central periodic orbit of the $x_1$ family becomes unstable in the region between the second ILR and the 4:1 resonance. This limit of the pitch angle is defined by the other two free paremeters of the model, i.e. the amplitude of the spiral perturbation and the pattern speed of the spiral arm as indicated in Table 2.1.

Table 2.1: The pitch angle below which the $x_1$ family becomes unstable outside the second ILR for various values of the amplitude of the spiral perturbation and the pattern speed.

| **amplitude** $\rho_0$ | **pattern speed** $\Omega_{sp}$ | **pitch angle** $a$ (in degrees) |
|---|---|---|
| 5 | 10 | 1 |
| 15 | 10 | 9 |
| 30 | 10 | 16 |
| 5 | 15 | 1 |
| 15 | 15 | 5 |
| 30 | 15 | 15 |
| 5 | 20 | 1 |
| 15 | 20 | 4 |
| 30 | 20 | 7 |

Table 2.1 shows how the three parameters ($\rho_0$ and $\Omega_{sp}$) collaborate so as to produce realistic spiral density waves. It can be used to estimate the permissible area of pitch angles which, for $\rho_0$ and $\Omega_{sp}$ as in the first two columns, should be larger than the value reported in the third column as a function of the amplitude of the spirals and the pattern speed. From these data we conclude that, using the stability of the $x_1$ family as a criterion, a correlation between the pitch angle and the amplitude of the spiral perturbation is suggesting that spirals formed by precessing ellipses should be stronger in amplitude when they are more open (larger $a$). Moreover, a correlation between the pitch angle and the pattern speed is indicated, namely the larger the value of the pattern speed, more tightly wound the spirals should be to maintain stability of the $x_1$ family.

### 2.2.4 Comparison with observations

In its classical version which we discussed in the section 1.1, the Hubble sequence for spiral galaxies implies that the bulge size and the spiral arm winding should be highly correlated. According to this classification, the "$Sa$" galaxies have tightly wound arms and fat nuclear bulges, "$Sb$" galaxies have moderately wound arms and moderate nuclear bulges and "$Sc$" galaxies have loosely wound arms and small nuclear bulges. However, modern classification schemes for spiral galaxies imply a considerable departure from the classic 'Hubble sequence' as regards the correlation between spiral arm winding type and bulge size. Early studies suggested that spiral arms become tighter with increasing mass of the bulge (Morgan (1958), Morgan (1959), Kennicutt (1981), Bertin et al. (1989)). Also, Seigar et al. (Seigar et al. (2005), Seigar et al. (2006)) reported a tight connection between pitch angle and morphology of the galactic rotation curve, quantified by the shear rate, with open arms associated with rising rotation curves and tightly wound arms connected to flat and falling rotation curves. On the other hand, more recently, Hart et al. in Hart et al. (2017) analyzed a large sample of galaxies selected from the Sloan Digital

Sky Survey (SDSS; York et al. (2000)) and found very weak correlations between pitch angle and galaxy mass, and a surprising trend, that the pitch angle increases with increasing bulge-to-total mass ratio. Yu & Ho (2019), found that the pitch angle decreases (arms are more tightly wound), in galaxies of earlier Hubble type, more prominent bulges, higher concentration, and larger total galaxy stellar mass. However, there is a significant scatter in their measures. Finally, Masters at Masters et al. (2019) and Díaz-García et al. in Díaz-García et al. (2019), found little or no correlation between spiral arm winding tightness and bulge size.

Given that there is no concluding evidence of correlation between the size of the bulge and the pitch angle of the grand design galaxies, we have tested various pitch angles in our galactic model keeping constant the mass of the bulge at a relatively high value. The results of the previous subsection suggest, indeed, a correlation between pitch angle and amplitude of the spiral perturbation, suggesting that galaxies with stronger perturbations should have more open spirals (greater value of the pitch angle). In comparison with real observations, Grøsbol (2002) found that the distribution of mean amplitudes of two-armed spirals as a function of the pitch angle shows a lack of stong in amplitude and at the same time tightly wound spirals. They have also found that most of the mean amplitudes of spiral arms are below 15% in forces and there is a correlation between the amplitude of spirals and the pitch angle, namely weak spirals often have more tight spiral arms. Díaz-García in Díaz-García et al. (2019) also, found that the mean amplitude of the arms increase with increasing pitch angle.

# Chapter 3

# Manifold spirals and the secular evolution in N-body models of barred galaxies

*Parts of the results of the present chapter were published as:*
*Efthymiopoulos C., Kyziropoulos P., Paez R., Zouloumi K., Gravvanis G., 2019, MNRAS 484, 1487*

In this chapter we are going to present the results of Efthymiopoulos et al. (2019). In this work the evolution of the observing morphologies and the non-axisymmetric features of an N-body simulation of a barred spiral galaxy of Kyziropoulos et al. (2016) is examined. A dynamical analysis is also conducted in the N-body, the manifold spirals are reproduced along with the vividly evolving structures of the N-body.

This Chapter is structured as follows: section 3.1 presents the N-body simulation (initial conditions, code, runs), as well as methods of analysis (extraction of the potential, Fourier transform etc.). Section 3.2 explains the computation of the invariant manifolds and its comparison with the disc morphology in the simulation. Section 3.3 compares the manifolds with the observed non-axisymmetric activity in the disc during secular evolution, as well as the phenomena related to secular evolution, i.e., the disc-halo interaction, triggering of new incidents, bar evolution and evolution of the disc's thermal profile.

## 3.1 Simulation and numerical computations

### 3.1.1 Description of the N body simulation

Here, as in Efthymiopoulos et al. (2019) we use in our study the N-body simulation named "$Q_1$" in Kyziropoulos et al. (2016). The simulation uses $10^7$ particles and contains the following components:

1) An initially exponential disc of mass $M_d = 5 \times 10^{10}\ M_\odot$, with exponential scale length $R_d = 3\ kpc$, vertical exponential scalelength $z_d = 0.2\ kpc$, and Gaussian velocity distribution arising from a profile of Toomre's Q-parameter rising in the center and tending to an asymptotic outward value $Q \to Q_\infty = 1$ (see equation (13) of Kyziropoulos et al. (2016)). The disc is simulated by $5 \times 10^6$ particles.

2) A Sercic-type spherical bulge of mass $M_b = 5 \times 10^9 M_\odot$, with Sersic index $n = 3.5$,

and scale length $R_b = 1\ kpc$. The bulge is simulated by $5 \times 10^5$ particles.

3) A Dehnen-type double-power law spherical dark matter halo (see Binney & Tremaine (2008)) with density amplitude $\rho_0 = 2.016 \times 10^8\ M_\odot/kpc^3$, scale length $R_h = 3\ kpc$ and asymptotic inner and outer exponents $\alpha = 1.3$, $\beta = 3.5$. The mass of the halo rises to $2 \times 10^{11}\ M_\odot$ at $R = 100\ kpc$. The halo is simulated by $4.5 \times 10^6$ particles.

The system goes through disc instabilities leading to the formation of a bar and of dynamically evolving spiral arms. The simulation lasts for 4 Gyrs. In all subsequent computations we obtain the information by 160 saved snapshots, separated by time steps of 0.025 Gyr.

One way to quantify the non-axisymmetric structures in the galactic disc is to Fourier-analyse the disc's surface density. We separate the space in a polar grid of 50 logarithmically equi-spaced radial bins from $r_0 = 0.1\ kpc$ to r = 15 kpc, and 180 azimuthal bins from $\varphi = 0$ to $\varphi = 2\pi$. The surface density at time t of the simulation in a bin $(\Delta r, \Delta\varphi)$ centered around $(r, \varphi)$ is defined by:

$$\Sigma(r, \varphi, t) = \frac{\Delta N(r, \varphi, t)}{r \Delta r \Delta \varphi} \tag{3.1}$$

where $\Delta N(r, \varphi, t)$ is the number of disc particles at time t within the area element $r\Delta r\Delta\varphi$.

We implement the usual Fourier transform with respect to the angle $\varphi$, at fixed time t, in order to decompose the surface density into 10 angular modes:

$$\Sigma(r, \varphi, t) = A_0(r, t) + \sum_{m=1}^{10} A_m(r, t) \cos(m\varphi) + \sum_{m=1}^{10} B_m(r, t) \sin(m\varphi) \tag{3.2}$$

where

$$A_0(r, t) = \frac{1}{2\pi} \int_0^{2\pi} \Sigma(r, \varphi, t) d\varphi,$$

$$A_m(r, t) = \frac{1}{\pi} \int_0^{2\pi} \Sigma(r, \varphi, t) \cos(m\varphi) d\varphi, \quad B_m(r, t) = \frac{1}{\pi} \int_0^{2\pi} \Sigma(r, \varphi, t) \sin(m\varphi) d\varphi \quad .$$

The relative amplitude $C_m(R)$ and phase $\phi_m(R)$ of the m-th Fourier mode are defined by

$$C_m(r, t) = \frac{\left(A_m^2(r, t) + B_m^2(r, t)\right)^{1/2}}{A_0(r, t)}, \quad \varphi_m(r, t) = \frac{1}{m} \tan^{-1}(B_m(r, t)/A_m(r, t)) \quad . \tag{3.3}$$

as well as a smoothed 'non-axisymmetric excess density'

$$D(r, \varphi, t) = \frac{\Sigma(r, \varphi, t) - A_0(r, t)}{A_0} \quad . \tag{3.4}$$

Besides quantities related directly to the particle distribution in the N-body run, in subsequent computations we make use of the total gravitational potential $V(x, y, t)$ on the disc plane ($(x, y)$ for $z = 0$, where the origin of the Cartesian co-ordinates is transfered at the center of mass of the disc). The N-body code returns the potential on the set of points $x_i = -L_0/2 + (i/N_p)L_0$, $y_j = L_0/2 + (j/N_p)L_0$, where $i, j = 0, 1, \ldots, N_p - 1$, $L_0 = 25.6$ kpc, $N_p = 256$. Based on the potential values at the grid points, we use bi-cubic interpolation for obtaining a smooth representation of the potential and forces within the domain $-L_0/2 < x < L_0/2$, $= L_0/2 < y < L_0/2$. This allows to perform any type of computation requiring smooth expressions for

the equations of motion, as, for example, the computation of the positions of the Lagrangian points and the associated invariant manifolds

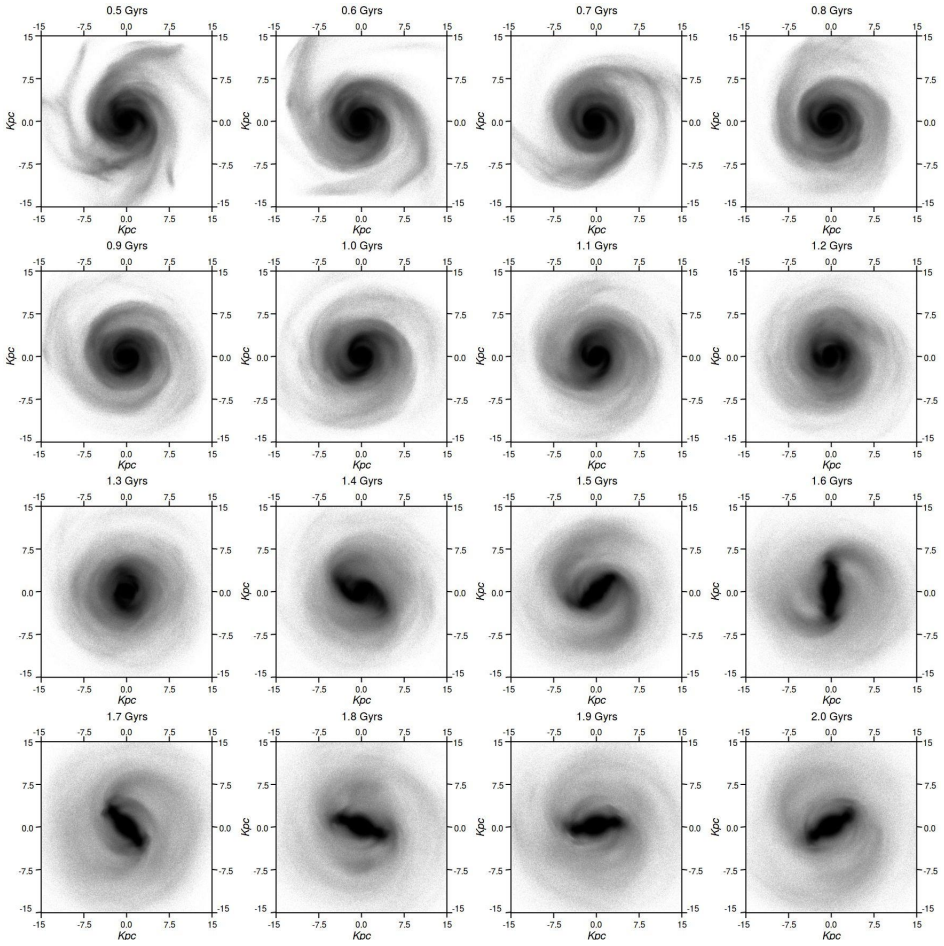


**Figure 3.1**: *Sixteen snapshots of the face-on disc view of the N-body simulation ("$Q_1$" in Kyziropoulos et al. (2016)) in the time interval $0.5 \leq t[Gyr] \leq 2.0$. Two- and three-armed spiral instabilities develop in the disc quickly after the simulation starts. The $m = 2$ spiral mode dominates in the interval $0.5 \leq t[Gyr] \leq 1.0$. The onset of the bar instability at about $t = 1.1$ Gyr leads to a fully developed bar at $t = 1.4$ Gyr, which is nearly imediately followed by a first birst of manifold-driven spirals beyond the bar (at $t = 1.5 - 1.6$ Gyr).*

### 3.1.2 Time evolution of non-axisymmetric patterns

Figure 3.1 shows snapshots of the time evolution of the simulated system ("$Q_1$" in Kyziropoulos et al. (2016)) in the time interval from $t = 0.5$ Gyr to $t = 2$ Gyr. The bar rotates counterclockwise and undegoes instabilities that give rise to m=2 or m=3 spiral modes, the formation of a bar or even the construction of rings or inner spirals. We observe all main successive phases of the generation and evolution of disc morphologies and of the non-axisymmetric structures.

As a consequence of the chosen value of $Q$ (=1), the disc exhibits a rapid initial growth of competing features (mainly $m = 3$ and $m = 2$) and undergoes two-armed or three-armed spiral instabilities. The $m = 2$ spiral mode becoming dominant after $t \sim 0.5$ Gyr. At this initial phase the simulated disc looks like a normal spiral galaxy in the Hubble classification. The spirals undergo about one and a half revolution (counterclockwise in Fig. 3.1) up to the time $t = 1.1$, maintaining a nearly constant pattern with features of density wave.

The morphology and the dynamics of the system change rapidly at $t = 1.1$ Gyr where the bar instability is activated on the disc. The bar evolves and takes its final

size at about $t = 1.4$ Gyr. The bar formation is accompanied by a first 'incident' of spiral activity, which is well described by manifold spirals, as discussed in detail below. Three more incidents of similar size take place up to $t = 2$ Gyr. One notices that the overall morphology of the galaxy presents significant variations over a timescale as small as even one bar period. In particular, features such as inner rings (e.g. snapshots $t = 1.5$ Gyr or $t = 2$ Gyr), or a secondary system of inner spiral arms (e.g. snapshot $t = 1.7$ or $t = 1.9$ Gyr) occasionally appear.

After the bar formation reccurent incidents of spiral activity are observed on the disc and they are illustrated in greater detail in Fig. 3.2, showing several snapshots of the time evolution of the system from $t = 1.65$ to $t = 3$ Gyr. The bar rotates counterclockwise, and performs slightly more than seven revolutions in the depicted time interval. One can recognise an oscillating profile in the strength of spiral arms and we observe an alteration from conspicuous maxima (e.g. at $t = 1.65$, $t = 1.95$, $t = 2.25$ Gyr) to very low minima (e.g. at $t = 2.025$, $2.325$, $2.7$, or $2.925$ Gyr), albeit never vanishing completely. An inner ring-like structure surrounding the bar is observed in particular snapshots (e.g. $t = 1.825$), material is distinguished transiting from the one end of the bar towards the other by moving along the ring (see also snapshot $t = 1.8$ Gyr in Fig. 3.1).

If the evolution of the disc is viewed edge-on (Fig. 3.3), we observe other instabilities that give rise to sevelar observable galactic features. The bar undergoes the buckling instability, accompanied by the vertical growth of a characteristic peanut, or 'X-shaped', pseudobulge. The onset of the instability follows soon after the bar formation (at $t \approx 1.8$ Gyr), while the edge-on bar profile after the instability reaches a nearly final extent at $t \approx 2.2$ Gyr. As shown below, manifold spiral appear during and beyond all this time interval. Thus, manifold spirals in our simulation do not appear to be halted by the buckling instability, as reported in Kwak et al. (2017) (see also Lokas (2016)).

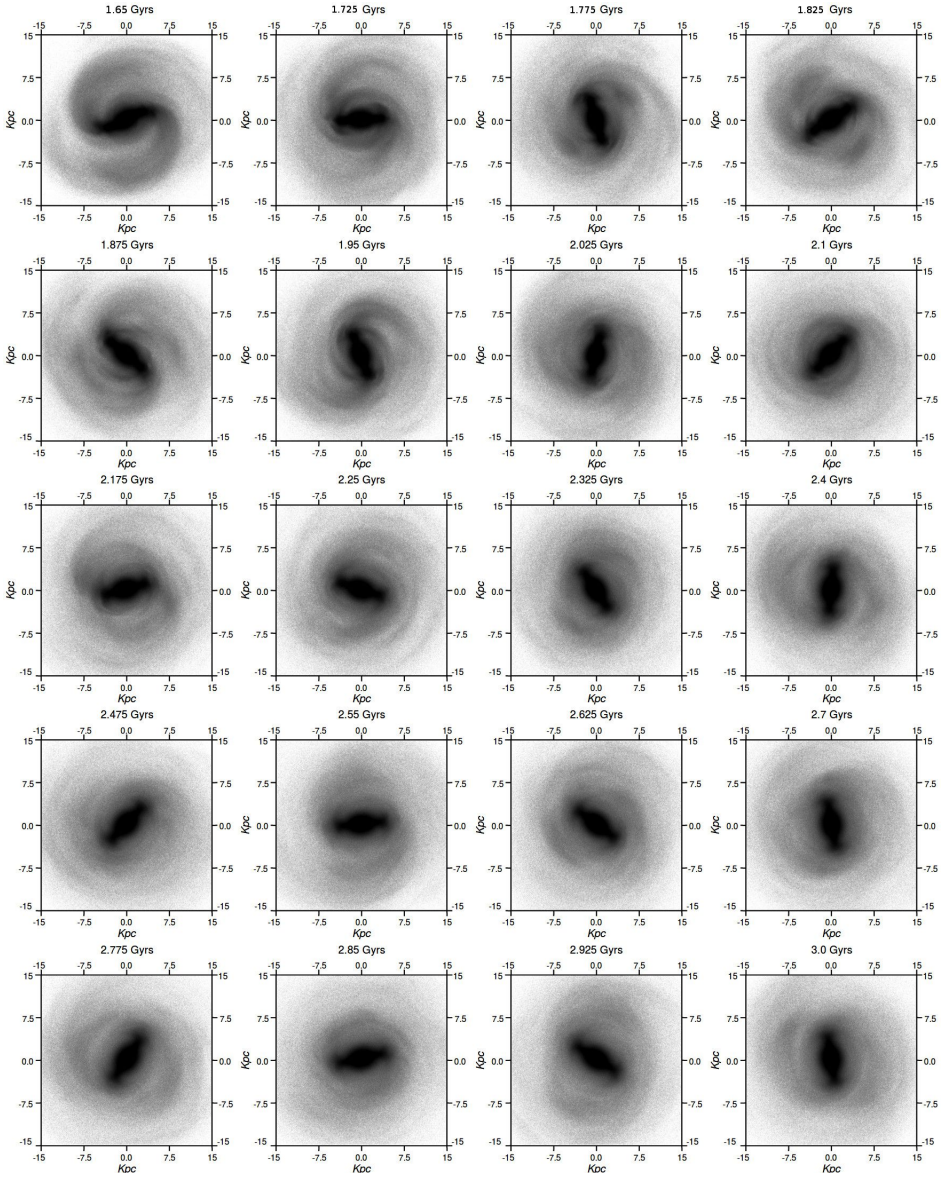


**Figure 3.2**: *Sixteen snapshots of the face-on disc view of the N-body simulation ("$Q_1$" in Kyziropoulos et al. (2016)) in the time interval* $1.65 \leq t[Gyr] \leq 3.0$. *The bar rotates counter-clockwise, while two-armed, four-armed spirals and ring-like structures appear in succession and with altering amplitudes and morphologies (see text).*

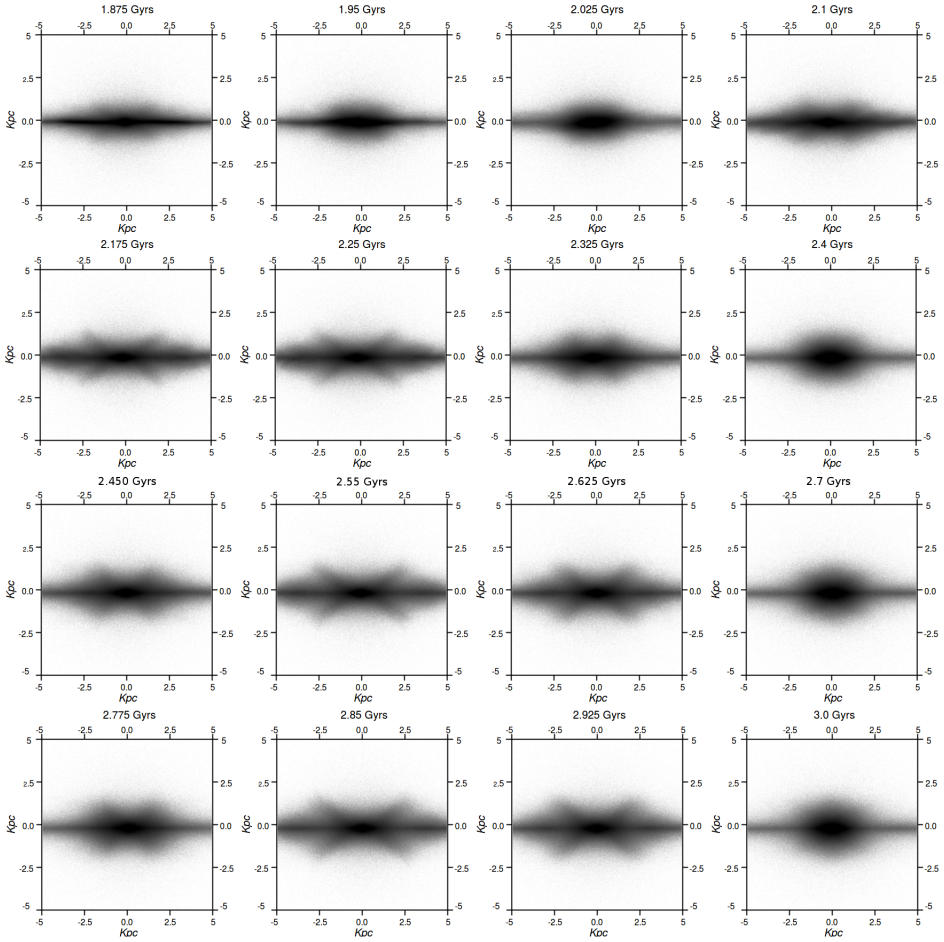


**Figure 3.3**: *Edge on view of the disc for the same snapshots as in Fig. 3.2. The growth in time of a peanut-shaped pseudo-bulge is clearly distinguished.*

### 3.1.3 Time evolution of the Fourier transform modes in the Surface Density

The description of the morphological evolution of the disc in section 3.1.2 is qualitative. However, the observed morphological features can be quantified through the time evolution of the modes of Fourier transform in the disc surface density, which is described by Eqs. (3.1)- (3.4). A construction of the maps of the non-axisymmetric excess density, obtained by Eq. (3.4) for the most important modes e.g. $m = 2, 3, 4$ can highlight the symmetry and thee nature of the observed morphological features in the disc in Figs. 3.1-3.2. This study helps us distinguish better the incidents of the spiral activity.

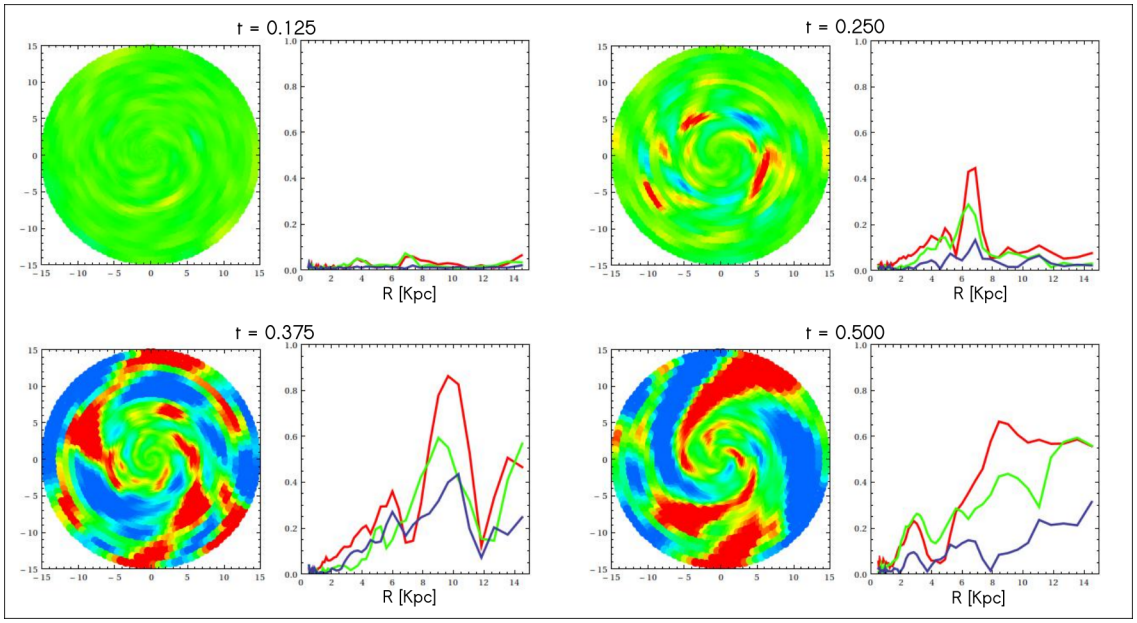


**Figure 3.4**: *Fourier decomposition of the disc non-axisymmetric excess density at the times $t = 0.125$ Gyr (top left block), $t = 0.250$ Gyr (top right block), $t = 0.375$ Gyr (down left block), and $t = 0.5$ Gyr (down right block). The left panels in each block show, in color scale, the non-axisymmetric excess density $D(r, \varphi, t)$ as viewed in an inertial frame of reference. The color scale is fixed from blue to red, representing values $D(r, \varphi, t) \leq -0.5$ in the blue limit, $D(r, \varphi, t) \geq 0.5$ in the red limit and $-0.5 < D(r, \varphi, t) < 0.5$ in between. The right panels show the relative Fourier amplitudes $C_m(r, t)$ as function of $r$ for the modes $m = 2$ (red), $m = 3$ (green) and $m = 4$ (blue).*

In Figure 3.4 the initial phase of rapid growth of non-axisymmetric features in the disc is depicted via maps of the non-axisymmetric excess density, obtained by Eq. (3.4), as well as the corresponding Fourier amplitude profiles, as function of the radial distance $r$ across the disc, for the most important modes, namely $m = 2, 3, 4$. We observe a competition between the growing $m = 2$ and $m = 3$ modes. However, the plots of the the non-axisymmetric excess density at the subsequent phases of the simulation, which are shown in Fig. 3.5 reveal that the $m = 2$ mode prevails after $t \approx 0.5$ Gyr, leading to a conspicuous bi-symmetric spiral pattern (Fig. 3.5). In the density excess map, the $m = 2$ spiral extends across the disc at nearly the disc's entire optical length, and it maintains a nearly constant pattern speed $\Omega_{spiral} \approx 15$ km/s/kpc in the time interval $0.5 \leq t[Gyr] \leq 1.1$.

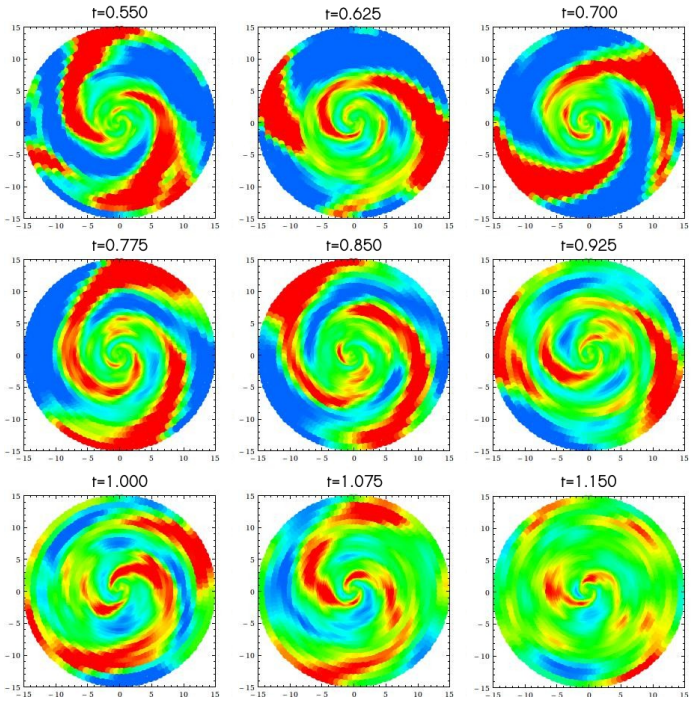


**Figure 3.5**: *The non-axisymmetric excess density $D(r, \varphi, t)$ (same color scale as in Fig. 3.4) in sixteen equidistant in time snapshots in the time interval $0.55 \leq t[Gyr] \leq 1.15$.*

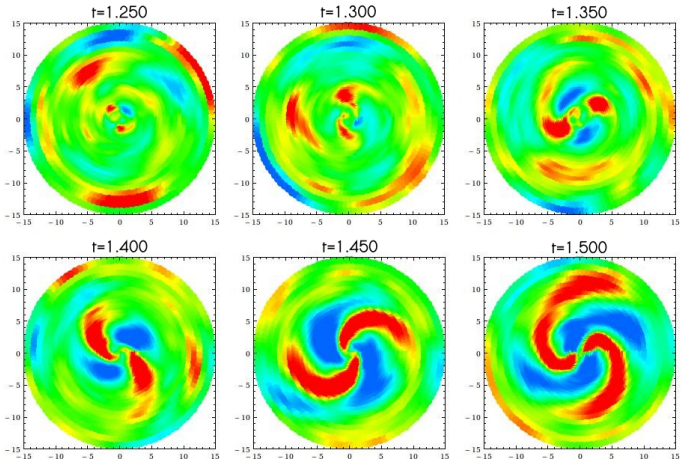


**Figure 3.6**: *The non-axisymmetric excess density $D(r, \varphi, t)$ in six snapshots in the time interval $1.25 \leq t[Gyr] \leq 1.5$. The onset of the bar instability leads to the bar formation, accompanied by the first manifold-driven incident of spiral activity.*

In Fig. 3.6 the onset of the bar instability is depicted through succesive maps of the non-axisymmetric excess density in the time interval $1.25 \leq t[Gyr] \leq 1.5$. By the time that bar prevails, all the traces of the previous spiral activity in the disc get dissolved. The bar grows rapidly (between $t = 1.25$ Gyr and $t = 1.4$ Gyr. This growth is followed, immediately, by a first conspicuous incident of spiral activity beyond the bar. The incident takes place between $t = 1.4$ Gyr and $t = 1.5$ Gyr. The initial pattern speed of the bar is about $\Omega_{bar} \approx 40$ km/s/kpc, yielding an initial period $T_{bar} \approx 0.16$ Gyr. The bar extends to a radial distance $R \approx 5$ kpc, while its co-rotation is initially at $R \approx 6.5$ kpc. The procedure of computation of the pattern speed of the bar is

described in section 3.2.

A second major incident of spiral activity occurs after nearly one more bar's full turn, at $t = 1.625$ Gyr. At that point, the $m = 2$ and $m = 4$ Fourier amplitudes inside the bar (i.e. for $R < 5$ kpc) are nearly stabilized, while the bar enters a phase of slower (secular) evolution. The snapshot $t = 1.625$ corresponds to the largest in time observed amplitude of the $m = 2$ mode in the region between the bar's co-rotation and outer Lindblad resonance. We examine the N-body disc morphologies at the snapshot at $t = 1.625$ (see Fig. 3.7) and we set this time conventionally as the time where the secular evolution of the bar initiates. In Fig. 3.7 we observe that the bar is very strong at this snapshot, with $m = 2$ and $m = 4$ Fourier amplitudes taking the maximum values $C_2 > 1$ and $C_4 \approx 0.8$ at $R \approx 4$ kpc. A secondary local maximum of $m = 2$ and $m = 4$ Fourier amplitudes is observed at larger distances ($R \approx 10-11$ kpc) which represents the dominant modes of the weaker non-axisymmetric pertubation (compared to the strong bar) in the disc, i.e. the one of the spiral arms. We can notice, however, also the presence of important power in the $m = 1$ and $m = 3$ Fourier terms in a domain which contains the bar ($R < 5$ kpc), with relative amplitude larger than 0.1 across the whole bar's extent and reaching $\sim 0.2$ in the central parts ($R < 2$ kpc). Such $m = 1$ amplitudes are distinguishable in several simulations (see, for example, Quillen et al. (2011), Minchev et al. (2012)). On the other hand, in the snapshot of Fig. 3.7, substantial $m = 1$ relative amplitudes are observed also at large distances ($R > 10$ kpc). This phenomenon is connected to the lopesidedness of the observed spirals (and manifolds, see below), a fact which hints towards nonlinear interaction of the outer disc modes.

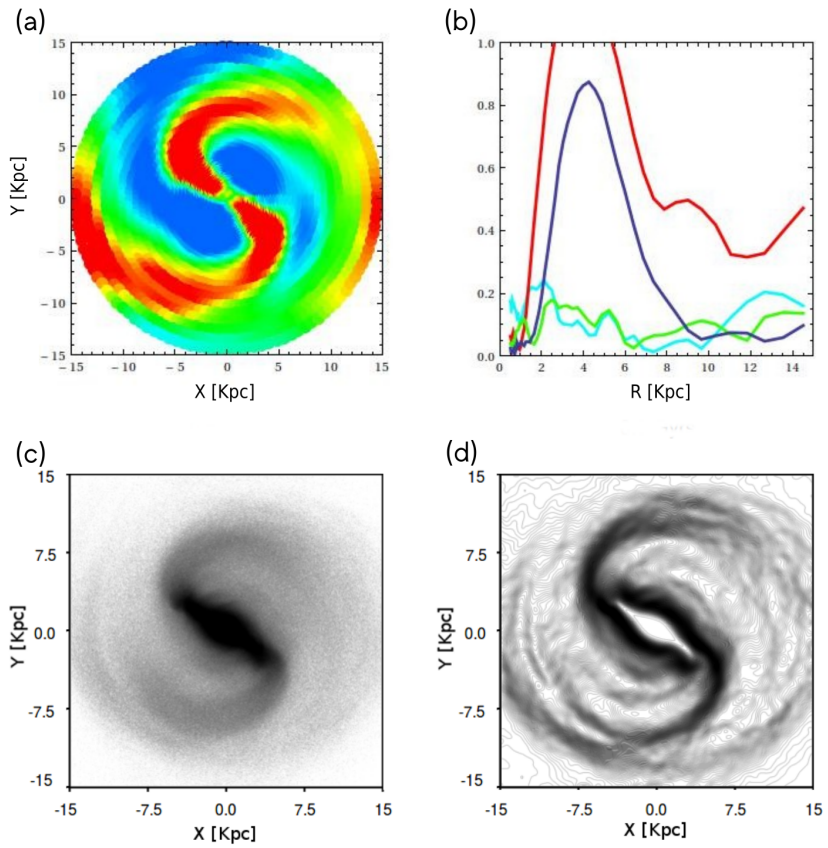


**Figure 3.7**: *(a) Color map of the non-axisymmetric excess density at the time snapshot $t = 1.625$ Gyr, conventionally set as the beginning of the phase of the bar's secular evolution. A second incident of spiral activity accompanies the bar. (b) The Fourier amplitudes $C_1$ (cyan), $C_2$ (red), $C_3$ (green) and $C_4$ (blue) as function of the radial distance $R$ accross the disc. (c) Plain image of the N-body snapshot, created by a logarithmic grayscale plot of the surface density $\Sigma(r, \varphi, t)$. (d) The image of the same snapshot after performing the Sobel-Feldman edge detection algorithm. Dimmer patterns in panel (c) are enhanced and clearly visible in panel (d).*

The density excess map (Fig. 3.7 (a)) and the plain N-body picture of the galaxy (Fig. 3.7 (c)) do not give a detailed and clear view of the morphological features and the patterns of the disc. In order to efficiently recover these patterns, a Gaussian filter is implemented, which smoothes the disc's surface density accompanied by the Sobel-Feldman edge-detection algorithm (e.g. Gonzalez & Woods (1992)). The result is shown in Fig. 3.7(d). The Sobel-Feldman filter enchances patterns already existing in the disc, but of amplitude significantly lower than the one of the main bi-symmetric spirals. The Sobel-Feldman filters reveals more structures, such as 'bridges', which are formed whenever weak extensions of the spiral arm emanating from one end of the bar join the spiral arm emanating from the opposite end or the bar, aproaching it from its exterior side. As a result, the Sobel-Feldman image shows the spiral patterns to extend and produce a morphology which is more ring-like in its outer parts than the corresponding morphology in the plain image of the disc. In the next sections we show how the manifolds allow to interpret such 'bridges', and the Sobel-Feldman disc images at different snapshots are compared to the manifold-induced patterns in the disc.

## 3.2 Manifold spirals in the N-body simulation

The computation of the apocentric manifolds $\mathcal{W}^{UA}_{PL1,2}$ in our N-body computation proceeds in the general way described in section 1.11.2. In this section we present the reproduction of the manifolds a time $t = 1.625$ Gyr of the simulation, and we discuss whether they support the morphological features of the snapshot, which we identified in section 3.1.3. The computation of the invariant manifolds, applied in our N-body first follows the following steps:

1) Having the potential of the N-body in a grid, we use an interpolating technique (see section 3.1 for more details), in order to continue with the computation the equations of motion.

2) We specify the value of the bar pattern speed as follows: computing the Fourier transform of the non-axisymmetric density excess (Eq. (3.2)), the $m = 2$ mode is largely dominant for the bar. The angular displacement, for fixed radial distance $r$, of the maxima of the $m = 2$ mode at two successive snapshots separated by a time $\Delta t$ yield the $m = 2$ pattern speed at the distance $r$:

$$\Omega_2(r) \simeq= \frac{\Delta\phi_2(r)}{\Delta t} \tag{3.5}$$

where $\Delta\phi_2(r) = \phi_2(r, t + \Delta t) - \phi_2(r, t)$, and

$$\phi_2(r, t) = \frac{1}{2}\tan^{-1}\left(\frac{B_2(r, t)}{A_2(r, t)}\right) \quad .$$

Equation (3.5) can be used also in order to compute the instantaneous pattern speed of the $m = 2$ mode as function of the radial distance $r$ via the N-body data at two successive snapshots. Therefore, we build the radial profile of the angular velocity of $m = 2$ mode, which can lead us to the estimation of the pattern speeds. We prefer this method over extending the Fourier transform (say of $A_2$, $B_2$) in the time domain, since the latter approach assumes that patterns are characterized by constant frequencies in a relatively long time window, while $\Omega_P$ appears to vary in time significantly over rather short time windows (see below).

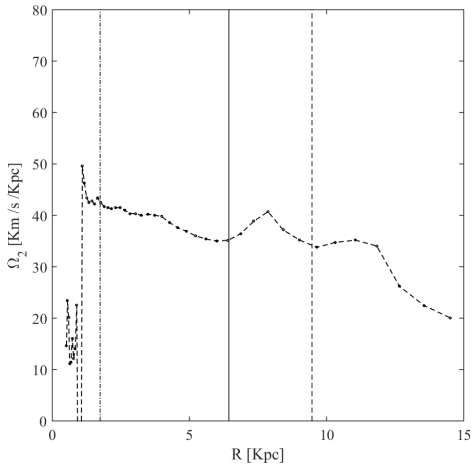


**Figure 3.8**: *The $m = 2$ mode pattern speed as function of the radial distance $R$ (Eq. (3.5)) for the N-body snapshot $t = 1.625$. The inner and outer dashed vertical lines mark the position of the Inner or Outer Linblad Resonance (ILR, OLR) respectively, while the solid vertical line marks the position of the co-rotation resonance (CR). The bar pattern speed is estimated as the mean value of $\Omega_P(R)$ in the interval 2.5 kpc $\leq R \leq$ 4 kpc.*

Figure 3.8 is the radial profile of the angular velocity of $m = 2$ mode $t = 1.625$ Gyr. We observe the formation of an approximate 'plateau' of the curve $\Omega_2(R)$ at

radii $2 \sim 5$ kpc, which is identified to the (constant) pattern speed of the bar. In subsequent computations we estimate the bar pattern speed $\Omega_{bar}$ as the mean value of $\Omega_2$ in the interval 2.5 kpc $< R <$ 4 kpc. The vertical lines mark the positions of the Inner Linblad Resonance (ILR), co-rotation (CR), and outer Linblad resonance estimated from the relations (see also section 1.5 for more details on the resonances):

$$\Omega(R_{ILR}) - \Omega_{bar} = \frac{1}{2}\kappa(R_{ILR}), \quad \Omega(R_{CR}) - \Omega_{bar} = 0, \quad \Omega(R_{OLR}) - \Omega_{bar} = -\frac{1}{2}\kappa(R_{OLR}) \quad . \tag{3.6}$$

where the epicyclic frequency $\kappa(r)$ is given by Eq. (1.31). One notes that the plateau is well formed after the ILR radius, and it corresponds to a pattern speed $\Omega_{bar} \simeq 42$ km/sec/kpc. Inside the ILR, the curve $\Omega_P(R)$ becomes noisy, as expected since the ILR radius nearly coincides with the interface between the bar and inner bulge components. On the other hand, the pleateau is lost, and and a varying form of the curve $\Omega_2(R)$ appears close to the corotation and OLR.

3) Having fixed $\Omega_{bar}$ we compute the unstable Lagrangian points $L_1$ and $L_2$ in the Hamiltonian (1.41). Since we use the full N-body potential, the Lagrangian points are not found at exactly symmetric positions with respect to the disc's center, while their Jacobi energies have also a small difference $2|E_{J,L1} - E_{J,L2}|/|E_{J,L1} + E_{J,L2}| \approx 10^{-4}$. Similar differences hold for the stable Lagrangian points $L_4$ and $L_5$.

4) The next step is the location of the apocenters of the unstable periodic orbits $PL_1$ or $PL_2$, from which the apocentric invariant manifolds $\mathcal{W}^{UA}_{PL1,2}$ emanate. This procedure is described in step 3) of section 1.11.2. In order to estimate the location of $PL_{1,2}$, we keep, in each case, the orbit of the family with Jacobi energy midway between the energies at $L_{1,2}$ and $L_{4,5}$, i.e., $E_{J,PL1} = (E_{J,L1} + E_{J,L4})/2$, $E_{J,PL2} = (E_{J,L2} + E_{J,L5})/2$. These energies roughly correspond to the median of the Jacobi energy distribution for the N-body particles in the corotation zone.

5) We finally compute the apocentric manifold spirals emanating from the co-rotation zone, emanating from the families $PL_1$ and $PL_2$ as explained in steps 4) and 5) of the section 1.11.2. For the computation of the manifolds $\mathcal{W}^{UA}_{PL1,2}$, we take an initial segment on the apocentric surface of section with N=10000 initial conditions distributed according to $\varphi_j = \varphi_{0,PL1} - j\Delta\varphi/N$, $p_{\varphi,j} = p_{\varphi,0,PL1} + j\Delta p_\varphi/N$, for the outer branch, and $\varphi_j = \varphi_{0,PL1} + j\Delta\phi/N$, $p_{\varphi,j} = p_{\varphi,0,PL1} - j\Delta p_\varphi/N$ for the inner branch of $\mathcal{W}^{UA}_{PL1}$, with $\Delta\varphi = 10^{-3}$ and $\Delta p_\phi = S_u\Delta\varphi$, where $S_u$ is the slope of the unstable eigendirection of the the monodromy matrix (see Eq. (1.52) at the fixed point $PL_1$ (and similarly for the orbit $PL_2$).

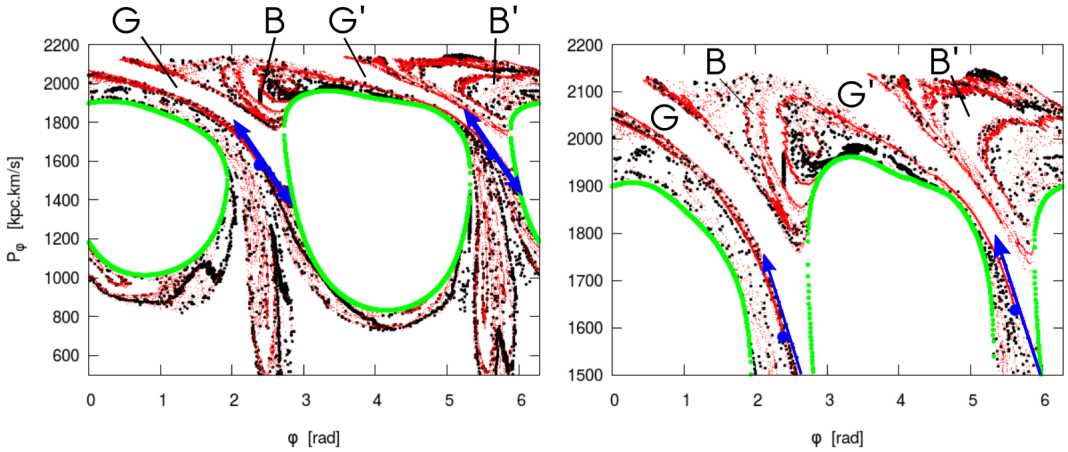


**Figure 3.9**: *The apocentric surface of section as defined in Eq. (1.49) for the energy $E_J = 0.5(E_{J,L1} + E_{J,L4})$, considering the equations of motion (1.42) under a frozen potential and bar pattern speed equal to those of the snapshot $t = 1.625$ Gyr. The orbits in this surface of section are strongly chaotic. The right panel is a magnification of the left panel in the region of angular momenta $p_\phi$ closer to corotation. The black thick points represent the successive iterates of orbits with initial conditions taken at various locations within the chaotic domain. The red points represent iterates of the apocentric invariant manifolds $\mathcal{W}^{UA}_{PL1,2}$ at the same energy. The Lyapunov periodic orbits PL1 and PL2 give two blue points (left and right respectively). The thick blue points mark the position of the fixed points corresponding to the periodic orbits PL1 and PL2, while the thick blue arrows indicate the corresponding unstable eigendirections. The closed green thick curves are the limiting curves of the apocentric surface of section, inside which the motion is energetically forbidden. The parts of the manifolds (and phase) space marked with $B, B'$ and $G, G'$ correspond to the manifolds' morphological features called 'bridges' and 'gaps' (see text). The right panel shows a magnification of the left panel in its upper part, where most lobes of the invariant manifolds develop homoclinic oscillations.*

For the snapshot at time $t = 1.625$ Gyr we proceed the construction of manifolds in the phase space and the configuration space. Figure 3.9 shows the apocentric surface of section (plane $(\varphi, p_\varphi)$, as well as the apocentric invariant manifolds of the $PL_1$ and $Pl_2$ orbits, at the snapshot $t = 1.625$ Gyr. The manifolds (red points) emanate as straight lines starting from the fixed points corresponding to the periodic orbits $PL_1$ and $PL_2$, but they soon develop a very complicated form and they reveal an intricate dynamics. Therefore, we observe a number of thin lobes, which are the signature of homoclinic dynamics. We can also observe some recognisable manifolds' morphological features, such as 'brisdges' and 'gaps' ($B, B'$ and $G, G'$ respectively in Fig. 3.9) .Taking segments of initial conditions in the interior of the manifolds defined by the lobes marked $B, B'$, we iterate these chaotic orbits (black points), and find that the distribution of the iterates covers more and more uniformly the area inside the manifolds' lobes.

All together, the phase portrait formed at the indicated level of energies (Jacobi constant $E_J = 0.5(E_{J,L1} + E_{J,L4})$) is strongly chaotic. While such level of chaos can be expected even in purely barred models (see Patsis et al. (1997)), the deformation of all phase space structures due to the strong spiral mode is evident in Fig. 3.9. This deformation affects the form of the closed limiting curves in the apocentric surface of section, inside which the motion is energetically forbidden. These curves are found by locating the pairs $(\varphi, p_\varphi)$ for which the effective potential satisfies the relation

$$V_{eff}(r_c; \varphi, p_\varphi) = \frac{p_\varphi^2}{2r_c^2} - \Omega_{bar} p_\varphi + V(r, \varphi) = E_J$$

where $r_c$ is the root of the equation $\partial V_{eff}/\partial r = 0$ at $r = r_c$ (see section 1.4). The above limiting curves are similar in shape to the usual curves of zero velocity, but

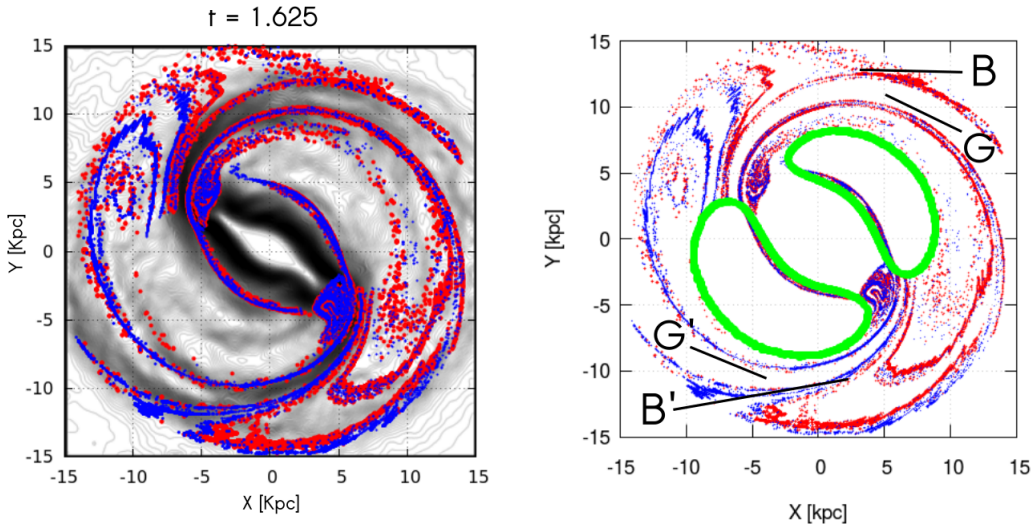


**Figure 3.10**: *Left: comparison between the Sobel-Feldman edge detection image of the N-body disc at $t = 1.625$ Gyr and the corresponding apocentric unstable invariant manifolds $\mathcal{W}^{UA}_{PL1}$ (red) and $\mathcal{W}^{UA}_{PL2}$ (blue), see text for definitions. Besides the overall agreement in the 'grand design' forms of spirals, the patterns formed by the manifolds clearly interpret also several secondary features of the observed patterns formed by the N-body disc beyond the end of the bar, such as 'gaps', 'bridges', 'ring-like structures' and 'bifurcations' of secondary spiral arms (see text for details). Right: the apocentric manifolds shown together with the limiting curves of the apocentric surface of section (green), and with the corresponding bridges and gaps marked (compare with Fig. 3.9).*

provide the most stringent limits for the apocentric surface of section (see Tsoutsis et al. (2009)).

In Fig. 3.9 the manifolds' lobes from $PL_1$ and $PL_2$ encircle the corresponding limiting curves. However, despite the lack of energetic barrier, we observe that the uppermost manifold lobes do not fill the whole area around the limiting curves, but perform a number of oscillations leaving narrow gaps ( $G, G'$) in the surface of section. This behavior of the manifolds is dictated by basic rules of dynamics, which assert that the manifold lobes of the same or different periodic orbits cannot intersect each other. In this way, we observe that the lobes of the manifold emanating from $PL_2$ approach the manifold emanating from $PL_1$ in the area marked $B$, but do not intersect it, leaving instead a gap $G$. Similarly, the lobes of the manifold from $PL_1$ approach the manifold from $PL_2$ in the area $B'$, leaving a gap $G'$. These features have a specific morphological correspondence in physical space, as shown below. Let us note also that the level of Jacobi energy of the surface of section in Fig. 3.9 is close to the median of the entire distribution of the simulation's particles in chaotic orbits, which is consistent with the general expectation that most particles supporting chaotic spirals should be distributed in the interval of energies between $E_{J,L1}$ and $E_{J,L4}$ (Patsis (2006), Tsoutsis et al. (2008))).

Figure 3.10 shows the comparison between the disc morphology and the apocentric manifolds in the configuration space at the snapshot $t = 1.625$ Gyr. The Sobel-Feldman image of the N-body disc shows a nearly bi-symmetric set of spirals, along with secondary ring and spiral features beyond the bar. We observe that the outer branch of the manifolds supports the spiral arms, while the inner branch of the manifolds supports the outer shell of the bar. We can also locate the morphological features of 'gaps' and 'bridges', which we pbserved in the phase space in Fig. 3.9. The gaps $G$ and $G'$ appear as narrow zones separating the manifolds at the bridges $B$, $B'$. In these 'bridges', the manifold emanating from the region of $L_1$ approaches, in a nearly-tangent direction, the exterior side of the manifold emanating from the

region of the Lagrangian point $L_2$, and vice versa. The approach takes place via several oscillations of the manifolds in space, forming patterns recognized in the plot as bundles of preferential directions occupied by the manifolds. Such bundles mostly form spiral patterns, while breaks, or 'bifurcations', are also observed, splitting in two some of these bundles. We observe that most of the morphological features of the apocentric manifolds have their counterparts in the Sobel-Feldman image of the real patterns of the N-body disc. Finally, the manifolds $\mathcal{W}^{UA}_{PL1}$ and $\mathcal{W}^{UA}_{PL2}$ exhibit some obvious lopesidedness, which is manifested also in the form of the limiting curves of the apocentric surface of section as projected in physical space. This effect implies that the outflow of particles in chaotic orbits, in the directions indicated by the manifolds, is not symmetric with respect to the disc center. Since the phase space outside corotation is open to escapes, particles escaping in chaotic orbits carry with them linear momentum with a distribution of orientations anisotropic with respect to the center. The consequences of this fact are discussed in the next section.

## 3.3 Secular evolution and manifold spirals

The various Fourier modes connected to spiral and other non-axisymmetric features beyond the bar in the galactic disc evolve in time along with the bar's secular evolution. We observe how the secular evolution makes the bar slowing down in our simulation and how the manifolds follow the vividly evolving structures in the disc. We note that the manifolds $\mathcal{W}^{UA}_{PL1}$ and $\mathcal{W}^{UA}_{PL2}$ are geometric objects, which can be defined at any time snapshot. Hence, these objects can be compared to the *shape*, but not to the *amplitude* of observed non-axisymmetric features. In this section we first examine the question of how spirals and other non-axisymmetric features are excited during the time evolution of the N-body system, and which mechanisms are responsible for the maintainance of appreciable levels of recurrent non-axisymmetric activity in the disc besides the bar. Then, we test the evolution of the manifolds along with the observed morphologies by comparing, for different snapshots representative of the entire secular evolution, the patterns constructed by the invariant manifolds and the observed morphologies in the disc.

### 3.3.1 Bar spin-down

Signs of secular evolution are conspicuous in the simulation. A basic manifestation of secular evolution in the disc is the bar's spin down, as shown in Fig. 3.11. The cyan solid curve in Fig. 3.11 represents an exponential decay law fitting to the decay of the values of the bar's angular velocity. The fitting is given by $\Omega_{bar}(t) = \Omega_0 - \left(1 - \Omega_1 \exp\left(-\frac{t-t_0}{t_d}\right)\right)$, with $\Omega_0 = 42$ km/sec/kpc, $\Omega_1 = 11$ km/sec/kpc, $t_0 = 1.625$ Gyr, $t_d = 2$ Gyr. The resonances also undergo an outward slow displacement as a result of the Eq. (3.6). As shown in Fig. 3.11 the co-rotation resonance in our simulation is dispaced gradually from $R_{CR} \simeq 6.5$ kpc immediately after the bar formation to $R_{CR} \simeq 7.5$ kpc at the end of the simulation, and the ILR and OLR radii from $R_{ILR} \simeq 1.75$ kpc, $R_{OLR} \simeq 9.5$ kpc to $R_{ILR} \simeq 3.1$ kpc, $R_{OLR} \simeq 12$ kpc. These secular evolution phenomena are disccussed in detail in section 1.13.

The bar's spin down is caused in our simulation also by the following factors: i) the outward transfer of angular momentum due to the spiral waves generated at the end of the bar. In fact, a portion of particles traveling with these waves are in escaping orbits. Thus, as they escape the system they carry with them energy, as well as linear and angular momentum (see below), ii) transfer of angular momentum due to the dynamical friction of the bar with the dark halo (see Debattista & Sellwood (1988),

Debattista & Sellwood (2000), Athanassoula (2002), Athanassoula & Misiriotis (2002)). In order to investigate the bar halo interaction we produced the Fourier decomposition of the non-axisymmetric excess density for the halo particles contained in a planar slab of thickness $\Delta z = 0.5$ kpc centered around the disc center of mass, at several times of our simulation (Fig. 3.12)). As it is shown in Fig. 3.12), the bar-halo interaction is accompanied by the generation of a bar-spiral response in the *halo* particles immediately after the formation of the bar (Fig. 3.12)). This response can reach significant $m = 2$ amplitude (up to $C_2 \sim 0.4$ at radii associated with the bar, and $C_2 \sim 0.2$ at radii associated with the spiral arms). However, after a time $t \sim 2.2$ Gyr it is observed to fade to rather negligible amplitudes.

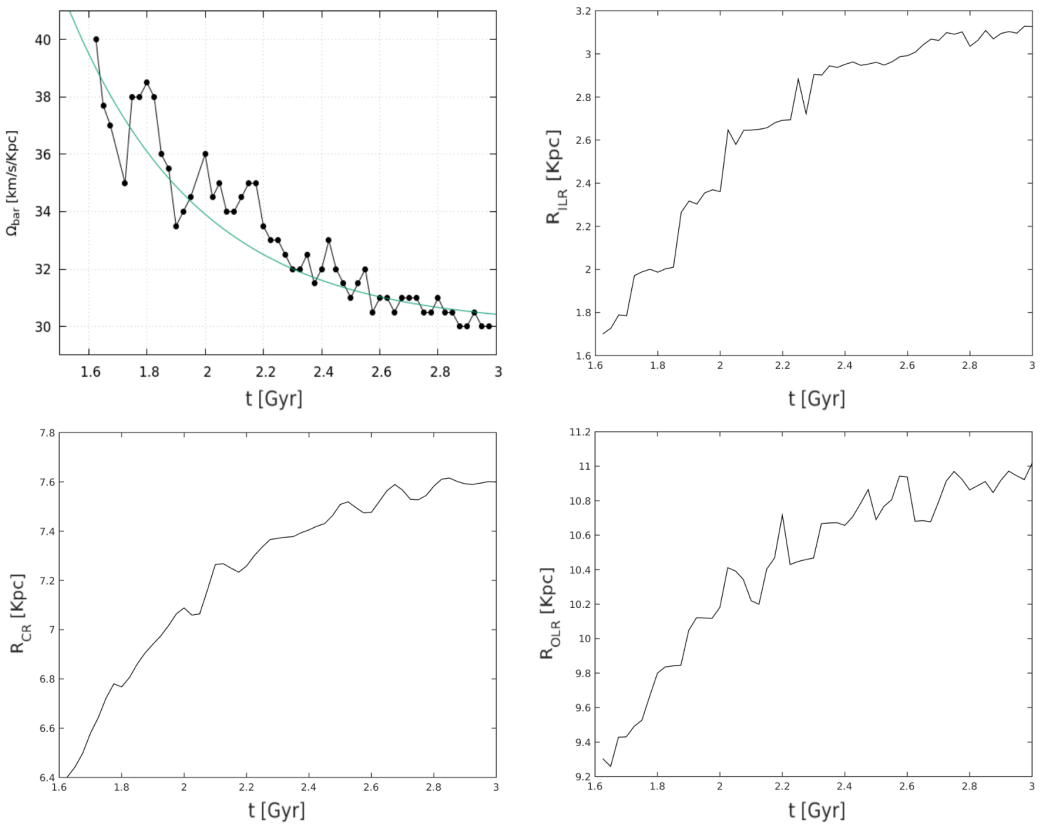


**Figure 3.11**: *Top left: Time evolution of the bar's pattern speed. The cyan solid curve represents an exponential decay law fitting, given by* $\Omega_{bar}(t) = \Omega_0 - \left(1 - \Omega_1 \exp\left(-\frac{t-t_0}{t_d}\right)\right)$, *with* $\Omega_0 = 42$ *km/sec/kpc*, $\Omega_1 = 11$ *km/sec/kpc*, $t_0 = 1.625$ *Gyr*, $t_d = 2$ *Gyr. The remaining panels show the time evolution of the radii where the basic disc resonances occur with pattern speed equal to* $\Omega_{bar}$, *namely* $R_{ILR}$ *(top right),* $R_{CR}$ *(down left) and* $R_{OLR}$ *(down right).*

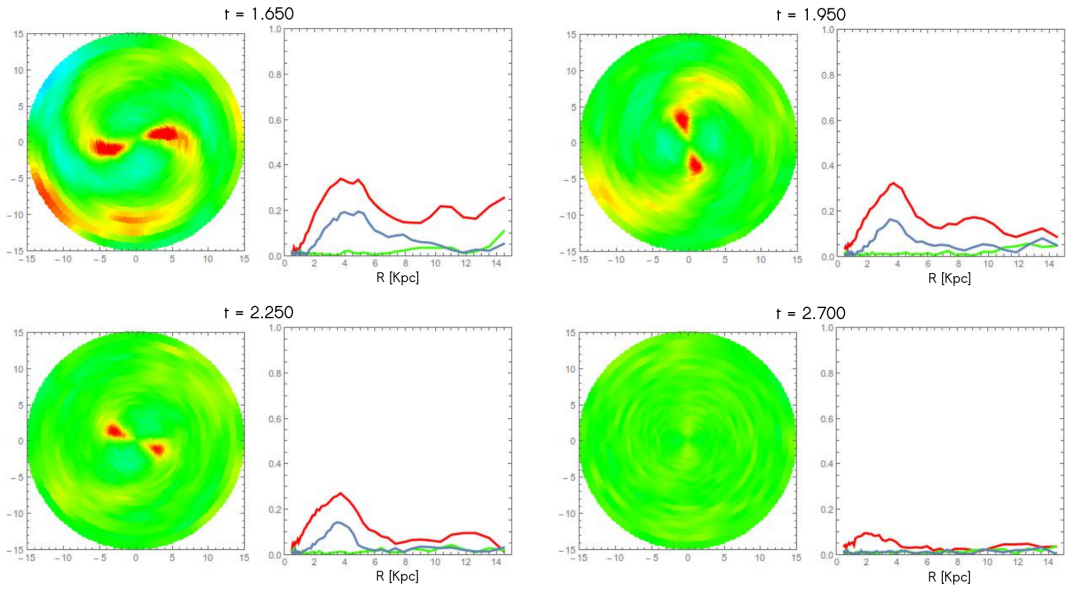


**Figure 3.12**: *Fourier decomposition of the non-axisymmetric excess density for the halo particles contained in a planar slab of thickness $\Delta z = 0.5$ kpc centered around the disc center of mass, at the times $t = 1.650$ Gyr (top left block), $t = 1.95$ Gyr (top right block), $t = 2.25$ Gyr (down left block), and $t = 2.7$ Gyr (down right block). Left panel in each block: non-axisymmetric density excess map. Right panel in each block: Fourier amplitudes $C_m(R)$ as function of $R$ for the modes $m = 2$ (red), $m = 3$ (green) and $m = 4$ (blue).*

### 3.3.2 Incidents of spiral and other non-axisymmetric activity

In this subsection we examine the incidents of spiral activity and we assume that they show an oscillating profile as they evolve in time. A quantification of the $m = 2$ oscillations associated with spiral and other non-axisymmetric activity in the disc can be done via the time variations of the Fourier amplitude $C_2(R)$ at specific radii $R$ (see Eq. (3.3)).

We examine the time variation of $C_2(R)$ for different radii (see the top panel of Fig. 3.13). An inner group of $C_2(R)$ curves, for $R = 3, 4$ and 5 kpc, correspond to the amplitude of the $m = 2$ mode at radii within the range of the bar's major axis. The bar growth is observed to continue up to $t = 1.6$ Gyr, leading to $m = 2$ bar amplitudes larger than unity. After this growth phase, the bar $m = 2$ mode stabilizes in a time interval between $t = 1.6$ and $t = 2.1$ Gyr, which overlaps with the evolution of the buckling instability. After a small in size but abrupt drop at $t = 2.1$, the bar's amplitude starts undergoing slow decay, which lasts for the whole remaining 2 Gyr of the simulation, but keeping always a value of the order of unity. The $m = 2$ amplitude in general falls with the radial distance $R$ at intermediate distances between CR and OLR, but it tends to stabilize to a mean level $\sim 0.2$ in an annulus of radii $8 \leq R[kpc] \leq R_{OLR}$.

The outer group of $C_2(R)$ curves corresponds to distances $R = 8, 9, 10$ kpc (solid red curves in the top panel of Fig. 3.13)), where the spiral arms in the disc are located. We observe that, after the bar formation, the amplitude $C_2$ within this annulus undergoes time oscillations which are nearly in-phase for all radii within the annulus. We observe a local maximum of these oscillations at approximately $t \sim 3$ Gyr, where the $C_2$ amplitude exceeds the value 0.2. Afterwars the oscillations become smaller and they do not exceed the value 0.2. As exemplified below, all consequent peaks of the $C_2$ mode found in the time interval $1.5 \leq t[Gyr] \leq 4$ are connected with 'incidents' of non-axisymmetric activity in the outer parts of the disc. In order

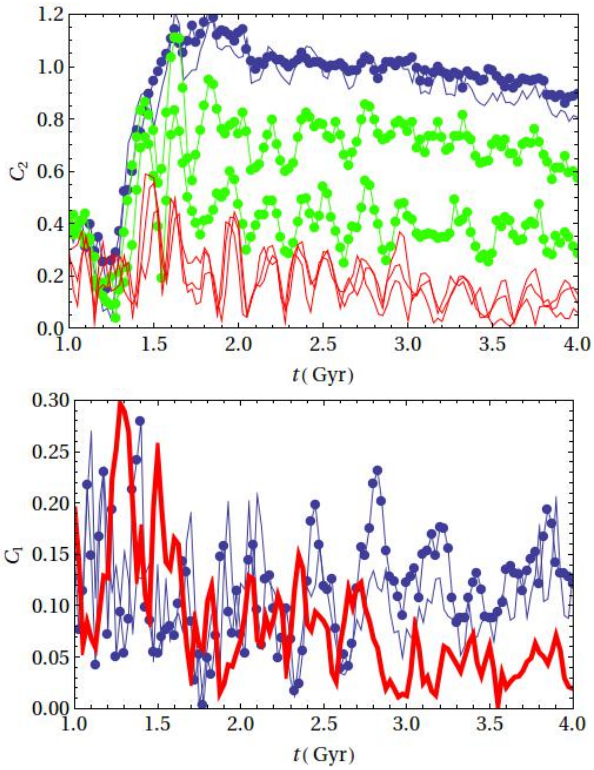


**Figure 3.13**: *(Top panel) Time evolution of the $m = 2$ Fourier amplitude $C_2$ in the time interval $1 \leq t[Gyr] \leq 4$. The value of $C_2$ is shown at the distances $R = 3, 4$ kpc (dotted blue), $R = 5$ kpc (solid line, blue), $R = 6, 7$ kpc (dotted green), and $R = 8, 9, 10$ kpc (solid red). (Bottom panel) Time evolution of the $m = 1$ Fourier amplitude $C_1$ at $R = 3$ kpc (dotted blue), $R = 4$ kpc, (solid blue), and $R = 12$ kpc (thick solid red).*

to estimate the period and the amplitude of these oscillations, we take the mean $\overline{C}_2$ of the values of $C_2$ at distances corresponding to the three lowermost curves in the top panel of Fig. 3.13. Through this method we locate the incidents by considering the times when the mean $\overline{C}_2$ reaches the maximum amplitude. We thus identify a sequence of incidents around the times:

$$t[Gyr]^{(incident)} = 1.625, 1.8, 1.95, 2.2, 2.375, 2.525, 2.725, 2.950, 3.1, 3.325, 3.75, 3.95. \tag{3.7}$$

By the above sequence, an approximate period $T \approx 0.2$ Gyr can be deduced, but with large fluctuations $\Delta T \sim 0.1$ Gyr. It is intriguing to note that the bar, in the same time interval, has a pattern speed $\Omega_{bar} \approx 40$ km/sec/kpc, i.e., period $T_{bar} \approx 0.15$ Gyr at the starting time of the sequence, and $\Omega_{bar} \approx 30$ km/sec/kpc, i.e., period $T_{bar} \approx 0.2$ Gyr at the ending time of the sequence. Thus, the $m = 2$ incidents of the sequence (3.7) seem to be roughly in resonance with the bar. However, in order to investigate the coupling between the bar and oscillations of the outer $m = 2$ modes, one must also remark that the bar also exhibits some extra phenomena relating to the time variations of the $m = 1$ mode.

As seen in the bottom panel of Fig. 3.13, after the bar's growth stabilizes at $t = 1.6$ Gyr important $m = 1$ oscillations with an amplitude exceeding the value of $C_1 \sim 0.1$, at distances inside the bar's length. In the time interval between $t = 2$ Gyr and $t = 3$ Gyr these oscillations have an approximate period $T \sim 0.4$ Gyr. These osxcillations show no significant decay in time over the whole simulation. Oscillations $m = 1$ appear also in the outer disc, but they are not in phase with those of the inner disc and they decay in time.

In order to observe the evolution and the periodicity of the incidents of the non-

asxisymmetric activity we construct density excess maps, and the corresponding radial profiles of the Fourier modes $m = 1, 2, 3, 4$, for different times of the simulation. We can also see how these incidents of non-axisymmetric activity appear to affect the disc's morphology beyond the bar. Based on phenomenological criteria, we distinguish two types of incidents, exemplified in Figs. 3.14 and 3.15 respectively, as follows:

-*Incidents of inner origin:* an incident of inner origin corresponds morphologically to a spiral wave emanating from the end of the bar, and travelling outwards, until it becomes gradually detached from the bar. An example is given in the sequence of left panels of Fig. 3.14, showing the density excess maps at nine snapshots around the time $t = 2.2$, which belongs to the sequence (3.7). In Fig. 3.14 a local maximum in $C_2(r)$ curve rises inside the corotation, and then it gradually propagates to the outer parts of the disc. This phenomenon corresponds to an outwards 'emission' of the spiral wave from the bar, which is evident after $t = 2.15$. A similar phenomenon, but to lesser extent, appears in the $m = 4$ mode. Notice also the significant rise of the $m = 1$ and $m = 3$ modes well inside the bar (at radii $R < 5$ kpc) at the initial phase of the incident. At earlier times, one observes the appearance of small *leading* extensions of the bar, so that the whole incident is reminiscent of swing amplification. The creation of a leading component can be associated with flow of material approaching the bar in the leading direction by moving along outer families of periodic orbits such as the 2:1 family (Patsis; private communication). Finally, the spiral wave starts fading out when it becomes detached from the bar.

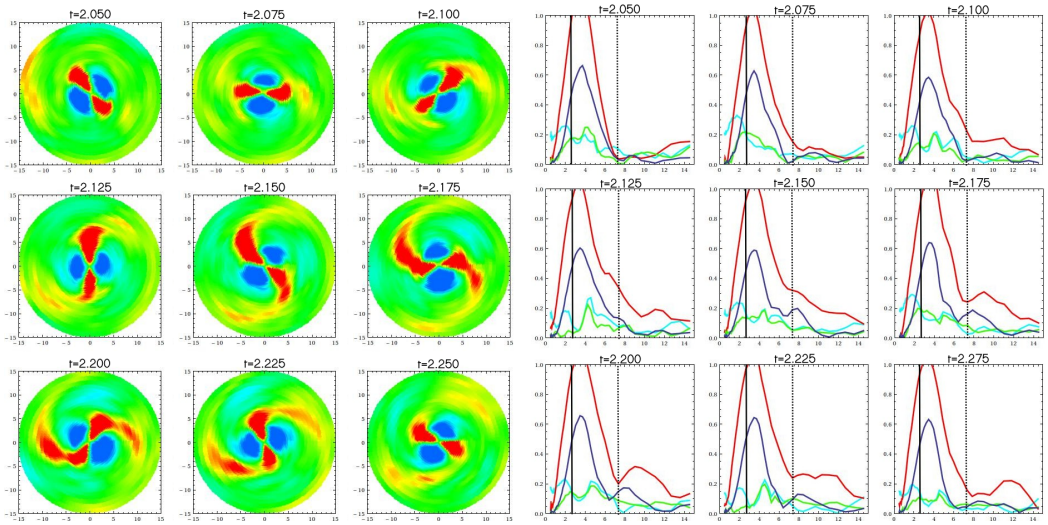


**Figure 3.14**: *Left: Snapshots of the density excess color map of the disc at the indicated times. An 'incident of inner origin' occurs, whose maximum, as measured in the $C_2$ average value in the outer disc, takes place around $t = 2.2$. Right: the profiles of the Fourier amplitudes $C_m$ as function of the radial distance $R$ at the same snapshots, for the modes $m = 1$ (cyan), $m = 2$ (red), $m = 3$ (green), and $m = 4$ (blue). The dotted vertical line marks the position of the bar's co-rotation. The incident appears mostly as an excitation of the $m = 2$ mode inside co-rotation, starting at $t = 2.075$, which propagates outwards (to larger $R$) at subsequent times.*

- *Incidents of outer origin:* an incident of outer origin corresponds morphologically to a rise of the of the $C_2(r)$ curve in the outer parts of the disc, as shown in Fig. 3.15. Contrary to incidents of inner origin, in those of outer origin the excitation of the $m = 2$ mode takes place entirely *outside* corotation, and propagates both inwards and outwards, apparently being reflected at corotation. Notice also, again, the significant rise of the $m = 1$ and $m = 3$ modes inside the bar at the initial phase of the incident (at radii $R < 5$ kpc). The left panels in Fig. 3.15 indicate that the $m = 2$ perturbation takes place at radial distances beyond $r = 12$ kpc, initially traveling inwards, and then appearing to be reflected at corotation (at $t = 2.95$) whereby the disturbance

appears to travel outwards. Note that this reflection provides the best criterion to characterize incidents of outer origin, since weak spiral extensions in the end of the bar may always be present, and hence appear to connect morphologically with the disturbance after the latter one reaches corotation.

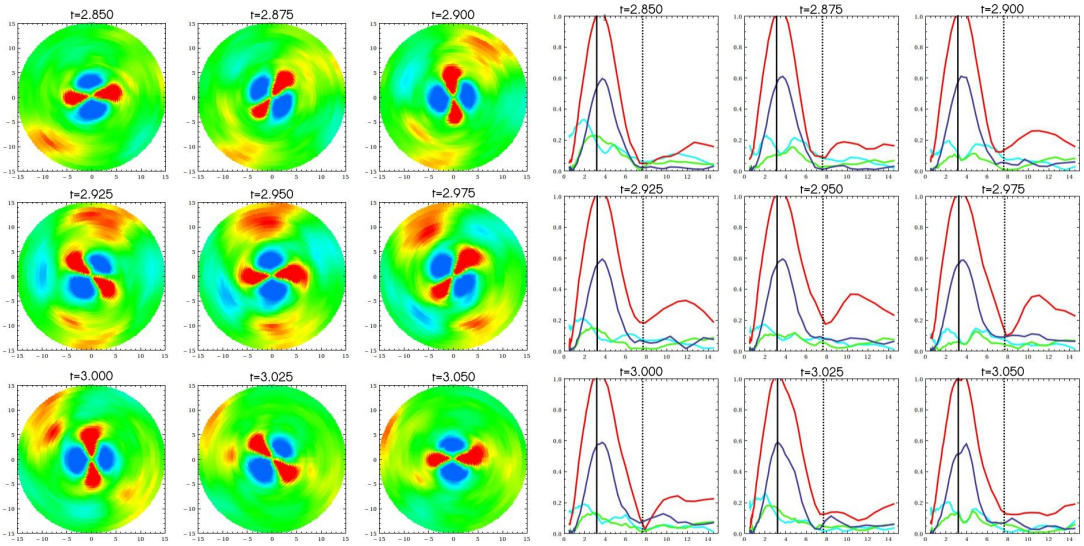


**Figure 3.15**: *Left: Snapshots of the density excess color map of the disc at the indicated times. An 'incident of outer origin' occurs around $t = 2.95$. Right: the profiles of the Fourier amplitudes $C_m$ at the same snapshots ($m = 1$ cyan, $m = 2$ red, $m = 3$ green, $m = 4$ blue). The dotted vertical line marks the position of the bar's co-rotation.*

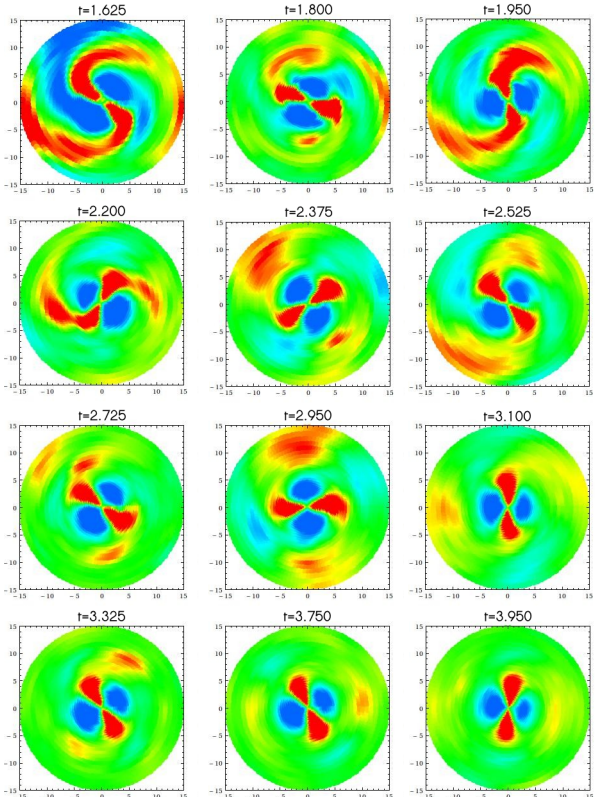


**Figure 3.16**: *Non-axisymmetric density excess image of the disc for all snapshots corresponding to the maxima of consecutive incidents of non-axisymmetric activity, taking place at the sequence of times given in Eq. (3.7).*

We then accumulate the density excess maps of the disc of all the snapshots

belonging to the sequence (3.7) in Fig. 3.16, corresponding to incidents of spiral activity and we attempt to distingish if they are of inner or outer origin. Incidents of inner origin are clearly associated with the time snapshots $t = 1.625$, $t = 1.95$, $t = 2.2$, $t = 2.725$ Gyr, while incidents of outer origin are associated to the snapshots $t = 2.375$, $t = 2.95$, $t = 3.75$, and $t = 3.95$ Gyr. On the other hand, the classification, either by the morphological criterion, or by the criterion of reflection of the $m = 2$ Fourier transform, is unclear for the incidents taking place at the snapshots $t = 1.8$, $t = 2.525$, $t = 3.1$, and $3.325$ Gyr. In general, most incidents of inner origin, which are those mainly connected with spiral activity, take place in the interval $1.6 < t[Gyr] < 3$, while incidents of outer origin are observed throughout the whole simulation time span. Finally, we observe that the disc overall becomes less responsive to non-axisymmetric perturbations as the time goes on, with a transition from stronger to weaker responses discernible at a time $t \approx 3$ Gyr.

### 3.3.3 Manifold spirals and the time evolution of non-axisymmetric patterns in the disc

One main question that arises from the above study of the N-body simulation is to what extent the response of the disc to internal or external perturbations is manifold-driven, as well as how a manifold-driven response can be reconciled with the presence of multiple pattern frequencies in the disc. In order to answer these questions we reproduce the apocentric manifolds $\mathcal{W}^{UA}_{PL1,2}$ for consecutive snapshots of the simulation (as in section 3.2) and we compare them with the morphologies of the disc both in minima and maxima of the non-axisymmetric activity.

As in Fig. 3.7 for snapshot $1.625$ Gyr, we reproduce the Sobel-Feldman images of the disc for several times of the simulation (see Fig. 3.17) in order to recover patterns which are quite fuzzy in simple surface-density processed images of the disc and distinguish the incidents of spiral activity in the pure N-body images. In Fig. 3.13 we observe nearly in-phase oscillations of the amplitude $C_2$ of $m = 2$ structures in the outer parts of the disc. We focus on such oscillations in the time interval $1.8 < t[Gyr] < 2.8$, in which we mostly observe incidents of non-axisymmetric activity of inner origin, i.e., connected with an enhancing of the spiral structure. To be more precise on the times of occurence of such incidents with respect to the approximate sequence (3.7), we choose a reference radius $R = 9$ kpc which is between the CR and OLR at all snapshots. Six consecutive local maxima and six minima of $C_2[9\text{kpc}]$ occur at the sequence of times

$$t^{(max,9\text{kpc})}[\text{Gyr}] = 1.8, 1.95, 2.2, 2.375, 2.525, 2.725$$

and minima at the sequence of times

$$t^{(min,9\text{kpc})}[\text{Gyr}] = 1.875, 2.05, 2.275, 2.425, 2.625, 2.85 \quad .$$

The left panels of Figure 3.18 show the Sobel-Feldman images of the disc in the above times, alternating between a maximum and a minimum of $C_2[9\text{kpc}]$. Within a timescale as short as one bar's period one finds vivid variations of the patterns identified in the disc beyond the bar. The Sobel-Feldman algorithm enables us to identify better the maxima and minima of the spiral activity. In particular, some form of spiral activity is identifiable in all snapshots, although the morphology of these spirals (number of arms, pitch angle, radial extent, luminosity etc) seem to rapidly change. This fact alone indicates that these spirals cannot be considered as one rigid pattern evolving with nearly fixed pattern speed. We note also that, besides

shape-evolving spiral patterns, we distinguish in these plots other features commonly observed in barred galaxies, which also appear and disappear in a recurrent form, as, for example, inner rings (as in the panels for $t = 1.8$ Gyr or $t = 2.375$ Gyr) or outer rings (e.g. at $t = 2.95$ Gyr in Fig. 3.17).

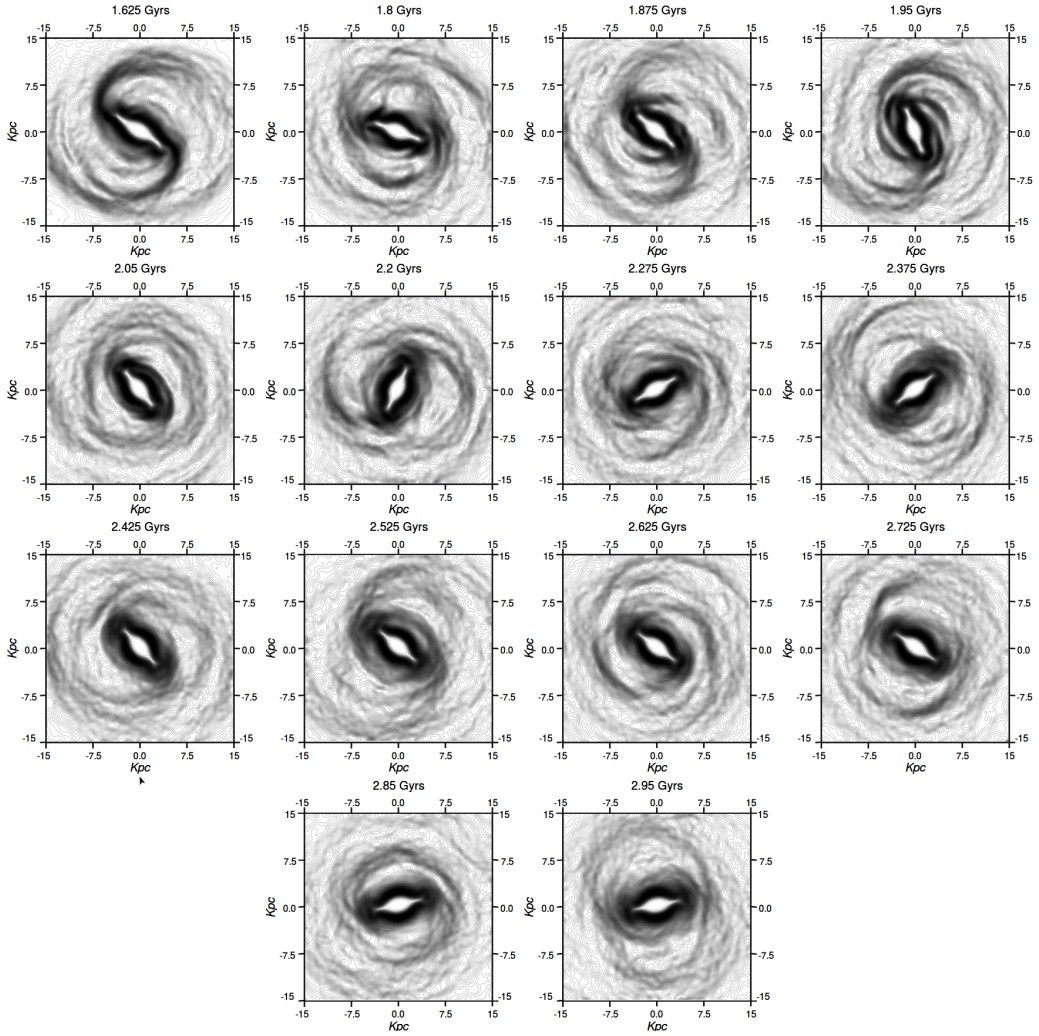


**Figure 3.17**: *The Sobel-Feldman images of the disc in fourteen snapshots corresponding to the alternating local maxima and minima of $C_2[9kpc]$ (except for the minimum at $t = 1.725$ Gyr, see text). Some spiral pattern is identifiable in all these plots, except for the last one at $t = 2.95$, a time which coincides with the maximum of an 'outer incident'. Inner ring, inner spiral or outer ring structures appear in several of these snapshots.*

Figure 3.18 shows the comparison between the Sobel-Feldman images of the disc in the above snapshots and the corresponding apocentric manifolds, computed in all cases as described in section 1.11.2. In particular the right panels of Figure 3.18 are obtained by a superposition of the apocentric manifolds calculated at the corresponding time of the simulation on top of the same Sobel- Feldman images as in the left panels of Fig. 3.18. The manifolds show an agreement with the Sobel-Feldman images in shape and orientation of the non-axisymmetric structures. The level of coincidence of the manifolds with the non-axisymmetric patterns detected by the Sobel-Feldman algorithm varies between snapshots. By (rather subjective) visual comparison, one distinguishes snapshots of generally good agreement (e.g. $t = 1.95, 2.275$ or $2.725$ Gyr, and other ones of worse agreement (e.g. $t = 2.425, 2.625$ Gyr). The following are some basic remarks regarding this comparison:

- The manifolds and the Sobel-Feldman detected patterns exhibit similar degrees

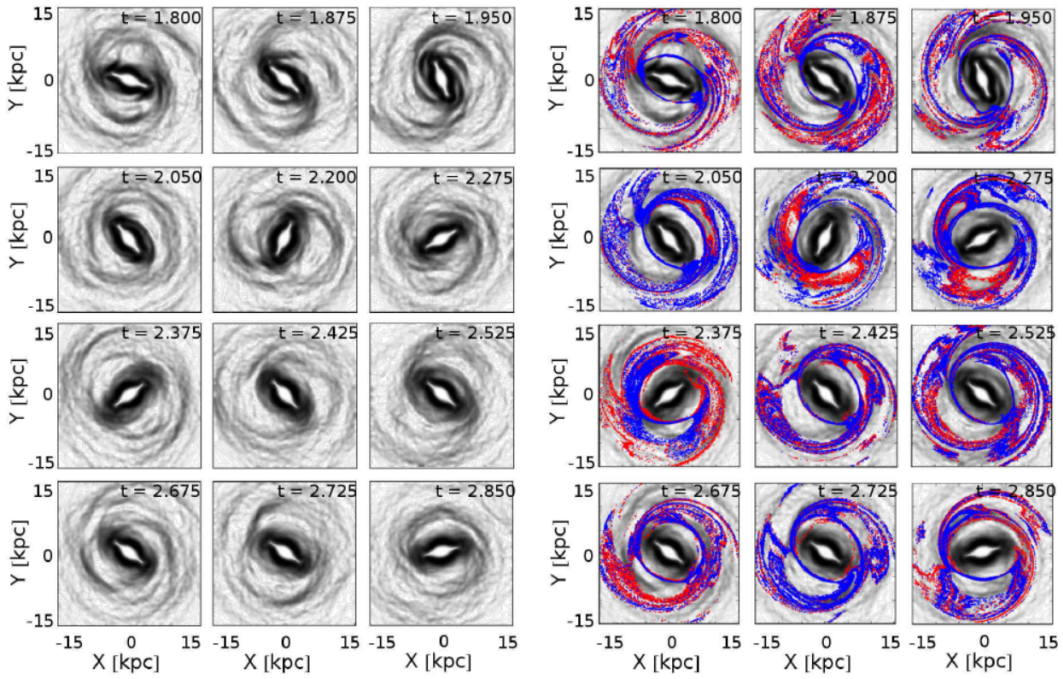


**Figure 3.18**: *Left: Sobel-Feldman images of the disc in twelve snapshotstext). Right: the apocentric manifolds for the same snapshots (colours as in Fig. 3.10), compared to the Sobel-Feldman detected patterns in the disc plane for the times of the sequence of successive maxima and minima of* $C_2[9kpc]$.

of complexity. In the case of the invariant manifolds, as explained in section 3.2 this complexity is associated with the chaotic structure of the phase space, which leads to the effect of homoclinic manifold dynamics. In the disc plane, the homoclinic lobes appear as oscillations of the patterns formed by the manifolds. Also, they result in the systematic appearance of the features called gaps, bridges and bifurcations, which are commonly recognized in nearly all panels of Fig. 3.18. Such features are also present in the Sobel-Feldman detected patterns in the disc. We note that gaps and bridges can be recognized also in plots of 'flux-tube' manifods (see Athanassoula (2012)), but they are better visualized using the apocentric manifolds.

- In nearly all patterns, here are small phase differences ($\leq 5^0$ between some manifold lobes and the corresponding (e.g. $t = 2.375$ Gyr), the patterns formed by the invariant manifolds agree in shape, but are in phase difference with the Sobel-Feldman detected patterns. This might be a dynamical phenomenon (disc response has delay with respect to the manifolds), but it may also be an artefact of the visualization by the apocentric manifolds, since the disc's local density maxima do not necessarily coincide with the individual orbits' apocenters (Tsoutsis et al. (2008)).

- In all these panels, for computational convenience we just choose one value of the Jacobi constant for computing the invariant manifolds, selected near the median of the distribution of particle Jacobi energies in the corotation region. Despite the fact that the invariant manifolds retain a rather robust pattern against small changes of the Jacobi energy (Tsoutsis et al. (2008)), small variations in shape, not captured in Fig. 3.18, are expected at energies different from the chosen ones. Superposed one on top of the other, these manifolds form a more robust spiral pattern called 'manifold coalescence' (Tsoutsis et al. (2008)). The manifold coallesence is a better representation of chaotic dynamics in the co-rotation zone than the manifolds of any

single family. Nevertheless, its computation for many snapshots is a voluminous work extending outside the scope of a manifold survey as in Fig. 3.18.

- Finally, although Fig. 3.18 shows a clear correlation bewteen manifolds and Sobel-Feldman detected non-axisymmetric patterns, not all patterns in the disc need necessarily be linked to the manifolds. In fact, structures such as outer rings or slowly rotating outer spirals may not be connected with chaotic flows at all, and be, instead, manifestations of a form of density wave theory using regular orbits (see, for example, Boonyasait et al. (2005), Struck (2015)).

### 3.3.4 Consistency with multiple pattern speeds

It is well known that most observations and N-body simulations of barred spiral galaxies give evidence for multiple pattern speeds in the galactic disc, as it is analysed in the subsection 1.12.1. In particular, the spiral arms rotate at a different pattern speed than the one of the bar. This is also an argument against manifold-supported spirals (see, for example, Speights & Rooke (2016)). In the paper of Efthymiopoulos et al. (2019), which we particularly analyse, however, the manifolds are computed with the assumption that the whole galactic structure corotates with a single pattern speed, the pattern speed of the bar and as it is shown in Fig. 3.18 they are in good agreement with the N-body morphological features. Note also that measured pattern speeds can be affected both by the change in morphology and by the transport of material along invariant manifolds (Athanassoula (2012).

In order to quantify the time evolution of the located pattern speeds in our N-body experiment, we produce radial profiles of the angular velocity of the $m = 2$ mode, as in Fig. 3.8, for different times of the simulation. Figure 3.19 shows these profiles for the same snapshots as in Fig. 3.18, corresponding to the consecutive maxima and minima of the $C_2[9\text{kpc}]$ amplitude. In all these snapshots, the inner plateau that is observed corresponds to a nearly constant value of $\Omega_2(R)$ ans it marks the pattern speed of the bar. This plateau extends up to a distance equal to $\sim 0.6 - 0.8$ the bar's co-rotation radius. However, important fluctuations of the pattern speed $\Omega_2$ beyond the corotation radius are observed at all time snapshots after $t = 1.8$ Gyr. In particular, these fluctuations correspond to the alterations from maxima to minima of the $m = 2$ spiral activity. Examining more carefully the fluctuating part of the $\Omega_2(R)$ profile between CR and the OLR, the following evolution pattern is identified: at the snapshots identified by the maxima of $C_2[9\text{kpc}]$ (denoted by 'max' in Fig. 3.19), the profile of $\Omega_2$, after a possible hump near corotation, starts decaying, but tends to stabilize again to a value $\Omega_2 < \Omega_{bar}$ forming a nearly outer plateau as it approaches the OLR . This outer plateau may reveal the coexistence of a second pattern speed in the galactic disc. The values of this second 'plateau' are estimated at $\sim 20$ km/sec/kpc, which are a factor $1.5-2$ smaller than the (time decaying) value of $\Omega_{bar}$. However, the second plateau disappears at the minima of $C_2[9\text{kpc}]$ (denoted by 'min' in Fig. 3.19). In these minima, the $\Omega_2$ profile beyond corotation becomes constantly decaying. Most notably, the decay leads to $\Omega_2 \approx 0$ at a radius $R$ found always to be very close to the OLR radius. Note that decaying profiles of the pattern speeds are reported in observations (e.g Speights & Westpfahl (2012), Speights & Rooke (2016)). It is of interest to check whether the criterion of where the decaying curve $\Omega_2(R)$ terminates can be exploited in real observations for the location of resonances. A systematic study of this topic is proposed.

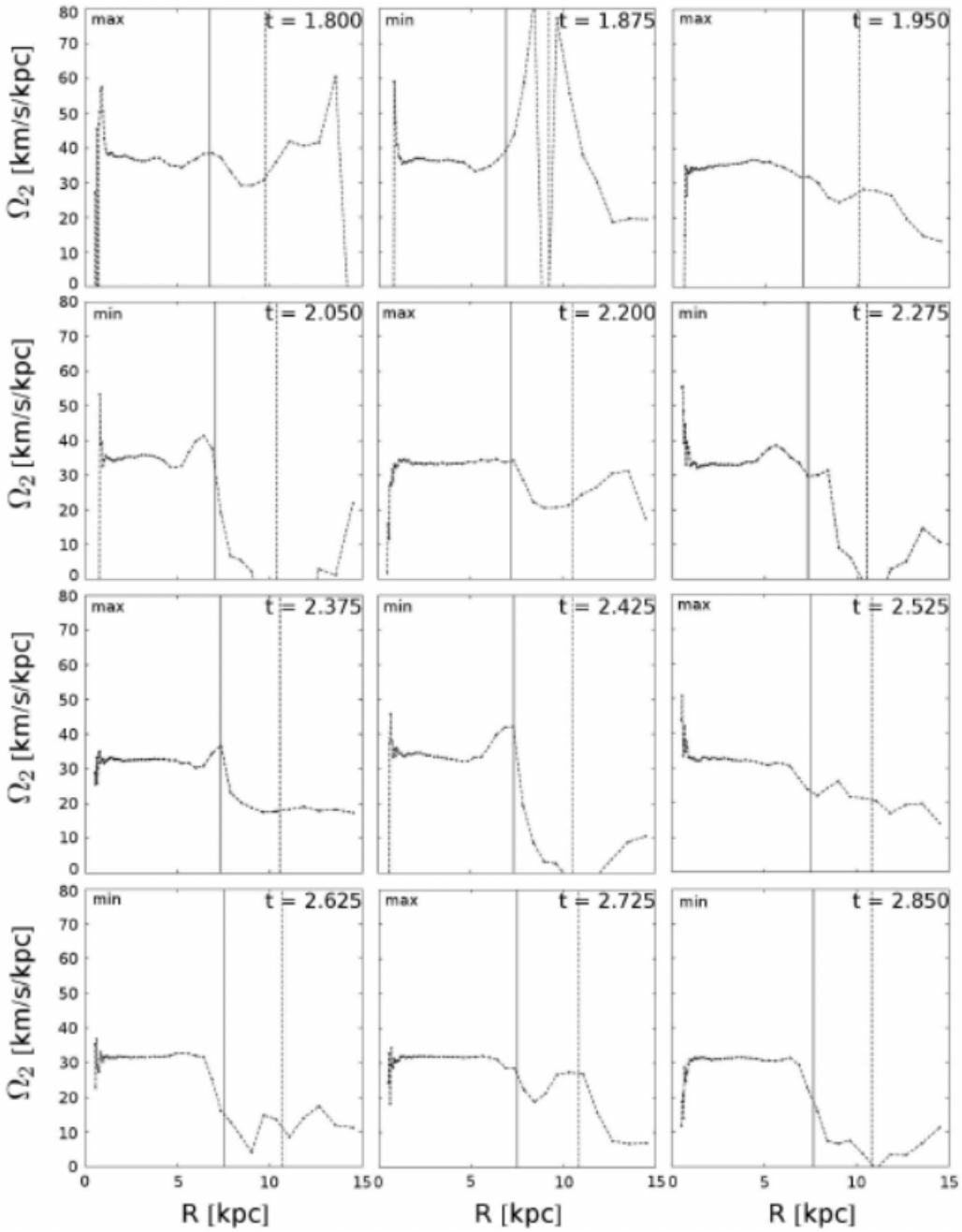


**Figure 3.19**: *The pattern speed of the $m = 2$ mode (Eq. (3.5)) as function of the distance $R$ from the disc center at the same snapshots as in Fig. 3.18. The inner plateau at distances between 2 kpc and 4 kpc determines the bar pattern speed. The two vertical lines in each panel mark the position of corotation and the OLR. The value $\Omega_2(R)$ undergoes fluctuations in the interval of distances between CR and OLR, which are co-related with whether we are close to a minimum or maximum of the $m = 2$ mode in this interval (see text).*

In the previous subsection we observed in Fig. 3.18 no appreciable difference in the levels of agreement between manifolds and the disc morphologies depending on whether we are at a maximum or min- imum of $C_2[9kpc]$. As a result, the level of coincidence of the manifolds to the observed N- body morphologies isindependent of the variability of the pattern speeds beyond the bar. One may remark, in this respect, that multiple patterns enhance chaos (Quillen (2003), Minchev & Quillen (2006)) and thus render more particles' orbits ruled by manifold dynamics. On the other hand, whether or not the manifolds are populated by sufficiently many particles to

dominate the global patterns in the disc depends on mechanisms able to inject new particles in chaotic orbits. Such mechanisms are distinct from the manifolds.

### 3.3.5 Disc thermalization

Disc thermalisation phenomena play an important role in the evolution of the disc morphologies and in the coherence of the structures. In this subsection we examine the time evolution of the disc's 'temperature', i.e., velocity dispersion profile, which is a crucial factor affecting the disc's responsiveness to all internal or external perturbations as those described in previous subsections. Regarding, in particular, the manifolds, the region of interest is the disc domain between $CR$ and the $OLR$. We quantify disc temperature in an annulus of width $\Delta R$ around the radius $R$ by the radial velocity dispersion $\sigma_R = \sum (V_{R,i} - \mu_R)^2$, where $V_{R,i}$ is the radial velocity of the i-th particle in the annulus and $\mu_R = \sum_i V_{R,i}$. Similar formulas hold for the dispersion in the transverse and vertical velocity components, but they are connected to the radial one via the epicyclic approximation (Binney & Tremaine (2008)).

Figure 3.20 shows the profile $\sigma_R(R)$ at four different times, namely $t = 1.625$, $t = 2$, $t = 2.5$ and $t = 3$ Gyr. The ordinate is in logarithmic scale, thus straight lines indicate exponential scalings with $R$. At $t = 1.625$ Gyr, the dependence of the radial velocity dispersion on $R$ can be approximated by the union of two exponential profiles, one for the inner part of the disc (in the interval $R_{in} \leq R \leq R_{CR}$), with law $\sigma_R \approx \sigma_1 \exp(-(R - R_{in})/R_1)$, with $\sigma_1 \approx 150$ Km/sec, $R_1 \approx 6$ kpc, $R_{in} \approx 2$ kpc, and another for the outer part of the disc ($R > R_{CR}$), with law $\sigma_R \approx \sigma_2 \exp(-(R - R_{CR})/R_2)$, with $\sigma_2 \approx 70$ Km/sec, $R_2 \approx 15$ kpc.

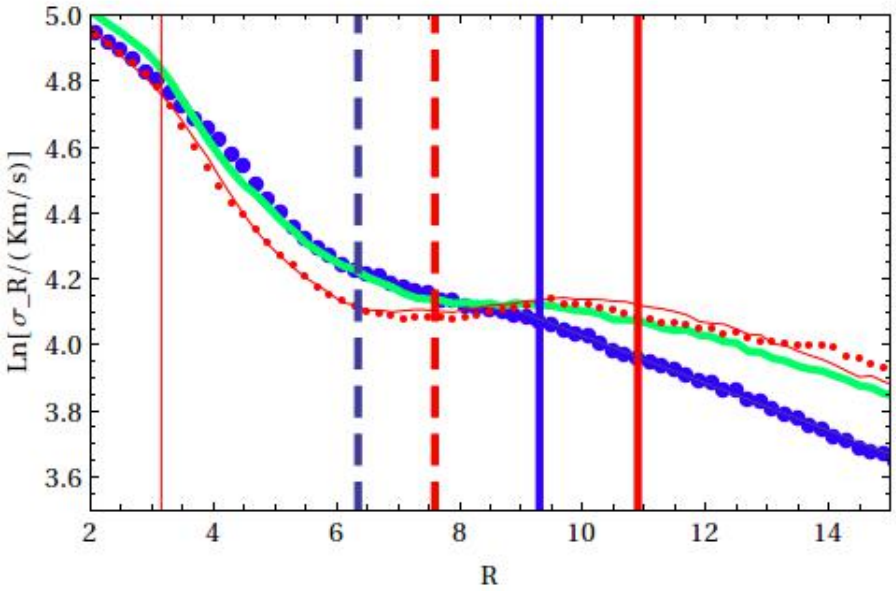


**Figure 3.20**: *Profile of the radial velocity dispersion $\sigma_R(R)$ at four different times, namely $t = 1.625$ Gyr (thick blue with points), $t = 2$ Gyr (thick green solid), $t = 2.5$ Gyr (dotted red) and $t = 3$ Gyr (solid red). The dashed vertical lines mark the position of CR, and the solid vertical lines mark the position of the OLR at $t = 1.625$Gyr (blue) and $t = 3$ Gyr (red) respectively.*

Three more curves in Fig. 3.20, corresponding to $t = 2, 2.5$ and 3 Gyr, show how the profile $\sigma_R$ vs. $R$ evolves in time. At radii beyond the last position of the OLR ($R > 11$ kpc), the velocity dispersion increases in time by a factor between 1.1 and 1.2 in a time interval $\sim 1.5$ Gyr, and the corresponding exponential profile becomes less steep. We notice, however, that the profile becomes nearly horizontal, leading

to an 'isothermalization' (i.e. constant velocity dispersion) in a domain of the disc roughly between $R = 6$ kpc and $R = 11$ kpc. As seen in Fig. 3.20, the inner limit of this domain nearly coincides with the innermost position of CR (at $t = 1.625$ Gyr), while the outer limit nearly coincides with the outermost position of the OLR (at $t = 3$ Gyr) in the considered time interval. One remarks that, as they move outward, these resonances scan nearly completely the domain where the isothermalization takes place. Physically, the domain $R_{CR} < R < R_{OLR}$ is where chaotic motions completely dominate the dynamics. The corresponding particles belong to the well known 'hot population' (Sparke & Sellwood (1987)), whose orbits span the whole domain while recurrently entering also inside corotation. As a result, the strongly chaotic dynamics brinks about an equalization of the velocity dispersion in the whole domain. On the other hand, we observe that the velocity dispersion profile remains practically invariant at distances smaller than the initial position of the ILR (at $\approx 3$ kpc). In fact, this resonance appears to act as a barrier for 'heat' (random kinetic energy) transfer across the disc.

The key remark, regarding the above time evolution, is that although the incidents and time evolution of non-axisymmetric activity appear to heat the outer parts of the disc, isothermalization in the domain scanned by the CR and OLR resonances implies that a part of the disc between the CR and OLR becomes *cooler* at later simulation times. Physically, particles in the outer parts of the bar migrate outwards, carrying with them kinetic energy in the form of random motions. In Fig. 3.20, the initial and final profiles $\sigma_R(R)$ intersect at a radius $R_c \approx 8.5$ kpc. The bar's co-rotation at the time of the initial profile is at $R_{CR} \approx 6.4$ kpc, while it shifts to $R'_{CR} \approx 7.5$ kpc at the final time. Estimating by $R_{CR} < R < R_c$ the disc domain where manifolds rule the response of particles' orbits to external perturbations, this domain has a width $\sim 2.1$ kpc at the initial time $t = 1.6$ Gyr, which is limited to $\sim 1$ kpc at $t = 3$ Gyr, while this domain is expected to shrink further to negligible widths as the bar's co-rotation keeps moving outwards.

# Chapter 4

# Multiple pattern speeds and the manifold spirals in a simulation of a barred spiral galaxy

*Parts of the results of the present chapter were published as:*
*Zouloumi K., Harsoula M. and Efthymiopoulos C., 2024, MNRAS,529(3), 1941–1957*

In sequence of the paper of Efthymiopoulos et al. (2019) described in Chapter 3. We revisit the same simulation of Kyziropoulos et al. (2016), where we estimated that the spiral arms rotate at a different pattern speed than the bar in Chapter 3 (see subsection 3.3.4). Although this work pointed out the existence of a second pattern speed in the N-body the manifold spirals were produced with the assumption of unique pattern speed. In this Chapter we introduce the application of NAFF (Numerical Analysis of the Fundamental Frequencies, Laskar (1990), Laskar et al. (1992), Laskar (1993)) for the determination of the pattern speeds in a N-body model simulation of a barred spiral galaxy (Efthymiopoulos et al. (2019)). Our main new results are: i) We demonstrate that the NAFF algorithm allows for a determination of pattern speeds far more precise than with traditional methods based on the time-Fourier spectrum of the m=2 mode. ii) We apply the theory of Efthymiopoulos et al. (2020), showing how the spiral arms in the simulation can be modelled by manifolds, despite the fact that, as NAFF clearly shows, the spiral arms have a pattern speed different than the one of the bar in the same simulation.

The structure of the paper is as follows: Section 4.1 summarises the fundamentals of the theory behind the NAFF algorithm as well as some general estimates on the method's precision. The presentation is made in a form adopted to the use of the method in the particular problem considered, namely the detection of the various pattern speeds in a galactic disc. Section 4.2 gives the results from the application of the method to the determination of the pattern speeds and the resulting semi-analytical modelling of the potential using the simulation's data. Section 4.3 gives the reconstruction of the manifolds in the two-pattern speed model as well as their comparison with the structures seen in the simulation.

## 4.1 The method of Numerical Analysis of the Fundamental Frequencies (NAFF)

In this section, we briefly summarise the method of Numerical Analysis of the Fundamental Frequencies (NAFF) for the determination of the fundamental frequencies via a time series extracted from a multiply periodic system. Our presentation below uses some formulas adapted to, and emphasizing, those points necessary for the implementation of the method to the data of our N-body simulation.

Besides the issue of accuracy, we point out already at this point, a main difference between the NAFF algorithm and the usual Discrete Fourier Transform, often applied for obtaining the pattern speeds in N-body experiments (Sellwood & Sparke (1988)), concerning the nature of the system to which each method is applied. The Discrete Fourier Transform can determine the fundamental frequencies of a periodic system which is represented by a sum of sine and cosine waves, whose frequencies are integer multiples of the same, unique fundamental frequency of the system. Instead, NAFF can locate the constituent frequencies of a multiply periodic system, represented by quasi-periodic time series. Such series are sums of sines and cosines of these constituent frequencies.

Consider a continuous in time series of the form:

$$H(t) = \sum_{k=1}^{N_k} C_k \cos(\omega_k t) + D_k \sin(\omega_k t) \tag{4.1}$$

where the $N_k$ frequencies $\omega_k$, with $k = 1, \ldots, N_k$, are not necessarily commensurate. The real quantities $C_k$ and $D_k$ are called the 'amplitudes'. Assume we possess a discretely sampled information on the time series through the values $H(t_i)$, $i = 0, 1, , ..., N$ in the time interval $t_0 < t_i < t_N$. The quantity $T = t_N - t_0$ is called the *time length* of the series.

Based on this discrete time series data, the NAFF algorithm allows to recover the frequencies $\omega_k$ with a precision $O(1/T^2)$ (or better, using a Hanning filter, see below), and the amplitudes $C_k, D_k$ with a $O(1/T)$ precision. To demonstrate this fact consider the integrals:

$$F_c(\sigma) = \frac{2}{T} \int_0^T \left[ \cos(\sigma t) \sum_k \left( C_k \cos(\omega_k t) + D_k \sin(\omega_k t) \right) \right] dt \tag{4.2}$$

$$F_s(\sigma) = \frac{2}{T} \left[ \int_0^T \sin(\sigma t) \sum_k \left( C_k \cos(\omega_k t) + D_k \sin(\omega_k t) \right) \right] dt \tag{4.3}$$

$\sigma \in \Re$, as well as the corresponding Power Spectrum function $P(\sigma)$ defined by:

$$P(\sigma) = F_c(\sigma)^2 + F_s(\sigma)^2. \tag{4.4}$$

For a fixed set ($C_k$, $D_k$, $\omega_k$), the integrals (4.2) and (4.3), as well as the power spectrum (4.4), are explicit functions only of $\sigma$. Pick now, one of the frequencies $\omega_k$ and define the variable $\delta\sigma = \sigma - \omega_k$. Let

$$G(\delta\sigma) = \frac{dP(\omega_k + \delta\sigma)}{d(\delta\sigma)} \quad . \tag{4.5}$$

Then, the power spectrum $P(\sigma)$ has a local maximum at a value $\delta\sigma = \delta\sigma_k$ satisfying:

$$G(\delta\sigma_k) = \left( \frac{dP(\omega_k + \delta\sigma)}{d(\delta\sigma)} \right)_{\delta\sigma = \delta\sigma_k} = 0 \quad . \tag{4.6}$$

The following bound is found below as regards the exact solution of Eq. (4.6):

$$|\delta\sigma_k| \leq \frac{6({C_k}^2 + C_k D_k + {D_k}^2)}{({C_k}^2 + {D_k}^2)\omega_k T^2} \quad . \tag{4.7}$$

This implies that the function $P(\sigma)$ has a local maximum at a distance which is $\mathcal{O}(1/\omega_k T^2)$ close to the frequency $\omega_k$.

Figure 4.1 shows a toy example of the behavior of the integrals $F_c(\sigma)$, $F_s(\sigma)$ as a function of $\sigma$ and of the corresponding power spectrum $P(\sigma)$, choosing a simple quasi-periodic function:

$$H(t) = 0.5\cos(t + \pi/6) + 0.8\cos(t + \pi/4) \tag{4.8}$$

corresponding to $N_k = 2$, $\omega_1 = 1$, $\omega_2 = \sqrt{2}$, $C_1 = 0.433$, $C_2 = -0.566$, $D_1 = -0.25$, $D_2 = -0.566$. The integrals $F_c(\sigma)$, $F_s(\sigma)$ of Eqs. (4.2) and (4.3) and the power spectrum $P(\sigma)$ of Eq. (4.4) are computed as a function of $\sigma$ with $\sigma$ in the range $0 \leq \sigma \leq 2.5$. We produce a discretely sampled time series with $N = 1000$ points equispaced in the interval $0 \leq t \leq T = 100$, and use the trapezoidal rule to compute the integrals $F_c(\sigma)$ and $F_s(\sigma)$.

As shown in Fig. 4.1 the power function $P(\sigma)$ takes locally the well known form of a sinc function $sinc(x) = \sin(x)/x$ (see derivation below, or Binney & Spergel (1982)) around two distinct local maxima which nearly correspond (with the error $d\sigma$) to the frequencies $\omega_1 = 1$, $\omega_2 = 1.414$. Also, the quantity $\sqrt{P(\sigma)}$ near each local maximum is nearly equal to the amplitudes 0.5 and 0.8 respectively. Errors in these numbers are due to the sidelobes of the sinc function around each principal lobe. These can be reduced using a Hanning filter $han = 1 + \cos\left(\frac{\pi t}{T}\right)$., i.e., computing

$$F_{ch}(\sigma) = \frac{2}{T}\int_0^T \cos(\sigma t)[C_k\cos(\omega_k t) + D_k\sin(\omega_k t)] \quad \times \left[1 + \cos\left(\frac{\pi t}{T}\right)\right] dt \tag{4.9}$$

$$F_{sh}(\sigma) = \frac{2}{T}\int_0^T \sin(\sigma t)[C_k\cos(\omega_k t) + D_k\sin(\omega_k t)] \quad \times \left[1 + \cos\left(\frac{\pi t}{T}\right)\right] dt \quad . \tag{4.10}$$

The respective power spectrum is:

$$P_h(\sigma) = F_{ch}(\sigma)^2 + F_{sh}(\sigma)^2 \quad . \tag{4.11}$$

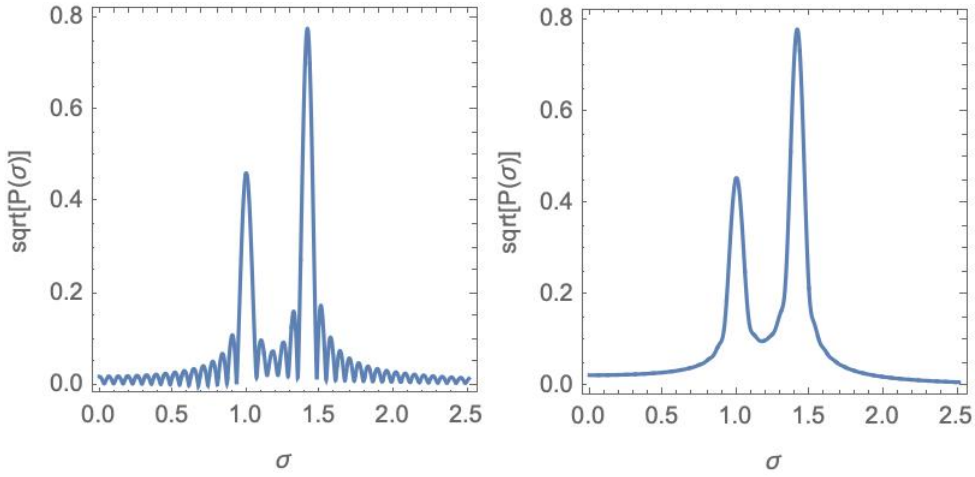


**Figure 4.1**: *(a) The NAFF power function $P(\sigma)$ in the case of the toy function $H(t)$ of Eq. (4.8) discretely sampled with $N = 1000$ points equispaced in the interval $0 \leq t \leq T = 100$. (b) The power function computed with a Hanning filter.*

Having obtained a numerical approximation for the power function $P(\sigma)$ we then select that value $\sigma = \sigma_{max}$ for which $P(\sigma_{max})$ is maximum. The fundamental frequency is then identified as: $\omega_1 = \sigma_{max}$, with an error $\mathcal{O}(1/T^2)$ (see the Appendix B), while the amplitudes $C_1$, $D_1$ are identified as $C_1 = F_c(\sigma_{j_{max}})$, $D_1 = F_s(\sigma_{j_{max}})$, with an error $\mathcal{O}(1/T)$.

Subtracting, now, the corresponding sine and cosine terms from the time series leads to a new time series $H^{(1)}(t_i) = H^{(0)}(t_i) - C_1 \cos(\omega_1(t_i - t_0)) - D_1 \sin(\omega_1(t_i - t_0))$, in which the procedure can be repeated. In general, working iteratively with the series

$$H^{(l)}(t_i) = H^{(l-1)}(t_i) - C_l \cos(\omega_l(t_i - t_0)) - D_l \sin(\omega_l(t_i - t_0)),$$
$$l = 1, \ldots, N_l \tag{4.12}$$

and recomputing the integrals (4.9) and (4.10) for the time series $H^{(l)}(t)$ allows to specify, one by one and by order of importance, the $N_l$ more important frequencies and corresponding amplitudes of the sine and cosine terms in the time series.

## 4.2 Mode (m=2) analysis in the N- body galatic model

### 4.2.1 NAFF determination of the pattern speeds

Section 4.1 provides a short description of the generic NAFF algorithm. In the present section we discuss how to apply NAFF to the determination of the two most important pattern speeds and amplitudes of the corresponding density/potential modes in the N-body simulation under study.

In the N-body simulation we quantify the non-axisymmetric structures in the disc by Fourier-analysing the disc's surface density/potential. We separate the space in a polar grid of 50 logarithmically equi-spaced radial bins from $r_0 = 0.1$ kpc to $r = 15$ kpc, and 180 azimuthal bins from $\varphi = 0$ to $\varphi = 2\pi$. The surface density (number of disc particles per bin area) at time $t$ $\Sigma(r, \varphi, t)$ is Fourier-analysed into 10 angular modes:

$$\Sigma(r, \varphi, t) = A_0(r, t) + \sum_{m=1}^{10} A_m(r, t) \cos(m\varphi) + \sum_{m=1}^{10} B_m(r, t) \sin(m\varphi) \quad . \tag{4.13}$$

In the present study we are interested mostly in the m=0,2 modes. From the N-body data we compute numerical time series $A_2(r,t_i)$, $B_2(r,t_i)$, $t_i = i \times 0.025$ Gyr, $i = 0, ..., 160$, covering the entire interval of 4 Gyrs and computed for all radii $r$ in the above logarithmic grid. In the sequel we focus on the m=2 modes coexisting in the disc at one epoch. Analysis of higher harmonics (m>2) does not alter significantly the picture.

In our simulation, we have in total $i = 1, ..., 160$ snapshots corresponding to the times $t_i = i \times 0.025$ Gyr. We divide the plane of the galactic disc into $q = 1 \ldots, 50$ rings of radius $r_q$ defined by a logarithmic grid in the interval $0.1\ kpc \leq r \leq 15\ kpc$, and 180 angular bins around the angles $\varphi_p = p\pi/180$, $p = 1, \ldots, 180$. Fixing a time $t_i$ and radius $r_q$, the angular dependence of $\Sigma(r_q, \varphi, t_i)$ is Fourier-analysed by the standard method, yielding the Fourier amplitudes $A_m(r_q, t_i)$, $B_m(r_q, t_i)$, $m = 0, \ldots, 10$ (see Eq. (4.13)). We then focus on the evolution of the functions $A_0(r_q, t)$, $A_2(r_q, t)$ and $B_2(r_q, t)$.

Due to the fact that the disc in the simulation undergoes significant secular evolution, it makes no sense to assume a quasi-periodic character for the functions $A_2(r_q, t)$ and $B_2(r_q, t)$, i.e., a constant in time spectrum of frequencies, over the whole time span of the simulation. At most we can assume that the frequencies remain nearly constant over time windows corresponding to few bar/spiral revolutions. Due to this, we work with the discretely sampled time series $A_2(r_q, t)$, $B_2(r_q, t)$ over time windows *of limited length* $T = 0.5\ Gyr$, with $n = 21$ data points $A_2(r_q, t_i)$ and $B_2(r_q, t_i)$ per ring, with $t_i = t_0 + i\Delta t$, where $t_0$ is the initial time of each time window and $\Delta t = 0.025$ Gyr. The sampling rate is imposed by the rate of saving of the N-body snapshots during the simulation.

Fixing one time window, to implement NAFF, we then proceed by the following steps:

i) Sample the frequency space by a dense grid of values $\sigma_k = k\Delta\sigma$, with $\Delta\sigma$ much smaller than the DFT (Discrete Fourier Transform) leakage limit $\Delta\sigma_k << 2\pi/T$. Here we take $\Delta\sigma_k = 1.256\ Gyr^{-1} = 0.2\pi/T$, but a finer frequency resolution can be chosen at practically no computational cost.

ii) Compute the NAFF Power Function

$$\begin{aligned} P_k(r_q, \sigma_k) &= {a_{ck}}^2(r_q, f_k) + {a_{sk}}^2(r_q, \sigma_k) \\ &+ {b_{ck}}^2(r_q, \sigma_k) + {b_{sk}}^2(r_q, \sigma_k) \end{aligned} \tag{4.14}$$

where the coefficients $a_{ck}$, $a_{sk}$, $b_{ck}$, $b_{sk}$ are computed by a Hanning-filter-weighted trapezoidal rule approximation to the integrals (4.9), (4.10), given by the sums:

$$a_{ck}(r_q, \sigma_k) \simeq \frac{2\Delta t}{T}\Bigg( A_2(r_q, t_0) + \sum_{i=1}^{n-1} A_2(r_q, t_i) \cos(\sigma_k(t_i - t_0)) \left[1 + \cos\left(\frac{\pi(t_i - t_0)}{T}\right)\right]\Bigg) \tag{4.15}$$

$$a_{sk}(r_q, \sigma_k) \simeq \frac{2\Delta t}{T}\Bigg( \sum_{i=1}^{n-1} A_2(r_q, t_i) \sin(\sigma_k(t_i - t_0)) \left[1 + \cos\left(\frac{\pi(t_i - t_0)}{T}\right)\right]\Bigg) \tag{4.16}$$

$$b_{ck}(r_q, \sigma_k) \simeq \frac{2\Delta t}{T}\Bigg( B_2(r_q, t_0) + \sum_{i=1}^{n-1} B_2(r_q, t_i)\cos(\sigma_k(t_i - t_0))\left[1 + \cos\left(\frac{\pi(t_i - t_0)}{T}\right)\right]\Bigg) \tag{4.17}$$

$$b_{sk}(r_q, \sigma_k) \simeq \frac{2\Delta t}{T}\Bigg( \sum_{i=1}^{n-1} B_2(r_q, t_i)\cos(\sigma_k(t_i - t_0))\left[1 + \cos\left(\frac{\pi(t_i - t_0)}{T}\right)\right]\Bigg) \quad . \tag{4.18}$$

iii) Use a frequency extraction method ('subtract and repeat') to extract the main modes and corresponding pattern speeds. This last step is presented in more details in the next subsection.

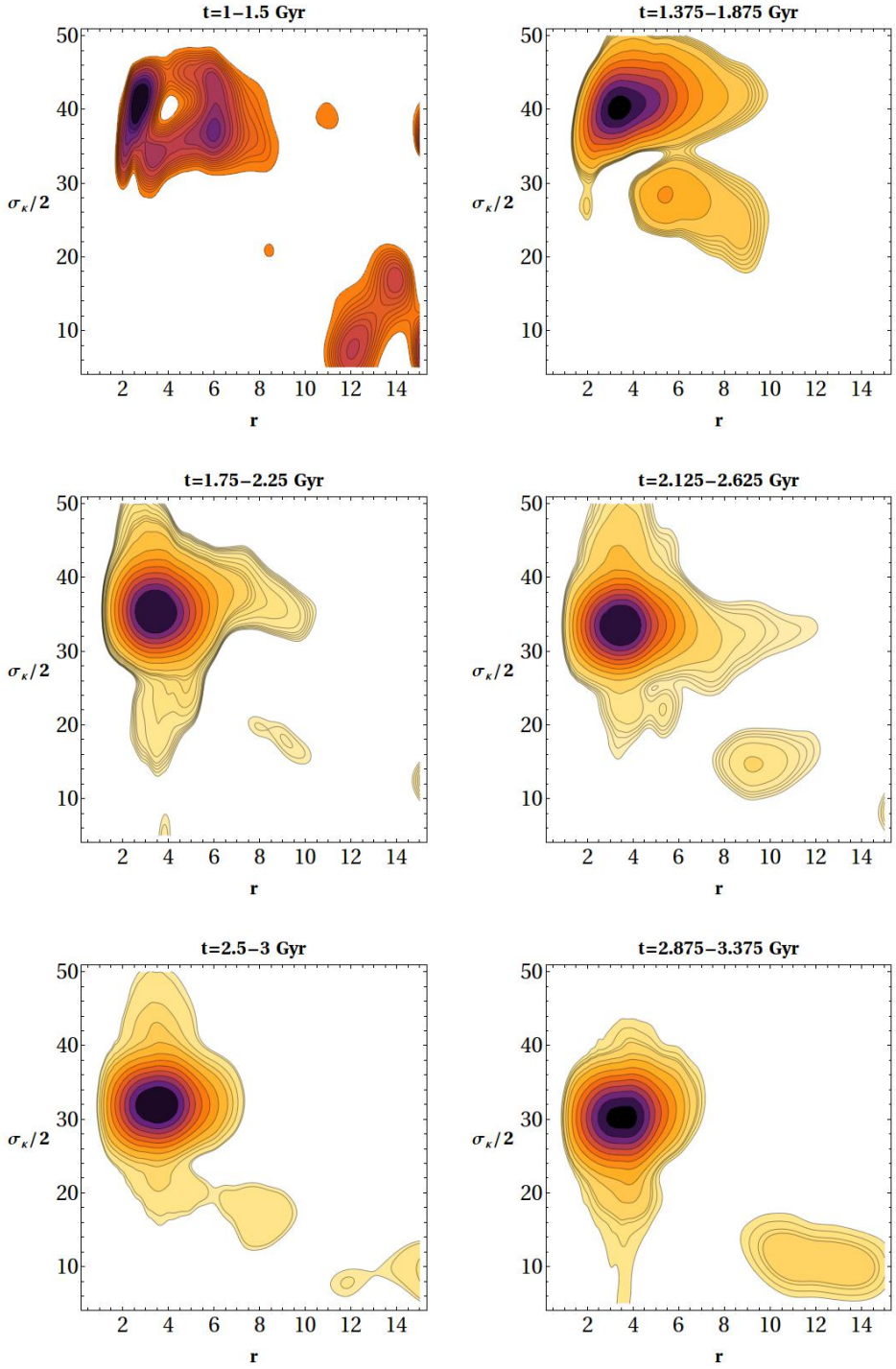


**Figure 4.2**: *The contours of the NAFF power function $P_k$ of Eq. (4.14) as functions of frequency $\sigma_k/2$ and radius $r$, derived from the application of NAFF in several consecutive time windows of the N-body simulation.*

Figure 3 shows the contours of the NAFF Power Function $P_k(r_q, \sigma_k)$ given by Eq. (4.14) as a function of the frequency $\sigma_k$ and the radius $r_q$ from the centre of the galactic disc for different time windows of length $T = 0.5$ Gyr, namely $t \in [1, 1.5]$ Gyr, $t \in [1.375, 1.875]$ Gyr, $t \in [1.75, 2.25]$ Gyr, $t \in [2.125, 2.625]$ Gyr, $t \in [2.5, 3.0]$ Gyr, $t \in [2.875, 3.375]$ Gyr. As observed in Fig. 4.2, the contours of the power spectrum $P_k(r_q, \sigma_k)$ give several local maxima in each time window of the simulation. As described in Efthymiopoulos et al. (2019), the time interval $t \in [1, 1.5]$ Gyr (top left panel in Fig. 4.2) corresponds to the phase of growth of the bar instability, thus

no quasi-steady structures can be found in this interval. On the other hand, all the remaining panels in Fig. 4.2 were chosen so that the center of each time interval corresponds to a maximum, or 'episode', of spiral activity (see Efthymiopoulos et al. (2019)). As shown in Fig. 4.2, in all these cases there is a well formed global maximum of the spectrum $P_k(r_q, \sigma_k)$ with the contours centered around the frequency $\sigma_{k,max} = 2f_{k,max}$ with $f_{k,max}$ decaying slowly from a value $f_{k,max} \simeq 40$ km/s/kpc at the second time window to $f_{k,max} \simeq 30$ km/s/kpc at the final time window considered. As regards the radial extent of the closed isocontours around this dominating maximum, we have $2\ kpc < r \leq r_{max}$, where $r_{max}$ undergoes a sharp transition from a value $r_{max} \simeq 10$ kpc, from the second to the fourth time window, to $r_{max} \simeq 6$ kpc in the last two time windows of Fig. 4.2.

The bar corresponds to the dominating m=2 maxima up to $r \simeq 6$ kpc, and with spiral extensions and/or distinct spiral modes to the local maxima in the spectrum formed at radii $r > 6$ kpc. The gradually decrease with time of the bar and spiral pattern speeds is associated with the secular evolution of the galaxy. The bar gradually spins down as angular momentum gets transfered to the outer structures of the galaxy (Debattista & Sellwood (1988), Debattista & Sellwood (2000), Athanassoula (2002), Athanassoula (2003), Efthymiopoulos et al. (2019)). A similar process affects the pattern speed of the spiral arms (Lynden-Bell & Kalnajs (1972)). Note, finally, that the overdensities observed in panels 4, 5 of Fig. 4.2 beyond $r = 10$ kpc correspond to additional pattern speeds, while, as the time goes on, the second most important pattern altogether shifts towards larger radii, exceeding $r = 10$ kpc in the last panel of the same figure.

### 4.2.2 Determination of the bar and spiral pattern speeds

We now refer to step (iii)) above of the frequency extraction algorithm. To implement the manifold theory, we choose two different time windows: $T_1 = 2.125 - 2.625$ Gyr (Fig. 4.3) and $T_2 = 2.500 - 3.000$ Gyr (Fig. 4.4). These are chosen to correspond to the two regimes discussed above, i.e., in which the closed contours of the power spectrum $P_k(r_q, \sigma_k)$ around the main (bar) maximum extend to radii overlapping, or not, with those of the second most important maximum (fourth and fifth panel in Fig. 4.2).

To determine the bar's pattern speed $\Omega_b$, we scan the contour plots of $P_k(r_q, \sigma_k)$ vertically in the region of the bar's radii. In every annulus $r_q$ we numerically locate the the frequency $f_{max_1}$ where $P_k(r_q, \sigma_k)$ has its global maximum, and specify at which frequency the maximum occurs. The semi-analytical time series $A_{2_{th_1}}(r_q, t_i)$, $B_{2_{th_1}}(r_q, t_i)$ are obtained by the formula

$$A_{2_{th_1}}(r_q, t_i) = a_{ck1}(r_q, f_{max_1}) \cos(f_{max_1}(t_i - t_0)) + a_{sk1}(r_q, f_{max_1}) \sin(f_{max_1}(t_i - t_0)) \tag{4.19}$$

$$B_{2_{th_1}}(r_q, t_i) = b_{ck1}(r_q, f_{max_1}) \cos(f_{max_1}(t_i - t_0)) + b_{sk1}(r_q, f_{max_1}) \sin(f_{max_1}(t_i - t_0)) \quad . \tag{4.20}$$

and compared to the N-Body time series of $A_2$ or $B_2$ at the same radii. The comparison (e.g. Fig. 4.3 for the $A_2$ amplitude at the time window $T_1 = 2.125 < t < 2.525$ Gyr, Fig. 4.4 at the time window $T_2 = 2.5 < t < 3$ Gyr) shows that the frequency of the bar's rotation is well recovered in both windows. We find $\Omega_b = 33.3$ km/s/kpc for the time window $T_1$ and $\Omega_b = 32.04$ km/s/kpc for the time window $T_2$.

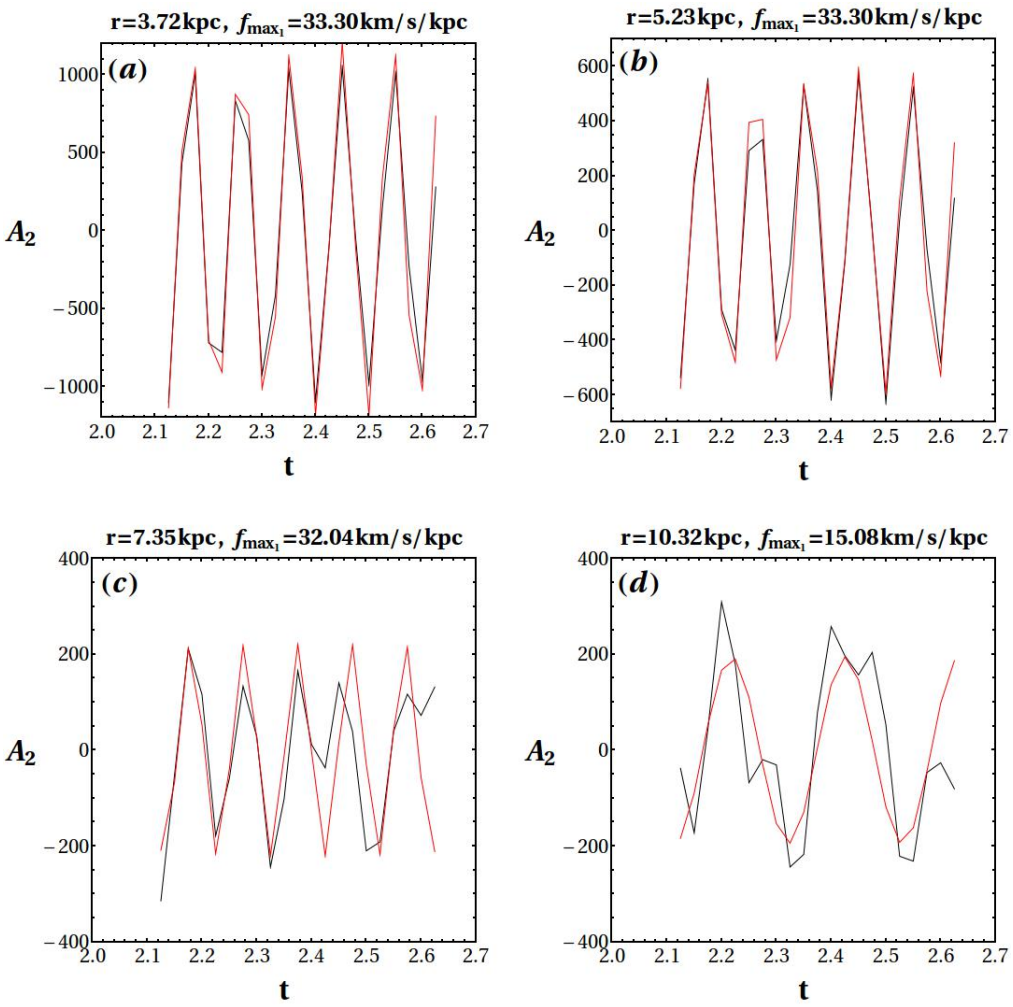


**Figure 4.3**: *The semi- analytical time series $A_{2_{th_1}}(r,t)$ (red curves) of the amplitude of m=2 pertubation in density produced by the frequency $f_{max_1}$, where we locate a maximum at the power spectrum for several radii ((a) r=3.72 kpc, (b) r=5.23 kpc, (c) r=7.35 kpc, (d) r=10.32 kpc), compared to the corresponding numerical time series $A_2(r,t)$ (black curves) in the same radii for the time window $T_1 = 2.125 - 2.625$ Gyr of the N-body simulation.*

At larger radii (beyond $r = 7$ kpc) the agreement of the analytical time series with the numerical ones (Figs. 4.3(c), 4.3(d), 4.4(c), 4.4(d)) is not so good. However, the power function $P_k(r_q, f_k)$ exhibits a second local maximum at radii $r > 7$ kpc (see Fig. 4.2). To exctract the second pattern speed, we compute the new time series

$$A_2{}'(r_q, t_i) = A_2(r_q, t_i) - A_{2_{th_1}}(r_q, t_i) \tag{4.21}$$

$$B_2{}'(r_q, t_i) = B_2(r_q, t_i) - B_{2_{th_1}}(r_q, t_i) \tag{4.22}$$

where $A_{2_{th_1}}(r_q, t_i)$ and $B_{2_{th_1}}(r_q, t_i)$ are given by Eqs (4.19) and (4.20), with $f_{max_1}$ in all radii substituted with a unique constant value $f_{max_1} = \Omega_b$. We then repeat the process, computing the first iterated amplitudes $a'_{ck}$, $a'_{sk}$, $b'_{ck}$, $b'_{sk}$ (formulas (4.15), (4.16), (4.17), (4.18) with $A'_2$, $B'_2$ in the place of $A_2$, $B_2$), and the first-iterated Power Function $P'_k(r_q, \sigma_k)$. For every fixed radius $r_q$ we now plot $P_k{}'(r_q, \sigma_k)$ as a function of $f_k = \sigma_k/2$ (Figs. 4.5, 4.6). Our criterion for choosing a second fundamental frequency $f_{max_2}$ stems from comparing the values of $f_k$ where $P_k{}'(r_q, f_k)$ exhibits a local maximum for all the different radii $r_q$.

As shown in Fig. 4.5, at all radii beyond $r = 7$ kpc we detect a local maximum at $f_k \approx 15$ km/s/kpc, which stabilises to the value $\Omega_2 = f_{max_2} = 14.45$ km/s/kpc in

the range of $8\ kpc < r_q < 11\ kpc$ while it tends to fall with $r_q$ for $r_q > 11$ kpc. This information for all radii $r_q$ is summarised in Fig. 4.7, which shows the computed values of the frequencies $\Omega_1(r_q) = \sigma_{1,max}(r_q)/2$, and $\Omega_2(r_q) = \sigma_{2,max}(r_q)/2$, where the power function was found to exhibit its first and second local maximum, along with the corresponding values $P_{k_{1,max}} = P_{k_1}(r_q, \sigma_{1,max})$, $P_{k_{2,max}} = P_{k_2}(r_q, \sigma_{2,max})$, as a function of radius $r = r_q$, in both time windows $T_1$ and $T_2$. From the bottom left panel of Fig. 4.7 we note that, despite the overall variation with $r$, we can define an approximately constant value in the range $8\ kpc < r_q < 11\ kpc$. Thus, we adopt a second (spiral) pattern speed $\Omega_{sp} = 14.45$ km/s/kpc in the first time window $T_1 = 2.125 - 2.625$ Gyr.

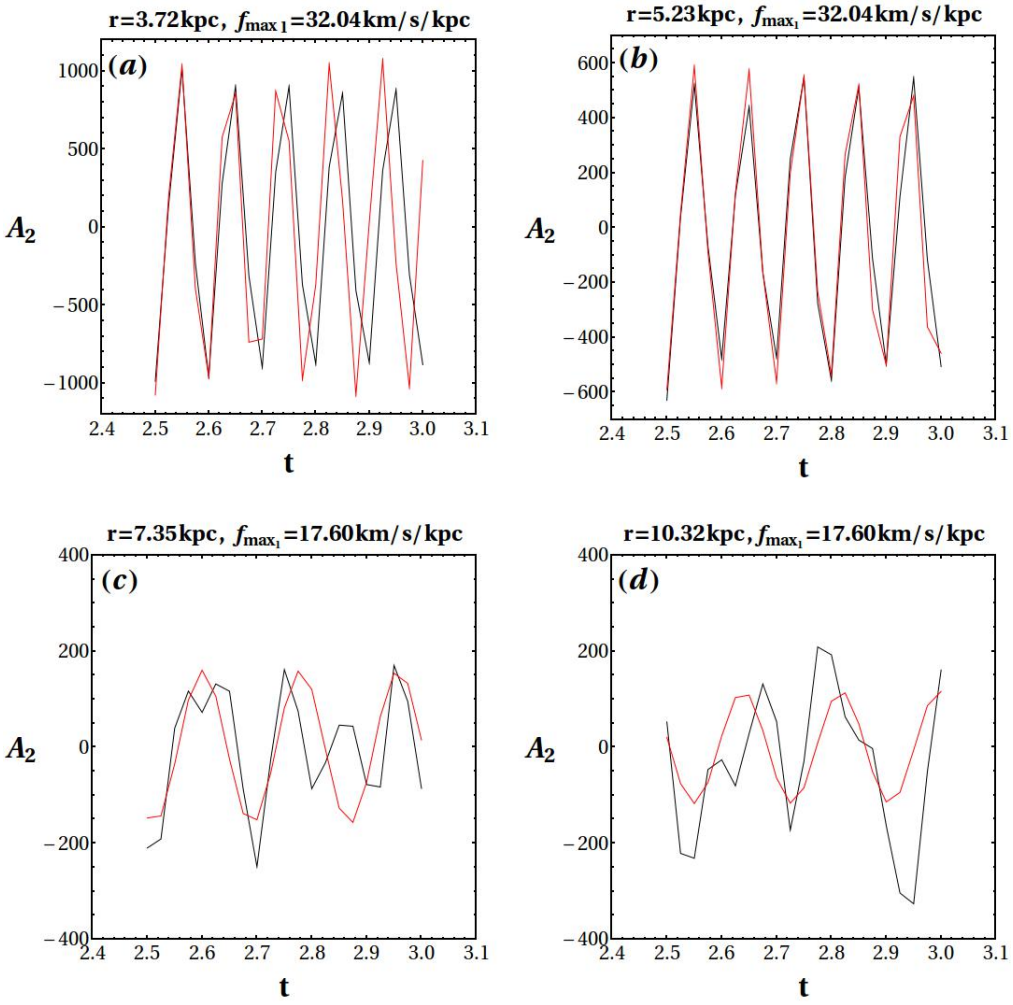


**Figure 4.4**: *The semi-analytical time series $A_{2_{th_1}}(r,t)$ (red curves) of the amplitude of m=2 pertubation in density produced by the frequency $f_{max_1}$, where we locate a maximum at the power spectrum for several radii ((a) r=3.72 kpc, (b) r=5.23 kpc, (c) r=7.35 kpc, (d) r=10.32 kpc), compared to the corresponding numerical time series $A_2(r,t)$ (black curves) in the same radii for the time window $T_2 = 2.5 - 3.0$ Gyr of the N-body simulation.*

In the second time window ($T_2 = 2.5 - 3$ Gyr), a plot of $P_k{}'(r_q, \sigma_k)$ (Fig. 4.6) reveals, instead, the existence of at least two important local maxima, whose presence is detected at practically all radii beyond $r_q = 7$ kpc. The first local maximum is dominant in the domain $7\ kpc < r_q < 10.5\ kpc$, and its value stabilises to $f_{max_2} = 17.6$ km/s/kpc, while the second local maximum becomes dominant for $r_q > 11$ kpc, with a value slightly decreasing with $r$, around $f_{max_3} = 7.5$ km/s/kpc. In the sequel, we ignore the effects of this third pattern and focus only on the pattern which is dominant in the radii $7\ kpc < r_q < 10.5\ kpc$, thus identifying a spiral pattern speed $\Omega_{sp} = 17.6$

km/s/kpc in the time window $T_2 = 2.5 - 3$ Gyr.

We note that the above specified values of the pattern speeds are in good agreement with those found with a crude method in Efthymiopoulos et al. (2019) (see, for example, panel $t = 2.375$ in figure 20 of Efthymiopoulos et al. (2019)).

So far, the simplification was made that we adopted constant values for the two pattern speeds throughout the whole disc, i.e., ignored the small variations in the values of $f_{max_1}$ and $f_{max_2}$ with radius yielded by the NAFF algorithm, and adopted the mean value of $f_{max_1}$ and $f_{max_2}$ in the corresponding range of radii as $\Omega_1 = \Omega_b$, $\Omega_2 = \Omega_s$. Figure 4.7, bottom, shows that this is essentially correct. The same figure (top) yields the relative amplitudes bar/spiral throughout the disc. As a further test of how accurately the surface density of the disc in the simulation is reproduced, we obtain a semi-analytical formula for the surface density $\Sigma_{th}(r, \varphi, t)$ given by:

$$\begin{aligned} \Sigma_{th}(r_q, \varphi_p, t_i) &= A_0(r_q, t_i) + A_{2_{th}}(r_q, t_i)\cos(2\varphi_p) \\ &+ B_{2_{th}}(r_q, t_i)\sin(2\varphi_p) \end{aligned} \tag{4.23}$$

where

$$\begin{aligned} A_{2_{th}}(r_q, t_i) = &\sum_{n=1}^{2} \left(a_{c_n}(r_q, \Omega_n)\cos(\Omega_n(t_i - t_0))\right) + \\ &\sum_{n=1}^{2} \left(a_{s_n}(r_q, \Omega_n)\sin(\Omega_n(t_i - t_0))\right) \end{aligned} \tag{4.24}$$

$$\begin{aligned} B_{2_{th}}(r_q, t_i) = &\sum_{n=1}^{2} \left(b_{c_n}(r_q, \Omega_n)\cos(\Omega_n(t_i - t_0))\right) + \\ &\sum_{n=1}^{2} \left(b_{s_n}(r_q, \Omega_n)\sin(\Omega_n(t_i - t_0))\right) \end{aligned} \tag{4.25}$$

and the index $n = 1, 2$ refers to the frequencies and amplitudes determined in the two iterations of the NAFF algorithm. Note that the above formula gives rise both to $\begin{matrix}\sin\\\cos\end{matrix}[2(\varphi_p - \Omega_b(t_i - t_0))]$ and $\begin{matrix}\sin\\\cos\end{matrix}[2(\varphi_p + \Omega_b(t_i - t_0))]$ terms. However, the terms of $\cos[2(\varphi_p + \Omega_b(t_i - t_0))]$ and $\sin[2(\varphi_p + \Omega_b(t_i - t_0))]$ can be neglected as one can check that their coefficients are small (no more than 10%) with respect to the coefficients of the $\cos[2(\varphi_p - \Omega_b(t - t_0))]$ and $\sin[2(\varphi_p - \Omega_b(t_i - t_0))]$ terms throughout the disc. Thus we finally adopt the approximate formula:

$$\begin{aligned} &\Sigma_{th}(r_q, \varphi_p, t_i) = A_0(r_q, t_i) + \\ &\frac{1}{2}\sum_{j=1}^{2} \left(a_{c_j}(r_q, \Omega_j) + b_{s_j}(r_q, \Omega_j)\right) cos[2(\varphi_p - \Omega_j(t_i - t_0))] + \\ &\left(b_{c_j}(r_q, \Omega_j) - a_{s_j}(r_q, \Omega_j)\right)\sin[2(\varphi_p - \Omega_j(t_i - t_0))] \end{aligned} \tag{4.26}$$

where $\Omega_1 = \Omega_b$, $\Omega_2 = \Omega_{sp}$.

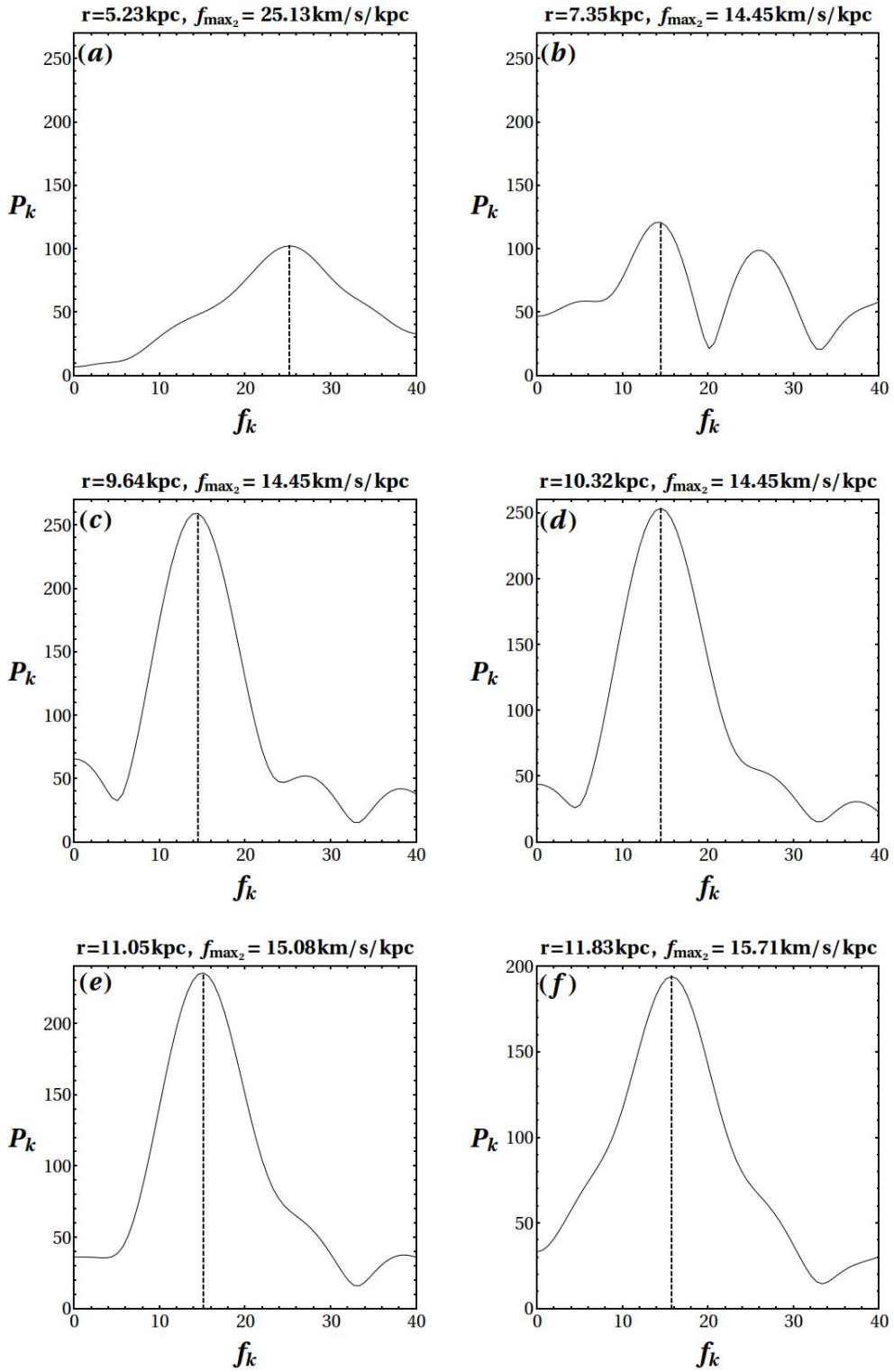


**Figure 4.5**: *The power function $P_k$ of the time series $A_2{}'(r,t)$ given by Eq. (4.21) as a function of the frequencies $f_k$ for the time window of $T_1$ of the N-body simulation. In every plot the frequency $f_{max_2}$, which corresponds to the second local maximum of the power function is indicated by a vertical line.*

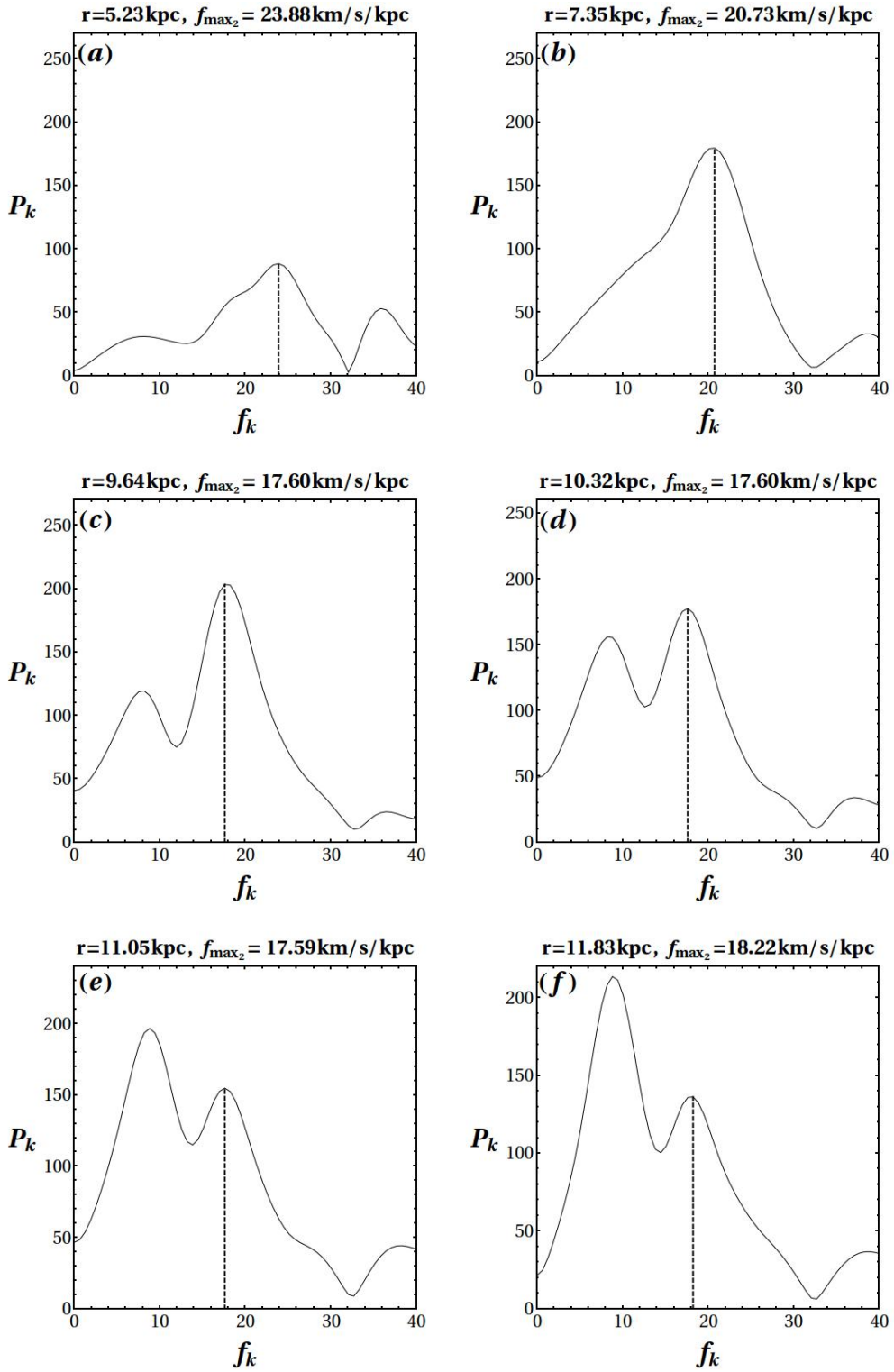


**Figure 4.6**: *The power function $P_k$ of the time series $A_2{}'(r,t)$ given by Eq. (4.21) as a function of the frequencies $f_k$ for the time window of $T_2$ of the N-body simulation. In every plot the frequency $f_{max_2}$, which corresponds to the second local maximum of the power function is indicated by a vertical line.*

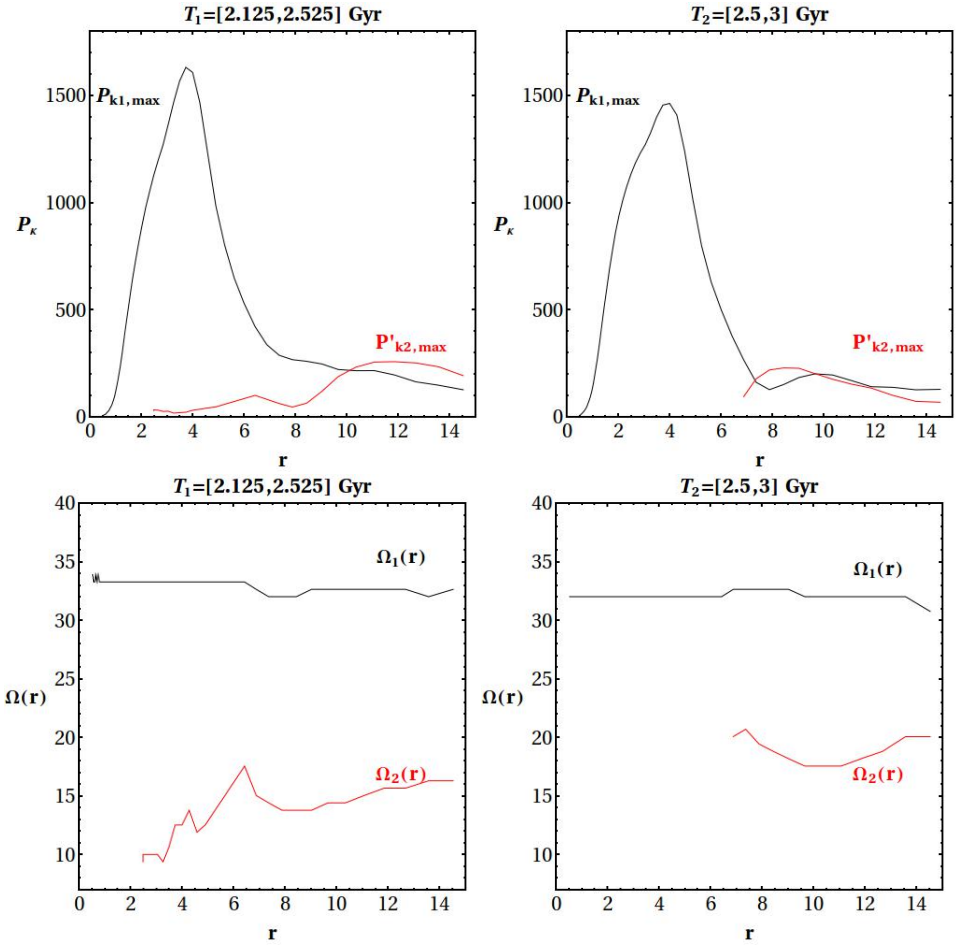


**Figure 4.7**: *Top: the maximum values* $P_{k_{1,max}} = P_k(r, \sigma_k = 2f_{max_1})$ *(black) or* $P_{k_{2,max}} = P_k(r, \sigma_k = 2f_{max_2})$ *(red) as a function of radius* $r$*, in the time window* $T_1$ *(left) and* $T_2$ *(right). Bottom: the values of* $\Omega_1(r) = \sigma_{1,max}(r)/2$*,* $\Omega_2(r) = \sigma_{2,max}(r)/2$ *where* $\sigma_{1,max}(r)$*,* $\sigma_{2,max}(r)$*, at the same time windows.*

Figures 4.8 and 4.9 show the comparison between the semi-analytical time series $A_{2_{th}}(r_q, t_i)$ from Eq. (4.24) and the numerical time series $A_2(r_q, t_i)$ of the $m = 2$ in Eq. (4.13) for the time windows $T_1$ and $T_2$ respectively. The superposition of the semi-analytical time series $A_{2_{th}}(r_q, t_i)$ and the numerical ones $A_2(r_q, t_i)$ at various radii shows an overall agreement up to r=14 kpc. Beyond that radius, the numerical time series exhibits patterns that cannot be recovered with the simple model of Eqs. (4.24) and (4.25).

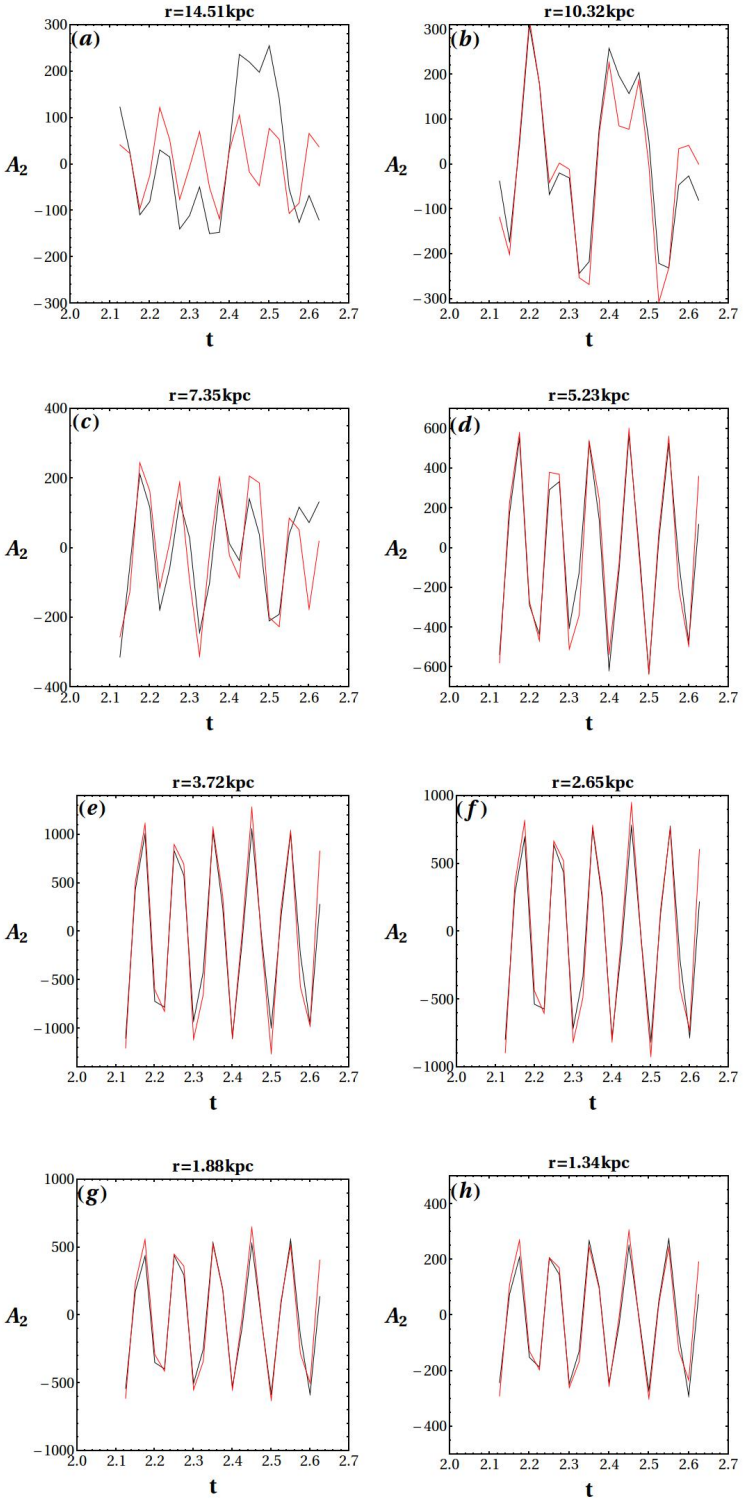


**Figure 4.8**: *The superposition of the semi-analytical time series of $m = 2$ pertubation $A_{2_{th}}(r_q, t_i)$ (red curves), which are obtained through NAFF algorithm, to the numerical one $A_2(r_q, t_i)$ (black curves) for the time window of $T_1 = 2.125 - 2.625$ Gyr.*

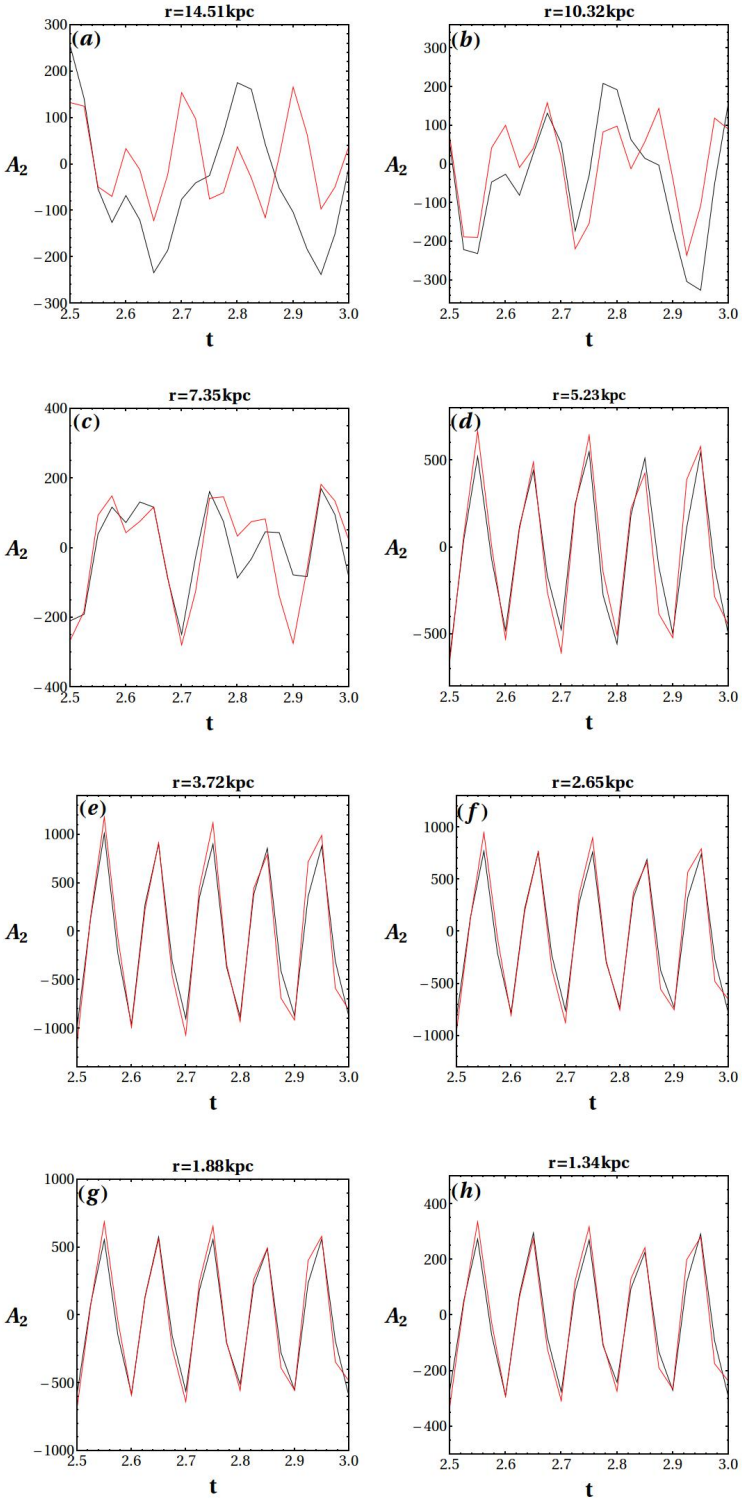


**Figure 4.9**: *The superposition of the semi-analytical time series $A_{2_{th}}(r_q, t_i)$ of $m = 2$ pertubation (red curves), which are obtained through NAFF algorithm, to the numerical one $A_2(r_q, t_i)$ (black curves) for the time window $T_2 = 2.500 - 3.000$ Gyr of the N-body simulation.*

Figures 4.10, 4.11 show that the semi-analytical formulas (4.23)-(4.25) reproduce with a good accuracy the numerical sums of the $m = 0, 2$ modes of the surface density of the galaxy. It is also remarkable that, notwithstanding the differences, with only the m=0,2 terms of the galaxy we can have a representative image of the galaxy in every snapshot, even when compared to the complete image of the surface density. Note, in

particular, that the NAFF model catches correctly the appearance of a leading spiral component extending beyond the bar in the snapshot $t = 2.625$ Gyr of Fig. 4.11. In Efthymiopoulos et al. (2019) the appearance of such leading components on the galactic disc was attributed to the flow of material approaching the bar from the leading direction by moving along outer families of periodic orbits.

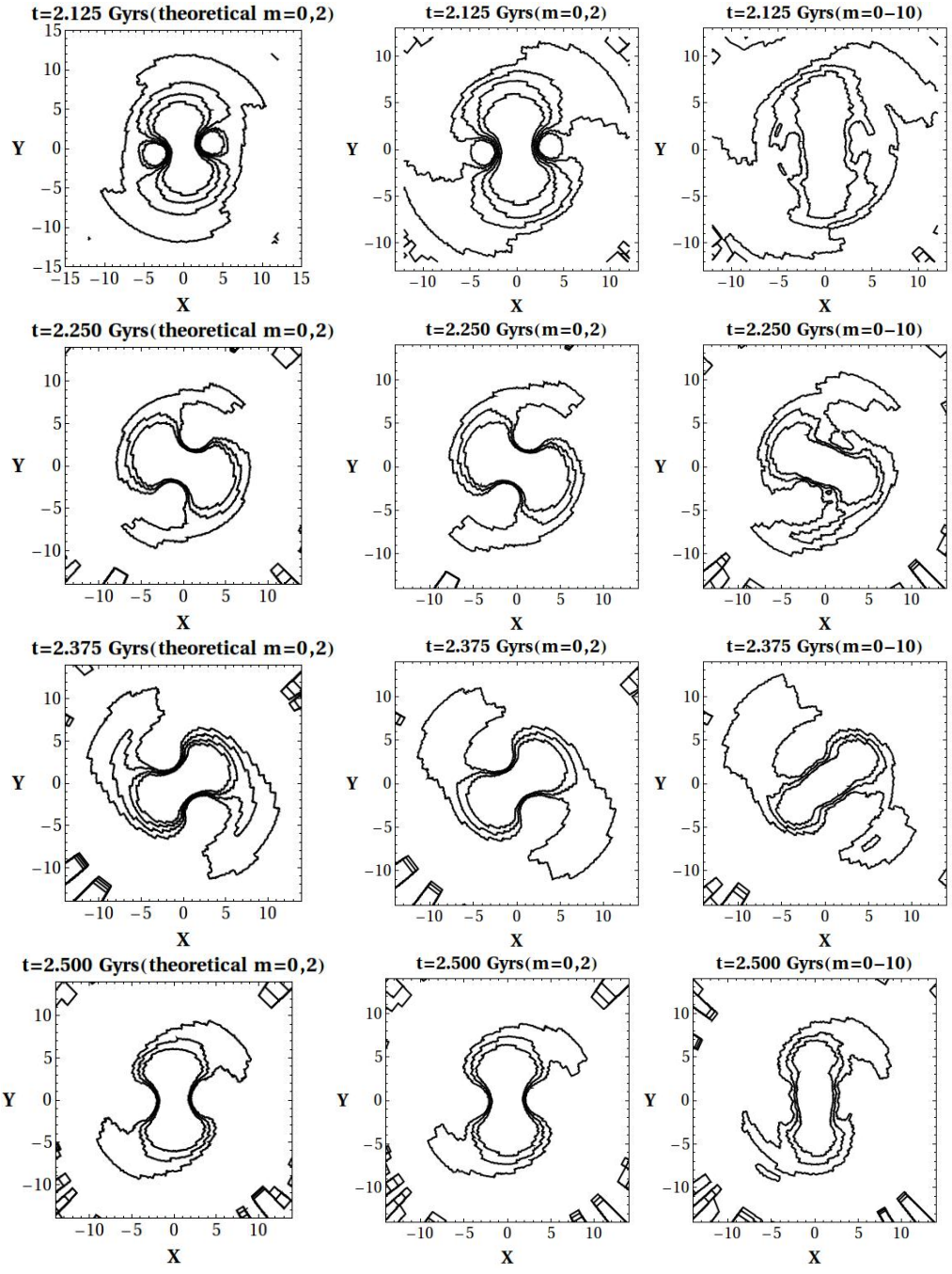


**Figure 4.10**: *The contours of the surface density for 4 snapshots of the time window $T_1 = 2.125 - 2.625$ Gyr of the N-body simulation that were produced in 3 ways: (a) with the use of the semi-analytical fitting form of Eq. (4.39) for the surface density of m=0,2 modes of the galaxy (b) by the numerical form of m=0,2 modes of Eq. (4.13) of the surface density of the N-body model (c) by the complete numerical form with all the modes (m=0-10) of Eq. (4.13) of the surface density of the N-body model.*

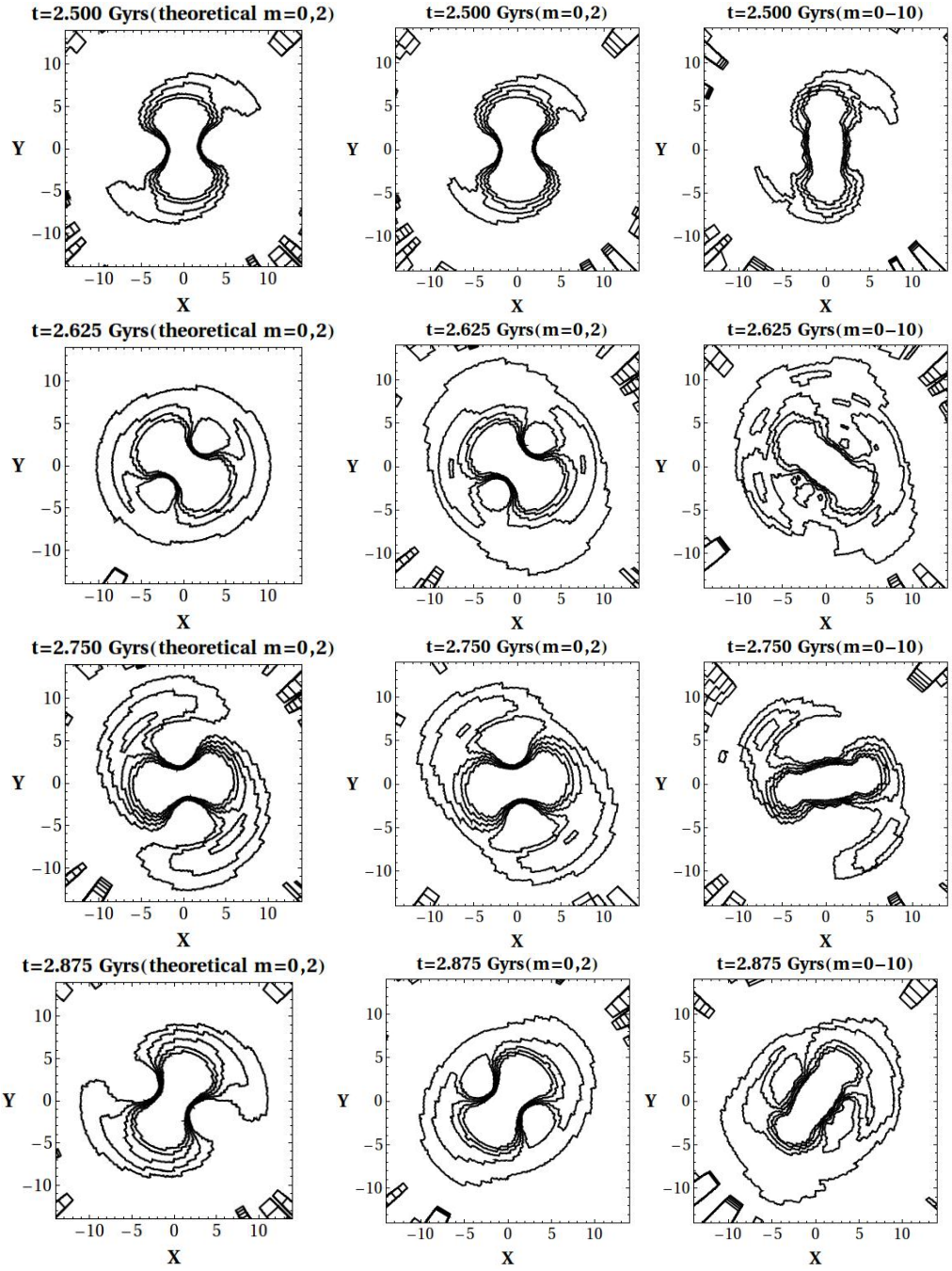


**Figure 4.11**: *The contours of the surface density for 4 snapshots of the time window of $T_2 = 2.500 - 3.000$ Gyr of the N-body simulation that were produced in 3 ways: (a) with the use of the semi-analytical fitting form of Eq. (4.39) for the surface density of m=0,2 modes of the galaxy (b) by the numerical form of m=0,2 modes of Eq. (4.13) of the surface density of the N-body model (c) by the complete numerical form with all the modes (m=0-10) of Eq. (4.13) of the surface density of the N-body model.*

### 4.2.3 Application of the NAFF algorithm to the gravitational potential

We now repeat the NAFF analysis as in subsection 4.2.2 for the gravitational potential of the N-body simulation in the same time windows $T_1 = 2.125 - 2.625$ Gyr and $T_2 = 2.5 - 3$ Gyr. In every snapshot the data for the gravitational potential are given in the form of a grid $N_g \times N_g$ in cartesian space, where $N_g = 511$. We thus obtain the values $V_{n_g}(x_{n_g}, y_{n_g})$ of the potential at the grid points $(x_{n_g}, y_{n_g})$, $n_g = 0, \ldots N_g$. We finally apply bilinear interpolation method in order to have the values of the potential

$V(x,y)$ in every point of the disc plane $(x,y)$. We finally follow the same procedure as in subsection 4.2.1 to Fourier analyse the potential $V(r_q,\varphi_p,t_i)$ of the i-th snapshot with respect to its periodical dependence on $\varphi$ in all the annuli defined by the radii $r_q$ of the logarithmic grid. This allows to compute the coefficients of the m-th mode of the Fourier decomposition:

$$\begin{aligned} V(r_q,\varphi_p,t_i) =& V_0(r_q,t_i) + \sum_m \Phi_m(r_q,t_i)\cos(m\varphi) + \\ & \sum_m \Psi_m(r_q,t_i)\sin(m\varphi) \quad . \end{aligned} \tag{4.27}$$

As in the previous subsections the integrals:

$$V_0(r_q,t_i) = \frac{1}{2\pi}\int_0^{2\pi} V(r_q,\varphi_p,t_i)d\varphi \tag{4.28}$$

$$\Phi_m(r_q,t_i) = \frac{1}{\pi}\int_0^{2\pi} V(r_q,\varphi_p,t_i)\cos(m\varphi)d\varphi \tag{4.29}$$

$$\Psi_m(r_q,t_i) = \frac{1}{\pi}\int_0^{2\pi} V(r_q,\varphi_p,t_i)\sin(m\varphi)d\varphi \tag{4.30}$$

are calculated through the trapezoidal rule on the discrete set of values $V(r_q,\varphi_p,t_i)$, $p=0,\ldots,180$. We apply the NAFF method in order to determine the fundamental frequencies of m=2 mode of the potential. We apply the same methods as in subsection 4.2.2 to compute the fundamental frequencies and amplitudes associated to the time series $\Phi_2(r_q,t_i)$ and $\Psi_2(r_q,t_i)$. As a control of the accuracy of the method, we checked that we obtain the same fundamental frequencies by the NAFF analysis of the potential as the ones by the NAFF analysis of the surface density.

The semi-analytical formula for the potential then is:

$$V_{th}(r_q,\varphi_p,t_i) = V_0(r_q,t_i) + \Phi_{2_{th}}(r_q,t_i)\cos(2\varphi_p) + \Psi_{2_{th}}(r_q,t_i)\sin(2\varphi_p) \tag{4.31}$$

where

$$\Phi_{2_{th}}(r_q,t_i) = \sum_{n=1}^{2}\left(a_{V_{c_n}}(r_q,\Omega_n)\cos(\Omega_n t_i) + a_{V_{s_n}}(r_q,\Omega_n)\sin(\Omega_n t_i)\right) \tag{4.32}$$

$$\Psi_{2_{th}}(r_q,t_i) = \sum_{n=1}^{2}\left(b_{V_{c_n}}(r_q,\Omega_n)\cos(\Omega_n t_i) + b_{V_{s_n}}(r_q,\Omega_n)\sin(\Omega_n t_i)\right) \tag{4.33}$$

where $a_{V_{c_n}}$, $a_{V_{s_n}}$, $b_{V_{c_n}}$, $b_{V_{s_n}}$ are the respective coefficients of the NAFF analysis and $\Omega_1=\Omega_b$, $\Omega_2=\Omega_{sp}$.

### 4.2.4 Modelling the gravitational potential

The semi-analytical formula for the bar potential given by (4.31)-(4.33) can be written as follows:

$$\begin{aligned} V_b(r_q,\varphi_p,t_i) = & \tfrac{1}{2}\left(a_{V_{c_1}}(r_q,\Omega_b) + b_{V_{s_1}}(r_q,\Omega_b)\right) \\ & \cos[2(\varphi_p - \Omega_b(t_i-t_0))] + \\ & \tfrac{1}{2}\left(a_{V_{c_1}}(r_q,\Omega_b) - b_{V_{s_1}}(r_q,\Omega_b)\right)\cos[2(\varphi_p + \Omega_b(t_i-t_0))] + \\ & \tfrac{1}{2}\left(b_{V_{c_1}}(r_q,\Omega_b) - a_{V_{s_1}}(r_q,\Omega_b)\right)\sin[2(\varphi_p - \Omega_b(t_i-t_0))] + \\ & \tfrac{1}{2}\left(a_{V_{s_1}}(r_q,\Omega_b) + b_{V_{c_1}}(r_q,\Omega_b)\right)\sin[2(\varphi_p + \Omega_b(t_i-t_0))] \quad . \end{aligned} \tag{4.34}$$

We notice that the NAFF formula gives rise both to $\begin{matrix}\sin\\ \cos\end{matrix}[2(\varphi_p - \Omega_b(t_i - t_0))]$ and $\begin{matrix}\sin\\ \cos\end{matrix}[2(\varphi_p + \Omega_b(t_i - t_0))]$ terms. However, the terms of $\cos[2(\varphi_p + \Omega_b(t_i - t_0))]$ and $\sin[2(\varphi_p + \Omega_b(t_i - t_0))]$ can be neglected as their coefficients are small with respect to the coefficients of the $\cos[2(\varphi_p - \Omega_b(t - t_0))]$ and $\sin[2(\varphi_p - \Omega_b(t_i - t_0))]$ terms. Figure 4.12 shows the quantity:

$$P_{coef} = \sqrt{\frac{\left(a_{V_{c_1}}(r_q,\Omega_b) - b_{V_{s_1}}(r_q,\Omega_b)\right)^2 + \left(a_{V_{s_1}}(r_q,\Omega_b) + b_{V_{c_1}}(r_q,\Omega_b)\right)^2}{\left(a_{V_{c_1}}(r_q,\Omega_b) + b_{V_{s_1}}(r_q,\Omega_b)\right)^2 + \left(b_{V_{c_1}}(r_q,\Omega_b) - a_{V_{s_1}}(r_q,\Omega_b)\right)^2}} \tag{4.35}$$

as a function of the radius r. From Fig. 4.12 we conclude that $P_{coef}$ remains smaller than 10% across the whole galactic disc, which is consistent with the $\mathcal{O}(1/T)$ error in the specification of the NAFF amplitudes. In the sequel, for simplicity we adopt for the bar potential the approximate formula:

$$\begin{aligned} &V_b(r_q,\varphi_p,t_i) = \\ &\frac{1}{2}\left(a_{V_{c_1}}(r_q,\Omega_b) + b_{V_{s_1}}(r_q,\Omega_b)\right)\cos[2(\varphi_p - \Omega_b(t_i - t_0))] \\ &+ \frac{1}{2}\left(b_{V_{c_1}}(r_q,\Omega_b) - a_{V_{s_1}}(r_q,\Omega_b)\right)\sin[2(\varphi_p - \Omega_b(t_i - t_0))] \quad . \end{aligned} \tag{4.36}$$

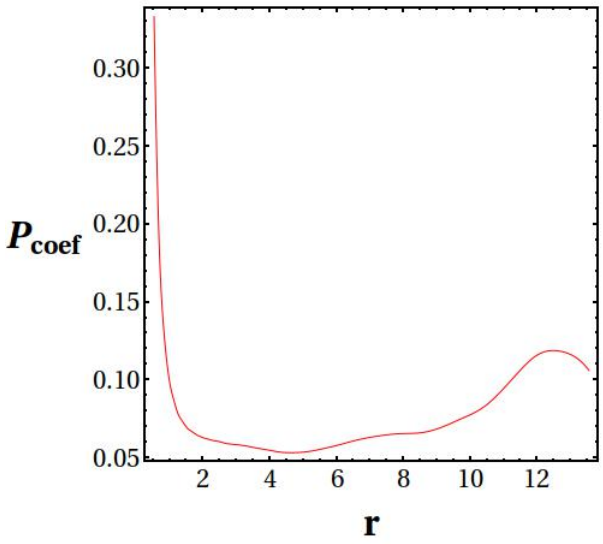


**Figure 4.12**: *The power spectrum $P_{coef}$ of Eq. (4.35) is plotted as a function of r.*

By a similar analysis we adopt for the potential of the spiral arms the approximate formula:

$$\begin{aligned} &V_{sp}(r_q,\varphi_p,t_i) = \\ &\frac{1}{2}\left(a_{V_{c_2}}(r_q,\Omega_{sp}) + b_{V_{s_2}}(r_q,\Omega_{sp})\right)\cos[2(\varphi_p - \Omega_{sp}(t_i - t_0))] \\ &+ \frac{1}{2}\left(b_{V_{c_2}}(r_q,\Omega_{sp}) - a_{V_{s_2}}(r_q,\Omega_{sp})\right)\sin[2(\varphi_p - \Omega_{sp}(t_i - t_0))] \quad . \end{aligned} \tag{4.37}$$

Therefore, the final semi-analytical potential model used below takes the form:

$$V(r_q, \varphi_p, t_i) = V_0(r_q, t_i) + V_b(r_q, \varphi_p, t_i) + V_{sp}(r_q, \varphi_p, t_i) \tag{4.38}$$

where $V_0(r_q, t_i)$ is the axisymmetric term of the potential, $V_b(r_q, \varphi_p, t_i)$ the potential of the galactic bar given by Eq. (4.36) and $V_{sp}(r_q, \varphi_p, t_i)$ the potential of the spiral arms given by Eq. (4.37).

Applying the same simplifications to the semi-analytical formula for the surface density of the galaxy we are led to the approximate formula:

$$\begin{aligned}
&\Sigma_{th}(r_q, \varphi_p, t_i) = A_0(r_q, t_i) + \\
&\frac{1}{2}\sum_{j=1}^{2}\left(a_{c_j}(r_q, \Omega_j) + b_{s_j}(r_q, \Omega_j)\right) cos[2(\varphi_p - \Omega_j(t_i - t_0))] + \\
&\left(b_{c_j}(r_q, \Omega_j) - a_{s_j}(r_q, \Omega_j)\right) \sin[2(\varphi_p - \Omega_j(t_i - t_0))]
\end{aligned} \tag{4.39}$$

where $\Omega_1 = \Omega_b$, $\Omega_2 = \Omega_{sp}$.

We perform now various tests of the above approximate formulas against the real potential at each snapshot of the simulation. Tests can be made as regards the precision of the semi-analytical formula yielding the galactic potential and the respective forces. For any fixed radius r we calculate the potential $V$ as a function of the azimuth $\varphi$ in the disc plane in three ways:

(a) by the semi analytical formula of the potential of Eqs. (4.36)-(4.38) for the m=0,2 modes.

(b) by the numerical form of the potential for m=0,2 modes of the potential of Eq. (4.27)

(c) by the complete numerical form of the potential obtained directly from the N-body code.

Figures 4.13, 4.15 show the comparison between the semi-analytical model for the potential and the corresponding numerical models (m=0,2 modes or complete) at some snapshots of the time windows $T_1$ (Fig. 4.13) and $T_2$ (Fig. 4.15), and for two indicative radii r=3.2 kpc and r=10.3 kpc. The m=0,2 curves (semi-analytical and numerical) are quite close to each other. The curves of the complete numerical potential, instead, deviate from the respective curves (both the numerical and semi-analytical) m=0,2 by about 10% at inner radii and about 2% at outer radii (observe the vertical scale in each panel). This deviation is due to the relative importance of the modes m>2 (but also m=1, see Efthymiopoulos et al. (2020)) which become relevant at radii covering the whole extent of the bar.

The deviation can be better quantified by computing the azimuthal forces $F_\varphi = \frac{1}{r}\frac{\partial V}{\partial \varphi}$ with the various models, as a function of $\varphi$ and for fixed r (Figs. 4.14 and 4.16 for the time windows $T_1$ and $T_2$ respectively). The calculation of the forces (derivatives of the potential) in the semi-analytical model is realised by implementing a cubic spline interpolation formula to smoothly connect the values of the coefficients $a_{V_{c_{1,2}}}$, $a_{V_{s_{1,2}}}$, $b_{V_{c_{1,2}}}$, $b_{V_{s_{1,2}}}$ given at the grid points $r = r_q$. Notwithstanding the agreement between the m=0,2 semi-analytical and numerical force models, we observe that the errors in the azimuthal force calculation due to the omission of the terms besides m=0,2 can be locally enhanced up to 40%. At any rate, these errors concern only the evaluation of the force due to the m=1, or m>2 terms, which is already a pertubation with respect to the leading component of the force (due to the axisymmetric (m=0) term). As a result plotting the isocontours of the effective potential

$$V_{eff}(r, \varphi, t) = V(r, \varphi, t) - \frac{1}{2}{\Omega_b}^2 r^2 \tag{4.40}$$

shows an overall agreement between all these potential models (Fig. 4.17), with the (m=0,2) model only failing to catch the asymmetry of the isocontours in the complete model.

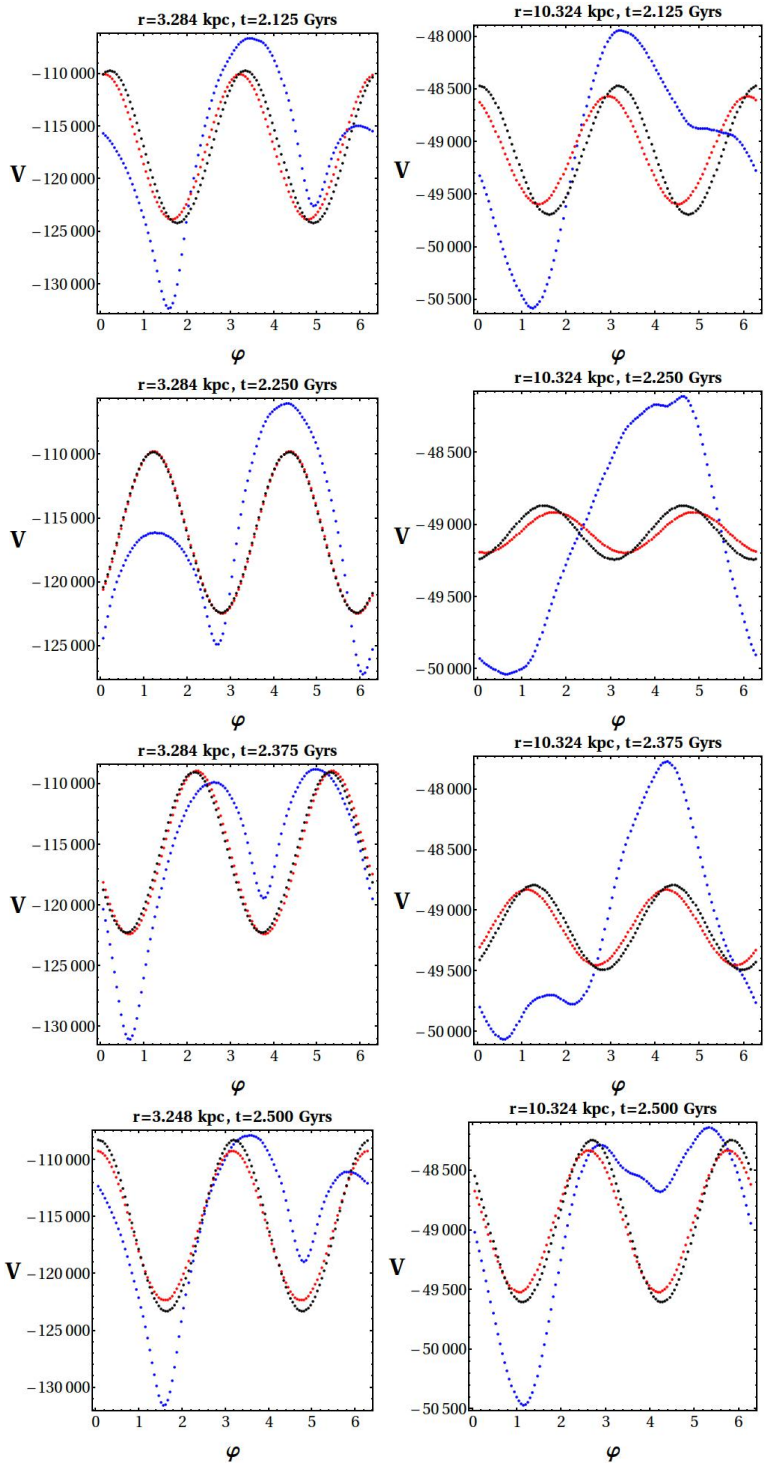


**Figure 4.13**: *The gravitational potential V as a function of the azimuthal angle $\varphi$, at the radii $r = 3.248$ kpc and $r = 10.324$ kpc for 4 different snapshots within the window $T_1 = 2.125 - 2.625$ Gyr. The potential is calculated in three ways: (a) by the semi-analytical formulas (4.36)-(4.38) (black curves) (b) by the numerical form of the potential for m=0,2 modes of the potential of Eq. (4.27) (red curves) (c) by the complete numerical form of the potential with all the modes of the galaxy (m=0-10) of the potential of Eq. (4.27) (blue curves).*

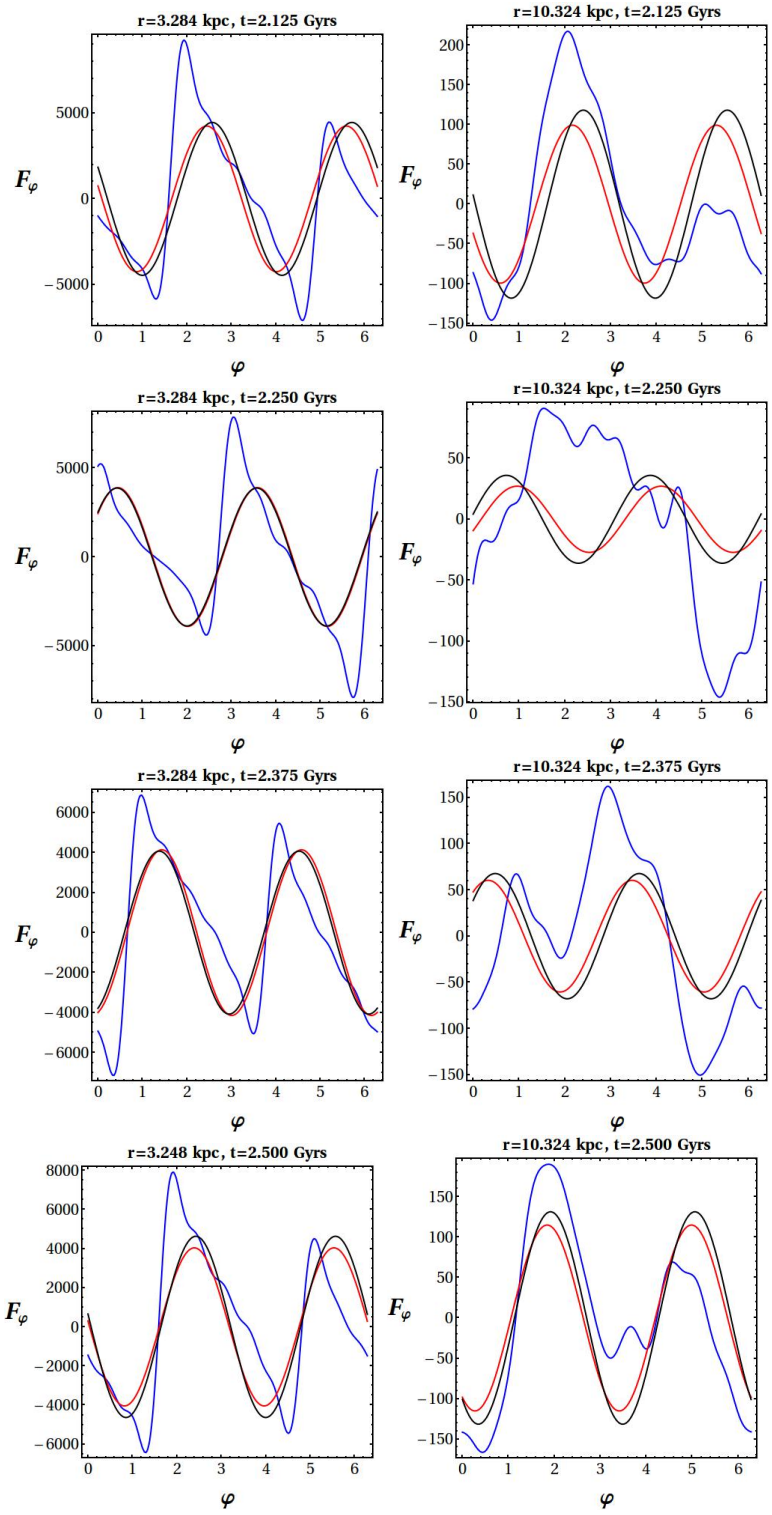


**Figure 4.14**: *The azimuthal gravitational force* $F_\varphi = \frac{1}{r}\frac{\partial V}{\partial \varphi}$ *as a function of the azimuthal angle* $\varphi$*, at the radii* $r = 3.248$ *kpc and* $r = 10.324$ *kpc for 4 different snapshots within the window* $T_1 = 2.125 - 2.625$ *Gyr, calculated in three ways: (a) by the derivatives of the semi-analytical formulas of the potential of Eqs. (4.36)-(4.38) for the m=0,2 modes of the galaxy (black curves) (b) by the derivatives of the numerical form of the potential for m=0,2 modes of the potential of Eq. (4.27) (red curves) (c) by the derivatives of the complete interpolated numerical form of the potential (blue curves).*

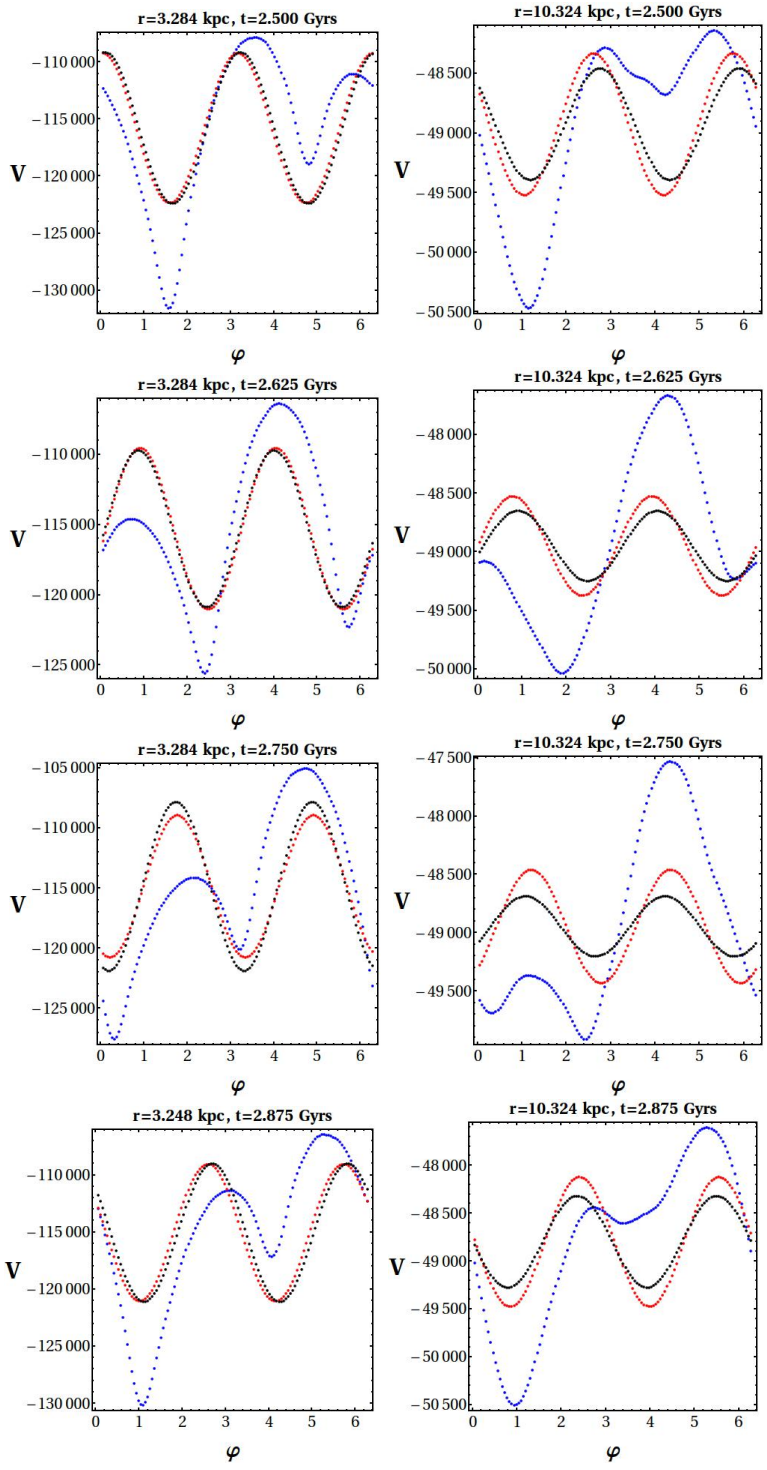


**Figure 4.15**: *The gravitational potential V as a function of the azimuthal angle $\varphi$, at the radii $r = 3.248$ kpc and $r = 10.324$ kpc for 4 different snapshots within the window $T_2 = 2.500 - 3.000$ Gyr. The potential is calculated in three ways: (a) by the semi-analytical formulas (4.36)-(4.38) (black curves) (b) by the numerical form of the potential for m=0,2 modes of the potential of Eq. (4.27) (red curves) (c) by the complete numerical form of the potential with all the modes of the galaxy (m=0-10) of the potential of Eq. (4.27) (blue curves).*

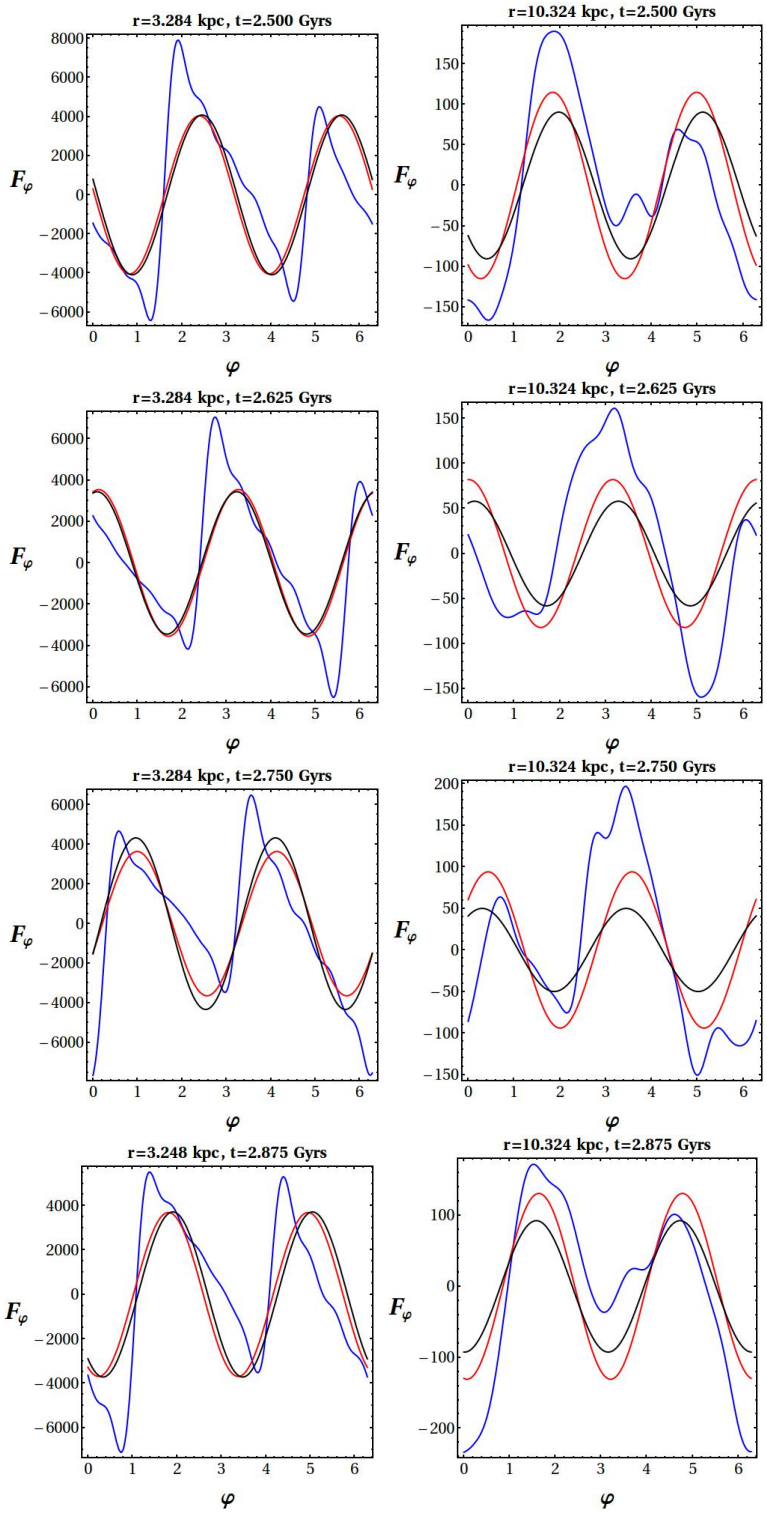


**Figure 4.16**: *The azimuthal gravitational force* $F_\varphi = \frac{1}{r}\frac{\partial V}{\partial \varphi}$ *as a function of the azimuthal angle* $\varphi$*, at the radii* $r = 3.248$ *kpc and* $r = 10.324$ *kpc for 4 different snapshots within the window* $T_2 = 2.500 - 3.000$ *Gyr, calculated in three ways: (a) by the derivatives of the semi-analytical formulas of the potential of Eqs. (4.36)-(4.38) for the m=0,2 modes of the galaxy (black curves) (b) by the derivatives of the numerical form of the potential for m=0,2 modes of the potential of Eq. (4.27) (red curves) (c) by the derivatives of the complete interpolated numerical form of the potential (blue curves).*

As explained in Efthymiopoulos et al. (2020), a computation of manifolds in the regime of multiple patterns (and pattern speeds) is possible by a pertubative calculation including modes of any value of m, as well as an arbitary number of pattern

frequencies $\Omega_1, \Omega_2, \ldots$. Since, however, the computation becomes quite cumbersome with the addition of many modes, in view of the above tests in the sequel we will limit ourselves to an investigation of the manifold model by the semi-analytical representation of the potential including only the m=2 non-axisymmetric modes (Eqs. (4.36) to (4.38)), and the pattern speeds $\Omega_b$ and $\Omega_{sp}$, as specified by just one iteration of the NAFF algorithm. We emphasize, however, that the construction of a precise potential model including more modes is straightforward as it only requires further iteration of the NAFF algorithm, and it was only omitted here for reasons of keeping low the cost of computations related to the manifolds (see section 4.3 below).

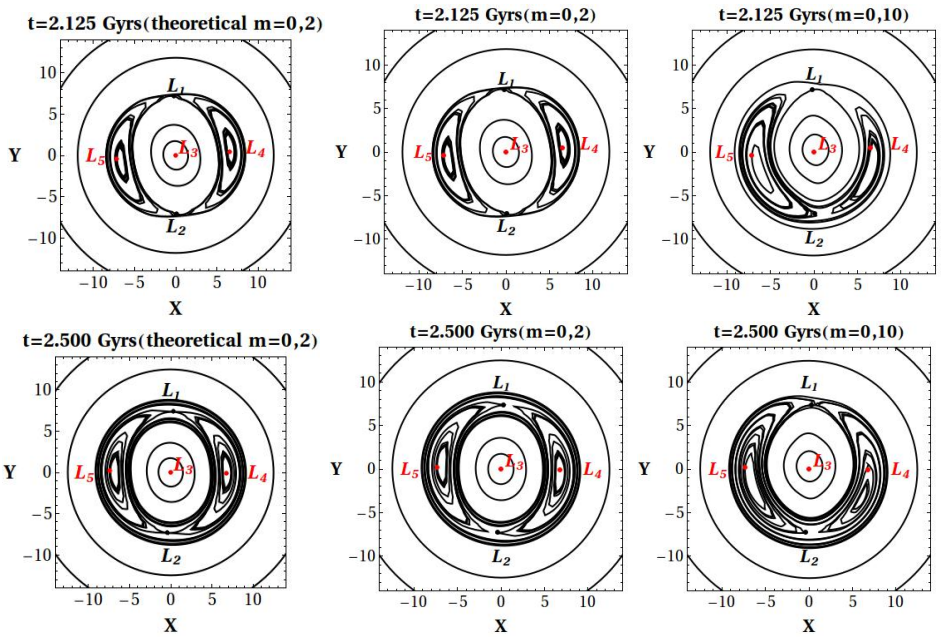


**Figure 4.17**: *The zero velocity curves given by Eq. (4.40) for the snapshot t=2.125 Gyr of the time window $T_1 = 2.125 - 2.625$ Gyr of the simulation (top row) and the snapshot t=2.500 Gyr of the time window $T_2 = 2.500 - 3.000$ Gyr (bottom row), calculated in 3 ways: (a) by the semi-analytical formula of the potential of Eqs. (4.36)-(4.38) for the m=0,2 modes of the galaxy (b) by the numerical form of the potential for m=0,2 modes of the potential of Eq. (4.27) (c) by the complete numerical form of the potential with all the modes of the galaxy (m=0-10) of the potential of Eq. (4.27). On the plots the red spots are the stable Lagrangian points $L_{3,4}$ and the black ones are the unstable Lagrangian points $L_{1,2}$.*

## 4.3 The manifolds in the NAFF model with two pattern speeds

### 4.3.1 Hamiltonian model and equations of motion

Consider a frame of reference which corotates with the bar. Introduce the angular variable:

$$\vartheta = \varphi_p - \Omega_b(t_i - t_0) \quad . \tag{4.41}$$

The semi-analytical formula for the bar potential (Eq. (4.36)) becomes:

$$V_b(r_q, \vartheta) = \tfrac{1}{2}\left(a_{V_{c_1}}(r_q, \Omega_b) + b_{V_{s_1}}(r_q, \Omega_b)\right)\cos(2\vartheta) + \tfrac{1}{2}\left(b_{V_{c_1}}(r_q, \Omega_b) - a_{V_{s_1}}(r_q, \Omega_b)\right)\sin(2\vartheta) \quad . \tag{4.42}$$

Let now $\vartheta_2$ be the phase difference between the bar and the spiral arms due to the different adopted values of the two pattern speeds:

$$\vartheta_2 = (\Omega_{sp} - \Omega_b)(t_i - t_0) \quad . \tag{4.43}$$

Using Eqs. (4.41) and (4.43), the angle $\varphi_p - \Omega_{sp}(t_i - t_0)$ in Eq. (4.37) takes the form:

$$\varphi_p - \Omega_{sp}(t_i - t_0) = \vartheta + \Omega_b(t_i - t_0) - (\vartheta_2 + \Omega_b(t_i - t_0)) = \vartheta - \vartheta_2 \quad . \tag{4.44}$$

As a result the potential of the spiral arms (Eq. (4.37)) takes the form:

$$\begin{aligned} V_{sp}(r_q, \vartheta, \vartheta_2) = \tfrac{1}{2}\left(a_{V_{c_2}}(r, \Omega_{sp}) + b_{V_{s_2}}(r_q, \Omega_{sp})\right)\cos[2(\vartheta - \vartheta_2)] \\ + \tfrac{1}{2}\left(b_{V_{c_2}}(r_q, \Omega_{sp}) - a_{V_{s_2}}(r_q, \Omega_{sp})\right)\sin[2(\vartheta - \vartheta_2)] \quad . \end{aligned} \tag{4.45}$$

The potential of Eq. (4.45) varies in time periodically with a period $T_P$ given by:

$$T_P = \frac{\pi}{|\Omega_{sp} - \Omega_b|} \quad . \tag{4.46}$$

Consider, finally, the Hamiltonian function

$$\begin{aligned} H(r, \vartheta, \vartheta_2, P_r, P_\vartheta, J_2) = \frac{{P_r}^2}{2} + \frac{{P_\vartheta}^2}{2r^2} + V_0(r) + V_b(r, \vartheta) \\ - \Omega_b P_\vartheta + (\Omega_{sp} - \Omega_b)J_2 + V_{sp}(r, \vartheta, \vartheta_2) \end{aligned} \tag{4.47}$$

where $(r, P_r)$, $(\vartheta, P_\vartheta)$, $(\vartheta_2, J_2)$ are canonical pairs. The equations of motion for a test particle (e.g. star) in the bar's rotating frame are given by:

$$\begin{aligned} \dot{r} = \tfrac{\partial H}{\partial P_r} \quad , \quad \dot{P}_r = -\tfrac{\partial H}{\partial r} = \tfrac{{P_\vartheta}^2}{r^3} - \tfrac{\partial V_0}{\partial r} - \tfrac{\partial V_b}{\partial r} - \tfrac{\partial V_{sp}}{\partial r} \\ \dot{\vartheta} = \tfrac{\partial H}{\partial P_\vartheta} = \tfrac{P_\vartheta}{r^2} - \Omega_b \quad , \quad \dot{P}_\vartheta = -\tfrac{\partial H}{\partial \vartheta} = -\tfrac{\partial V_b}{\partial \vartheta} - \tfrac{\partial V_{sp}}{\partial \vartheta} \quad . \\ \dot{\vartheta}_2 = \tfrac{\partial H}{\partial J_2} = \Omega_{sp} - \Omega_b \quad , \quad \dot{J}_2 = -\tfrac{\partial H}{\partial \vartheta_2} = -\tfrac{\partial V_{sp}}{\partial \vartheta_2} \end{aligned} \tag{4.48}$$

The last equation, for $J_2$, can be used as a control for the conservation of the energy $E = H(r(t), \vartheta(t), \vartheta_2(t), P_r(t), P_\vartheta(t), J_2(t))$ along the numerical propagation of any individual trajectory.

We will employ the equations of motion (4.48) in all subsequent computations related to periodic orbits and their manifolds in our model.

### 4.3.2 Locating the periodic equilibrium orbit $GL_{1,2}$

According to the manifold theory of spirals (Romero-Gomez et al. (2006), Voglis et al. (2006)) in galactic models with a single pattern speed the manifolds emanate from the unstable Lagrangian equilibrium points $L_{1,2}$, which lie in the end of the bar. In the case of multiple pattern speeds, instead, the Lagrangian equilibrium point solutions $L_{1,2}$ generalise to periodic equilibrium orbits $GL_{1,2}$, whose period is equal to the period $T_P$ of Eq. (4.46) (Efthymiopoulos et al. (2020)). The manifolds emanating from $GL_{1,2}$ have also a periodic dependence on time.

To compute the periodic orbit $GL_1$ (and, analogously, $GL_2$) in our N-body model we first locate the Lagrangian equilibrium point $L_1$ of the 'bar-only' Hamiltonian $H_b$ defined by

$$H_b(r, \vartheta, P_r, P_\vartheta) = \frac{1}{2}\left({P_r}^2 + \frac{{P_\vartheta}^2}{2r^2}\right) - \Omega_b P_\vartheta + V_0(r) + V_b(r, \vartheta) \tag{4.49}$$

by computing numerically the fixed points of Hamilton's equations:

$$\frac{\partial H_b}{\partial r} = \frac{\partial H_b}{\partial \vartheta} = \frac{\partial H_b}{\partial P_r} = \frac{\partial H_b}{\partial P_\vartheta} = 0 \quad . \tag{4.50}$$

The Lagrangian equilibrium point $L_1$ (solution of Eq. (4.50)) has coordinates $(r_{L_1}, \vartheta_{L_1}, P_{r_{L_1}}, P_{\vartheta_{L_1}} = \Omega_b r_{L_1}^2)$. Consider, then, the Hamiltonian

$$\mathcal{H}_\varepsilon = H_b + (\Omega_{sp} - \Omega_b) J_2 + \varepsilon V_{sp}(r, \vartheta, \vartheta_2) \tag{4.51}$$

which coincides with the full Hamiltonian of the problem for $\varepsilon = 1$. We finally consider a local expansion of the canonical variables around $L_1$:

$$\begin{aligned} r &= r_{L_1} + \Delta r(t) \\ \vartheta &= \vartheta_{L_1} + \Delta\vartheta(t) \\ P_r &= P_{r_{L_1}} + \Delta P_r(t) \\ P_\vartheta &= P_{\vartheta_{L_1}} + \Delta P_\vartheta(t) \quad . \end{aligned} \tag{4.52}$$

The periodic orbit GL1 corresponds to a periodic solution of Hamilton's equations under the full Hamiltonian with period equal to $T_P$, for which $\Delta r(T_P) = \Delta r(0)$, $\Delta\theta(T_P) = \Delta\theta(0)$, $\Delta P_r(T_P) = \Delta P_r(0)$, $\Delta P\theta(T_P) = \Delta P_\theta(0)$. Defining the 4D stroboscopic mapping for the Hamiltonian $\mathcal{H}_\varepsilon$ given by $\mathcal{M}_\varepsilon$:($\mathcal{M}_{\varepsilon,r}$, $\mathcal{M}_{\varepsilon,\vartheta}$, $\mathcal{M}_{\varepsilon,P_r}$, $\mathcal{M}_{\varepsilon,P_\vartheta}$) where:

$$\begin{aligned} r' &= \mathcal{M}_{\varepsilon,r}(r, \vartheta, P_r, P_\vartheta) \\ &= r(t = T_P, r(0) = r, \vartheta(0) = \vartheta, P_r(0) = P_r, P_\vartheta(0) = P_\vartheta) \\ \vartheta' &= \mathcal{M}_{\varepsilon,\vartheta}(r, \vartheta, P_r, P_\vartheta) \\ &= \vartheta(t = T_P, r(0) = r, \vartheta(0) = \vartheta, P_r(0) = P_r, P_\vartheta(0) = P_\vartheta) \\ P_r' &= \mathcal{M}_{\varepsilon,P_r}(r, \vartheta, P_r, P_\vartheta) \\ &= P_r(t = T_P, r(0) = r, \vartheta(0) = \vartheta, P_r(0) = P_r, P_\vartheta(0) = P_\vartheta) \\ P_\vartheta' &= \mathcal{M}_{\varepsilon,P_\vartheta}(r, \vartheta, P_r, P_\vartheta) \\ &= P_\vartheta(t = T_P, r(0) = r, \vartheta(0) = \vartheta, P_r(0) = P_r, P_\vartheta(0) = P_\vartheta) \quad . \end{aligned} \tag{4.53}$$

one may attempt to find the periodic orbit $GL_1$ purely numerically, as a period-one fixed point of $\mathcal{M}_\varepsilon$ for $\varepsilon = 1$. Experience shows that a quick trial, e.g., with the Newton-Raphson method, setting the $L_1$ state vector as initial guess, typically fails. Alternatively, one can try to use the Newton-Raphson method as above, but computing the entire family $GL_1$ for parameter values $\varepsilon_{min} \leq \varepsilon \leq 1$, where $\varepsilon_{min} << 1$. In our model this works if $\varepsilon_{min}$ is taken equal to $0.01$ and the computation of the fixed point of the mapping is continued forward up to $\varepsilon = 1$ with steps $\Delta\varepsilon = 0.01$. The computation, however, is greatly accelerated, if, instead, one computes a partially hyperbolic normal form around $L_1$, expanding first the Hamiltonian with respect to the variables $\Delta r$, $\Delta\theta$, $\Delta P_r$, $\Delta P_\theta$, diagonalizing the quadratic part to obtain linear local normal form, and then computing few steps of the nonlinear local normal form. All necessary steps are described in detail in Efthymiopoulos et al. (2020). In the sequel we are going to present this procedure:

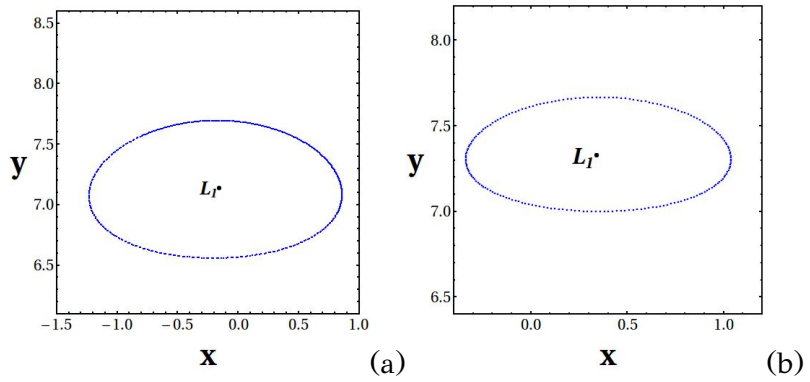


**Figure 4.18**: *The equlibrium periodic orbits $GL_1$ as computed by the procedure of subsection 4.3.2 and the potential data in the two time windows (a) $T_1 = 2.125 - 2.625$ Gyr (b) $T_2 = 2.500 - 3.000$ Gyr.*

1) The new Hamiltonian, after the expansion, reads:

$$H_0 = H_0(\Delta r, \Delta\vartheta, \Delta P_r, \Delta P_\vartheta) = H_b(r_{L_1}, \vartheta_{L_1}, P_{r_{L_1}}, P_{\vartheta_{L_1}}) + (\Delta r, \Delta\vartheta, \Delta P_r, \Delta P_\vartheta)\mathcal{M}\begin{pmatrix}\Delta r\\ \Delta\vartheta\\ \Delta P_r\\ \Delta P_\vartheta\end{pmatrix} \tag{4.54}$$

where $\mathcal{M}$ is the variational matrix at the point $L_1$:

$$\mathcal{M} = \begin{bmatrix} \frac{\partial^2 H_b}{\partial r^2} & \frac{\partial^2 H_b}{\partial r \partial\vartheta} & \frac{\partial^2 H_b}{\partial r \partial P_r} & \frac{\partial^2 H_b}{\partial r \partial P_\vartheta} \\ \frac{\partial^2 H_b}{\partial\vartheta \partial r} & \frac{\partial^2 H_b}{\partial\vartheta^2} & \frac{\partial^2 H_b}{\partial\vartheta \partial P_r} & \frac{\partial^2 H_b}{\partial\vartheta \partial P_\vartheta} \\ \frac{\partial^2 H_b}{\partial P_r \partial r} & \frac{\partial^2 H_b}{\partial P_r \partial\vartheta} & \frac{\partial^2 H_b}{\partial P_r^2} & \frac{\partial^2 H_b}{\partial P_r \partial P_\vartheta} \\ \frac{\partial^2 H_b}{\partial P_\vartheta \partial r} & \frac{\partial^2 H_b}{\partial P_\vartheta \partial\vartheta} & \frac{\partial^2 H_b}{\partial P_\vartheta \partial P_r} & \frac{\partial^2 H_b}{\partial P_\vartheta^2} \end{bmatrix}_{r_{L_1}, \vartheta=\vartheta_{L_1}, P_r=P_{r_{L_1}}, P_\vartheta=P_{\vartheta_{L_1}}} . \tag{4.55}$$

2) Diadonalization of the Hamiltonian $H_0$: the variational matrix $\mathcal{M}$ has two real eigenvalues $\pm\mu$ and two imaginary eigenvalues $\pm i\kappa$, where $\mu, \kappa > 0$. Thus, it has also four eigenvectors, of which two, $(e_1, e_2)$, are associated with the real eigenvalues $\pm\mu$, and the other two, $(e_3, e_4)$, are associated with the imaginary eigenvalues $\pm i\kappa$. Each eigenvector can be written as a vertical column with four components. We then define the matrix $\mathcal{B} = (c_1 e_1 \quad c_2 e_2 \quad c_1 e_3 \quad c_2 e_4)$ with unspecified coefficients $c_i$, $i = 1, 2$. The symplectic condition allows us to specify the coefficients $c_i$ and thus all the components of $\mathcal{B}$. The symplectic condition is:

$$\mathcal{B}^{\mathcal{T}} \mathcal{J} \mathcal{B} = \mathcal{J} \tag{4.56}$$

where $\mathcal{J}$ is the fundamental symplectic matrix:

$$\mathcal{J} = \begin{bmatrix} 0 & I_2 \\ -I_2 & 0 \end{bmatrix} \tag{4.57}$$

and $I_2$ is the $2 \times 2$ identity matrix.

We also define the matrix:

$$\mathcal{C} = \begin{bmatrix} 1 & 0 & 0 & 0 \\ 0 & \frac{1}{\sqrt{2}} & 0 & \frac{-i}{\sqrt{2}} \\ 0 & 0 & 1 & 0 \\ 0 & \frac{-i}{\sqrt{2}} & 0 & \frac{1}{\sqrt{2}} \end{bmatrix} . \tag{4.58}$$

Define, now, the $4\times4$ matrix $\mathcal{A}=\mathcal{BC}$, as well as the linear tranformation $(\Delta r, \Delta\vartheta, \Delta P_r, \Delta P_\vartheta) \rightarrow (u,q,v,p)$ given by:

$$\begin{pmatrix} \Delta r \\ \Delta\vartheta \\ \Delta P_r \\ \Delta P_\vartheta \end{pmatrix} = \mathcal{A} \begin{pmatrix} u \\ q \\ v \\ p \end{pmatrix} \quad . \tag{4.59}$$

Substituting the transformation (4.59) into the Hamiltonian $H_0$ (Eq. (4.54)), the latter obtains a diagonal form:

$$H_0'(u,q,v,p) = \mu(vu) + \frac{\kappa}{2}\left(q^2+p^2\right) \quad . \tag{4.60}$$

Note that the term $\frac{\kappa}{2}\left(q^2+p^2\right)$ has the form of a harmonic oscillator and it is physically related to epicyclic oscillations with frequency $\kappa = \sqrt{\frac{\partial^2 V_0}{\partial r_{L_1}^2} + \frac{3p_{\varphi,L_1}^2}{r_{L_1}^4}}$. On the other hand, at the neighbourhood of the equilibrium point $L_1$ the term $\mu(vu)$ describes an exponential deviation from the Lagrangian point of the form $u=u_o e^{\mu t}$ following the unstable direction. Therefore, the Hamiltonian $H_0'(u,q,v,p)$ consists of two terms whose combination describes the motion of the guiding centre and of the epicycle that travels along the manifold.

3) Applying, now, the linear transformation (4.59) the complete Hamiltonian $H(r,\vartheta,\vartheta_2,P_r,P_\vartheta,J_2)$ of Eq. (4.47) leads to the Hamiltonian expressed in the variables $(u,q,\vartheta_2,v,p,J_2)$:

$$\begin{aligned} H'(u,q,\vartheta_2,v,p,J_2) &= H_0'(u,q,v,p) + (\Omega_{sp}-\Omega_b)J_2 \\ &+P_1(u,q,v,p) + P_2(\vartheta_2,u,q,v,p) \end{aligned} \tag{4.61}$$

where $P_1(u,q,v,p)$ is a polynomial independent of $\vartheta_2$:

$$P_1(u,q,v,p) = \sum_{s=3}^{\infty} \sum_{k_1+k_2+l_1+l_2=s} c_{k_1,k_2,l_1,l_2} u^{k_1} q^{k_2} v^{l_1} p^{l_2} \tag{4.62}$$

with $c_{k_1,k_2,l_1,l_2}$ constants, while $P_2(\vartheta_2,u,q,v,p)$ is a polynomial depending on $\vartheta_2$, of the form:

$$P_2(\vartheta_2,u,q,v,p) = \sum_{s=1}^{\infty} \sum_{k_1+k_2+l_1+l_2=s} V_{(2),k_1,k_2,l_1,l_2}(\vartheta_2) u^{k_1} q^{k_2} v^{l_1} p^{l_2} \quad . \tag{4.63}$$

By using Hamilton's equations under the Hamiltonian (4.61) it is now easy to see that the point $L_1$ with coordinates $(u=q=v=p=0)$ is no longer equilibrium point, since we have non-zero corresponding velocities $\dot{u},\dot{q},\dot{v},\dot{p}\neq 0$. This happens because the function $V_{(2),k_1,k_2,l_1,l_2}(\vartheta_2)$ is non-zero for $k_1+k_2+l_1+l_2=1$. Physically, the phase space coordinates of $L_1$ no longer imply equlibrium due to the time dependency of the system.

We then introduce a near-to-identify nonlinear canonical transformation:

$$(u,q,v,p,\vartheta_2,J_2) \rightarrow (\xi,q',\eta,p',\vartheta_2,J_2') \tag{4.64}$$

where

$$\begin{aligned} u &= \xi + F_u(\xi,q',\eta,p';\vartheta_2) \\ q &= q' + F_q(\xi,q',\eta,p';\vartheta_2) \\ v &= \eta + F_v(\xi,q',\eta,p';\vartheta_2) \\ p &= p' + F_p(\xi,q',\eta,p';\vartheta_2) \end{aligned} \tag{4.65}$$

in such a way that the final form of the Hamiltonian has no longer terms linear in the variables $(\xi, q', \eta, p')$ :

$$H_f(\xi, q', \eta, p', \vartheta_2, J_2') = v\xi\eta + \frac{\kappa}{2}\left(q'^2 + p'^2\right) + (\Omega_{sp} - \Omega_b)J_2' \\ +\Phi_1(\xi, q', \eta, p') + \Phi_2(\vartheta_2, \xi, q', \eta, p') \tag{4.66}$$

where $J_2'$ is the conjugate action of the angle $\vartheta_2$, $\Phi_1(\xi, q', \eta, p')$ is a polynomial independent of $\vartheta_2$:

$$\Phi_1(\xi, q', \eta, p') = \sum_{s=3}^{\infty} \sum_{k_1+k_2+l_1+l_2=s} g_{k_1,k_2,l_1,l_2} \xi^{k_1} q'^{k_2} \eta^{l_1} p'^{l_2} \tag{4.67}$$

and $\Phi_2\vartheta_2, \xi, q', \eta, p')$ of the form:

$$\Phi_2(\vartheta_2, \xi, q', \eta, p') = \sum_{s=2}^{\infty} \sum_{k_1+k_2+l_1+l_2=s} V'_{k_1,k_2,l_1,l_2}(\vartheta_2) \eta^{k_1} q'^{k_2} \xi^{l_1} p'^{l_2} \quad . \tag{4.68}$$

The procedure to obtain the nonlinear transformation (4.65) is described in detail in Efthymiopoulos et al. (2020) . In summary, we work with the method of the composition of Lie series for the generation of the transformation of Eq. (4.65). In our actual computations in the N body model, as we are only able to compute Poisson brackets involving up to the second derivatives in the potential (due to the cubic spline interpolation scheme), we just perform two steps of the algorithm, with generating functions $\chi_1$, $\chi_2$. This yields the required $GL_1$ orbit with limited precision (see step 5 below), which, however, can be refined by use of a Newton algorithm. Note, also, that the transformation of Eq. (4.65) leaves the angular variable $\vartheta_2$ unaltered.

4) The point $\xi = q' = \eta = p' = 0$ is now an equilibrium point of the system, as Hamilton's equations give zero respective velocities $\dot{\xi} = \dot{q'} = \dot{\eta} = \dot{p'} = 0$. We apply a procedure of backward transformation in order to visualise the equilibrium solution in the original phase space with the initial coordinates. Using the transformation of Eq. (4.65) the equilibrium solution ($\xi = q' = \eta = p' = 0$, $\dot{\xi} = \dot{q'} = \dot{\eta} = \dot{p'} = 0$) takes the following form in the variables $(u, q, v, p)$:

$$\begin{aligned} u_{GL_1} &= F_u(0, 0, 0, 0; \vartheta_2) \\ q_{GL_1} &= F_q(0, 0, 0, 0; \vartheta_2) \\ v_{GL_1} &= F_v(0, 0, 0, 0; \vartheta_2) \\ p_{GL_1} &= F_p(0, 0, 0, 0; \vartheta_2) \end{aligned} \tag{4.69}$$

Through the linear transformation of Eq. (4.59) we then obtain ($\Delta r_{GL_1}$, $\Delta\vartheta_{GL_1}$, $\Delta P_{r_{GL_1}}$, $\Delta P_{\vartheta_{GL_1}}$), which are functions of $\vartheta_2$, i.e. functions of time. Hence, in the original variables $(r, \vartheta, P_r, P_\vartheta)$, the equlibrium solution (4.69) is mapped to time-dependent expression, function of $\vartheta_2 = (\Omega_{sp} - \Omega_b)t$. The time-depedency through the frequency $(\Omega_{sp} - \Omega_b)$ maps equilibrium solution $GL_1$ to a periodic orbit in the original variables. This equilibrium periodic orbit $(\xi_{GL_1}, q'_{GL_1}, \eta_{GL_1}, p'_{GL_1})$ is simply unstable (the variational matrix has one pair of real eigenvalues $\mu$ and two imaginary ones $\pm i\kappa$).

As discussed in Efthymiopoulos et al. (2020), the above method for the computation of $GL_1$ involves series which are convergent with the order of normalization. However, owing to the limitation from our modeling of the N-body potential, we cannot compute any series terms involving derivatives of the Hamiltonian in the canonical variables of order higher than the second, we are enforced to work with a very low truncation of the series yielding the transformation of Eq. (4.69). We can easily

check that this leads to a rather imprecise semi-analytical determination of the initial condition for the orbit $GL_1$, which, when integrated numerically lead actually to no periodicity (even approximately) in the computed orbit. To bypass this difficulty, we work as follows: consider a fictitious Hamiltonian model in which the amplitude of the spiral mode in the potential has been artificially reduced by a small factor $\varepsilon \ll 1$:

$$\begin{aligned}\mathcal{H}_{f,\varepsilon} =& H_0{}'(u,q,v,p) + (\Omega_{sp} - \Omega_b)J_2 + P_1(u,q,v,p) + \\ & \varepsilon P_2(\vartheta_2, u, q, v, p) \quad .\end{aligned} \tag{4.70}$$

We set $\varepsilon$ sufficently small so that the semi-analytical orbit $GL_1$ obtained by the transformation (4.69) computed on the Hamiltonian $\mathcal{H}_{f,\varepsilon}$ be sufficintly accurate. More precisely, knowing the period of the spiral pertubattion $P_2$, $T_P = \frac{\pi}{|\Omega_{sp}-\Omega_b|}$, for any initial condition $(r, \vartheta, P_r, P_\vartheta)$ we can propagate the corresponding trajectory under Hamilton's equations for the Hamiltonian $\mathcal{H}_{f,\varepsilon}$ and obtain fictitious trajectories defined by:

$$\begin{aligned}& r(t; r(0) = r, \vartheta(0) = \vartheta, P_r(0) = P_r, P_\vartheta(0) = P_\vartheta) = \\ & f_{\varepsilon,r}(r, \vartheta, P_r, P_\vartheta; \vartheta_2 = 0) \\ & \vartheta(t; r(0) = r, \vartheta(0) = \vartheta, P_r(0) = P_r, P_\vartheta(0) = P_\vartheta) = \\ & f_{\varepsilon,\vartheta}(r, \vartheta, P_r, P_\vartheta; \vartheta_2 = 0) \\ & P_r(t; r(0) = r, \vartheta(0) = \vartheta, P_r(0) = P_r, P_\vartheta(0) = P_\vartheta) = \\ & f_{\varepsilon,P_r}(r, \vartheta, P_r, P_\vartheta; \vartheta_2 = 0) \\ & P_\vartheta(t; r(0) = r, \vartheta(0) = \vartheta, P_r(0) = P_r, P_\vartheta(0) = P_\vartheta) = \\ & f_{\varepsilon,P_\vartheta}(r, \vartheta, P_r, P_\vartheta; \vartheta_2 = 0)\end{aligned} \tag{4.71}$$

where $f_\varepsilon$=($f_{\varepsilon,r}$, $f_{\varepsilon,\vartheta}$, $f_{\varepsilon,P_r}$, $f_{\varepsilon,P_\vartheta}$) defines the flow under the Hamiltonian $\mathcal{H}_{f,\varepsilon}$.

The mapping $\mathcal{M}_\varepsilon$ from Eq. (4.53) yields the image, after time equal to the period $T_P$, of any initial condition $(r, \vartheta, P_r, P_\vartheta)$ in the disc plane under the flow of the Hamiltonian $\mathcal{H}_{f,\varepsilon}$. Since the periodic orbit $GL_1$ has period equal to $T_P$, setting $r = r_{GL_1}(t=0)$, $\vartheta = \vartheta_{GL_1}(t=0)$, $P_r = P_{rGL_1}(t=0)$, $P_\vartheta = P_{\vartheta GL_1}(t=0)$ yields a fixed point of the mapping $\mathcal{M}_\varepsilon$. We then use the semi-analytical computation of the quantities ($r = r_{GL_1}(t=0)$, $\vartheta = \vartheta_{GL_1}(t=0)$, $P_r = P_{rGL_1}(t=0)$, $P_\vartheta = P_{\vartheta GL_1}(t=0)$) as initial guess in the Newton-Rapshson method, to accurately compute the periodic orbit $GL_1$ by the numerically found fixed point of the mapping $\mathcal{M}_\varepsilon$.

Finally, having been able to compute the orbit $GL_1$ on a fixed point of the mapping $\mathcal{M}_\varepsilon$, the whole characteristic family of $GL_1$ as a function of $\varepsilon$ can be now computed, by slowly varying $\varepsilon$ to $\varepsilon + \delta\varepsilon$, with $\delta\varepsilon$ sufficiently small to ensure the convergence of Newton-Raphson method, and using the computed fixed point of the mapping $\mathcal{M}_\varepsilon$ as initial guess for the computation of the fixed point of the mapping $\mathcal{M}_{\varepsilon+\delta\varepsilon}$. This eventually leads to the computation of the periodic orbit $GL_1$ (and, analogously, $GL_2$) for the actual potential model, i.e., for $\varepsilon = 1$. These orbits are shown in Fig. 4.19.

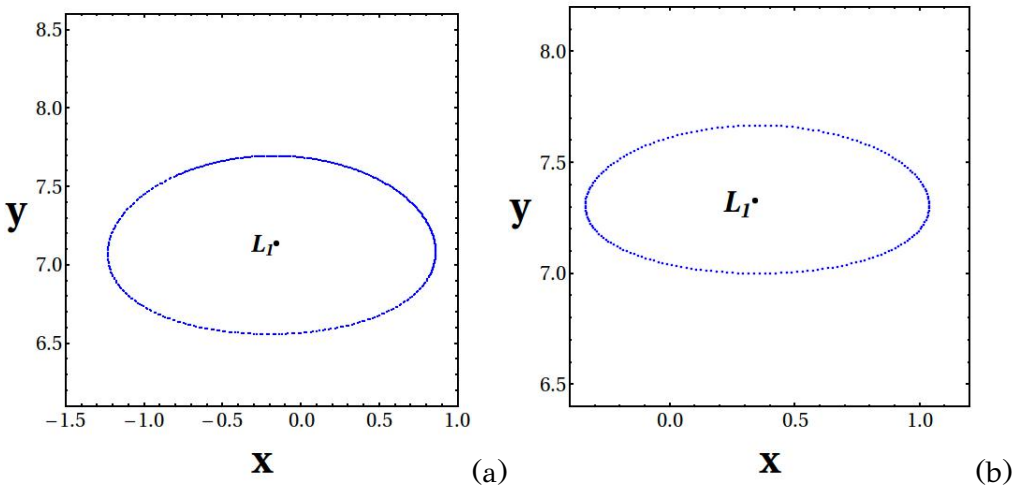


**Figure 4.19**: *The equlibrium periodic orbits $GL_1$ as computed by the procedure of subsection 4.3.2 and the potential data in the two time windows (a) $T_1 = 2.125 - 2.625$ Gyr (b) $T_2 = 2.500 - 3.000$ Gyr.*

### 4.3.3 The manifolds in the model with two pattern speeds

The dependence of the Hamiltonian $H(r, \vartheta, \vartheta_2, P_r, P_\vartheta, J_2)$ (Eq. (4.47)) on the angle $\vartheta_2$, i.e, on time, implies that, to visualise the manifolds of the periodic orbit $GL_1$ we are in need of plotting sections, not only in space, but also in time. To this end, we construct a stroboscopic and at the same time apocentric section of the orbits.

Let $t_0$ be the starting time of a particular window, i.e., $t_0 = 2.125$ Gyr for the time window $T_1$ and $t_0 = 2.500$ Gyr for time window $T_2$. The 'flux tube' manifolds of a snapshot $t$ within the considered window will be hereafter denoted as $W^U_{GL_{1,2}}(t_{sec})$, where we define the 'section time' $t_{sec}$ as $t_{sec} = t - t_0$. By definition $W^U_{GL_{1,2}}(t_{sec})$ is the set of all possible initial conditions in the disc plane, which, integrated backwards in time, starting from the time $t = t_{sec} + t_0$, lead to trajectories which tend asymptotically, as $t \to -\infty$, to the periodic orbits $GL_1$ (or $GL_2$). The manifolds $W^U_{GL_{1,2}}(t_{sec})$ can be computed by the following steps:

1) We first compute the Jacobian matrix $\Lambda$ of the mapping (4.53) evaluated at the fixed point of $GL_1$ (or $GL_2$) for $\varepsilon = 1$:

$$\Lambda = \left( \frac{\partial(\mathcal{M}_r, \mathcal{M}_\vartheta, \mathcal{M}_{P_r}, \mathcal{M}_{P_\vartheta})}{\partial(r, \vartheta, P_r, P_\vartheta)} \right)_{r=r_{GL_1}, \vartheta=\vartheta_{GL_1}, P_r=P_{r\,GL_1}, P_\vartheta=P_{\vartheta\,GL_1}} . \tag{4.72}$$

The matrix $\Lambda$ satisfies the symplectic condition $\Lambda J \Lambda^T = J$ and it has two real reciprocal eigenvalues $\lambda_1, \lambda_2$ and two complex ones $\lambda_{3,4} = e^{\pm i\omega T_P}$ with $\omega > 0$. The computation of the partial derivatives in the Jacobian matrix $\Lambda$ is done by iterating the mapping $\mathcal{M}$ numerically for nearby initial conditions and using centered finite differences.

2) We consider the unitary eigennvector $e^U_{GL_1}$ of $\Lambda$ which is associated to the real eigenvalue $\lambda_1$. This eigenvector defines the unstable eigendirection emanating from the unstable periodic orbit $GL_1$ with coordinates on the phase space ($r_{GL_1}$, $\vartheta_{GL_1}$, $P_{r_{GL_1}}$, $P_{\vartheta_{GL_1}}$). We then take a small initial segment of 3000 initial conditions $(r_i(0), \vartheta_i(0), P_{r_i}(0), P_{\vartheta_i}(0))$, $i = 1, ..., 3000$, that are distributed along the unstable eigendirection covering a total length $dS$=$10^{-3}$. Thus ($r_i(0)$, $\vartheta_i(0)$, $P_{r_i}(0)$, $P_{\vartheta_i}(0)$)=($r_{GL_1} + \delta r_i(0)$, $\vartheta_{GL_1} + \delta\vartheta_i(0)$, $P_{r_{GL_1}} + \delta P_{r_i}(0)$, $P_{\vartheta_{GL_1}} + \delta P_{\vartheta_i}(0)$) with ($\delta r_i(0)$, $\delta\vartheta_i(0)$, $\delta P_{r_i}(0)$, $\delta P_{\vartheta_i}(0)$)=$(i/3000) \times dS \times e^U_{GL_1}$

3) Given these initial conditions we propagate the orbits in time using Hamilton's equations for the Hamiltonian of Eq. (4.47). We then collect the points which, at a

time range $t = nT_P + t_{sec} \pm \Delta T_P$, with $n = 1, ...25$ and $\Delta T_P = 0.2T_P$, are close to a local apocentric passage of the orbit, i.e., they satisfy the condition $|P_r| < 0.1$ and $\dot{P}_r < 0$ for the corresponding periodic orbit.

4) The ensemble of points collected by the above procedure constitutes the 'apocentric manifold' at the section time $t_{sec}$, denoted as $W^{U,A}_{GL_1}(t_{sec})$ or $W^{U,A}_{GL_2}(t_{sec})$. In order to visualise the manifolds in physical space and in the inertial system of reference (X,Y) we apply the rotation:

$$\begin{aligned} X_j &= x_j \cos(\Omega_b t_{sec}) - y_j \sin(\Omega_b t_{sec}) \\ Y_j &= x_j \sin(\Omega_b t_{sec}) + y_j \cos(\Omega_b t_{sec}) \end{aligned} \tag{4.73}$$

where ($x_j = r_j \cos(\vartheta_j t)$, $y_j = r_j \sin(\vartheta_j t)$), $j = 1, 2, \ldots$ denotes the j-th point in the collection of all the points of, say, the apocentric manifold $W^{U,A}_{GL_1}(t_{sec})$.

Figure 4.20 shows the manifolds $W^{U,A}_{GL_1}(t_{sec})$ (blue points) and the manifolds $W^{U,A}_{GL_2}(t_{sec})$ (red points) in the inertial frame of reference at four different snapshots within the first time window $T_1 = 2.125 - 2.625\ Gyr$, corresponding to four different fractions of the period $T_P$, i.e. at $t_{sec} = 0$, $0.45\ T_P$, $0.9\ T_P$, $2.4\ T_P$. In the same way Fig. 4.21 shows the manifolds $W^{U,A}_{GL_{1,2}}(tsec)$ in the inertial frame of reference in the time window $T_2 = 2.500 - 3.000\ Gyr$ at the times $t_{sec} = 0, 0.625T_P, 1.25T_P, 2.375T_P$. In both figures we also plot the manifolds of $L_{1,2}$ derived in a pure bar model, in which the term $V_{sp}$, and the corresponding pattern speed $\Omega_{sp}$, are ignored altogether in the Hamiltoniam (4.47).

In Figs. 4.20, 4.21 the manifolds give a rich in structure and complexity outflow in the space away form $GL_{1,2}$. This outflow of chaotic trajectories can support dynamically and morphologically both the outer shell of the bar and the spiral arms of the galaxy. Note also in Figs. 4.20, 4.21 that the manifolds with the two pattern speeds assumption are not very different, but only exhibit small deformation with respect to the manifolds by the pure bar case. In particular, several features such as the 'bridges' that connect the manifolds emanating from one end of the bar to the other, as well as the 'gaps' between these bridges, are created by the main pertubation (potential term $V_b$), while, as emphasized in Efthymiopoulos et al. (2020), the role of the pertubation $V_{sp}$ is instead to introduce a small periodic oscillation of the manifolds with respect to the pure bar case, taking place with a period equal to $T_P = \frac{\pi}{|\Omega_{sp} - \Omega_b|}$. The most notable effect of this oscillation, as regards the morphology of these structures supported by the manifolds, is a periodic variation of the length of the manifold lobes, which leads to a periodic change of the morphology from 'ring' to 'pseudoring' (Buta (2012)). As shown in Figs. 4.22 and 4.23, in which the images of several snapshots of the N-body simulation, after performing the Sobel-Feldman edge detection algorithm (see Efthymiopoulos et al. (2019)), are compared to the morphology of the manifolds in the inertial frame of reference, such a periodic alternation of the 'ring' with 'pseudoring' morphology also appears in the images of the simulation, in particular in the second time window $T_2$ (Fig. 4.23).

(a) t=2.125 Gyr

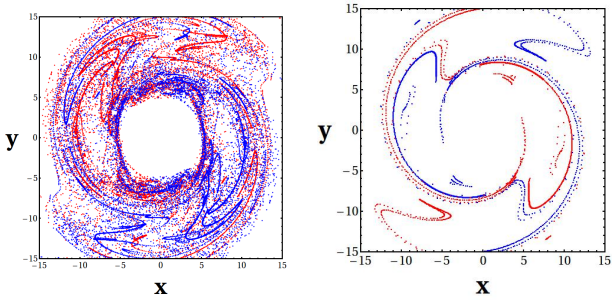


(b) t=2.200 Gyr

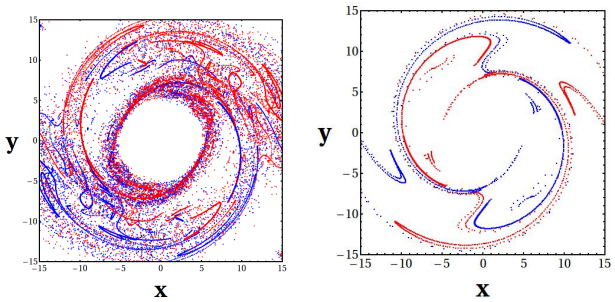


(c) t=2.275 Gyr

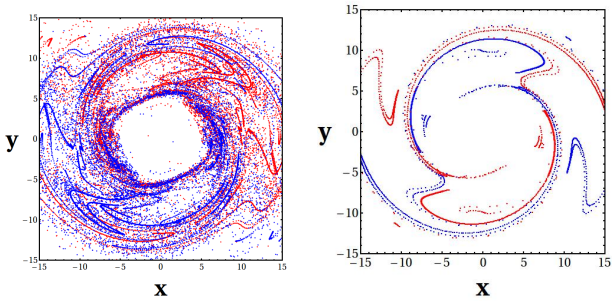


(d) t=2.525 Gyr

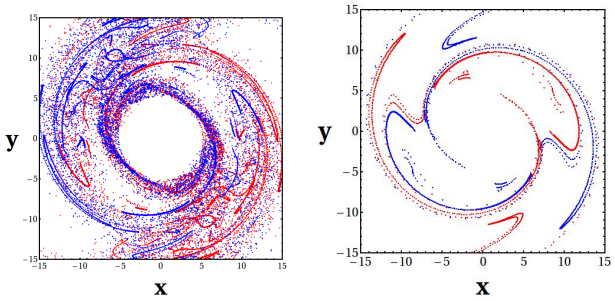


**Figure 4.20**: *The manifolds at four differnt snapshots in the time window* $T_1 = 2.125 - 2.625$ *Gyr with a period* $T_P$*= 0.525 Gyr. The snapshots corrspond to times: (a) t=2.125 Gyr, at time* $t_{sec} = 0$ *(beginning of the period) (b) t=2.200 Gyr, at time* $t_{sec} = 0.45T_P$ *(c) t=2.275 Gyr, at time* $t_{sec} = 0.9T_P$ *(d) t=2.525 Gyr, at time* $t_{sec} = 2.4T_P$*. The blue points correspond to the manifolds emanating from* $GL_1$ *and the red points to the manifolds emanating from* $GL_2$*. Left: manifolds in the model with two pattern speeds. Right: manifolds in a pure bar model (see text).*

(a) t=2.500 Gyr

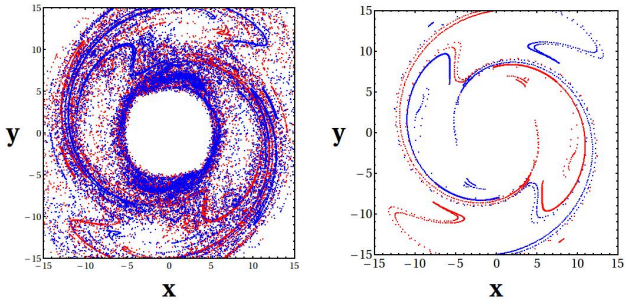


(b) t=2.625 Gyr

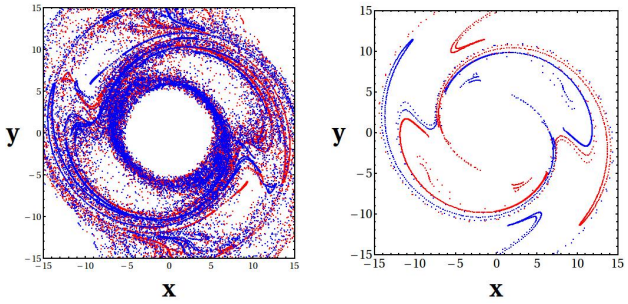


(c) t=2.750 Gyr

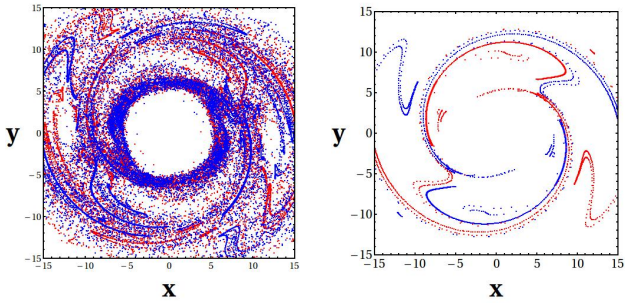


(d) t=2.975 Gyr

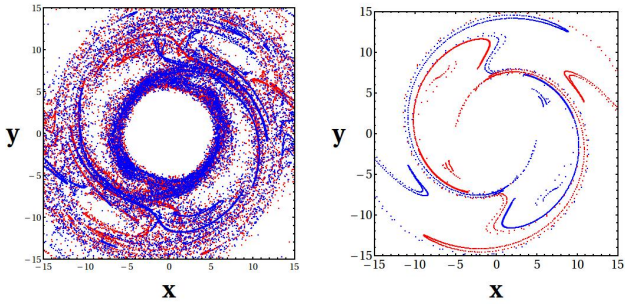


**Figure 4.21**: *Same as in Fig. 4.20 but for the time window* $T_2 = 2.500 - 3.000$ *Gyr. The period is* $T_P$*=0.2 Gyr at the times of the snapshots are: (a) t=2.500 Gyr, at time* $t_{sec} = 0$ *(beginning of the period) (b) t=2.625 Gyr, at time* $t_{sec} = 0.625 T_P$ *(c) t=2.750 Gyr, at time* $t_{sec} = 1.25 T_P$ *(d) t=2.975 Gyr,* $t_{sec} = 2.375 T_P$.

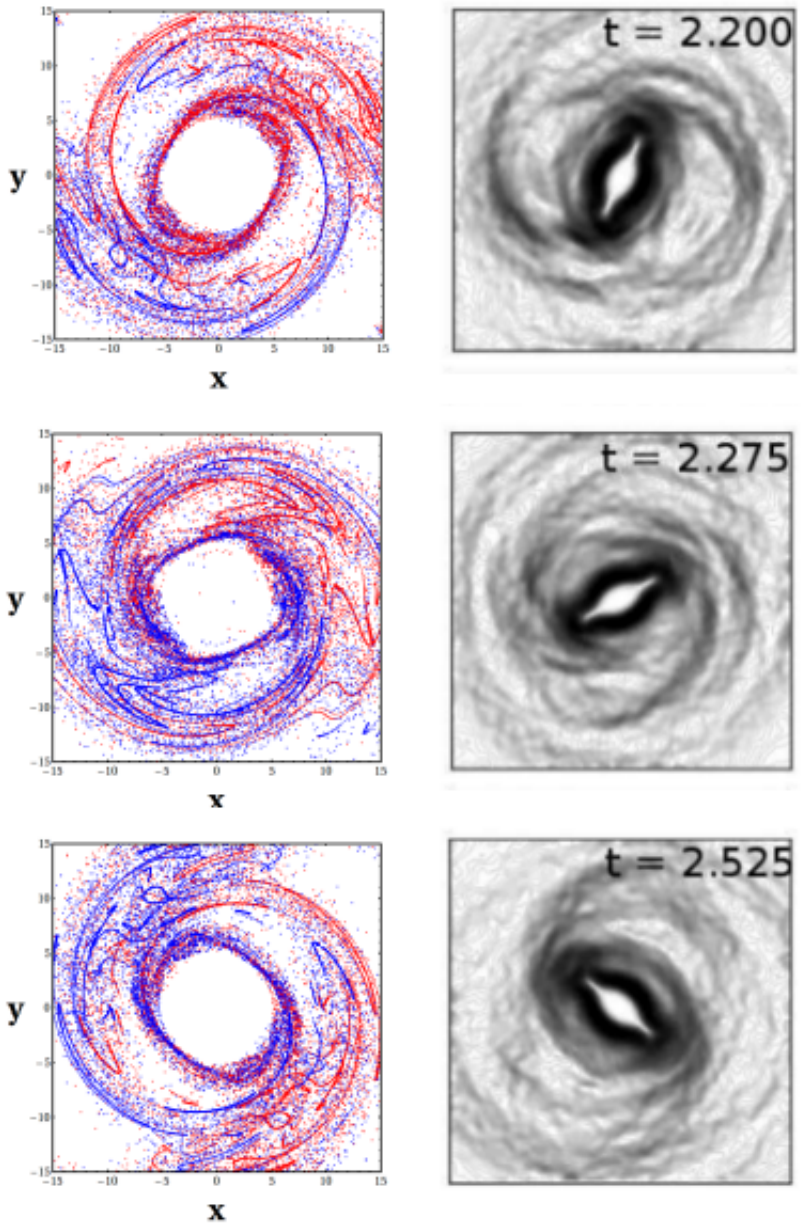


**Figure 4.22**: *The manifolds calculated as described in section 4.3.3 compared to the respective images of the snapshots of the N-body simulation at the times (a) t=2.200 Gyr (top), (b) t=2.275 Gyr (center) and (c) t=2.525 Gyr (bottom) of the first time window* $T_1$.

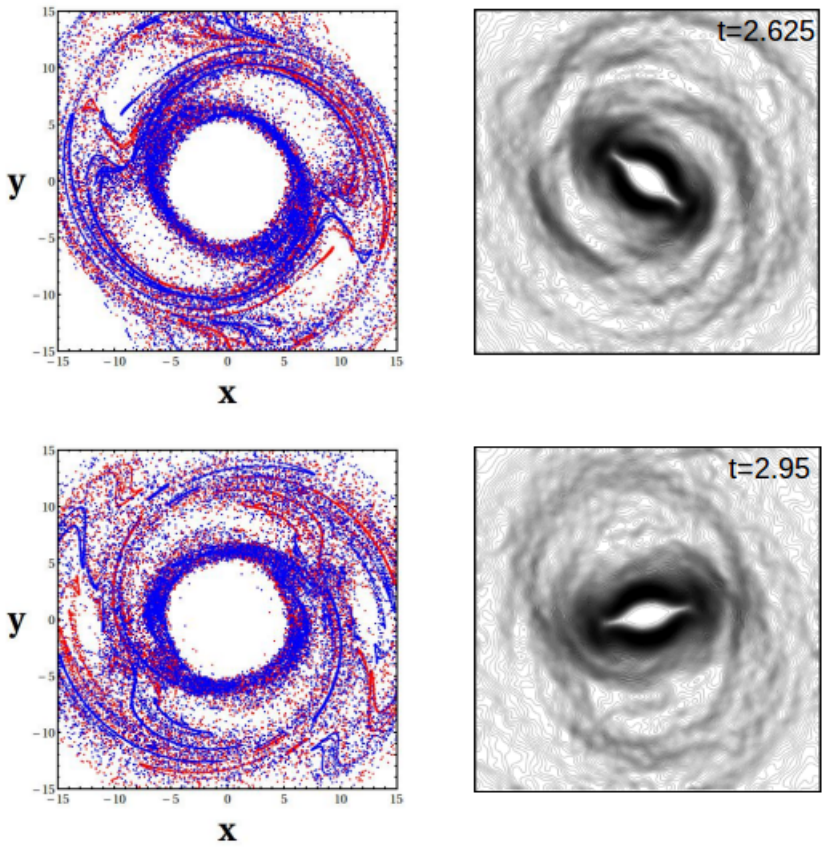


**Figure 4.23**: *The manifolds calculated as described in section 4.3.3 compared to the respective images of the snapshots of the N-body simulation at the times (a) t=2.625 Gyr (top) and (b) t=2.95 Gyr (bottom) of the second time window $T_2$.*

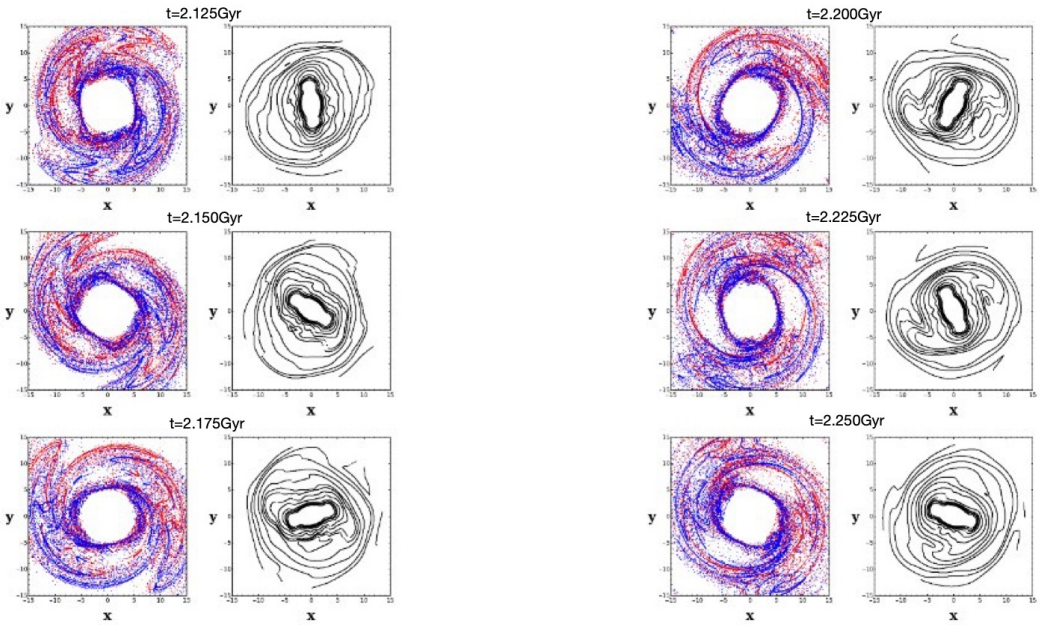


**Figure 4.24**: *The manifolds calculated as described in section 4.3.3 compared to the contours of the disc surface density at six successive snapshots $t = 2.125,\ 2.150,\ 2.175,\ 2.200,\ 2.225,\ 2.250$ Gyr of the first time window $T_1$, covering about one relative period $T_P$.*

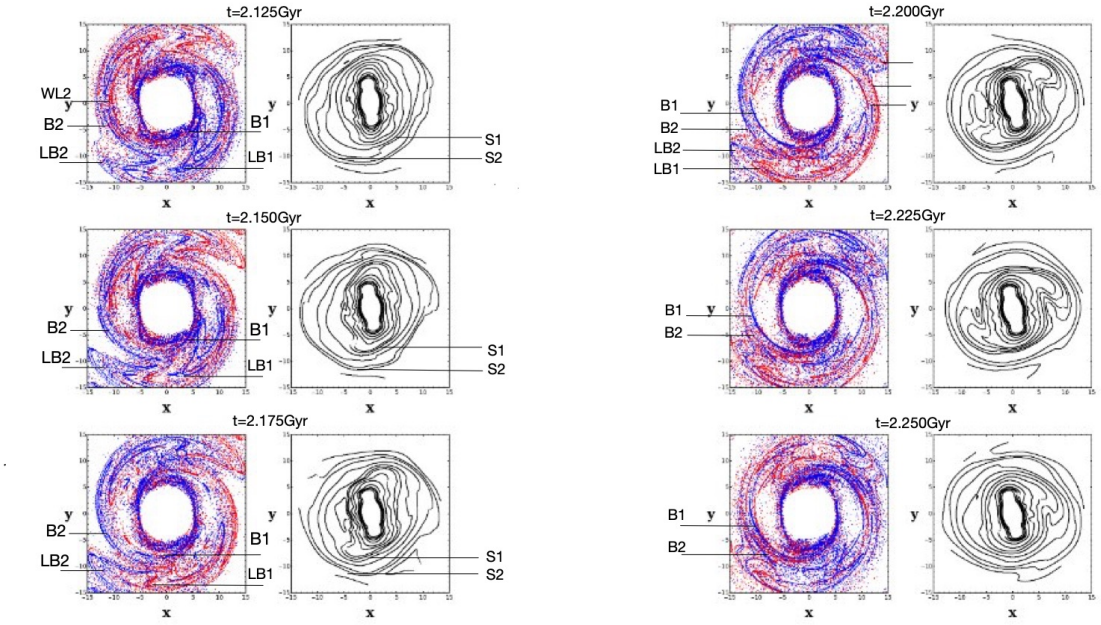


**Figure 4.25**: *Same as in Fig. 4.24, but now the manifolds and contours are shown in a rotating frame with angular velocity $\Omega_b$. The lobes and bridges formed by the manifolds are described in the text.*

The creation of 'bridges' is a generic phenomenon created by the manifold lobes as a consequence of Poincaré's 'homoclinic chaos', and as shown in the previous figures, persists even when the chaotic motions around the bar's $L_{1,2}$ points are modulated by more frequencies besides the bar's $\Omega_b$. In particular, the manifolds emanating from the orbit $GL_1$, after half a turn, start approaching the neighborhood of $L_2$ and create a sequence of lobes which start, now, supporting the spiral arm connected to $L_2$ (instead of their origin, i.e., $L_1$), and vice versa. As first discussed in Tsoutsis et al. (2008) (see also Efthymiopoulos et al. (2019), Efthymiopoulos et al. (2020)), the role of the 'bridges' is essential in understanding how the manifold lobes create density enhancements supporting particular ring or spiral morphologies. Figures 4.24 and 4.25 allow to see how the variation in time of the position of the bridges, due to the second pattern speed, is correlated with the variation in morphology of the spiral structure during a cycle of relative period $T_P$. Both figures show six consecutive snapshots in the first time window roughly covering a time interval equal to $T_P$. In Fig. 4.24 all structures are projected in a fixed frame, while in Fig. 4.25 the same structures are visualized in a rotating frame of angular speed $\Omega_b$, as determined by NAFF. Thus, in the latter case, the bar co-rotates with the frame, as evident from the innermost iso-densities, which keep a practically constant orientation.

While an exact comparison of the manifold structures (computed only with the $m = 2$ potential) with the full density is not possible, the main qualitative comparison yields the following picture. At the beginning of this interval, the bar is detached from the spiral arms (Figure 4.24, $t = 2.125$ Gyr) and altogether the spiral arms are weak in amplitude. Progressively the bar approaches the starting points of the spiral arms ($t = 2.175$ Gyr to $t = 2.225$ Gyr) and the spiral arms gain amplitude. Near the end of the cycle ($t = 2.25$ Gyr) the spiral amplitude starts reducing again. By visualising the system in the frame co-rotating with the bar we can identify the effect of the second pattern speed in the manifold structure. The most important feature is the evolution in time of the system of lobes, and of the bridges formed by them, as shown in Fig. 4.25. We identify two main homoclinic lobe systems, marked as LB1 and LB2,

shown in the bottom part of all the manifold plots, which correspond to lobes of the $GL_1$ manifolds forming 'bridges' with the initial parts of the $GL_2$ manifolds (denoted WL2 in the figure), marked by B1 and B2 respectively. Symmetric lobes and bridges exist also in the upper part of the manifold plots, connecting the manifolds of $GL_2$ with $GL_1$ respectively. Two main effects are produced by the second pattern speed: i) the lobe system LB2 gets enhanced in the middle of the time interval, and ii) the position of the bridge B1 rotates clockwise (compare the snapshots $t = 2.125$ Gyr with $t = 2.200$ Gyr). As a result, in the middle of the considered time interval the bridges B1 and B2 are almost in phase, while at the beginning ($t = 2.125$ Gyr) they have a phase difference of almost $\pi/2$. Finally, near the end of the interval, B1 exceeds in phase B2, while altogether the lobe system LB2 becomes again weak. Furthermore, the bridges B1 and B2 can be roughly associated with the spiral overdensities S1 and S2 seen in the isodensity plots for the same snapshots. Note that all these time variations are exclusively due to the presence of a second pattern speed, while the structure of the manifolds with a unique pattern speed remains invariant in time (see figure 4.20).

Note that this type of homoclinic dynamics produced by the manifolds' lobes and bridges affects not only the orbits strictly on the manifolds, but essentially all the orbits which belong to the outflows from $L_{1,2}$. Figure 4.27 shows an example of this effect in the inertial frame of reference. A ball of initial conditions centered at the bar's $L_1$ (and, symmetrically, $L_2$), is allowed to propagate forward in time under the semi-analytical potential model with both pattern speeds present. We observe that the points in these initial balls propagate in the disc, at the beginning being stretched along the linear eigendirections of the unstable manifolds. Up to time $t = 0.2$ Gyr these orbits then create the usual thin structures that define the spiral arms and the envelope of the bar. Later, however, the same strings of stars develop a sequence of lobe-like chaotic oscillations. In particular, at time $t = 0.35$ Gyr the orbits from $L_1$ start approaching asymptotically the neighborhood of $L_2$, and then, they develop thin lobes which support the spiral arm connected to $L_2$, instead of $L_1$, and vice versa. As time goes on ($t = 0.6$ Gyr) the lobes grow in size, keeping the same connection to the points $L_1$ and $L_2$. Later on, however, the same mechanism generates anew a reversal, as the lobes connected with $L_1$ form a complete turn, thus returning to the neighborhood of $L_1$ and supporting anew the spiral arm connected to it. The overall picture gives rise to a so-called 'lagrangian coherent structure' (Sánchez-Martín et al. (2018)), which acts as a skeleton for a continuous chaotic flow of particles. In practical terms, this flow implies that, independently of its origin (outflow from $L_1$ or $L_2$) the same group of particles can sometimes support the spiral arm connected to $L_1$, and other times the one connected to $L_2$.

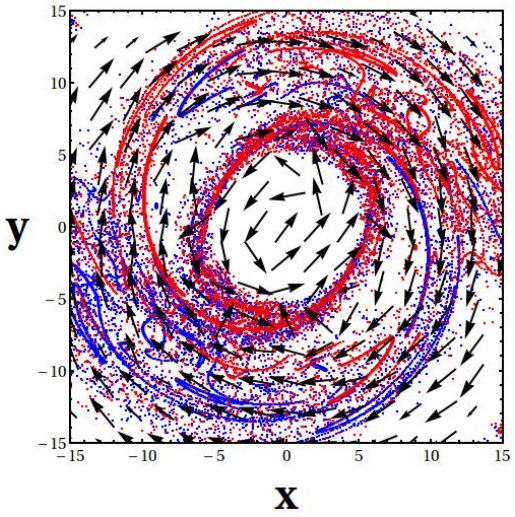


**Figure 4.26**: *The velocity vector field positioned over the manifolds at the time t=2.200 Gyr of the simulation.*

Finally, as shown in Fig. 4.26, the invariant manifolds in two pattern speed case in the inertial frame of reference are consistent with the residual velocity flow model for the trajectories along density waves of the 'chaotic spiral' type (Patsis (2006), Patsis & Tsigaridi (2017)). The residual velocity flow corresponds to the mean velocity of the N-body particles in the frame co-rotating with the bar at any fixed time t, and it can be computed as follows: Given the positions in cartesian coordinates ($x$, $y$) and the respective velocities ($V_x$, $V_y$) of the bodies of the N-body simulation at the particular snapshot, we divide the cartesian space into a grid. For the construction of the grid we divide the cartesian space in 50 cells of size $dx \simeq 0.61$ kpc, $dy \simeq 0.61$ kpc, considering that the grid is limited by the values: $x_{max} \simeq 15$ kpc, $x_{min} \simeq -15$ kpc, $y_{max} \simeq 15$ kpc, $y_{min} \simeq -15$ kpc. In every cell of the grid, we calculate the mean velocity components ($\langle V_x \rangle$, $\langle V_y \rangle$) in the rotating system of reference of the bodies within this cell. We then construct the vectors

$$\left( \frac{\langle V_x \rangle}{\sqrt{{V_x}^2 + {V_y}^2}}, \frac{\langle V_y \rangle}{\sqrt{{V_x}^2 + {V_y}^2}} \right) \tag{4.74}$$

and plot the corresponding residual velocity vector field superposed to the manifolds, as in Fig. 4.26, corresponding to the time t=2.200 Gyr. In Fig. 4.26 we observe that the velocity vector field yields prograde orbits at the region inside the corotation and retrograde outside corrotation. However, we observe that the mean flow in the region of the manifolds $W^{U,A}_{GL_1}(t_{sec})$ and $W^{U,A}_{GL_2}(t_{sec})$ is along the manifold spirals, in accordance with the predictions of chaotic spirals model (Patsis (2006)). The manifolds $GL_{1,2}$ illustrated in Fig. 4.26 are unstable braches and the motions of stars travelling along them are forced to travel outwards and support the outflow away from the corrotation.

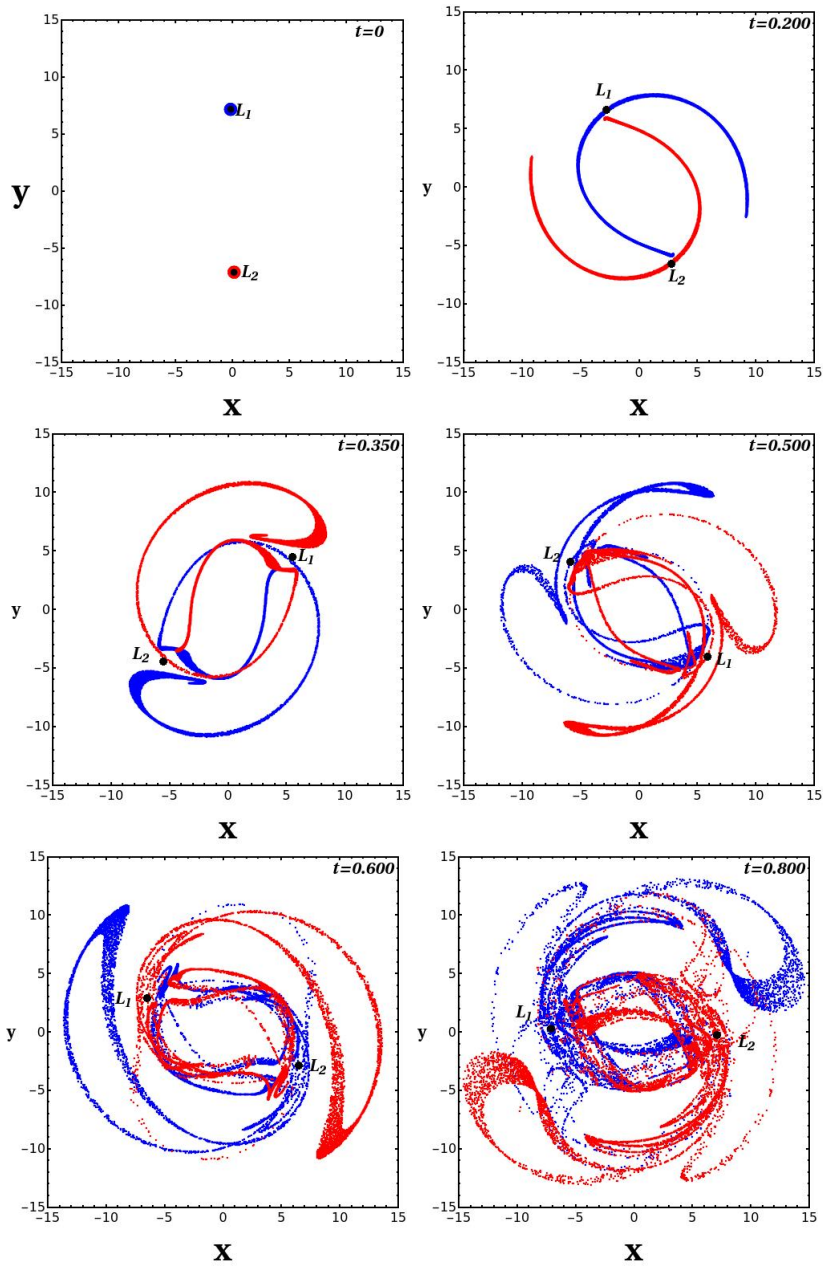


**Figure 4.27**: *Propagation of a ball of initial conditions around the bar's points L1 (blue) and L2 (red) under the semi-analytical potential with both pattern speeds included. The orbital evolution of these groups of particles generates a 'lagrangian coherent structure' (LCS, see text). The flow of particles through the LCS implies that the same group (blue of red) sometimes supports the spiral connected to L1, and othertimes the spiral connected to L2. The switch from one to the other type of support can be explained by the underlying manifold dynamics, in particular by the phenomenon of 'bridges' created by the invariant manifolds.*

# Chapter 5

# Conclusion

In the present thesis we attempted to investigate the problem of the spiral structure of the galaxies from an orbital point of view. The study of the orbits in galaxies can give evidence for the mechanism that generates the spirals. Our research attempted to approach the open subjects of spiral structure, which we presented in the introduction (the morpholology of the spiral arms, their mechanism, their longevity and their evolution). We concluded that all these open problems commute and orbits of different nature contribute respectively to different mechanisms for the spiral structure, as well as, different morphologies and evolution of the galaxy. We also discovered that chaos is a key factor for the cooherence of the structure. In barred spiral galaxies chaos and the intricate dynamics enhances the spiral structure and leads through the manifold dynamics to long lived spirals. However, in normal galaxies where the spiral arms are supported by ordered orbits, chaos makes these orbits unstable and dissolves the spiral structure.

In this final chapter we are going to summarise the main results of the thesis and present some ideas for future work that yield from our research. We are going to present in detail the results of our study in the case of the N-body simulation of a barred spiral galaxy (Chapter 3-4) and in the case of a Milky Way theoretical model (Chapter 2).

I) In **Chapter 2** we studied the case of spiral density waves generated by ordered orbits. These "precessing ellipses" model of elliptical orbits are considered to approach the spiral density waves in grand design spiral galaxies.

We initially proved that these ordered elliptical periodic orbits can be located through analytical calculations and consecutive transformations of the Hamiltonian of the system. The Lie method of generating functions enabled us to write the Hamiltonian in resonant normal form and get three solutions which correspond to the three different families of periodic orbits $x_1$, $x_2$, $x_3$ which are known in the bibliography. There have been works in the past for the calculation of these periodic orbits, but there was still the need for a consise algorithm which sets in order and clarity the steps for the analytical calculation of these periodic orbits.

The algorithm that was developed and presented in Chapter 2 can be applied in any galactic model whose spirals are generated by the precessing ellipses mechanism. It is a tool for several experiments in order to test the parameters of the galactic models.

A parametric study can also be made in a range of free geometric and dynamical parameters of galactic models such as the pattern speed of the spiral arms $\Omega_{sp}$, the amplitude of the spiral pertubation or the pitch angle of the spiral arms. This parametric study shows how the parameters collaborate in a way that a realistic spiral density wave is generated. Moreover, the knowledge of the right values of parame-

ters for a realistic density wave may give us the ability to make long-lasting N-body simulations. N-body simulations of normal galaxies based on the precessing ellipses mechanism is a difficult task for the astronomers and a lot of work needs to be done in this field.

A comparison with numerical results can enhance this research. In section 2.2.2 a comparison of the analytical elliptical orbit $x_1$ to a numerical elliptical orbit was made. For the particular model and the particular free parameters we used the two orbits were in good agreement. However, a parametric study needs to be done, in order to show us in which range of the parameters this agreement of the numerical and analytical orbits holds.

We also investigated when these orbits become unstable and no spiral density waves can be supported. We used a theoretical potential Milky Way- like model consisting of a bulge, a disc, a halo and a spiral potential. The free parameters of our model were: the amplitude of the spiral density perturbation ($\rho_0$), the pattern speed of the spiral potential ($\Omega_{sp}$) and the pitch angle of the spiral arms of the model ($a$). By testing the effect of the variation of the free parameters of the model on the response spirals, formed by elliptical periodic orbits we extracted the following conclusions:

1) In all models under study the $x_1$ family is responsible for the creation of response spirals consisted with the imposed ones. The repsonse spirals extend in the region from the center of the galaxy up to the radius of the 4:1 resonance. The $x_2$ and $x_3$ families of orbits exist between the first and the second ILR. They are created simultameously near the first ILR at a tangent bifurcation and they join and disappear near the second ILR in all the models, except in the case of a very small pitch angle where they still exist outside the second ILR but do not contribute to the response spirals. The $x_2$ family of orbits has main axes perpendicular to the main axes of the $x_1$ family and the $x_3$ family is always unstable in the whole range of the radii.

2) By increasing the amplitude of the spiral density perturbation in our model chaos is introduced gradually and the $x_1$ family of orbits becomes unstable. An upper limit for the spiral density perturbation is $\rho_0 = 30 \times 10^7 M\odot/\text{kpc}^3$ where the $x_1$ family is unstable in the whole range between the second ILR and the 4:1 resonance.

3) Regarding influence of the value of the pattern speed $\Omega_{sp}$, when $\Omega_{sp}$ decreases, all the resonances are shifted outwards and therefore the spiral density waves can reach larger radii. However, the ellipses become rounder when they get closer to the 4:1 resonance and therefore the spiral density wave becomes less cospicuous at larger radii. Moreover, the elliptical orbits of the $x_1$ family become much more elongated and intersect each other, thus destroying a coherent spiral response.

4) Regarding the influence of the value of the pitch angle, we conclude that for increasing pitch angle (more open spiral arms), more order is introduced in the phase space and the chaotic areas shrink in size, while for decreasing pitch angle (more tight spiral arms) chaos dominates on the phase space and the $x_1$ family of orbits can no longer support the spiral density wave.

5) Summarizing the above, the main result of this research in the "precessing ellipse model" is a quantitative estimation of the range of the free parameters of our galactic model for generating realistic spiral density waves, via the "precessing ellipses" model of elliptical closed orbits (and their surrounding quasi-periodic ones). In particular, a correlation between the pitch angle and the amplitude of the spiral perturbation was shown, where stronger spirals can be statistically less tight than weaker ones. Moreover, a corellation between the pitch angle and the pattern speed showed, where spirals than spin faster can be statistically tighter that slower ones.

The results of this research, which are associated to the range of free parameters in the dispertion relation for the generation of realistic density waves, can be used for

the construction of an N-body model of a long living density wave, which is in lack in bibliography. These orbits can be reproduced analytically and be compared with the numerical results.

The mechanism that generates the spiral arms in the Milky Way is still unknown. This work arises the need for a correlation of the pattern speed of the bar with the mechanism that generates the spiral arms in the Milky Way case. Milky Way is a barred spiral galaxy and one would expect the spiral arms to be chaotic. A rapidly rotating bar may be related to a precessing ellipses mechanism for the construction of the spiral arms. We have shown that in the case of the spiral arms produced by the invariant manifolds the velocity vectors are parallel to the manifolds. This can give us an observational tool through which we can investigate if the spirals are produced by chaotic or organised orbits.

II) In **Chapters 3-4** we studied the case of barred spiral galaxies, where the co-existence and possible non-linear coupling of multiple patterns hints towards the chaotic nature of spiral arms. To the extent that spirals are bar driven, they are affected in a non-trivial way by the bar's secular evolution. Within this context, the main contribution of the manifold theory is to describe what should be the expected form of the bar-driven spiral mode when the disc's region between the bar's corotation and Outer Lindblad Resonance is largely chaotic. It should be stressed that the manifold theory poses no requirement that chaos originates exclusively from the bar. Nonlinear interaction of the bar mode with additional patterns beyond co-rotation actually enhances chaos. Furthermore, it is a basic rule of dynamics that the unstable manifolds of one periodic orbit cannot intersect themselves or the unstable manifolds of any other periodic orbit of equal Jacobi energy. Thus, all these manifolds have to 'coalesce' in nearly parallel directions, thus enhancing chaotic spirals.

The manifolds emanating from the region of the bar's $L_1$ and $L_2$ points provide the simplest representation of these chaotic outflows. In the present thesis, we found that the manifold spirals provide the dynamical skeleton for these structures and they pave the direction that the trails of the orbits will follow. The study of the manifold spirals with an assumption of a single or a second pattern speed has been presented in Chapters 3 and 4. We are presenting the main results of these two chapters which examine the application of the manifold theory in an N-body galactic model:

-In **Chapter 3** we gave evidence that these manifolds provide a dynamical skeleton in phase space, or, the dynamical avenues to be followed by new particles injected in the domain between CR and OLR at reccurent 'incidents' of non-axisymmetric activity. In particular:

1) We proved that the manifolds evolve and support the secularly evolving structures. We gave a characterization of such incidents as of i) inner, or ii) outer origin, depending on whether the spectral analysis shows a wave originating inside CR and propagating outwards (in (i)), or originating outside CR, moving initially inwards, then being reflected at CR, and then moving outwards (in (ii)). Morphologically, spirals are connected mainly with incidents of inner origin. However, pattern detection algorithms such as Sobel-Feldman allow to detect the co-existence of various patterns, including spiral ones, both at maxima and minima of the $m = 2$ amplitude beyond the bar, i.e., both close to and far from incidents of non-axisymmetric activity. We interpret the importance of manifolds as follows: whatever causes these incidents, at every incident the particles' orbits (and in particular chaotic ones) are perturbed. Then, new particles injected in the CR zone tend to follow and populate the manifolds to a large extent, according to general rules of dynamics.

2) We argued that the continuous in time change of the form of the manifolds, as well as the motion, along the manifolds, of the matter which populates them, allows

to compromise the above picture on the role of manifolds with the multiplicity of pattern speeds in the disc. Most notably, we unravel a basic behavior of the radial profile of the pattern frequency $\Omega_2(R)$ beyond the bar, connected with alteration between maxima and minima of the non-axisymmetric activity. Namely, besides the always present plateau in the graph of $\Omega_2(R)$ representing the bar's pattern speed, we observe that $\Omega_2(R)$ tends to form a second plateau, indicating a second pattern with distinct frequency outside CR, whenever we are near *maxima* of the non-axisymmetric activity. However, this second plateau disappears near minima of non-axisymmetric activity, giving its place, instead, to a shear-like decaying profile of the curve $\Omega_2(R)$, which, remarkably, terminates at a value $\Omega_2 \sim 0$ near $R = R_{OLR}$. Five full cycles of this behavior are seen in our simulation, in a period of $\sim 1$ Gyr (see Fig. 3.19), leading to an approximate period of $\sim 0.2$ Gyr. This is in rough resonance with the bar's period, but with large uncertainties in the numbers. On the other hand, since the comparison between manifolds and Sobel-Feldman-recognized patterns in the disc (Fig. 3.18) shows no appreciable differences between snapshots of minima and maxima of the non-axisymmetric activity, we argued that the degree to which manifolds are able to dictate the dynamics outside CR seems to be rather independent of the strength of any additional pattern in the disc.

3) We also discussed the 'thermal' evolution of the disc, i.e., the way in which the radial profile of the velocity dispersion appears to be influenced in time due to non-axisymmetric activity. Owing, again, to the large degree of chaos between CR and OLR, we argued that the gradual outward shift of both the CR and OLR radii as the bar slows down, causes part of the disc, beyond the end of the bar, to acquire a nearly constant radial velocity dispersion. In fact, this 'isothermalization' causes a part of the disc, starting from inside the bar and ending at a point midway between CR and OLR to cool down as the time goes on. We interpret this effect as a hint that chaotic populations of particles gradually migrate outwards, carrying with them kinetic energy in the form of randomly oriented motions. Regarding, however, the responsiveness of the disc to manifold dynamics, we provide a heuristic argument showing that good levels of responsiveness should be limited in a domain which shrinks in time, as the CR radius moves outwards, while the radius beyond which the disc gets hotter in time is nearly fixed.

-In **Chapter 4** we presented another version of application of the manifold theory in the same N-body model of barred spiral galaxies, which, in this case, evolves multiple pattern speeds. The purpose of the present study was twofold: i) we illustrated the applicability of the algorithm of the 'Numerical Analysis of the Fundamental Frequencies' (NAFF, Laskar (1990), Laskar et al. (1992), Laskar (1993), Laskar (2003), Fu & Laskar (2019)) to the problem of detecting and computing the accurate values of more than one pattern speeds, and of the amplitudes of the corresponding modes, in the disc plane of a N-body simulation of a barred-spiral galaxy, ii) we used the outcome of (i) in order to build two-pattern speed models of manifold spirals in the same simulation, implementing the algorithm proposed to this end in Efthymiopoulos et al. (2020). Our main conclusions are:

1) The NAFF method was implemented in the time series yielding the evolution of the amplitudes of the $m = 2$ sine and cosine modes obtained by an angular-Fourier analysis of the surface density, or the potential, within concentric rings in the simulation's disc plane. We demonstrated that this leads to a determination of the frequencies of rotation of the $m = 2$ patterns with an error scaling far better than the $O(1/T)$ error of the simple time-Fourier method, where $T$ is the length of the time series considered. We showed how to adapt theoretical estimates on the NAFF method to our problem, actually yielding an error scaling only as $O(1/T^2)$, or better

(by use of the Hanning filter, see section 4.1).

2) Due to the above behavior of the error of the NAFF method, we were actually able to use time series of a length $T$ short enough with respect to the timescale of the secular evolution in the galactic disc, but still long enough for the NAFF method to produce nearly-constant estimates of the pattern speeds for both the bar and the spiral arms in the simulation, within moving time windows of length $T$.

3) Implementing the above to a particular simulation, we provided clear evidence of the presence of multiple pattern speeds in the galactic disc. In particular, in many cases we clearly detected the dominant $m = 2$ bar mode, as well as one or more spiral modes evolving at radii beyond the bar's corotation. At earlier phases of the evolution of the system, we clearly detected a second spiral $m = 2$ mode at radii which partly overlap with those where the bar mode is still present. At later phases, the second most important spiral mode had practically no overlap with the bar mode (albeit having, in all cases, a clearly different pattern speed), but it has a partial overlap with a third mode important at the outermost parts of the disc.

4) Ignoring any extra modes beyond the bar and most dominant spiral $m = 2$ modes, we arrived at a rough model of the gravitational potential in the disc plane, consisting of the superposition of the $m = 0$ and $m = 2$ bar and spiral modes, the latter rotating with the pattern speeds $\Omega_b$ and $\Omega_{sp}$ respectively. We provided various tests on the degree of approximation of this model with respect to the full potential and surface density data obtained numerically by the simulation.

5) In the framework of the above $m = 0, 2$ model, we implemented the algorithm of Efthymiopoulos et al. (2020) in order to compute the manifold spirals emanating from the periodic orbits $GL_1$ and $GL_2$ at the two ends of the bar. The algorithm requires a perturbative computation using canonical perturbation theory, whose implementation, however, requires an analytical knowledge of high order derivatives of the gravitational potential. Since, in our case, we could produce only a low-order smooth interpolation of potential coefficients provided by the NAFF method, we substituted the high order perturbative computation with one based only on second order perturbation theory, combined with a numerical (Newton-Raphson) determination of the crucial periodic orbits GL1 and GL2 as the fixed points of a suitably defined stroboscopic symplectic map (subsection 5.2). This led, in turn, to a numerical determination of the manifold spirals ('flux tube' $W^U(t_{sec})$, or 'apocentric' $W^{UA}(t_{sec})$), at different times $t_{sec}$ corresponding to a fraction of the main period $T_P = \pi/|\Omega_{sp} - \Omega_b|$ present in the potential in the two-pattern speed regime (see subsection 5.3 for the corresponding definitions).

6) We finally compared the computed manifolds $W^{UA}(t_{sec})$ with the observed bar and spiral morphologies in the simulation at different snapshots, translated to different values of the time-parameter $t_{sec}$. Besides recovering the main spirals obtained in the simulation through the manifolds, we also recovered several secondary morphological features such as the 'bridges' discussed in past works (Efthymiopoulos et al. (2019), Efthymiopoulos et al. (2020)). We also recovered the basic property of the manifolds in the two-pattern speed case, which is an oscillation (with period equal to $T_P$) with respect to the static bar-driven manifolds of the simple pattern speed case. In fact, this oscillation allows to reproduce several changes in the apparent spiral morphology observed along one time window, in particular the change between more open spiral arms forming bridges and more closed, oscillating between the 'ring' and the 'pseudo-ring' like ones, as $t_{sec}$ moves from the beginning to half the way along a period of oscillation.

7) Finally, we checked that the mean residual velocity field (i.e. mean velocity in the disc plane with respect to a frame co-rotating with the bar) in the simulation

follows the model of 'chaotic spirals' (Patsis , 2006), i.e., the mean velocities are parallel to the invariant manifolds computed in the two-pattern speed model.

As an overall conclusion, we find that the modelling of chaotic spirals by manifolds, including the hypothesis of multiple pattern speeds, gives a consistent picture of the complexity of the non-axisymmetric structures like pseudo-rings and spirals observed beyond the bar in N-body simulations of barred-spiral galaxies. We attribute this connection of the manifolds to the chaotic spirals to a dynamical mechanism. Namely, the manifolds provide pathways in phase-space, which play, for the phase-space orbital flow, a role analogous to the lagrangian coherent structures in chaotic fluid-dynamics (Haller & Yuan (2000), Sánchez-Martín et al. (2018)). In particular, the manifold lobes created in the neighborhood of the homoclinic or heteroclinic tangles among unstable periodic orbits in the co-rotation region create preferential directions which sculpt the orbital flow for all chaotic orbits. Thus, they generate coherent patterns, such as the observed spiral ones, which can persist in timescales surpassing by far the Lyapunov times (i.e., inverses of the Lyapunov exponents) of individual trajectories. On the other hand, a detailed study of such chaotic structures in a simulation requires a precise identification of all the patterns (and pattern speeds) in the decomposition of the gravitational potential in Fourier modes. This can be efficiently achieved with methods as NAFF. In the present study, we limited ourselves to a modelling of the two most dominant modes, using the NAFF method to accurately fit the corresponding amplitudes and frequencies. We leave open the question of the effects of adding to the analysis more modes of the spectrum detected by NAFF, thus leading to a consistent study of the full complexity of the dynamical interactions between various modes co-existing in a galactic disc over a long fraction of the bar or spiral lifetimes.

# Bibliography


Athanassoula E. 1980, Bar-driven spiral structure. A& A, vol. 88, no. 1-2, Aug. 1980, p. 184-193., 88, 184-193.

Athanassoula E., 1984, Phys. Rep., 114, 319

Athanassoula E., 2002, ApJ, 569, L83

Athanassoula, E. & Misiriotis, A.: 2002, MNRAS, 330, 35

Athanassoula E., 2003, MNRAS, 341, 1179

Athanassoula E., Romero-Gómez M., and Masdemont J. J., 2009a, MNRAS, 394, 67

Athanassoula E., Romero-Gómez M., Bosma A., and Masdemont J.J., 2009b, MNRAS, 400, 1706

Athanassoula E., Romero-Gómez M., Bosma A., and Masdemont J.J., 2010, MNRAS, 407, 1433

Athanassoula E., 2012, MNRAS, 426, L46

Athanassoula E., 2013, in 'Secular Evolution of Galaxies', XXIII Canary Islands Winter School of Astrophysics. J Falcon-Barroso and J. H. Knapen (eds), Cambridge University Press, pp.305-352.

Antoja T, Helmi, A., and Dehnen W., et al., 2014, A&A, 563, 60

Avila-Reese V., Carrillo A., Valenzuela O., and Klypin A., 2005, MNRAS, 361, 997

Baade, 1963, W. "Evolution of stars and galaxies, Harvard U.".

Baba J., Saitoh T.R., and Wada K., 2013, ApJ, 763, 46

Baba J., 2015, MNRAS, 454, 2954

Benjamin R. A., Churchwell E., and Babler B. L., 2005, ApJ, 630, L149

Berentzen I., Shlosman I., and Jogee S., 2006: ApJ, 637, 582

Berry C. L., & Smet D. J., 1979, Astron. J., 84, 964

Bertin G., Lin C. C., Lowe S. A., and Thurstans R. P.,1989 , ApJ, 338, 104.

Bertin G. & Lin C.C., 1996, MIT press.

Binney, J., & Spergel, D., 1982, ApJ, 252, 308.

Binney J., Tremaine S., 2008, Galactic Dynamics, second edn. Princeton University Press

Binney J., 2013, in 'Secular Evolution of Galaxies', XXIII Canary Islands Winter School of Astrophysics. J Falcon-Barroso and J. H. Knapen (eds), Cambridge University Press, pp.259-304.

Birkhoff G. D.,1917, Dynamical systems with two degrees of freedom. Proceedings of the National Academy of Sciences, 3(4), 314-316.

Bland-Hawthorn J., & Gerhard O., 2016, Annu. Rev. Astron. Astrophys., 54, 529

Boonyasait V., Patsis P.A., and Gottesman, 2005, NYASA, 1045, 203

Bureau M. & Athanassoula E., 1999, ApJ, 522, 686

Bureau M. & Athanassoula E., 2005, ApJ, 626, 159

Burton W.B., 1988, In Galactic and Extragalactic Radio Astronomy (pp. 295-358). New York, NY: Springer New York.

Block D. L., Buta, R. , Knapen J. H., Elmegreen D. M., Elmegreen B.G., and Puerari I., 2004, Ap J, 128, 183,

Buta R. J., Knapen J. H., Elmegreen B. G., Salo H., Laurikainen E., Elmegreen D. M., Puerari I., and Block D. L., 2009, Astron. J., 137, 4487

Buta R., 2012, in 'Secular Evolution of Galaxies', 23, 155, Cambridge University Press

Chakrabarti S., Laughlin G., and Shu F. H., 2003, ApJ, 596, 220, 2003

Cohen R.S., & Thaddeus P., 1977, Astrophysical Journal, Part 2-Letters to the Editor, vol. 217, Nov. 1, 1977, p. L155-L159., 217, pp.L155-L159.

Combes F., & Sanders R.H., 1981, A&A, 96, 164

Combes F., Debbasch F., Friedli D., and Pfenniger D., 1990, A&A, 233, 82

Contopoulos G., 1966, ApJ, 144, 1260

Contopoulos G., 1970, ApJ, 160, p.113.

Contopoulos G., 1975, ApJ, 201, pp.566-584.

Contopoulos G., & Papayannopoulos T., 1980 A&A, 92, 33-46.

Contopoulos G., 1980, A&A, 81, 198-209.

Contopoulos G., 1981,A&A, 102, 265-278.

Contopoulos G., 1985, Comments on Astroph., 11, 1

Contopoulos G., & Grøsbol P., 1986,A&A, 155, 11-23.

Contopoulos G., & Grøsbol P., 1988, A&A, 197, 83-90.

Contopoulos G., & Grøsbol P., 1989, Astronomy and Astrophysics Review, 1(3-4), 261-289.

Contopoulos G., & Polymilis C., 1995, Celestial Mechanics and Dynamical Astronomy 63, pp.189-197.

Contopoulos G., 2002, Order and chaos in dynamical astronomy (Vol. 21). Berlin: Springer.

Contopoulos G., & Harsoula M., 2008, Int. J. Bifurcat. Chaos 18, 2929–2949

Contopoulos G., & Harsoula M., 2010, Int. J. Bifurcat. Chaos 20(07), 2005-2043.

Cox D. P, & Gómez G. C., 2002, ApJ Sup., 142, 261

Dame T. M., Hartmann D., and Thaddeus P., 2002, ApJ, 547, 792

Debattista V.P., Sellwood J.A., 1998, ApJ, 493, L5

Debattista V.P., Sellwood J.A., 2000, ApJ, 543, 704

Debattista V.P., Gerhard O., and Sevenster M.N., 2002, MNRAS, 334(2), pp.355-368.

Debattista V. P., Mayer L., Carollo C. M., Moore B., Wadsley J., and Quinn T., 2006, ApJ, 645, 209

Dehnen W., 1993, MNRAS, 265, 250

Dehnen, W., 2000, ApJ, 119(2), p.800.

De Vaucouleurs G., 1959, Astrophysik iv: Sternsysteme/astrophysics iv: Stellar systems (pp. 275-310). Berlin, Heidelberg: Springer Berlin Heidelberg.

De Vaucouleurs G., 1964. Comparison of the Magellanic Clouds by other irregular barred spirals. In Symposium-International Astronomical Union (Vol. 20, pp. 269-276). Cambridge University Press.

Dias W.S. & Lépine J.R.D., 2005, ApJ, 629(2), p.825.

Díaz-García S., Salo H., Knapen J. H., and Herrera-Endoqui M., 2019, A&A, 631A, 94.

Dobbs C. & Baba J., 2014, Dawes review 4: spiral structures in disc galaxies. Publications of the Astronomical Society of Australia, 31, e035.

Donner K. J. & Thomasson M., 1994, A&A, 290, 475

Dubinski J., Berentzen I., and Shlosman I., 2009, ApJ 697, 293

Efthymiopoulos C., Contopoulos G., Voglis, N., and Dvorak R., 1997, Journal of Physics A: Mathematical and General, 30(23), p.8167.

Efthymioulos C., Contopoulos G., and Voglis N., 1999, Cantori, islands and asymptotic curves in the stickiness region. In International Astronomical Union Colloquium (Vol. 172, pp. 221-230). Cambridge University Press.

Efthymiopoulos C., 2010, Eur. Phys. J. Special Topics, 186, 91

Efthymiopoulos C., 2012, In Cincotta P.M., Giordano C.M., Efthymiopoulos C. (eds.) "Third La Plata Internat. School on Astron. Geophys.", Asociación Argentina de Astronomía, La Plata

Efthymiopoulos C., Kyziropoulos P., Paez R., Zouloumi K., and Gravvanis G., 2019, MNRAS 484, 1487

Efthymiopoulos C., Contopoulos G., Harsoula M., 2020, A& A, 636, A44

Englmaier P. & Gerhard O., 1999, MNRAS, 304(3), pp.512-534.

Elmegreen D. M., & Elmegreen B. G., 1982, MNRAS, 201, 1021

Elmegreen D.M., 1985. Spiral structure of the Milky Way and external galaxies. In Symposium-International Astronomical Union (Vol. 106, pp. 255-272). Cambridge University Press.

Elmegreen D. M., & Elmegreen B. G., 1987, ApJ, 314, 3

Falcon-Barroso J., & Knapen J.H., 2013, 'Secular Evolution of Galaxies', XXIII Canary Islands Winter School of Astrophysics. Cambridge University Press

Fernández D., Figueras F., and Torra J., 2001, A&A, 372, 833

Font J., Beckman J.E., Querejeta M., Epinat B., James P.A., Blasco-herrera J., Erroz-Ferrer S., and Pérez I., 2014, ApJS, 210, 2

Fu Y. N., & Laskar J., 2019, A&A, 628, A84.

Fux R., 1999, 3D self-consistent N-body barred models of the Milky Way: II. Gas dynamics. arXiv preprint astro-ph/9903154.

Georgelin Y.M., & Georgelin Y.P., 1976, A& A, 49, pp.57-79.

Gerhard O., 2002, Space Science Reviews, 100(1-4), pp.129-138.

Gerhard O., 2010, Pattern speeds in the Milky Way. arXiv preprint arXiv:1003.2489.

Gerhard O., 2011, Mem. Soc. Astron. It. Sup., 18, 185.

Goldreich P., & Tremaine S., 1978, ApJ, 222(1), 850-858.

Gonzalez R., & Woods R., 1992, 'Digital Image Processing', Addison Wesley

Grobman D.M., 1959, Dokl. Akad. Nauk SSSR 128, 880

Grøsbol P. J., & Patsis P. A., 1998, A& A, 336, 840-854.

Grosbøl P., Pompei E., and Patsis P.A., 2002, ASP conference series, 275, 305

Haller G., & Yuan G. , 2000, Physica D: Nonlinear Phenomena, 147(3-4), 352-370.

Grosbøl P., Patsis P.A., and Pompei E., 2004, A&A 423, 849

Harsoula M., Efthymiopoulos C., and Contopoulos G., 2016, MNRAS, 459, 3419

Harsoula M., Zouloumi K., Efthymiopoulos C., and Contopoulos G., 2021, A& A, 655, A55.

Hartman P., 1960, Proc. Amer. Math. Soc. 11, 610

Hart R. E., Bamford S. P., and Hayes W.B., 2017, MNRAS, 472, 2263

Hénon M., 1982, A&A, 114, p.211.

Hohl F., 1971, ApJ, 168, 343

Holley-Bockelmann K., Weinberg M., and Katz N., 2005, MNRAS, 363, 991

Hou L.G., & Han J.L., 2014, A& A, 569, p.A125.

Junqueira T.C., Lépine J.R.D., Braga C.A.S., and Barros D.A., 2013, A& A, 550, p.A91.

Hubble E. P., 1926b, ApJ, 64, 321

Junqueira T.C., Chiappini C., Lépine J.R.D., Minchev I., and Santiago B.X., 2015, MNRAS, 449, 2336

Jeans J.H., 1919, Phil. Trans. R. Soc. London A, 218, 157

Kalapotharakos, C., Patsis, P.A., and Grosbøl, P, 2010, MNRAS, 403, 83

Kalnajs A.J., 1971, Dynamics of flat galaxies. I. ApJ, p.275.

Kalnajs A., 1973, Proc. Astron. Soc. Australia 2, 174

Kalnajs A.J., 1991, p.323.

Kalnajs A.J., 1991. Pattern speeds of density waves. Dynamics of Disc Galaxies, p.323.

Kaufmann D. E., & Contopoulos G., 1996, A&A, 309, 381

Kennicutt R. C., 1981, Astron. J., 86, 1847

Kwak S., Kim W.T, Rey S.C, and Kim S., 2017, ApJ, 839, 24

Kormendy J., & Kennicutt R.C., 2004, A&A, 42, 603

Kormendy J., 2013, in 'Secular Evolution of Galaxies', XXIII Canary Islands Winter School of Astrophysics. J Falcon-Barroso and J. H. Knapen (eds), Cambridge University Press, pp.1-154.

Kyziropoulos P., Efthymiopoulos C., Gravannis G., and Patsis P., 2016, MNRAS, 463, 2210

Kyziropoulos P., Filelis-Papadopoulos C.K., Gravvanis G., and Efthymiopoulos C., 2017, J. Supercomputing, 73, 5197-5220.

Kyziropoulos P., Filelis-Papadopoulos C.K., Gravvanis G., and Efthymiopoulos C., 2017, J. Supercomputing

Laskar J., 1990, Icarus, 88, 266-291.

Laskar J., Froeschlé C., and Celletti A., 1992, Physica D, 56(2-3), 253-269

Laskar J., 1993, Physica D 67, 257281

Laskar J., 2003, ArXiv e-prints [arXiv:math/0305364]

Lépine J. R. D., Roman-Lopes A., Abraham Z., Junqueira T. C., and Mishurov Y. N., 2011, MNRAS, 414(2), 1607-1616.

Lin C.C., & Shu F.H., 1964, ApJ, 140, 646

Lin C.C., & Shu F.H., 1966, Proceedings of the National Academy of Sciences, 55(2), pp.229-234.

Lindblad B., 1941, Stockholm Obs. Ann., 13, pp.10-1.

Lindblad, B., 1942, Stockholm Obs. Ann., 14, pp.1-1.

Lindblad, B., 1948, Stockholm Obs. Ann, 15(5), pp.1-11.

Lindblad B., 1955, Stockholm Obs. Ann., 18, 6

Lindblad B., 1956, Stockholm Obs. Ann., 19, 7

Lindblad B., 1957, Stockholm Obs. Ann., 19, 9

Lindblad B, & Lindblad P.O., 1958, "On rotating ring orbits in galaxies." Symposium-International Astronomical Union. Vol. 5. Cambridge University Press, 1958., Bertil, and Per Olof Lindblad. "On rotating ring orbits in galaxies." Symposium-International Astronomical Union. Vol. 5. Cambridge University Press.

Lindblad B., 1960, Stockholm Obs. Ann. 21, 4

Lindblad B., 1961, Stockholm Obs. Ann. 21, 8

Lindblad, B., 1962, Problems of Extra-Galactic Research (Vol. 15, p. 146).

Lindblad, B., 1963, Stockholm Obs. Ann., 5, p.5.

Lintott C.J., Schawinski K., Slosar A., Land K., Bamford S., Thomas D., Raddick M.J., Nichol R.C., Szalay A., Andreescu D., and Murray P., 2008, MNRAS, 389(3), pp.1179-1189.

Lintott C., Schawinski K., Bamford S., Slosar A., Land K., Thomas D., Edmondson E., Masters K., Nichol R.C., Raddick M.J., and Szalay A., 2011, MNRAS, 410(1), pp.166-178.

Little B., & Carlberg R.G., 1991, MNRAS, 250, 161

Lokas E, 2016, ApJ, 830, 20L

Lynden-Bell D., & Kalnajs A.J., 1972, MNRAS, 157, 1

Lynden-Bell D.,1979, MNRAS, 187(1), 101-107.

Lynden-Bell D., & Kalnajs A. J., 1972, MNRAS, 157(1), 1-30.

Martinez-Valpuesta I., & Shlosman I., 2004, 2004, ApJ, 613, 29

Martinez-Valpuesta I., Shlosman I., and Heller C., 2006, ApJ, 637, 214

Masters K.L., Lintott C.J., Hart R.E., Kruk S.J., Smethurst R.J., Casteels K.V., Keel W.C., Simmons B.D., Stanescu D.O., Tate J., and Tomi S., 2019, MNRAS, 487, 1808

Meidt S.E., Rand R.J., and Merrifield M.R., 2009, ApJ, 702, 277

Mertzanides, 1976, A&A, 50, 395

Minchev I., Quillen A.C., 2006, MNRAS, 368, 623

Minchev I., Famaey B., Quillen A.C., Di Matteo P., Combes F., Vlajić M., Erwin P., and Bland-Hawthorn J., 2012, A&A, 548, 126

Miyamoto M., & Nagai R., 1975, Publ. Astron. Soc. Japan, 27, 533

Morgan W. W., 1958, PASP, 70, 364

Morgan W. W., 1959, PASP, 71, 394

Monet D. G, & Vandervoort PO, 1978, ApJ, 221, 87,

Mosenkov A., Savchenko S., and Marchuk A., 2020, Res. Astron. Astroph., 20, 120

Moser J., 1956, Commun. Pure Appl. Math., 9, 673

Moser J., 1958, Commun. Pure Appl. Math., 11, 257

Norman C. A., 1978, MNRAS, 182, 457

O'Neill J.K., & Dubinski J., 2003, MNRAS, 346, 251

Patsis P. A., Contopoulos G., and Grosbol P., 1991, A& A(ISSN 0004-6361), vol. 243, no. 2, March 1991, p. 373-380., 243, 373-380.

Patsis P. A., Hiotelis N., Contopoulos G.,and Grosbol P., 1994, A& A, 286, 46-59.

Patsis P. A., & Grosbøl P., 1996, A&A, 315, 371

Patsis P. A., Grosbol P., and Hiotelis N.,1997, A& A, 323, 762-774.

Patsis P.A., 2006, MNRAS, 369, L56

Patsis P.A., Kaufmann D.E., Gottesman S.T., and Boonyasait V., 2009, MNRAS, 394, 142

Patsis P.A., & Tsigaridi L., 2017, Ap SS, 362(7), 1-17

Pettitt A. R., Dobbs C. L., Acreman D. M., and Price D. J., 2014, MNRAS, 444, 919

Pfenniger D., & Friedli D., 1991, A&A, 252, 75

Pichardo B., Martos M., Moreno E., and Espresate J., 2003, ApJ, 582, 230

Poincaré H., 1912, Sur un théoreme de géométrie. Rendiconti del Circolo Matematico di Palermo (1884-1940), 33(1), 375-407.

Poincaré H., 1957, Les Méthodes Nouvelles de la Mécanique Céleste Gauthier Villars. Paris I (1892); Paris II (1893); Paris III (1899).

Quillen A.C., 2003, ApJ, 125, 785

Quillen A.C., Dougherty J., Bagley M.B., Minchev I., and Comparetta J., 2011, MNRAS, 417, 762

Raha N., Sellwood J.A., James R.A., and Kahn F.D., 1991, Nat, 352, 411

Rautiainen P., & Salo H., 1999, A&A, 348, 737

Reynolds J.H., 1927, The classification of the spiral nebulae. The Observatory, Vol. 50, p. 185-189 (1927), 50, pp.185-189.

Roca-Fàbrega S, Valenzuela O., Figueras F., Romero-Gómez M., Vel'azquez H., Antoja T., and Pichardo B, 2013, MNRAS, 432, 2878

Romero-Gomez M., Masdemont J.J., Athanassoula E., and Garcia-Gomez C., 2006, A&A, 453, 39

Romero-Gomez M., Athanassoula E., Masdemont J.J., and Garcia-Gomez C., 2007, A&A, 472, 63

Rosenbluth M. N., Sagdeev R. A., Taylor J. B., and Zaslavsky G. M., 1966, Nucl. Fusion, 6, 217

Rosse E. o., 1850, Philosophical Transactions of the Royal Society, 140, 499

Safronov V. S., 1960, Ann. d'ap. y 23, 979.

Sánchez-Martín P., Masdemont J.J., and Romero-Gómez M., 2018, A&A, 618, A72

Savchenko S., Marchuk A., Mosenkov A., and Grishunin K., 2020, MNRAS, 493, 390

Seigar M. S., Block D. L., Puerari I., Chorney N. E., and James P. A., 2005, MNRAS, 359, 1065

Seigar M. S., Bullock J. S., Barth A. J., and Ho L. C., 2006, ApJ, 645, 1012

Sellwood J. A., 1980, A&A, 89, 296

Sellwood J. A., & Carlberg R. G., 1984, ApJ, 282, 61

Sellwood J.A., & Sparke L.S., 1988, MNRAS, 231, 25

Sellwood J.A., & Binney J.J., 2002, MNRAS, 336, 785

Sellwood J. A., 2000, Astrophysics and Space Science, 272, 31-43.

Sellwood J. A., 2010, in Gilmore G., Planets Stars and Stellar Systems, Vol. 5. Springer, Heidelberg, preprint (arXiv:1006.4855)

Sellwood J.A., 2014, RvMP, 86, 1

Sparke L. S., & Sellwood J. A., 1987, MNRAS, 225(3), 653-675.

Speights J.C., & Westpfahl D.J., 2012, ApJ, 752, 52

Speights J.C., & Rooke P., 2016, ApJ, 826, 2

Schwarz M. P., 1984, MNRAS, 209(1), 93-109.

Struck C., 2015, MNRAS, 450, 2217

Toomre A., 1964, ApJ, 139, 1217

Toomre A., 1977, A&A, 15, pp.437-478.

Tremaine S., & Weinberg M. D., 1984, ApJ, 282, L5

Tremaine S., & Weinberg M. D., 1984b, MNRAS, 209, 729

Tsoutsis P., Efthymiopoulos C., and Voglis N., 2008, MNRAS, 387, 1264

Tsoutsis P., Kalapotharakos C., Efthymiopoulos C., and Contopoulos G., 2009, A&A, 495, 743

Vandervoort P. O., 1971, ApJ, 166, 37

Vandervoort P. O., 1973, ApJ, 180, 739

vandervoort P. O., & Monet D. G, 1975, ApJ, 201, 311

Vera-Villamizar N., Dottori H., Puerari I., and de Carvalho R., 2001, ApJ, 547, 187

Voglis N., Tsoutsis P., and Efthymiopoulos C., 2006a, MNRAS, 373, 280

Voglis N., Stavropoulos I., and Kalapotharakos C., 2006, MNRAS, 372(2), pp.901-922.

Walker G. H., & Ford J., 1969, Phys. Rev., 188, 416

Weaver H., 1970, in Becker W., Kontopoulos G. I., eds, Proc. IAU Symp. 38, The Spiral Structure of our Galaxy. Reidel, Dordrecht, p. 126

Weinberg M.D., 1985, MNRAS, 213(3), pp.451-471.

Weinberg M.D. & Katz N., 2007, MNRAS, 375, 460

Wiggins S., 1990, 'Introduction to Nonlinear Dynamical Systems and Chaos', Springer, New York

Willett K.W., Lintott C.J., Bamford S.P., Masters K.L., Simmons B.D., Casteels K.R., Edmondson E.M., Fortson L.F., Kaviraj S., Keel W.C., and Melvin T., 2013, MNRAS, 435(4), pp.2835-2860.

Wu Y-T, Pfenniger D., and Taam R.E., 2016, ApJ, 830, 111

York D. G., Adelman J., and Anderson J. E., 2000, A&A, 120, 1579

Yu S., & Ho L., 2019, ApJ, 871, 194

Zhang X., 2018, De Gruyter

Zouloumi K., Harsoula M., and Efthymiopoulos C., 2024, MNRAS,529(3), 1941–1957

# Appendix A

# Asymptotic analysis in the integrals of NAFF algorithm

The integrals (4.2) and (4.3) give terms of the following form:

$$F_c(\sigma) = \sum_k \frac{D_k\omega_k}{({\omega_k}^2 - \sigma^2)T} - \frac{D_k\omega_k\cos((\omega_k-\sigma)T)}{({\omega_k}^2-\sigma^2)T} + \frac{D_k\omega_k}{({\omega_k}^2-\sigma^2)T} - \frac{D_k\sigma\cos((\omega_k-\sigma)T)}{({\omega_k}^2-\sigma^2)T} - \frac{D_k\cos((\omega_k+\sigma)T)}{(\omega_k+\sigma)T} + \frac{C_k\sin((\omega_k+\sigma)T)}{(\omega_k+\sigma)T} + \frac{C_k\sin((\omega_k-\sigma)T)}{(\omega_k-\sigma)T} \tag{A.1}$$

$$F_s(\sigma) = \sum_k -\frac{C_k\sigma}{({\omega_k}^2-\sigma^2)T} + \frac{C_k\omega_k\cos((\omega_k-\sigma)T)}{({\omega_k}^2-\sigma^2)T} - \frac{C_k\sigma}{({\omega_k}^2-\sigma^2)T} + \frac{C_k\sigma\cos((\omega_k-\sigma)T)}{({\omega_k}^2-\sigma^2)T} - \frac{C_k\cos((\omega_k+\sigma)T)}{(\omega_k+\sigma)T} - \frac{D_k\sin((\omega_k+\sigma)T)}{(\omega_k+\sigma)T} + \frac{D_k\sin((\omega_k-\sigma)T)}{(\omega_k-\sigma)T} \quad . \tag{A.2}$$

We make asymptotic analysis in equations (A.1), (A.2) in order to examine the limiting behaviour of these integrals as $\sigma \to \omega_k$ and the series' length T becomes a large quantity.

For the integral of $F_c$ in (A.1) we have:

-The first two terms in (A.1) can be simplified using the relation $\cos((\omega_k-\sigma)T) = 1 - 2\sin^2\left(\frac{(\omega_k-\sigma)T}{2}\right)$ and the limit as $\sigma \to \omega_k$ is zero :

$$\lim_{\sigma\to\omega_k} \frac{D_k\omega_k}{({\omega_k}^2-\sigma^2)T} - \frac{D_k\omega_k\cos((\omega_k-\sigma)T)}{({\omega_k}^2-\sigma^2)T} = \lim_{\sigma\to\omega_k} \frac{D_k\omega_k}{\omega_k+\sigma} \frac{\sin^2\left(\frac{(\omega_k-\sigma)T}{2}\right)}{\left(\frac{(\omega_k-\sigma)T}{2}\right)} = 0 \quad . \tag{A.3}$$

-Similarly, the 3rd and the 4th term in (A.1) give a limit of the following form:

$$\lim_{\sigma\to\omega_k} \frac{D_k\omega_k}{({\omega_k}^2-\sigma^2)T} - \frac{D_k\sigma\cos((\omega_k-\sigma)T)}{({\omega_k}^2-\sigma^2)T} = \lim_{\sigma\to\omega_k} \frac{D_k}{(\omega_k+\sigma)T} + \lim_{\sigma\to\omega_k} \frac{D_k\sigma}{\omega_k+\sigma} \frac{\sin^2\left(\frac{(\omega_k-\sigma)T}{2}\right)}{\left(\frac{(\omega_k-\sigma)T}{2}\right)} = \frac{D_k}{2\omega_k T} \quad . \tag{A.4}$$

-The limit of the 5th and 6th term in (A.1) as $\sigma \to \omega_k$ is :

$$\lim_{\sigma\to\omega_k} \frac{D_k \cos((\omega_k+\sigma)T)}{(\omega_k+\sigma)T} = \frac{D_k \cos(2\omega_k T)}{2\omega_k T}$$
$$\lim_{\sigma\to\omega_k} \frac{C_k \sin((\omega_k+\sigma)T)}{(\omega_k+\sigma)T} = \frac{C_k \sin(2\omega_k T)}{2\omega_k T} \quad . \tag{A.5}$$

-The limit of the 7th term in (A.1) as $\sigma \to \omega_k$ gives the amplitude of the time series (4.1) $C_k$:

$$\lim_{\sigma\to\omega_k} \frac{C_k \sin((\omega_k-\sigma)T)}{(\omega_k-\sigma)T} = C_k \quad . \tag{A.6}$$

We conclude that:

$$F_c(\sigma=\omega_k) = C_k + \mathcal{O}(1/T) \quad . \tag{A.7}$$

In the same way we find that:

$$F_s(\sigma=\omega_k) = D_k + \mathcal{O}(1/T) \quad . \tag{A.8}$$

# Appendix B

# The error of the NAFF algorithm in the determination of the fundamental frequencies

The calculation of the solution of (4.6) leads us to the error $d\sigma$ of the NAFF algorithm for the determination of the fundamental frequencies $\omega_k$ of a quasi-periodic time series (4.1). Approximating the solution with the Newton's method, we find the following expression for the error $d\sigma$, which is a rational function of T:

$$d\sigma = \frac{P_n(T)}{P_d(T)} \tag{B.1}$$

where $P_n(T)$ in the numerator is a 2nd degree polynomial in $T$:

$$P_n(T) = \sum_{n=1}^{2} a_n T^n \tag{B.2}$$

with coefficients $a_n$ given by:

$$\begin{aligned}
a_0 &= 6\omega_k \left( {C_k}^2 \cos(2\omega_k T) - {C_k}^2 + {D_k}^2 \cos(2\omega_k T) - {D_k}^2 \right) \\
a_1 &= 6\omega_k \left( 2C_k D_k \omega_k \cos(2\omega_k T) - 2C_k D_k \omega_k + 2{D_k}^2 \omega_k \sin(2\omega_k T) \right) \\
a_2 &= 6\omega_k \left( {C_k}^2 {\omega_k}^2 \cos(2\omega_k T) + {C_k}^2 {\omega_k}^2 + 2C_k D_k {\omega_k}^2 \sin(2\omega_k T) \right) \\
&- 6\omega_k \left( {D_k}^2 {\omega_k}^2 \cos(2\omega_k T) + {D_k}^2 {\omega_k}^2 \right)
\end{aligned} \tag{B.3}$$

and $P_n(T)$ in the denominator is a 4th degree polynomial in $T$:

$$P_d(T) = \sum_{n=1}^{4} b_n T^n \tag{B.4}$$

with coefficients $b_n$ given by:

$$\begin{aligned}
b_0 &= 9{C_k}^2 \cos(2\omega_k T) - 9{C_k}^2 + 9{D_k}^2 \cos(2\omega_k T) - 9{D_k}^2 \\
b_1 &= 6{C_k}^2 \omega_k \sin(2\omega_k T) + 12 C_k D_k \omega_k \cos(2\omega_k T) - 12 C_k D_k \omega_k + \\
&18 {D_k}^2 \omega_k \sin(2\omega_k T) \\
b_2 &= 6{C_k}^2 {\omega_k}^2 + 12 C_k D_k {\omega_k}^2 \sin(2\omega_k T) - 12{D_k}^2 {\omega_k}^2 \cos(2\omega_k T) - \\
&6{D_k}^2 {\omega_k}^2 \\
b_3 &= 4{C_k}^2 {\omega_k}^3 \sin(2\omega_k T) - 8 C_k D_k {\omega_k}^3 \cos(2\omega_k T) + 8 C_k D_k {\omega_k}^3 - \\
&4{D_k}^2 {\omega_k}^3 \sin(2\omega_k T) \\
b_4 &= 2{C_k}^2 {\omega_k}^4 + 2{D_k}^2 {\omega_k}^4 \quad .
\end{aligned}$$

For T large, we then obtain:

$$d\sigma \approx \frac{a_2}{b_4 T^2} + \dots \tag{B.5}$$

We conclude that the error $d\sigma$ is proportional to $T^{-2}$.

Furthermore, since $F_c(\sigma)$ and $F_s(\sigma)$ have a local extreme at any of the values $\sigma = \omega_k$, with $k = 1, \dots, N_k$, we obtain: $F_c(\omega_k + d\sigma_k) = F_c(\omega_k) + \mathcal{O}({d\sigma_k}^2) = C_k + \mathcal{O}(1/T) + \mathcal{O}(1/T^4)$, that is:

$$F_c(\omega_k + d\sigma_k) = C_k + \mathcal{O}(1/T) \tag{B.6}$$

and, analogously,

$$F_s(\omega_k + d\sigma_k) = D_k + \mathcal{O}(1/T) \tag{B.7}$$

In summary, scanning the frequency space with small steps $\Delta\sigma << |d\sigma_k|$ in an interval $\sigma_{min} < \omega_k < \sigma_{max}$, and computing the integrals $F_c(\sigma_j)$, $F_s(\sigma_j)$ for any of the values $\sigma_j = \sigma_{min} + j\Delta\sigma$, with $j = 0, \dots, N_\sigma$ with $N_\sigma = \left[\frac{\sigma_{max} - \sigma_{min}}{\Delta\sigma}\right]$, allows to compute the values $\sigma_{j_{max}}$ such that $P(\sigma_{j_{max}}) = F_c(\sigma_{j_{max}})^2 + F_s(\sigma_{j_{max}})^2$ is maximum with respect to any of the remaining values $\sigma_j$, $j \neq j_{max}$ in the interval. We then have a determination of the frequency $\omega_k \approx \sigma_{j_{max}}$ with an error $\mathcal{O}(1/T^2)$, and of the amplitudes $C_k = F_c(\sigma_{j_{max}})$, $D_k = F_s(\sigma_{j_{max}})$, with an error $\mathcal{O}(1/T)$.